GeoPlanet: Earth and Planetary Sciences

Ewa Niemczura
Barry Smalley
Wojtek Pych *Editors*

Determination of Atmospheric Parameters of B-, A-, F- and G-Type Stars

Lectures from the School of Spectroscopic Data Analyses

Springer

GeoPlanet: Earth and Planetary Sciences

For further volumes:
http://www.springer.com/series/8821

Ewa Niemczura · Barry Smalley
Wojtek Pych
Editors

Determination of Atmospheric Parameters of B-, A-, F- and G-Type Stars

Lectures from the School of Spectroscopic Data Analyses

Springer

Editors
Ewa Niemczura
Astronomical Institute
University of Wrocław
Wrocław
Poland

Wojtek Pych
Nicolaus Copernicus Astronomical Centre
Polish Academy of Sciences
Warszawa
Poland

Barry Smalley
Astrophysics Group
Keele University
Newcastle-under-Lyme, Staffordshire
UK

The GeoPlanet: Earth and Planetary Sciences Book Series is in part a continuation of Monographic Volumes of Publications of the Institute of Geophysics, Polish Academy of Sciences, the journal published since 1962 (http://pub.igf.edu.pl/index.php).

ISSN 2190-5193 ISSN 2190-5207 (electronic)
ISBN 978-3-319-06955-5 ISBN 978-3-319-06956-2 (eBook)
DOI 10.1007/978-3-319-06956-2
Springer Cham Heidelberg New York Dordrecht London

Library of Congress Control Number: 2014943745

Printed on acid-free paper

Springer is part of Springer Science+Business Media (www.springer.com)

Series Editors

Managing Editor

Anna Dziembowska
Institute of Geophysics, Polish Academy of Sciences

Advisory Board

Kon-Kee Liu
Institute of Hydrological
and Oceanic Sciences
National Central University Jhongli
Jhongli, Taiwan

Teresa Madeyska
Research Centre in Warsaw
Institute of Geological Sciences
Warszawa, Poland

Stanisław Massel
Institute of Oceanology
Polish Academy of Sciences
Sopot, Polska

Antonio Meloni
Instituto Nazionale di Geofisica
Rome, Italy

Evangelos Papathanassiou
Hellenic Centre for Marine Research
Anavissos, Greece

Kaja Pietsch
AGH University of Science
and Technology
Kraków, Poland

Dušan Plašienka
Prírodovedecká fakulta, UK
Univerzita Komenského
Bratislava, Slovakia

Barbara Popielawska
Space Research Centre
Polish Academy of Sciences
Warszawa, Poland

Tilman Spohn
Deutsches Zentrum für Luftund
Raumfahrt in der Helmholtz
Gemeinschaft
Institut für Planetenforschung
Berlin, Germany

Krzysztof Stasiewicz
Swedish Institute of Space Physics
Uppsala, Sweden

Ewa Szuszkiewicz
Department of Astronomy
and Astrophysics
University of Szczecin
Szczecin
Poland

Roman Teisseyre
Earth's Interior Dynamics Lab
Institute of Geophysics
Polish Academy of Sciences
Warszawa, Poland

Jacek Tronczynski
Laboratory of Biogeochemistry
of Organic Contaminants
IFREMER DCN_BE
Nantes, France

Steve Wallis
School of the Built Environment
Heriot-Watt University
Riccarton, Edinburgh
Scotland, UK

Wacław M. Zuberek
Department of Applied Geology
University of Silesia
Sosnowiec, Poland

Piotr Życki
Nicolaus Copernicus Astronomical
Centre
Polish Academy of Sciences
Warszawa
Poland

Preface

During the past years, asteroseismology has greatly benefited from space missions such as *Kepler*, *CoRoT* and *MOST*. Data of unprecedented quality have challenged both observers and theorists, allowing us to improve our knowledge of stars significantly. However, during this process it became very clear that ground-based follow-up spectroscopy is crucial for an in-depth seismic study, as it provides information on different stellar parameters. Keeping this in mind, the 'Spring School of Spectroscopic Data Analyses' was organised by the Astronomical Institute of the University of Wrocław, Poland, from April 8 to 12, 2013.

The aim of this school was to provide researchers with an introduction to methods used to obtain the atmospheric parameters of B-, A-, F- and G-type stars. The lecture topics included the determination of atmospheric models and synthetic spectra, application of LTE and NLTE analysis and the analysis of high- and low-resolution data. The practical exercises undertaken during the workshop not only allowed the participants to learn how to compute atmospheric models and synthetic spectra, but also how to determine the atmospheric parameters (effective temperature, surface gravity, microturbulence, etc.), abundances of chemical elements and stellar rotation.

The school was an initiative of *Kepler* Asteroseismic Science Consortium (KASC) working group on main-sequence pulsators and was primarily intended for Ph.D. students and postdocs. The lectures presented here were given by experienced scientists who actively work on stellar atmospheres. We are confident that these lectures will provide an important tool for all students interested in stellar spectroscopy.

The school was sponsored by the Nicolaus Copernicus Astronomical Centre of the Polish Academy of Sciences, Polish Academy of Arts and Sciences, Astronomical Institute of the University of Wrocław and Copernicus Foundation for Polish Astronomy.

Ewa Niemczura
Barry Smalley
Wojtek Pych

Contents

Contributors

Maria Bergemann Institute of Astronomy, University of Cambridge, Cambridge, UK

Giovanni Catanzaro INAF, Osservatorio Astrofisico di Catania, Catania, Italy

Ben Davies Astrophysics Research Institute, Liverpool John Moores University, Liverpool, UK

Richard Gray Appalachian State University, Boone, NC, USA

Swetlana Hubrig Leibniz-Institut für Astrophysik Potsdam, Potsdam, Germany

Jiří Kubát Astronomický ústav AV ČR, Ondřejov, Czech Republic

Rolf-Peter Kudritzki Institute for Astronomy, University of Hawaii, Honolulu, HI, USA; Max-Planck-Institute for Astrophysics, Garching, Germany

Robert L. Kurucz Harvard-Smithsonian Center for Astrophysics, Cambridge, MA, USA

Thomas Nordlander Division of Astronomy and Space Physics, Department of Physics and Astronomy, Uppsala University, Uppsala, Sweden

Nikolai Piskunov Department of Physics and Astronomy, Uppsala University, Uppsala, Sweden

Tatiana Ryabchikova Institute of Astronomy, Russian Academy of Sciences, Moscow, Russia

Markus Schöller European Southern Observatory, Garching, Germany

Aldo Serenelli Institut de Ciències de l'Espai, Facultat de Ciències, Campus UAB, Bellaterra, Spain

Barry Smalley Astrophysics Group, Keele University, Keele, Staffordshire, UK

Sérgio G. Sousa Centro de Astrofísica, Universidade do Porto, Rua das Estrelas, Porto, Portugal

Brankica Šurlan Astronomický ústav AV ČR, Ondřejov, Czech Republic; Matematički Institut SANU, Beograd, Republic of Serbia

Katrien Uytterhoeven Instituto de Astrofísica de Canarias, La Laguna, Tenerife, Spain; Departamento de Astrofísica, Universidad de La Laguna, La Laguna, Tenerife, Spain

Spring School of Spectroscopic Data Analyses: Determination of Atmospheric Parameters of B, A, F and G-type Stars—Introduction

Katrien Uytterhoeven

Abstract Several aspects of astrophysics require accurate atmospheric parameters and abundances. A powerful way of retrieving information on a star's effective temperature, surface gravity, rotation rate, and chemical composition is through the stellar spectrum. This spectroscopic school aims at training researchers in performing spectral analyses, with the motivation of recruiting manpower to join the project on a systematic characterisation of *Kepler* Main Sequence pulsators, for which a collection of low-, mid-, and high-resolution spectra is available for more than 1,000 asteroseismic targets of spectral types B, A, and F.

Keywords Stars: fundamental parameters · Stars: abundances · Stars: general

1 The Need for Accurate Atmospheric Parameters and Abundances from an Astrophysical Point of View

Why has it been important to develop methods on derivation of stellar effective temperature ($T_{\rm eff}$) and surface gravity ($\log g$)? Why are we interested in a refined picture of the chemical composition of a particular star? Because $T_{\rm eff}$, $\log g$, and chemical composition are stepping-stones towards the characterisation of the star.

Stars are described by mass (M), luminosity (L), radius (R), age, chemical composition, angular momentum, and magnetic field, among other parameters. Generally, not many of these stellar parameters can be directly observed, and hence other ways must be found to infer them. Effective temperature and $\log g$ are key parameters as they not only define the physical conditions of the stellar atmosphere, but are also directly related to M, L, and R through the relations:

K. Uytterhoeven (✉)
Instituto de Astrofísica de Canarias, 38205 La Laguna, Tenerife, Spain
e-mail: katrien@iac.es

K. Uytterhoeven
Departamento de Astrofísica, Universidad de La Laguna, 38200 La Laguna, Tenerife, Spain

E. Niemczura et al. (eds.), *Determination of Atmospheric Parameters of B-, A-, F- and G-Type Stars*, GeoPlanet: Earth and Planetary Sciences,
DOI: 10.1007/978-3-319-06956-2_1,

$$L = 4\pi R^2 \sigma T_{\rm eff}^4 \tag{1}$$

$$g = GM/R^2\,, \tag{2}$$

with σ the Stefan–Boltzmann constant and G the gravitational constant. Subsequently, the stellar age can be estimated through theoretical evolutionary tracks in the Hertzsprung–Russell (H–R) diagram.

Several aspects of astrophysics require accurate atmospheric parameters, chemical abundances, and/or values of the projected rotational velocity ($v \sin i$). As an illustration we mention a few.

- **Stellar classification** is an important prerequisite to detailed spectral analyses. Stars are classified in spectral classes, which depend on their surface temperature and luminosity. For most stars, excluding (chemically) peculiar stars, an accurate spectral type is a good indicator of their $T_{\rm eff}$ and $\log g$.
- **Stellar atmosphere models** are governed and defined by processes in the stellar atmosphere. Effective temperature, $\log g$, element abundances, the stellar rotation rate (projected rotational velocity $v \sin i$), and less well-understood parameters such as microturbulence ($\xi_{\rm t}$) play an important role in a good description of the models. To improve stellar atmosphere models, observed spectra of stars with well-known atmospheric parameters for stars of all ages and at different positions in the H–R diagram are needed.
- A precise determination of the stellar rotation rate in combination with element abundances allow the study of **abundance surface inhomogeneities** (stellar spots).
- What causes **chemical peculiarity**? Is there a relation between chemical peculiarity, rotation, and/or magnetic field?
- Models of **convection** can be tested through the mechanism of microturbulence $\xi_{\rm t}$. In massive stars $\xi_{\rm t}$ finds its origin in sub-surface convection zones, while for less massive stars outer convection layers are the places of origin.
- In **asteroseismic studies**, accurate values of $T_{\rm eff}$ and $\log g$ are crucial to define the best-fitting and unique asteroseismic model. Moreover, they are indispensable to test instability strips of specific pulsating classes along the Main Sequence (MS), such as β Cep, Slowly Pulsating B stars (SPBs), δ Sct and γ Dor stars. A good knowledge of the stellar rotation rate, on the other hand, is needed to understand and recognise rotational splitting of stellar pulsation modes. Moreover, in case of rapidly rotating pulsating stars the rotation causes a deformation of the surface velocity fields. To be able to test and improve pulsational models for rapidly rotating stars, a careful determination of $v \sin i$ is very important.
- Understanding **stellar structure and evolution of the Milky Way** requires a detailed knowledge of fundamental properties, such as mass, age, kinematics and chemical abundances of its stellar populations. An accurate characterisation of stars at various stages of their lives and at different positions in the H–R-diagram is needed.
- Analysis of the chemical composition of different populations of stars probes **galactic chemical evolution** and test models on element production by thermonu-

clear reactions in stellar interiors and by supernovae. Additionally, comparison of observations and models of chemical evolution test abundance gradients across the Milky Way disk, gas infall episodes, and star formation rates.

2 Spectra as a Powerful Tool

Several methods are in use to derive atmospheric parameters. We refer to Chap. 8 for an overview of methods involving photometric indices and spectrophotometry. Here we focus on spectra. High-resolution spectra are a powerful tool for the characterisation of stars, as information on $T_{\rm eff}$ as well as $\log g$, element abundance, $v \sin i$ and $\xi_{\rm t}$ can be inferred.

2.1 How to Choose the Ideal Spectrograph?

Spectrographs come in different types and with different specifications. When selecting a spectrograph, one needs to keep in mind what information one would like to derive from the spectra and what scientific goals one wants to achieve. Some important spectrograph specifications are: the resolving power of the spectrograph (R), available wavelength range, and instrumental efficiency, i.e. throughput of the starlight, which affects the signal-to-noise ratio (SNR).

2.1.1 Spectral Resolution

Low-resolution spectra ($R < 5{,}000$) are suited to perform a spectral classification, to distinguish between rapid and slow rotation, and to detect chemical peculiarities. For hotter stars, and depending on the available wavelength range, information on $T_{\rm eff}$ can mainly be derived from Balmer lines. Medium-resolution spectrographs ($5{,}000 < R < 40{,}000$) are generally well-suited for the spectral analysis of many stars, provided that non-blended, well-resolved lines are selected. For fast rotating stars ($v \sin i > 100\,{\rm km\,s^{-1}}$), medium-resolution spectra are generally sufficient for a spectral analysis. In the case of slow rotators, one optimally would prefer high-resolution spectra ($R > 40{,}000$). The higher the spectral resolution, the higher the confidence in the results from the chemical analysis, and in derived values of $T_{\rm eff}$, $\log g$, $v \sin i$, and $\xi_{\rm t}$.

2.1.2 Wavelength Range

The available wavelength range varies from instrument to instrument. Slit spectra focus on a limited range, while échelle spectra can cover the entire optical spectrum,

often with gaps. If possible, adapt the order definition such that the most important spectral lines you are interested in are completely recorded. Make also sure that sufficient numbers of element lines are available for a reliable analysis. Slit spectra with a limited wavelength range limit the output of the spectral analysis. When planning on using Balmer lines, make sure that they are well defined in the spectrum. In case of échelle spectra, the broad wings of Balmer lines are often located at the edge of spectral orders or fall in interorder gaps, making them unusable for a reliable analysis. Using spectral lines that are 'reconstructed' by merging two different orders is not advisable.

2.1.3 Signal-to-Noise Ratio

The accuracy of the spectral analysis depends not only on the spectral resolution, but also on the SNR value of the spectra. For a good analysis, a SNR value of at least 100–150 is needed. The higher the SNR value, the better! However, keep in mind that for fainter targets ($V > 11$) obtaining a spectrum with SNR >100 becomes very time consuming with 1–2 m-class telescopes, or is simply not feasible. In these cases, multiple spectra can be obtained and combined to one spectrum with a higher SNR value (e.g. two spectra of SNR ∼80 or three spectra of SNR ∼60 result in one combined spectrum with SNR ≥100).

3 KASC and the Characterisation of Asteroseismic *Kepler* Targets

Successful asteroseismic modelling depends strongly on the accuracy of the parameters $T_{\rm eff}$ and $\log g$, while information on $v \sin i$ and chemical abundances is important for the understanding of the internal processes. Many of the thousands of stars observed continuously for several months to years with the NASA *Kepler* space mission (Borucki et al. 2010) are pulsating and of interest to the Kepler Asteroseismic Science Consortium (KASC) for asteroseismic studies. However, the *Kepler* one-filter photometric observations do not provide information on stellar atmospheric parameters. Although a characterisation of all *Kepler* targets based on multi-band photometry in Sloan filters and 2MASS HJK bands is available through the Kepler Input Catalogue (KIC), (Latham et al. 2005; Brown et al. 2011), an alternative characterisation of the asteroseismic targets is needed for stars of spectral types earlier than F-type as the KIC values are less reliable in these cases (Lehmann et al. 2011; Molenda-Żakowicz et al. 2011). In particular, KIC values of $T_{\rm eff}$ are not accurate for hot stars ($T_{\rm eff} > 7{,}000$ K) as the Sloan filters and 2MASS photometry do not include the Balmer jump, from which $\log g$ is derived. Also, the general KIC uncertainty on $\log g$ is 0.5 dex which is not good enough for asteroseismic modelling. Therefore, an independent derivation of atmospheric parameters is needed.

To this end, a systematic ground-based follow-up campaign has been set up to obtain multi-colour photometry and/or spectra for as many of the over 5,000 KASC targets as possible (Uytterhoeven et al. 2010a, b). This ambitious task has many challenges. First of all, it is a time consuming project knowing that at most 14 stars can be observed per night with a high-resolution spectrograph on a 2 m-class telescope. Also, a systematic spectral characterisation is only feasible for bright targets ($V < 11$) even though the majority of *Kepler* targets are fainter than $V = 12$. This restriction follows from the requirement of SNR >100 to perform a reliable spectral analysis, the fact that with a high-resolution spectrograph on a 2.5 m telescope exposure times to obtain SNR =100 are of the order of 20, 45, and >90 min for a star of magnitude $V = 9$, 10, 11, respectively, and the sparse number of high-resolution spectrographs on large (>4 m-class) telescopes.

The KASC ground-based observations so far involved 40 different instruments at 35 telescopes at 23 observatories in 12 countries in the Northern Hemisphere, and resulted in over 1,500 observing nights.

4 Motivation of the Spectroscopic School

The aim of the spectroscopic school is to train researchers in performing spectral analyses, including the derivation of $T_{\rm eff}$, $\log g$, $v \sin i$, and chemical abundances. The motivation of the school lies within the project on the systematic characterisation of pulsators of spectral types B, A, and F of the KASC Working Group on MS pulsators (KASC WG#3). The spectral characterisation is needed to describe the pulsational nature of these stars and to investigate possible connections between stellar oscillations, rotation, and chemical peculiarity. In particular, the instability strips of various classes of pulsating stars need to be tested. For instance, it needs to be verified that δ Sct, γ Dor and hybrid δ Sct/γ Dor stars are not confined to the current observational pulsation instability strips but are ubiquitous, as suggested from *Kepler* observations by Uytterhoeven et al. (2011), which would call for a new explanation for the observed pulsational behaviour.

A collection of low-, mid-, and high-resolution spectra is currently available for more than 1,000 asteroseismic targets of spectral types B, A, and F, that partly still need to be analysed, while more data is coming. As within KASC there is a lack of manpower with time and expertise in spectral analysis, new experts in spectral analysis need to be trained.

4.1 Available Spectra of Kepler Main Sequence Pulsators

So far and within KASC WG#3, spectra have been collected for 1,014 out of 3,119 (i.e. 33 %) classified δ Sct, γ Dor, β Cep, and SPB stars. Table 1 lists the instruments involved, sorted according to increasing spectral resolution. The different columns

Table 1 Spectroscopic instruments used for the ground-based follow-up observations of B-, A-, and F-type *Kepler* pulsators

Spectrograph	Telescope	Observatory*	Resolution
IDS	2.5 m INT	ORM (E)	1,400
Multi-object	LAMOST	Xinglong (CN)	1,000/2,000
B&C	2.12 m	OAN-SPM (MX)	2,000
BFOSC	1.5 m Cassini	Loiano (I)	5,000
TWIN	3.5 m	CAHA (E)	10,000
FRESCO	0.91 m	Catania (I)	21,000
ARCES	3.5 m ARC	APO (USA)	33,000
HRS	9.2 m HET	McDonald (USA)	30,000/60,000
FIES	2.56 m NOT	ORM (E)	25,000 /46,000/67,000
Coudé échelle	2.0 m Alfred Jensch	TLS (D)	35,000/67,000
SOPHIE	1.92 m	OHP (F)	46,000
SARG	3.58 m TNG	ORM (E)	57,000
SES	2.1 m Otto Struve	McDonald (USA)	60,000
CS23	2.7 m Harlan J. Smith	McDonald (USA)	60,000
HES	3.0 m Shane	Lick (USA)	60,000–100,000
ESPADONS	3.6 m CFHT	Mauna Kea (USA)	81,000
NARVAL	2.0 m TBL	Pic du Midi (F)	81,000
HERMES	1.2 m Mercator	ORM (E)	90,000

* *APO* Apache Point Observatory, New Mexico
CAHA Calar Alto Astronomical Observatory
OAN-SPM Observatorio Astronómico Nacional, San Pedro Mártir
OHP Observatoire de Haute Provence
ORM Observatorio Roque de Los Muchachos, La Palma
TLS Karl Schwarzschild Observatory, Tautenburg

give the name of the instrument, the telescope, the observatory, and the spectral resolution. Note that some instruments have various settings of spectral resolution.

Table 2 gives an overview of the total number of the considered sample of candidate B-type (β Cep and SPB), δ Sct, γ Dor, and hybrid δ Sct/γ Dor pulsators that have been identified through analysis of *Kepler* light curves. The remaining columns subsequently indicate for each group the number of stars for which low-resolution ($R < 5{,}000$), medium-resolution ($5{,}000 < R < 40{,}000$), and high-resolution ($R > 40{,}000$) spectra are available, and the total number of stars for which spectra have been obtained, together with the percentage with respect to the total sample. We note that there is an observational bias towards bright targets ($V < 11$), as obtaining spectra with SNR >100 becomes very time consuming for fainter targets.

Figure 1 illustrates the location of the candidate δ Sct (top, left panel), γ Dor (top, right panel), and hybrid δ Sct/γ Dor (bottom panel) pulsators with respect to the observed instability strips of δ Sct and γ Dor stars in the ($T_{\rm eff}$, $\log g$)-diagram. The low-resolution, medium-resolution, and high-resolution spectra available for analysis are indicated by asterisks, bullets, and stars, respectively. Note that this concerns candidate γ Dor, hybrid, δ Sct stars [see discussion in Uytterhoeven et al. (2011)].

Table 2 Number of currently available low-resolution, medium-resolution, and high-resolution spectra for candidate B-type, δ Sct, γ Dor, and hybrid δ Sct/γ Dor pulsators

Type	# Stars	# Low-res	# Mid-res	# High-res	# Stars with spectra
B-type	48	13	15	39	45 (=94 %)
δ Sct	1,607	389	37	151	513 (=32 %)
γ Dor	1,205	281	12	70	331 (=27 %)
Hybrid	259	84	10	67	125 (=48 %)

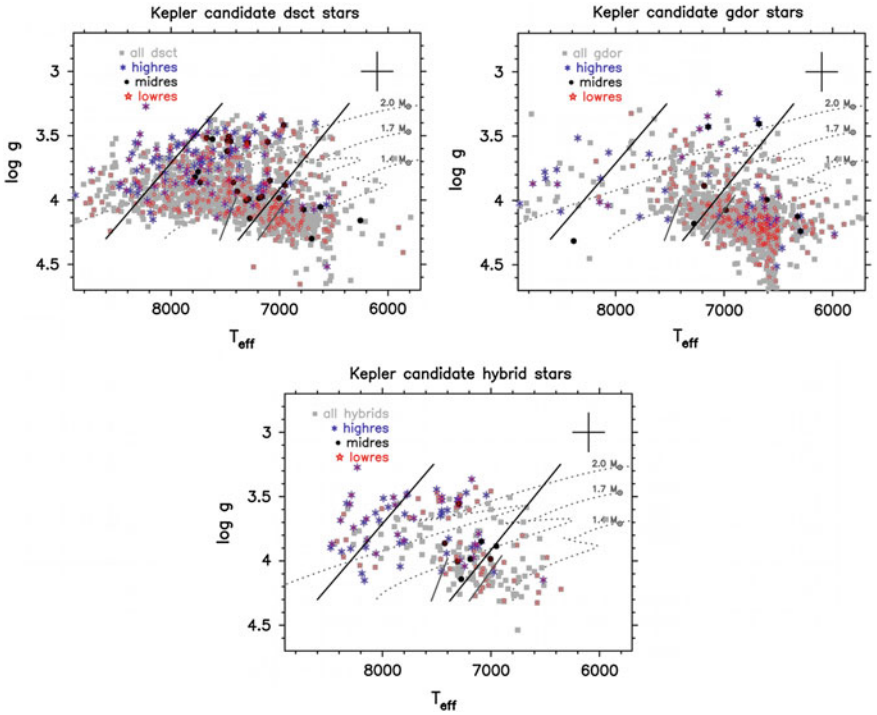

Fig. 1 ($T_{\rm eff}$, log g)-diagram for candidate δ Sct (*top*, *left panel*), γ Dor (*top*, *right panel*), and hybrid δ Sct/γ Dor (*bottom panel*) pulsators observed by *Kepler*. All values plotted are taken from the KIC. Light *grey squared symbols* represent the total sample of stars. *Asterisks*, *bullets*, and *stars* indicate the pulsators that have been observed with high-resolution, medium-resolution, and low-resolution spectrographs, respectively. The *solid thick black* and *light grey lines* mark the *blue* and *red edge* of the observed instability strips of δ Sct and γ Dor stars. Evolutionary tracks for *MS stars* with masses 1.4 $M_\odot$, 1.7 $M_\odot$, and 2.0 $M_\odot$ have been calculated with the code CLES (Scuflaire et al. 2008) using input physics similar as described in Dupret et al. (2005), and are plotted with *grey dotted lines* (for a full description of the evolutionary tracks see Uytterhoeven et al. (2011). The cross at the top of each panel indicates the typical error bar on $T_{\rm eff}$ and log g values.

4.2 Outlook

It is obvious that the collection of spectra for so many variable B-, A-, and F-type stars is very valuable. This unique sample together with the high-quality *Kepler* light curves promise progress and breakthroughs in the understanding of the pulsational mechanisms and other physical processes occurring inside MS pulsators. To observe also the fainter *Kepler* stars ($V > 11$) in a systematic way and to complete the sample, a significant amount of observing time on high-resolution spectrographs at large telescopes (>4 m) in the Northern Hemisphere is needed. Unfortunately, this is currently not feasible to achieve due to the limited number of specialised high-resolution instruments available and the high demand for observing time. The spectral analysis of over 1,000 stars requires a large effort. Additional manpower is needed. This spectroscopic school has trained new people for joining the project.

Acknowledgments KU acknowledges financial support by the Spanish National Plan of R&D for 2010, project AYA2010-17803.

References

Borucki WJ, Koch DG, Brown TM et al (2010) Kepler planet-detection mission: introduction and first results. Science 327:977

Brown TM, Latham DW, Everett ME, Esquerdo GA (2011) Kepler input catalogue: photometric calibration and Stellar classification. AJ 142:112

Dupret M-A, Grigahcène A, Garrido R, Gabriel M, Scuflaire R (2005) Convection-pulsation coupling. II. excitation and stabilization mechanisms in δ Sct and γ Dor stars. AA 435:927

Latham DW, Brown TM, Monet DG, Everett M, Esquerdo GA, Hergenrother CW (2005) The Kepler input catalog. BAAS 37:1340

Lehmann H, Tkachenko A, Semaan T et al (2011) Spectral analysis of Kepler SPB and β Cephei candidate stars. AA 526:A124

Molenda-Żakowicz J, Latham DW, Catanzaro G, Frasca A, Quinn SN (2011) Characterizing Kepler asteroseismic targets. MNRAS 412:1210

Scuflaire R, Théado S, Montalbán J et al (2008) CLÉS, Code Liégeois d'Évolution Stellaire. AAS 316:83

Uytterhoeven K, Briquet M, Bruntt H et al (2010a) Ground-based follow-up in relation to Kepler asteroseismic investigation. AN 331:993

Uytterhoeven K, Szabo R, Southworth J et al (2010b) Ground-based observations of Kepler asteroseismic targets. AN 331:P30

Uytterhoeven K, Moya A, Grigacène A et al (2011) The Kepler characterisation of the variability among A- and F-type stars.I. General overview. AA 534:A125

Stellar Atmospheres: Basic Processes and Equations

Giovanni Catanzaro

Abstract The content of this chapter is a very quick summary of key concepts that concern the interaction between photons created in the stellar interior and plasma, which is the basis of the physical processes occurring in stellar atmospheres. The dominant mechanism of energy transport through the surface layers of a typical star is radiation. This is the reason why radiative transfer is our main focus here. We start by setting up the differential equation describing the flow of radiation through an infinitesimal volume and all the related quantities. We conclude with a generic description of the equations used to compute an atmospheric model.

Keywords Stars: atmospheres · Stars: fundamental parameters

1 Introduction

The main goal of this school was to provide students with the tools to analyse stellar spectra with particular reference to the determination of the atmospheric parameters of B, A, F, and G type stars. It is obvious that a careful spectral analysis is not possible without knowledge of the theory of stellar atmospheres. So the purpose of this introductory lesson on this important subject is to provide students with a refresher on the main equations describing the physical processes that occur when the radiation, generated in the interior of the star, interacts with the stellar matter which composes the atmosphere.

If we consider a star as a succession of layers of gas, we know that going deep in the atmosphere gas becomes opaque and our line-of-sight cannot penetrate into the interior layers. We call the stellar atmosphere the ensemble of the outer layers to which the energy, generated in the nucleus, is carried, either by radiation,

G. Catanzaro (✉)
INAF, Osservatorio Astrofisico di Catania, Catania, Italy
e-mail: giovanni.catanzaro@oact.inaf.it

E. Niemczura et al. (eds.), *Determination of Atmospheric Parameters of B-, A-, F- and G-Type Stars*, GeoPlanet: Earth and Planetary Sciences,
DOI: 10.1007/978-3-319-06956-2_2,

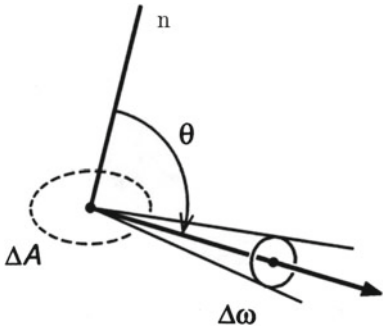

Fig. 1 The increment of area ΔA of a radiating element of material, is seen under an increment of solid angle $\Delta\omega$ and tilted by an angle θ with respect the direction of the normal to the surface.

convection or conduction, before flowing away in the interstellar medium. Interacting with the matter present in the outer layers, this energy finally produces the observed electromagnetic spectrum.

In general, we can say that the theory of stellar atmospheres translates into the study of how the radiation produced in the stellar interior propagates and interacts with the external layers of the star. That is why, during the reading of this introductory lecture on stellar atmospheres we must have always clear in mind this schematic description:

- we call the stellar atmosphere the external layers of a star,
- these are the layers where radiation created in the stellar interior can escape freely into the interstellar medium,
- the atmosphere is the only part from which we receive photons.

Of course, this lecture does not claim to be exhaustive of the topic, but rather a quick recall of the main concepts and definitions. Please refer to specific texts, (i.e. Gray 2005; Hubeny 1996; Mihalas 1978), for a complete and rigorous discussion. In the next sections, before getting to the heart of our topic, we draw some important definitions useful to properly describe light and its interaction with the atmospheric material.

2 Basic Definitions

2.1 Specific Intensity

Looking at the situation represented in Fig. 1, the **specific intensity** is the quantity of energy ΔE_ν that flows through the element ΔA toward the generic direction θ, in the solid angle $\Delta\omega$, during the time Δt, in the interval of frequency $\Delta\nu$. When all these increments become smaller, we can take the limit toward zero:

$$I_\nu = \lim \frac{\Delta E_\nu}{\cos\theta \Delta A \, \Delta\omega \, \Delta t \, \Delta\nu} = \frac{dE_\nu}{\cos\theta dA \, d\omega \, dt \, d\nu}. \quad (1)$$

The right side of this equation is the energy that flows through an element of area dA in the unit of time dt, in the unit of solid angle $d\omega$, and in the unit of frequency $d\nu$. Its physical dimensions are, for example, erg rad^{-1} cm^{-2} s^{-1} Hz^{-1}.

Integrating Eq. 1 over all the directions, we obtain the so-called **mean intensity**:

$$J_\nu = \frac{1}{4\pi} \oint I_\nu d\omega, \tag{2}$$

where the integral is calculated over the whole solid angle.

2.2 Flux

Flux represents the total energy passing across an element of area ΔA over the unit of time and frequency. As the specific intensity, we can consider the limit of all the small quantities diminishing toward zero. In this case we will have:

$$F_\nu = \lim \frac{\sum \Delta E_\nu}{\Delta A\, \Delta t\, \Delta \nu} = \frac{\oint \Delta E_\nu}{\Delta A\, \Delta t\, \Delta \nu}, \tag{3}$$

where again we consider a complete integration over all directions. Flux and intensity could be easily related to each other. If we replace in the left side of Eq. 3 the relation for the energy derived from Eq. 1, we obtain:

$$F_\nu = \oint I_\nu \cos\theta d\omega, \tag{4}$$

that represents the component of the net flux in the direction θ.

We can develop this equation for an emitting point on the physical boundary, i.e. the stellar surface. In this case the flux coming in from the outside is null, and if we suppose that there is no azimuthal dependence for F_ν, we get:

$$F_\nu = \int_0^{2\pi} d\phi \int_0^{\pi/2} I_\nu \sin\theta \cos\theta d\theta = 2\pi \int_0^{\pi/2} \sin\theta \cos\theta d\theta = \pi I_\nu. \tag{5}$$

This is the equation that we must solve if we want to compute a theoretical spectrum of a particular star. The importance of this equation is then obvious.

2.3 K-integral

It is useful to define another equation using the second moment of θ, that is, the so-called **K-integral**:

$$K_\nu = \frac{1}{4\pi} \oint I_\nu \cos^2\theta d\omega. \tag{6}$$

It represents the z-component of the radiation stress tensor written in Cartesian coordinates. Physically this integral is linked to the radiation pressure, and it is easy to show the validity of the following equation:

$$P_R = \frac{4\pi}{c} \int_0^\infty K_\nu d\nu. \tag{7}$$

3 Absorption Coefficient and Optical Depth

Let us consider a slab of plasma and let I_ν^0 be the specific intensity of the light before the interaction with the slab and $I_\nu + dI_\nu$ the intensity after the interaction. Let us suppose that only true absorption and scattering give contribution to dI_ν while no emission is present. In this case, we can write:

$$dI_\nu = -\kappa_\nu \rho I_\nu dx, \tag{8}$$

where κ_ν is the absorption coefficient that has units of area per mass ($[\kappa_\nu] = \mathrm{cm}^2\ \mathrm{g}^{-1}$) and is therefore a mass absorption coefficient, ρ is the density in mass per unit volume and dx is the slab thickness, that has units of length. At this point I have to stress an important concept: the way in which the radiation propagates through the stellar material depends both on the physical conditions of the plasma at a given frequency and on the length of the path. We can say that at a given frequency, the radiation sees the combination of these two factors, namely $\kappa_\nu \rho dx$. Define the **optical depth** along the photon direction of propagation as follows:

$$d\tau_\nu = \kappa_\nu \rho dx, \tag{9}$$

which, integrated over some path length L, becomes:

$$\tau_\nu = \int_0^L \kappa_\nu \rho dx, \tag{10}$$

where τ_ν is the optical depth at a given frequency ν and x is the geometrical depth. It measures a characteristic of matter and radiation coupled together, and corresponds, for a given frequency and absorption coefficient, to the distance at which the intensity is reduced by a factor of $1/\mathrm{e}$. Using optical depth, Eq. 8 can be written as:

$$dI_\nu = -I_\nu d\tau_\nu, \tag{11}$$

for which the trivial solution is given by

$$I_\nu = I_\nu^0 \, \mathrm{e}^{-\tau_\nu}. \tag{12}$$

In a plasma of astrophysical interest, we distinguish from optically thick, for which $\tau_\nu \gg 1$, and optically thin, for which $\tau_\nu \ll 1$. I would like to stress again here the importance of frequency: the same plasma (same chemical composition and physical conditions) could be optically thick at a certain frequency, say ν_1, but optically thin for another frequency, say ν_2.

4 Emission Coefficient

Like we did in the previous section, we consider the increase dI_ν undergone by the radiation when passing through a slab of plasma. We suppose now that the processes contributing to dI_ν are true emission and photons scattering into direction of propagation, with no absorption. In this context, scattering refers mainly to photons previously absorbed and then immediately re-emitted in the direction from the same atomic transition.

If we denote by j_ν the emission coefficient (units $[j_\nu] = \mathrm{erg\ rad^{-1}\ s^{-1}\ Hz^{-1}\ g^{-1}}$), we define the increment of the radiation as:

$$dI_\nu = j_\nu \rho dx. \tag{13}$$

5 Source Function and Its Physical Meaning

We can now introduce a new quantity given by the ratio between the absorption and emission coefficients and called the **source function**:

$$S_\nu = \frac{j_\nu}{k_\nu}. \tag{14}$$

This quantity has the same units of the specific intensity and can be seen as the specific intensity of a radiation emitted in some point in a hot gas.

To better understand the meaning of S_ν, we can refer to Hubeny (1996) and consider this example: Let us write the number of photons emitted in an volume element $dV = dx \cdot dA$, in all directions. From the definition of the emission coefficient, it follows that:

$$N_{em} = \frac{4\pi}{h\nu}(j_\nu \rho \, dx \, dA \, d\nu \, dt), \tag{15}$$

where the quantity in parenthesis represents the energy emitted in the volume dV, the factor 4π comes from an integration over the solid angle, and $h\nu$ transforms energy to the number of photons. By using the definition of the optical depth and the source function, and after some elementary algebra, we obtain

$$N_{em} = S_\nu d\tau_\nu \frac{4\pi}{h\nu} \rho \, dA \, d\nu \, dt. \tag{16}$$

In other words, we have:

$$S_\nu \propto \frac{N_{em}}{d\tau_\nu}. \tag{17}$$

Hence, the source function is proportional to the number of photons emitted per unit of optical depth interval.

5.1 Two Simple Cases

In two "extreme" cases, the algebraic form of S_ν is simple: pure isotropic scattering and pure absorption.

5.2 Pure Isotropic Scattering

All the emitted energy is due to photons being scattered into the direction under consideration. In this case the contribution to the emission dj_ν is proportional to the solid angle $d\omega$ facing the observer and to the energy "absorbed" $\kappa_\nu I_\nu$:

$$dj_\nu = \frac{1}{4\pi} \kappa_\nu I_\nu \, d\omega, \tag{18}$$

where $\frac{1}{4\pi}$ is the normalization factor for unit solid angle, valid under the hypothesis that the energy is isotropically re-radiated.

To obtain all the contributions to j_ν, we proceed with an integration over the solid angle, keeping in mind that κ_ν is independent of ω, and using Eq. 2, we can write:

$$j_\nu = \frac{1}{4\pi} \oint \kappa_\nu I_\nu d\omega = \frac{\kappa_\nu}{4\pi} \oint I_\nu d\omega = \kappa_\nu J_\nu. \tag{19}$$

From this equation it is straightforward to show that:

$$S_\nu = \frac{j_\nu}{k_\nu} = J_\nu. \tag{20}$$

In short, in the simple case of pure isotropic scattering, the source function is the mean intensity. Moreover, when thermodynamic equilibrium holds, the radiation intensity is equal to the Planck function, i.e. $J_\nu = B_\nu$.

5.3 Pure Absorption

Now we are assuming that all the absorbed photons are destroyed and all the emitted photons are newly created with a distribution governed by the physical state of the gas. The source function for this case is given by Planck's radiation law:

$$S_\nu(T) = \frac{2h\nu^3}{c^2}\frac{1}{\mathrm{e}^{\frac{h\nu}{kT}} - 1} = B_\nu(T). \tag{21}$$

This is the specific intensity emitted by a gas of a temperature T and for a given frequency ν.

6 The Transfer Equation

In the previous sections we have discussed separately the cases of radiation travelling in a slab of stellar material in which it is affected either by losses, expressed in the absorption coefficient κ_ν, or gains, expressed in the emission coefficient j_ν. Now we consider the general case in which the change in specific intensity, dI_ν, over an increment of linear path length ds, is the sum of those losses and gains, expressed as:

$$dI_\nu = -\kappa_\nu \rho I_\nu ds + j_\nu \rho ds. \tag{22}$$

This equation can be written in a more useful form, by dividing both sides by $\kappa_\nu \rho ds$, and using the definition of source function (Eq. 14):

$$\frac{dI_\nu}{\kappa_\nu \rho ds} = -I_\nu + \frac{j_\nu}{\kappa_\nu} = -I_\nu + S_\nu. \tag{23}$$

Finally, we have the differential form of the **equation of radiative transfer**

$$\frac{dI_\nu}{d\tau_\nu} = -I_\nu + S_\nu. \tag{24}$$

The integration follows from a standard integrating-factor scheme. After some manipulation, we obtain the so-called integral form of the radiative transfer equation:

$$I_\nu(\tau_\nu) = \int_0^{\tau_\nu} S_\nu(t_\nu)\mathrm{e}^{-(\tau_\nu - t_\nu)} dt_\nu + I_\nu(0)\mathrm{e}^{-\tau_\nu}. \tag{25}$$

The meaning of this equation can be easily understood: radiation along the line at the point τ_ν is composed of the sum of intensities, S_ν, originating at the generic points t_ν along the line, but suffering extinction according to the optical-depth separation $\tau_\nu - t_\nu$ (first term of the sum), plus the radiation due to the original intensity $I_\nu(0)$ that has suffered an exponential extinction $e^{-\tau_\nu}$ (second term of the sum).

Equation (24) holds along a line. In stellar atmospheres applications, it is useful to define the optical depth relative to the star along a stellar radius, and not along the line of sight. We are also assuming, in the following discussion, that as the atmosphere is thin with respect to the radius, a plane-parallel approximation can be used.

Assuming spherical coordinates originating in the centre of the star and with the z axis toward the observer, we write the transfer equation in the form:

$$\frac{1}{\kappa_\nu \rho}\frac{dI_\nu}{dz} = -I_\nu + S_\nu. \tag{26}$$

Let us write $\dfrac{dI_\nu}{dz}$ according to spherical geometry; if we assume I_ν has no azimuthal dependence, we obtain:

$$\frac{1}{\kappa_\nu \rho}\left(\frac{\partial I_\nu}{\partial r}\frac{dr}{dz} + \frac{\partial I_\nu}{\partial \theta}\frac{d\theta}{dz}\right) = -I_\nu + S_\nu. \tag{27}$$

We know, from geometrical consideration, that, $dr = \cos\theta dz$ and $r d\theta = -\sin\theta dz$. Then, by substitution of these expressions, and keeping in mind that for a plane-parallel atmosphere θ does not depend upon z, the transfer equation becomes:

$$\frac{1}{\kappa_\nu \rho}\left(\frac{\partial I_\nu}{\partial r}\cos\theta\right) = -I_\nu + S_\nu. \tag{28}$$

Adopting the convection of using a new geometrical depth variable, defined as $dx = -dr$ and writing $d\tau_\nu$ for $\kappa_\nu \rho dx$, we have the basic form of the radiative transfer equation used in the stellar atmosphere applications:

$$\cos\theta\frac{dI_\nu}{d\tau_\nu} = I_\nu - S_\nu. \tag{29}$$

6.1 Elementary Solutions

Following the outline depicted in Hubeny (1996), in this section, we describe the simplest solutions of the 1-D plane-parallel radiative transfer equation.

6.2 No Absorption, No Emission

In this elementary case, $\kappa_\nu = j_\nu = 0$, the transfer equation reads $\dfrac{dI}{dz} = 0$, which has a trivial solution:

$$I_\nu = \text{const.} \tag{30}$$

That is, in absence of any interaction with the medium, the radiation specific intensity remains constant.

6.3 No Absorption, Only Emission

In this case, $\kappa_\nu = 0$ and $j_\nu > 0$, the solution is simply:

$$I_\nu(x, \cos\theta) \;=\; I_\nu(0, \cos\theta) + \int_0^x j_\nu(x') \sec\theta dx'. \tag{31}$$

This equation is often used for describing an outgoing radiation from an optically thin radiating slab. For instance, a forbidden line radiation from planetary nebulae, or a radiation from the solar transition region and/or corona.

6.4 No Emission, Only Absorption

In this case, $\kappa_\nu > 0$ and $j_\nu = 0$, the transfer equation becomes $\cos\theta \dfrac{dI_\nu}{d\tau_\nu} = I_\nu$, and the solution is simply:

$$I_\nu(0, \cos\theta) \;=\; I_\nu(\tau_\nu, \cos\theta)\mathrm{e}^{-\tau_\nu \cdot \cos\theta} \tag{32}$$

6.5 General Case: Absorption and Emission

The full intensity at the position τ_ν on the line-of-sight through the photosphere is factorized in the sum of two terms, radiation coming outward $I_\nu^{\text{out}}(\tau_\nu)$ and radiation going inward $I_\nu^{\text{in}}(\tau_\nu)$:

$$\begin{aligned} I_\nu(\tau_\nu) &= I_\nu^{\text{out}}(\tau_\nu) + I_\nu^{\text{in}}(\tau_\nu) \\ &= \int_{\tau_\nu}^{0} S_\nu e^{-(t_\nu - \tau_\nu)\sec\theta} \sec\theta dt_\nu - \int_{\infty}^{\tau_\nu} S_\nu e^{-(t_\nu - \tau_\nu)\sec\theta} \sec\theta dt_\nu. \end{aligned} \tag{33}$$

An important special case occurs at the stellar surface. In this case $I_\nu^{\rm in}(\tau_\nu) = 0$ and then:

$$I_\nu(0) = \int_0^\infty S_\nu e^{-t_\nu \sec\theta} \sec\theta dt_\nu. \tag{34}$$

Here we are assuming that intensity of the radiation coming from other stars, galaxies and so forth, is completely negligible compared to the star's own radiation. For most stars, for which we do not resolve the disk, we must still integrate $I_\nu^{\rm out}$ over the star's disk, i.e. we observe the flux.

6.6 Special Case: Linear Source Function

A special case is an emergent intensity from a semi-infinite atmosphere, with a source function being a linear function of optical depth:

$$S_\nu(\tau_\nu) = a + b\tau_\nu. \tag{35}$$

In this case, substituting this form of S_ν in the Eq. 34, we obtain the solution given by:

$$I_\nu(0) = \int_0^\infty (a + b\tau_\nu) e^{-t_\nu \sec\theta} \sec\theta dt_\nu = a + b\cos\theta, \tag{36}$$

or more simply:

$$I_\nu(0, \cos\theta) = S_\nu(\tau_\nu = \cos\theta). \tag{37}$$

This important expression is called the "Eddington-Barbier relation". It shows that the emergent intensity, for instance in the normal direction ($\cos\theta = 1$) is given by the value of the source function at the optical depth of unity. The values of emergent intensity for all angles θ for which $\cos\theta$ ranges between 0 and 1, map the values of the source function between optical depths 0 and 1. Even though the source function is not a linear function of τ_ν, it can usually be well approximated by it in the vicinity of $\tau_\nu = 1$.

7 The Flux Integral

The transformation in spherical coordinates that we did for specific intensity, can also be done for the integral flux, as already defined in Eq. 3. Assuming there is no azimuthal dependence in I_ν, we can write:

$$F_\nu = 2\pi \int_0^\pi I_\nu \cos\theta \sin\theta d\theta$$
$$= 2\pi \int_0^{\pi/2} I_\nu^{out} \cos\theta \sin\theta d\theta + 2\pi \int_{\pi/2}^{\pi} I_\nu^{in} \cos\theta \sin\theta d\theta. \quad (38)$$

Using the expressions for the specific intensity and assuming that S_ν is isotropic (no θ dependence), we obtain for the flux the following expression:

$$F_\nu(\tau_\nu) = 2\pi \int_{\tau_\nu}^{\infty} S_\nu(t_\nu) E_2(t_\nu - \tau_\nu) dt_\nu - 2\pi \int_0^{\tau_\nu} S_\nu(t_\nu) E_2(t_\nu - \tau_\nu) dt_\nu, \quad (39)$$

where E_2 is the exponential integral of second order.

At the stellar surface, where $\tau_\nu = 0$, we have:

$$F_\nu(0) = 2\pi \int_0^{\infty} S_\nu(t_\nu) E_2(t_\nu) dt_\nu, \quad (40)$$

which is the theoretical stellar spectrum.

8 Computing a Model Atmosphere

To solve the radiative transfer equation, we must know the source function S_ν that, as we have learnt previously, is the ratio between emission and absorption coefficients. These coefficients have a strong dependence on the physical properties of the atmospheric layers: j_ν and κ_ν depend on temperature, pressure, population of the atomic levels, electronic density and so on. Hence, to compute S_ν, and then solve the radiative transfer equation, we must know the distributions of T, P, n_i, n_e, and other quantities with optical depth. This process is what we commonly refer to as the calculation of a model atmosphere.

By the term "model atmosphere" we indicate a specification of all the atmospheric state parameters as functions of depth. Since the problem is very complex, we cannot construct analytic solutions. Therefore, we discretize the depth coordinate and consider a finite number of depth points (typically of the order of several tens to few hundreds). A model atmosphere is then a table of values of the state parameters in these discrete depth points.

8.1 Basic Equations of Stellar Atmospheres

Let us summarize in this section the basic equations of stellar atmospheres for the case of a horizontally-homogeneous, plane-parallel, static atmosphere.

8.1.1 Radiative Transfer Equation

The radiative transfer equation (see Eq. 29) has been the topic of previous sections, so we do not treat it any more, but we just remember that its solution gives us information on the mean intensity of the radiation.

8.1.2 Hydrostatic Equilibrium Equation

By solving the hydrostatic equilibrium equation we get information on the total gas pressure, and then on total particle density. If P is the total pressure, the equation reads:

$$\frac{dP}{dz} = \rho g. \tag{41}$$

Introducing the optical depth, the previous equation can be written as:

$$\frac{dP}{d\tau_\nu} = \frac{g}{\kappa_\nu}. \tag{42}$$

It should be kept in mind that the total pressure is generally composed of several parts: the gas pressure, P_{gas}, the radiation pressure, P_{rad}, the turbulent pressure, P_{turb}, and if a magnetic field is present also magnetic pressure, P_B, has a contribution. In general, the equation is:

$$P = P_{gas} + P_{rad} + P_{turb} + P_B = NkT + \frac{4\pi}{c}\int_0^\infty K_\nu d\nu + \frac{1}{2}\rho v_{turb}^2 + \frac{B^2}{8\pi}. \tag{43}$$

Neglecting turbulent and magnetic pressure (that in general cases do not give a significant contribution) the hydrostatic equilibrium equation may then be written as:

$$\frac{dP_{gas}}{d\tau_\nu} = \frac{g}{\kappa_\nu} - \frac{dP_{rad}}{d\tau_\nu}. \tag{44}$$

We may think of the right side of this equation as the effective gravity acceleration, since it expresses the action of the true gravity acceleration (acting toward the centre of the star) minus the radiative acceleration (acting outward).

8.1.3 Radiative Equilibrium

The radiative equilibrium equation expresses the fact that the total flux is conserved, and solving it we know the distribution of temperature along the atmosphere:

$$\frac{dF(x)}{dx} = 0 \longrightarrow F(x) = F_0, \tag{45}$$

$$\int_0^\infty F_\nu(\tau_\nu)d\nu = F_0. \tag{46}$$

Other two important equilibrium equations are easily derived from the radiative transfer equation. Let us write Eq. 29 in this way:

$$\cos\theta \frac{dI_\nu}{dx} = \kappa_\nu \rho I_\nu - \kappa_\nu \rho S_\nu. \tag{47}$$

Then, integrating first over solid angle and over frequencies, we have:

$$\frac{d}{dx}\int_0^\infty F_\nu d\nu = 4\pi\rho \int_0^\infty \kappa_\nu J_\nu d\nu - 4\pi\rho \int_0^\infty \kappa_\nu S_\nu d\nu. \tag{48}$$

Considering condition expressed by Eq. 45, we can write this as:

$$\int_0^\infty \kappa_\nu J_\nu d\nu = \int_0^\infty \kappa_\nu S_\nu d\nu. \tag{49}$$

If we multiply by $\cos\theta$ and then we integrate over solid angle and over frequencies, we obtain:

$$\int_0^\infty \frac{dK_\nu}{d\tau_\nu} d\nu = \frac{F_0}{4\pi}. \tag{50}$$

Equations (46), (49), and (50) are the so-called **Milne equations**.

8.1.4 Statistical and Charge Conservation Equations

Two other important ingredients of an atmospheric model are the distribution of the level population, n_i, and electronic density, n_e. Statistical and charge conservation equations are helpful to know how these quantities vary along optical depth.

Let us consider two generic atomic levels, i and j, and if R and C are the radiative and collisional rates, respectively, then the set of equations:

$$n_i \sum_{j \neq i} (R_{ij} + C_{ij}) = n_j \sum_{j \neq i} (R_{ji} + C_{ji}) \tag{51}$$

expresses the equilibrium between the total number of transition out of level i (left hand side) and the total number of transition into level i from all other levels (right hand side).

Another important equation expresses the global electrically neutrality of the medium:

$$\sum_i n_i Z_i - n_e = 0, \tag{52}$$

where Z_i is the charge associated with the level i (i.e. equal to 0 for levels of neutral atoms, 1 for levels for once ionized atoms, etc.). The summation extends over all levels of all ions of all species. This equation is useful to obtain the distribution of the electron density, n_e, along the stellar atmosphere.

8.2 A Pedagogical Example: The Grey Atmosphere

A very simplified case is the so-called grey atmosphere model. The basic assumption of this model is that the absorption coefficient is independent of frequency, that is, $\kappa_\nu = \kappa$. Electron scattering is the only opacity source relevant to stellar atmospheres that is grey, and it is usually a minor contributor to κ_ν, at least in the case of cool stars. The grey case is not very realistic, but nevertheless is useful to understand the interplay between radiative equilibrium and radiative transfer, or in other words, to understand the behaviour of temperature as a function of depth:

$$\cos\theta \frac{dI}{d\tau} = I - S. \tag{53}$$

Using the Milne's equation re-formulated for the grey case, and skipping all the mathematical steps, we arrive at the solution for the source function:

$$S(\tau) = \frac{3F_0}{4\pi} \left(\tau + \frac{2}{3} \right). \tag{54}$$

In this simple case, the source function varies linearly with optical depth. Using the frequency-integrated form of Planck's law, we can write $S(\tau) = \frac{\sigma}{\pi} [T(\tau)]^4$ and $F_0 = \sigma T_{\rm eff}^4$, so the previous equation in LTE becomes:

$$T(\tau) = \left[\frac{3}{4}\left(\tau + \frac{2}{3}\right)\right]^{1/4} T_{\rm eff}. \tag{55}$$

At $\tau = 2/3$ the temperature is equal to the effective temperature ($T_{\rm eff}$)[1], and $T(\tau)$ scales in proportion to the effective temperature.

9 Conclusions

The conclusions of this lecture can be summarized according to the following outline:

- Modelling stellar spectrum means computing the flux emerging at the stellar surface.
- To accomplish this task we need to know the radiation specific intensity along the atmosphere.
- The calculation of how the radiation propagates within a stellar atmosphere requires knowledge of the source function.
- The source function depends on emission and absorption coefficients.
- Both j_ν and κ_ν depend on the physical conditions of the stellar material: T, P, electronic density and so on.
- We need to solve the equations of the model atmosphere.

References

Gray DF (2005) The observation and analysis of stellar photospheres. Cambridge University Press, New York

Hubeny I (1996) Stellar Atmospheres Theory: and introduction. In: De Greve JP, Blomme R, Hensberge H (eds) Stellar atmospheres: theory and observations. Springer, Brussels

Mihalas D (1978) Stellar atmospheres, 2nd edn. W. H. Freeman & Company, San Francisco

[1] We recall here the definition of effective temperature of a star; it is defined as the temperature of a black body having the same power output per unit area as the star.

How to Build a Model of the Atmosphere and Spectrum

Robert L. Kurucz

Abstract We want to include the opacity of millions or hundreds of millions of lines in model stellar atmosphere calculations, then generate detailed, realistic spectra from those model atmospheres, then model the observation process, and finally compare the calculated spectra to observed spectra to determine the properties of stars so that we can understand their evolution and the evolution of galaxies.

Keywords Stars: atmospheres · Convection

1 Introduction

Building an LTE, hydrostatic equilibrium model starts by specifying $T_{\rm eff}$, $\log g$, and abundances. Then you guess a temperature-optical depth relation (using a starting model) for many layers in the photosphere. Then you iterate through the following steps until the flux is constant and temperature is stationary at each layer in the atmosphere:

Compute the equation of state to determine the population of each species and the pressure in each layer.
Compute the line and continuum opacity.
Compute the radiation field and the total radiative flux in each layer.
Compute the convective flux in each layer.
Compute the total flux error and correct the temperature in each layer.

All of this was described in SAO Special Report 309 more than 40 years ago. Some of the coding has not changed since before SR 309 was written about ATLAS5.

R. L. Kurucz (✉)
Harvard-Smithsonian Center for Astrophysics,
60 Garden Street, Cambridge, MA 02138, USA
e-mail: rkurucz@cfa.harvard.edu

E. Niemczura et al. (eds.), *Determination of Atmospheric Parameters of B-, A-, F- and G-Type Stars*, GeoPlanet: Earth and Planetary Sciences,
DOI: 10.1007/978-3-319-06956-2_3,

Current versions of ATLAS are much more sophisticated. The report is on my website http://kurucz.harvard.edu/papers as are the previous series of talks I gave in Trieste in 2005:

`/SAO309` ATLAS: A computer program for calculating model stellar atmospheres (Kurucz 1970).
`/triesteatlas12` ATLAS12, SYNTHE, ATLAS9, WIDTH9, etc. (Kurucz 2005a).
`/triestelimits` Physical, numerical, and computational limits for Kurucz codes (Kurucz 2005b).
`/triesterapid` Rapid computation of line opacity in SYNTHE and DFSYNTHE (Kurucz 2005c).
`/triestelines` Including all the lines (Kurucz 2005d).
`/triestesolar` New atlases for solar flux, irradiance, central intensity, and limb (Kurucz 2005e).

Here I will discuss details of topics that are not in textbooks but that affect the accuracy of the results you are able to obtain: observational and computational pipelines, rotation, equation of state, convection and microturbulent velocity.

In Chap. 4 I write about three treatments of opacity and the corresponding programs: Resolved spectra and SYNTHE, Sampled spectra and ATLAS12, Low resolution distribution functions and DFSYNTHE and ATLAS9.

2 Observational and Computational Pipelines

Radiation from a star is affected by a series of interactions before it appears on your terminal screen as a spectrum. These are outlined in the observational pipeline column in Fig. 1. Each interaction can be modelled computationally, although, in practice, some are treated empirically and some are ignored.

3 Rotation

All stars rotate. Except for a tiny percentage that are observed exactly pole-on, the rotation broadens the lines in the spectrum. Observationally the star sends a ray of intensity spectrum toward us from each point on the disk and it Doppler shifts that spectrum by the projected rotation velocity at that point. The total flux spectrum directed at us is the integral over all the rays.

For a slowly rotating, spherical star, computing the flux spectrum is a straightforward process. In ROTATE I tabulate intensity spectra as a function of angle from disk center (limb-darkened spectra). I put a grid over the disk, say 200 $\times$ 200 or 400 $\times$ 400 points, and determine the angle and Doppler shift at each point (Symmetries are taken into account). I interpolate to each grid point, Doppler shift the spectrum, and add it to the integrand for the rotated flux spectrum.

Observational Pipeline	Computatonal Pipeline	Programs
	Grid of models and	ATLAS9/12+
Rotating star	intensity spectra	SYNTHE
	Interp. rotated flux spectrum	ROTATE
Circumstellar material	Circumstellar transmission	not yet
ISM reddening	ISM reddening	REDDEN
ISM lines	ISM lines	not yet
ISM diffuse bands	ISM diffuse bands	not yet
Telluric airglow	Telluric airglow	not yet
Anthropogenic light	Anthropogenic light	not yet
Telluric broad features	Telluric broad features	TRANSYNTHE
Telluric lines	Telluric lines	TRANSYNTHE
Aerosols	Aerosols	not yet
Telescope transmission	From reduction procedure	
Instrumental transmission	From reduction procedure	
Scattered light	From reduction procedure	
Detector sensitivity	From reduction procedure	
Cosmic rays+radioactivity	Removed by red. procedure	
Instrumental profile	From reduction procedure	BROADEN
Observed spectrum	Computed spectrum	
Compare to observed spectrum		PLOTSYN
Iterate		

Fig. 1 Observational and computational pipelines

One complication is that if you look at the Sun with high quality spectra you can actually see differential rotation in the line profiles. Presumably, rapidly-rotating stars have strong differential rotation as well. I have put in an option in ROTATE to compute differential rotational broadening.

The spherical assumption is fine for old, tired stars but young stars are fast rotators, and early type stars can be so fast that they are oblate and have gravity darkening. Figure 2 shows the observed structure of Altair from interferometry by Peterson et al. (2006a). Figure 3 shows Vega determined by Peterson et al. (2006b). Vega looks almost spherical because it is observed almost pole-on. Until recently spectra and the SED (spectral energy distribution) were not determined well enough to show the oblateness and gravity-darkening. The star could be well matched with a simple plane-parallel model, Figs. 4 and 5 (Kurucz 1979). This shows that you can get away with an awful lot if you stick to low resolution.

If we assume that we understand gravity darkening, these stars can be straightforwardly modelled (but we probably do not). As before we place a grid over the star. At each point we determine the angle, the velocity, $T_{\rm eff}$, and $\log g$. We compute a grid of models and spectra covering the whole range of $T_{\rm eff}$ and log g that are possible on the surface. For each model we compute the intensity spectrum as a function of angle. Then we interpolate the spectrum in $T_{\rm eff}$, $\log g$, angle, and Doppler shift at

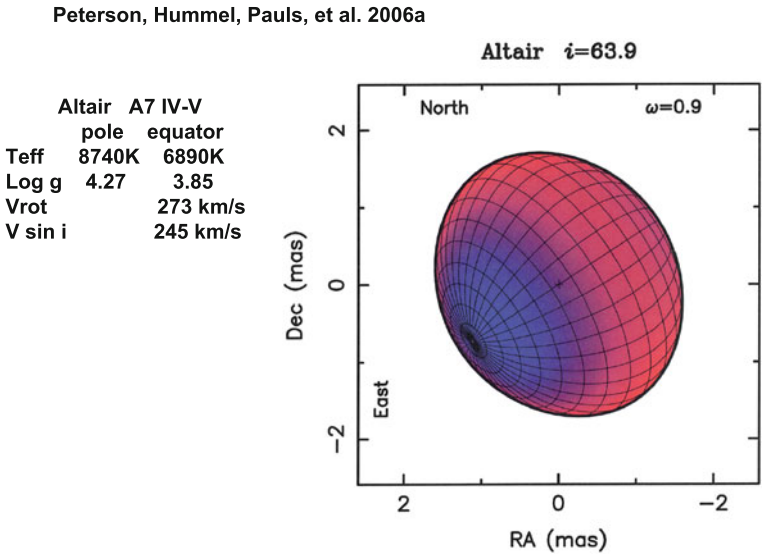

Fig. 2 Altair projected against the sky with derived parameters

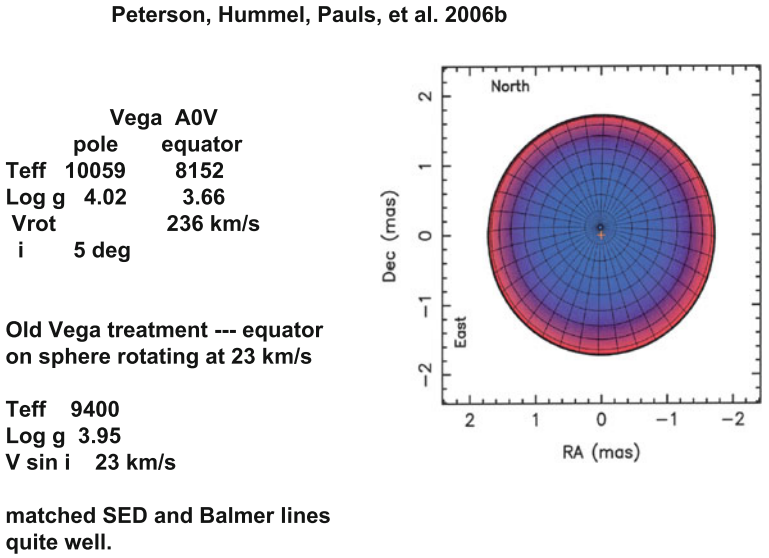

Fig. 3 Vega projected against the sky with derived parameters

each point and add it to the integrand for the rotated flux spectrum. (I am not yet distributing this version of ROTATE).

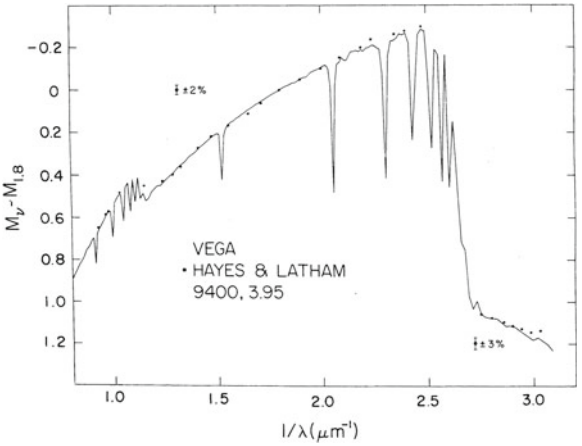

Fig. 4 Old fit to Vega SED from Hayes and Latham (1975) (Kurucz 1979)

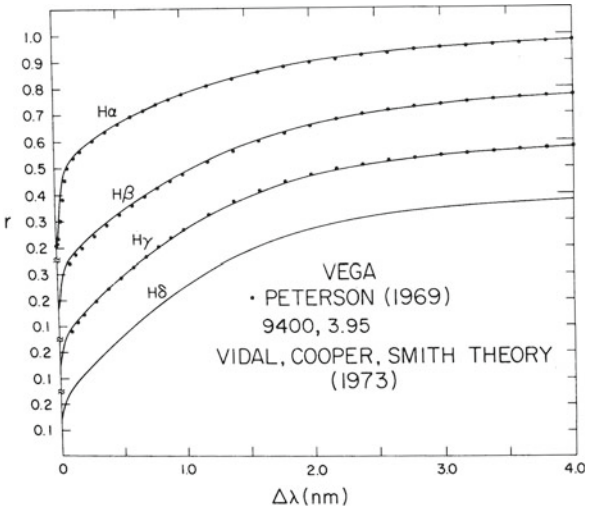

Fig. 5 Old fit to Vega Balmer profiles measured by Peterson (1969) (Kurucz 1979)

4 Circumstellar and Interstellar Absorption

Continuing through the pipeline, Fig. 1:

Circumstellar material: Gas and dust from mass loss, thick disks, zodiacal disks can absorb and produce spectral features and modify the SED.
Interstellar reddening: Program REDDEN reddens SEDs with simple models.
Interstellar diffuse bands: Herbig (1995) has a catalogue of bands.

Interstellar lines: Just search through my line lists for strong lines with lower energies less than 300 cm^{-1}.

These programs are not yet written. Any of you could do it. At present be aware of interstellar features and avoid them.

5 Telluric Spectra

Continuing through the earth's atmosphere:

Telluric airglow: O_2, OH, NO, and other radicals at altitudes above 70 km add emission lines to the spectrum. There are atlases and line catalogues by Osterbrock et al. (2000) and by Cosby et al. (2006), for example. I have not yet programmed it.

Anthropogenic light: There are many city lights in southern Arizona and at other sites that add emission lines to the spectrum. There is a line catalogue by Slanger et al. (2003). I have not yet programmed it.

Any of you could write these programs. In the meantime be aware of the possibility of emission lines.

I have written programs for atmospheric transmission. Given an atmospheric model, which is like a stellar model, temperature and pressure as a function of altitude, program TRANSYNTHE computes the opacity. Then program TRANSPECTR computes the mean transmission from beginning to end of an observation through the atmosphere down to the telescope.

Figure 6 shows absorption by ozone O_3 and O_2 dimer $[O_2]_2$. Figure 7 shows absorption by O_2 and H_2O lines in the visible. Including telluric lines requires very high resolution. I typically use a resolving power of 2 million. That same resolution is then required in computing the stellar spectrum because the spectra are multiplied together point by point by program TRANSMIT. Most of the line data come from the HITRAN line list by Rothman et al. (2005), formerly US Air Force, now Smithsonian Astrophysical Observatory. There is a new edition at http://www.cfa.harvard.edu/hitran. I reformat the HITRAN data into Kurucz format so they can be used as stellar opacity as well.

I have not yet programmed aerosols. They are not significant for residual spectra but matter for absolute spectrophotometry.

6 Comparison to Observed Spectra

Program BROADEN runs the computed spectrum through the measured instrumental profiles. The profile can range from a simple Gaussian to a complicated asymmetric shape with wing structure. (At this stage you can generate spectra at any lower resolution as well, even down to resolving power 100.)

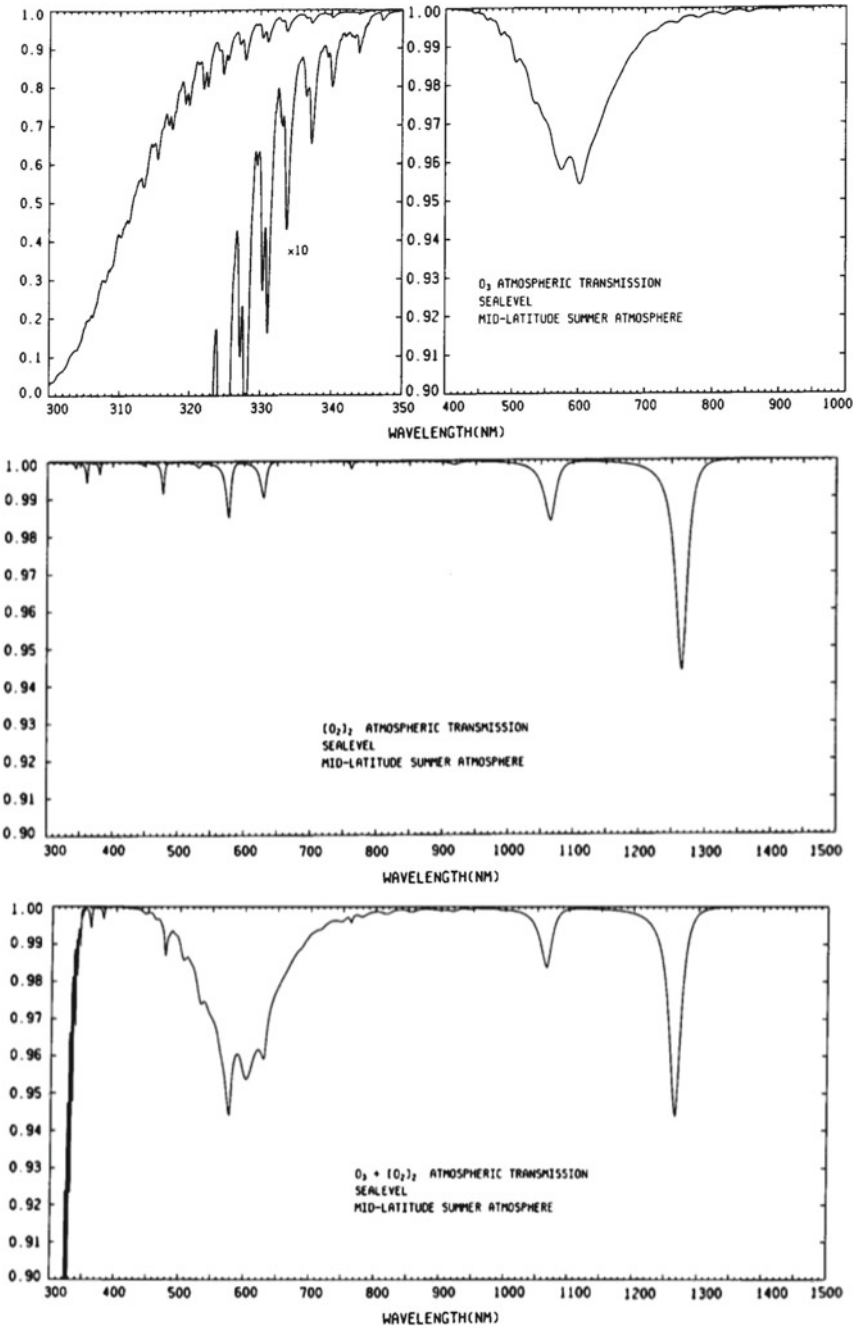

Fig. 6 Atmospheric absorption by ozone and O_2 dimer

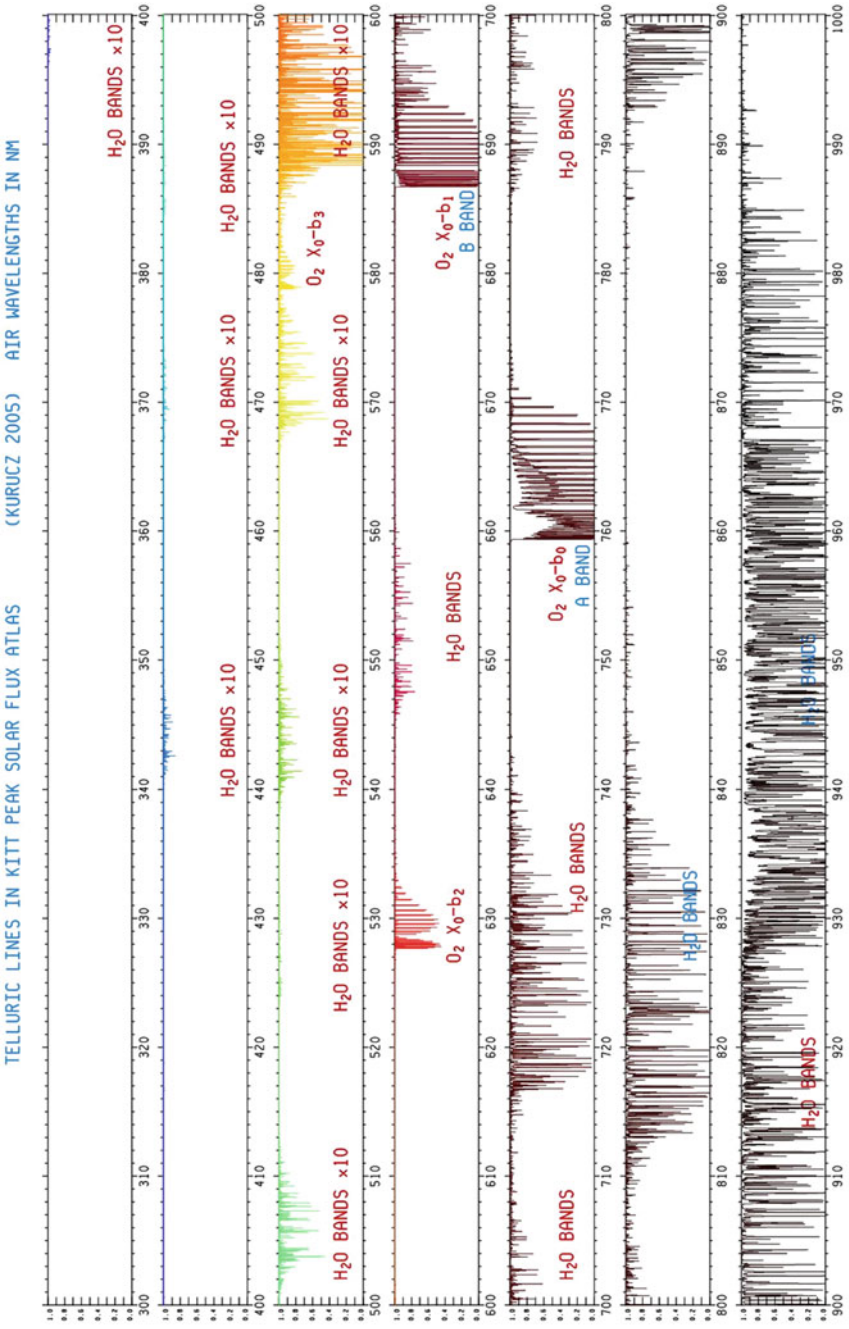

Fig. 7 Telluric lines in Kitt Peak Solar Flux Atlas (Kurucz 2005f)

Then I plot the observed and computed spectra on top of each other with the lines labelled using program PLOTSYN to identify the features and to see what is wrong and what is right. Figure 8 is a Space Telescope spectrum of Sirius at 201 nm. I like it because it illustrates a number of problems.

The observed structures in black are not lines but features that are blends of lines. The 16 km s^{-1} rotation blends the lines together. I have also plotted the spectrum computed with no rotation in blue. This helps indicate the composition of blends.

The minima of the features are not line positions. They frequently fall in between two lines as at 201.1 and 201.41 nm. They cannot be used to set or check a wavelength scale.

Some lines are computed too weak, (201.14 nm); or missing, (201.11 nm); or computed too strong, (201.49 nm).

Figure 9 shows a section of solar spectrum at 599 nm where each spectrum is plotted twice, once at normal scale and once at 10 times scale to show small differences. The observed spectrum is black, the computed solar spectrum is red, the telluric spectrum is blue, and the transmitted spectrum is magenta.

7 Equation of State

All physical data change, hopefully for the better, as time goes by. Even the speed of light has been revised over the lifetime of these programs but is now fixed. Laboratory analyses of atoms and molecules have improved tremendously. There are much more accurate energies and with many more levels known. There are many more lines and with better wavelengths. Partition functions, ionization potentials, and equilibrium constants have changed. I am computing new partition functions and equilibrium constants as I compute new line lists to update the equation of state sections of my programs. You should be aware that the data for ions or molecules that have not been updated can be 30 or 40 years out of date.

8 Convection and Microturbulent Velocity

Figure 10 is the empirical solar model C from Fontenla et al. (1993). The upper darker line is the temperature distribution which drops through the photosphere to the temperature minimum and then rises in the chromosphere. They also determined the microturbulent velocity which drops through the photosphere to a minimum and then rises in the chromosphere. The maximum microturbulent velocity in the photosphere is also the maximum mixing-length convective velocity in my solar model ASUN. I interpret the photospheric microturbulent velocity as convective motions that go to zero in the radial direction toward the surface (Kurucz 1996). Then waves and magnetic motions produce an outwardly increasing chromospheric microturbulent velocity.

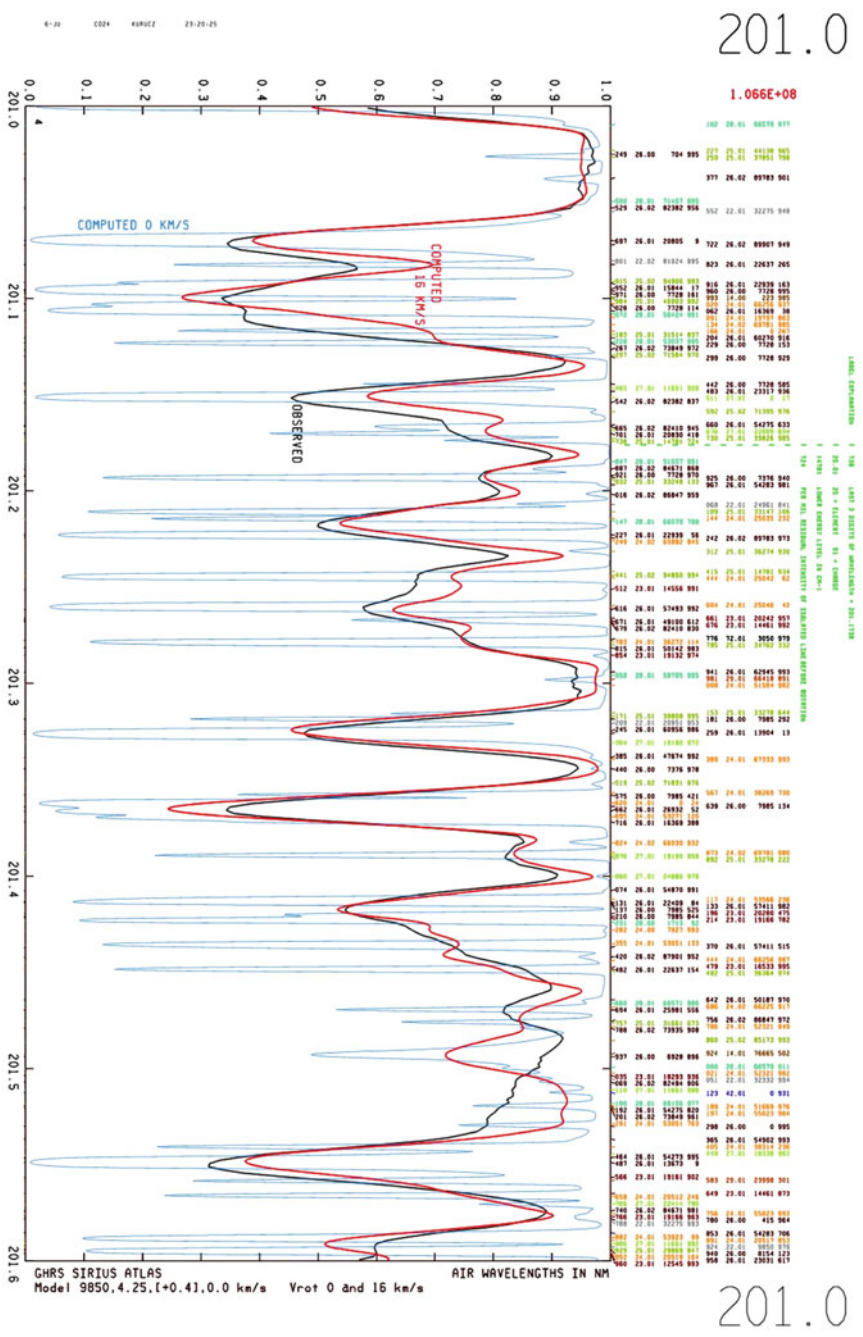

Fig. 8 Comparison of computed and observed Space Telescope GHRS spectra of Sirius

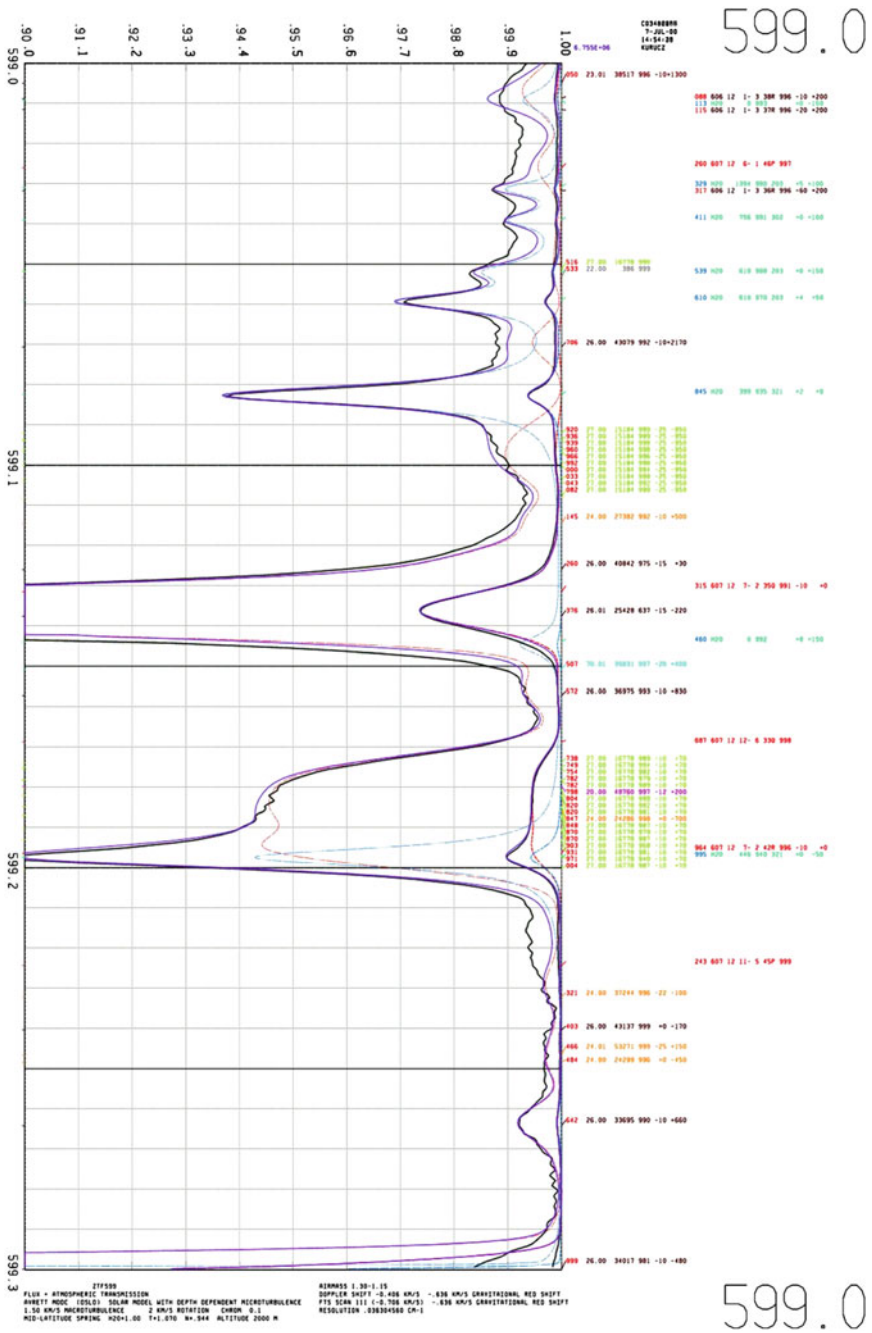

Fig. 9 Comparison of computed and observed Kitt Peak FTS solar spectra

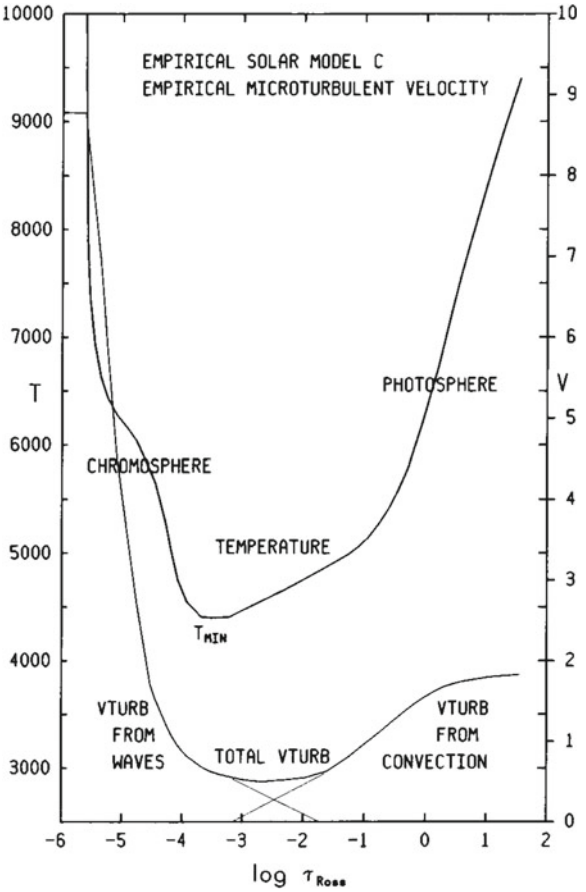

Fig. 10 Empirical temperature and microturbulent velocity distributions in the sun (Fontenla et al. 1993)

I assume that the microturbulent velocity varies the same way in all convective models and I scale the solar profile by the ratio of the maximum convective velocity over a grid of models to the solar maximum convective velocity. The left panel in Fig. 11 shows the maximum convective velocity for a solar abundance grid running from 3,500 to 8,500 K and in $\log g$ from 5.0 down to 0.0. You can see that for a $T_{\rm eff}$ = 3,500 K, $\log g$ = 5.0 M-dwarf the maximum is about 0.25 km s^{-1}; for $T_{\rm eff}$ = 6,000 K, $\log g$ = 4.5 it is about 2 km s^{-1}. You also see that there is a family of smoothly increasing curves as the temperature increases until each curve reaches a maximum and the convection catastrophically falls off and disappears.

The center panel shows the maximum fraction of total flux carried by convection. In the right panel I weight the maximum convective velocities by this fraction and they are the numbers I use to scale the microturbulent velocity.

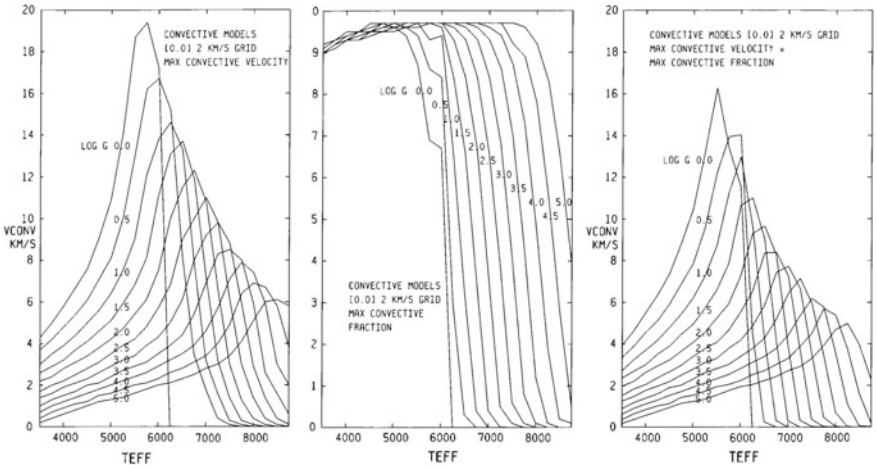

Fig. 11 The maximum convective velocity in a solar abundance grid of models; the maximum convective fraction; the product

At the higher temperatures convective microturbulence decreases and disappears. The microturbulence may actually be zero or other kinds of "microturbulence" may take over. For example, pulsation produces differential velocities that broaden lines.

References

Cosby PC, Sharpee BD, Slanger TG, Huestis DL, Hanuschik RW (2006) J Geophys Res 111:A12307
Fontenla JM, Avrett EH, Loeser R (1993) Astrophys J 406:319
Hayes DS, Latham DW (1975) Astrophys J 197:593
Herbig GH (1995) Ann Rev Astron Astrophys 33:19
Kurucz RL (1970) SAO Spec Rep 309:291
Kurucz RL (1979) Astrophys J Supp 40:1
Kurucz RL (1996) Astron Soc Pacific Conf Ser 108:2
Kurucz RL (2005a) Mem Soc Astron Ital Suppl 8:10
Kurucz RL (2005b) Mem Soc Astron Ital Suppl 8:69
Kurucz RL (2005c) Mem Soc Astron Ital Suppl 8:72
Kurucz RL (2005d) Mem Soc Astron Ital Suppl 8:83
Kurucz RL (2005e) Mem Soc Astron Ital Suppl 8:158
Kurucz RL (2005f) Kitt Peak Solar Flux Atlas (2005f). http://kurucz.harvard.edu/sun/fluxatlas2005
Kurucz RL (2005g) Kitt peak solar irradiance Atlas. http://kurucz.harvard.edu/sun/irradiance2005
Kurucz RL (2008) Irradiance in the H and K bands. http://kurucz.harvard.edu/sun/irradiance2008
Osterbrock DE, Waters RT, Barlow TA, Slanger TG, Cosby PD (2000) PASP 112:733
Peterson DM (1969) SAO Spec Rep 293:199
Peterson DM, Hummel CA, Pauls TA et al (2006a) Nature 440:896–899
Peterson DM, Hummel CA, Pauls TA et al (2006b) Astrophys J 636:1087
Rothman LS et al (2005) JQSRT 96:139
Slanger TG, Cosby PC, Osterbrock DE, Stone RPS, Misch AA (2003) PASP 115:869
Vidal CR, Cooper J, Smith EW (1973) Astroph J Supp 25:37

Model Atmosphere Codes: ATLAS12 and ATLAS9

Robert L. Kurucz

Abstract I present three different treatments of opacity and the corresponding programs: Resolved spectra and SYNTHE; Sampled spectra and ATLAS12; Low resolution distribution functions and DFSYNTHE and ATLAS9. I also report on producing high-resolution, high signal-to-noise atlases for use in verifying the line data and spectrum calculations.

Keywords Stars: atmospheres · Opacity · Atlases

1 Introduction

I continue from my previous paper on "How to build a model of the atmosphere and spectrum". I gave a series of talks in Trieste in 2005 that can be found on my website http://kurucz.harvard.edu/papers.

`/triesteatlas12`	ATLAS12, SYNTHE, ATLAS9, WIDTH9, etc. (Kurucz 2005a)
`/triestelimits`	Physical, numerical, and computational limits for Kurucz codes. (Kurucz 2005b)
`/triesterapid`	Rapid computation of line opacity in SYNTHE and DFSYNTHE. (Kurucz 2005c)
`/triestelines`	Including all the lines. (Kurucz 2005d)
`/triestesolar`	New atlases for solar flux, irradiance, central intensity, and limb. (Kurucz 2005e)

R. L. Kurucz (✉)
Harvard-Smithsonian Center for Astrophysics, 60 Garden Street, Cambridge, MA02138, USA
e-mail: rkurucz@cfa.harvard.edu

E. Niemczura et al. (eds.), *Determination of Atmospheric Parameters of B-, A-, F- and G-Type Stars*, GeoPlanet: Earth and Planetary Sciences,
DOI: 10.1007/978-3-319-06956-2_4,

Here I present three different treatments of opacity and the corresponding programs: Resolved spectra and SYNTHE, and producing high-resolution, high signal-to-noise atlases for use in verifying the line data and spectrum calculations; Sampled spectra and ATLAS12; Low resolution distribution functions and DFSYNTHE and ATLAS9.

2 SYNTHE

The original paper on SYNTHE was SAO Special Report No. 387 (Kurucz and Furenlid 1979) which is a sample atlas for Sirius showing both the observed and calculated spectrum with line identifications. It is on my website under `/papers/SAO387`. SAO Special Report No. 391 (Kurucz and Avrett 1981) added a few details about ultraviolet metal line series merging into continua and about including precomputed departure coefficients in the spectrum calculations. Gene Avrett would compute departure coefficients with his program PANDORA-and then I would compute spectra using those departure coefficients.

SYNTHE can compute only at high resolution because it sets up a grid of evenly spaced points in Doppler space and moves line centres to the nearest point on the grid. The Voigt profile is symmetric and only one wing need be computed, and I do that by table lookup. The grid can have more than a million points. I typically run at resolving power of 500 000 (0.6 km s^{-1}) if there are no telluric lines, as in satellite observations. If there are telluric lines I use 2 million (0.15 km s^{-1}) and I have gone up to as high as 10 million (0.03 km s^{-1}).

Some lines, such as autoionizing lines, can be specially treated with arbitrary profiles at their exact positions.

The Doppler point spacing allows Doppler shifts just by changing the point index. Radial velocity shifts between telluric and stellar spectra or between two components of a binary become simple. SYNTHE also allows depth-dependent Doppler shifts from convection or pulsation, but the shifts must be pre-specified (a snapshot of pulsation.)

Another big time-saver is that SYNTHE begins each calculation by pre-tabulating the number densities of all atomic and molecular species and the continuum opacity at selected points (program XNFPELSYN). It then reads the line list and writes a new selected line list. For each line it reads it computes the line absorption coefficient and interpolates the approximate continuum opacity. If the line opacity is below a cutoff factor times the continuum opacity the line is rejected. The cutoff can be specified. I normally use 0.001 for stars and 0.0001 for the sun. You can try different numbers to find the value below which the spectrum does not change. This matters especially in molecular bands where there are sometimes 100 lines/Ångstrom.

The new selected line list is used for the detailed line profile calculations. Radiative, Stark, and van der Waals damping constants are included in the line list. The wings of each line are computed only out to the cutoff. That can be more then 100 nm for the strongest lines at high gravities.

All the lines that mattered in the spectrum calculation are saved in a file that can be read in as a new input line list. After comparison to observed spectra as described in Sect. 4, the wavelengths, gf values, and damping constants can be hand edited to improve the fits.

Once a spectrum has been computed it can be broadened with Gaussian or arbitrary profiles to any lower resolution. You can predict the appearance of the spectrum with various resolution spectrographs down to resolving power of 100.

I generally make a number of runs that cover the whole spectrum and merge them into one 4 million point spectrum for the whole SED (stellar energy distribution) from 1 nm to 300 μm. For cool stars I start at 91 nm. You can find examples of various resolution spectra on my website at `/stars`. Remember that these are computed photospheric spectra from models that do not include chromospheres. Real stars typically have chromospheric emission lines in the ultraviolet.

3 High Resolution Atlases

High-resolution, high-signal-to-noise spectra are needed to test the line data and the spectrum synthesis programs and to determine the stellar parameters.

There are no high-quality solar spectra taken above the atmosphere in the ultraviolet, visible, or infrared out to 2.2 μm. There is a recent central intensity atlas produced with an FTS on the ACE satellite (Hase et al. 2010) that covers from 2.2 to 14 μm.

In the ultraviolet there are not even "good" quality solar spectra. There are various good quality solar spectra taken through the atmosphere in the visible and infrared. I have been trying to reduce the FTS spectra taken by Jim Brault from Kitt Peak to produce central intensity, limb intensity, flux, and irradiance atlases.

Figure 1 shows the visible flux atlas from Kurucz (2005f). I have shown the telluric spectrum deduced from this atlas in my "How to" paper as part of the pipeline for atmospheric transmission.

Figure 2 is the residual irradiance spectrum determined by removing the telluric lines from the flux spectrum (Kurucz 2005g). This is the spectrum at the top of the atmosphere.

Figure 3 is the absolute irradiance spectrum determined by multiplying the residual irradiance times the continuum of my solar model ASUN seen from a distance of 1 AU (Kurucz 2005g). This is the spectrum of the Sun as a star, the spectrum seen by all the bodies in the solar system. It is the spectrum studied by exoplanetary scientists on distant exoplanets searching unsuccessfully for habitable planets orbiting Sol.

Figure 4 shows a sample residual irradiance spectrum for part of the H and K bands that I have worked on thus far (Kurucz 2008).

All of the above spectra can be found on my web site under `/sun`.

And, of course, spectra of bright stars, Arcturus, Procyon, etc., are also needed for comparisons.

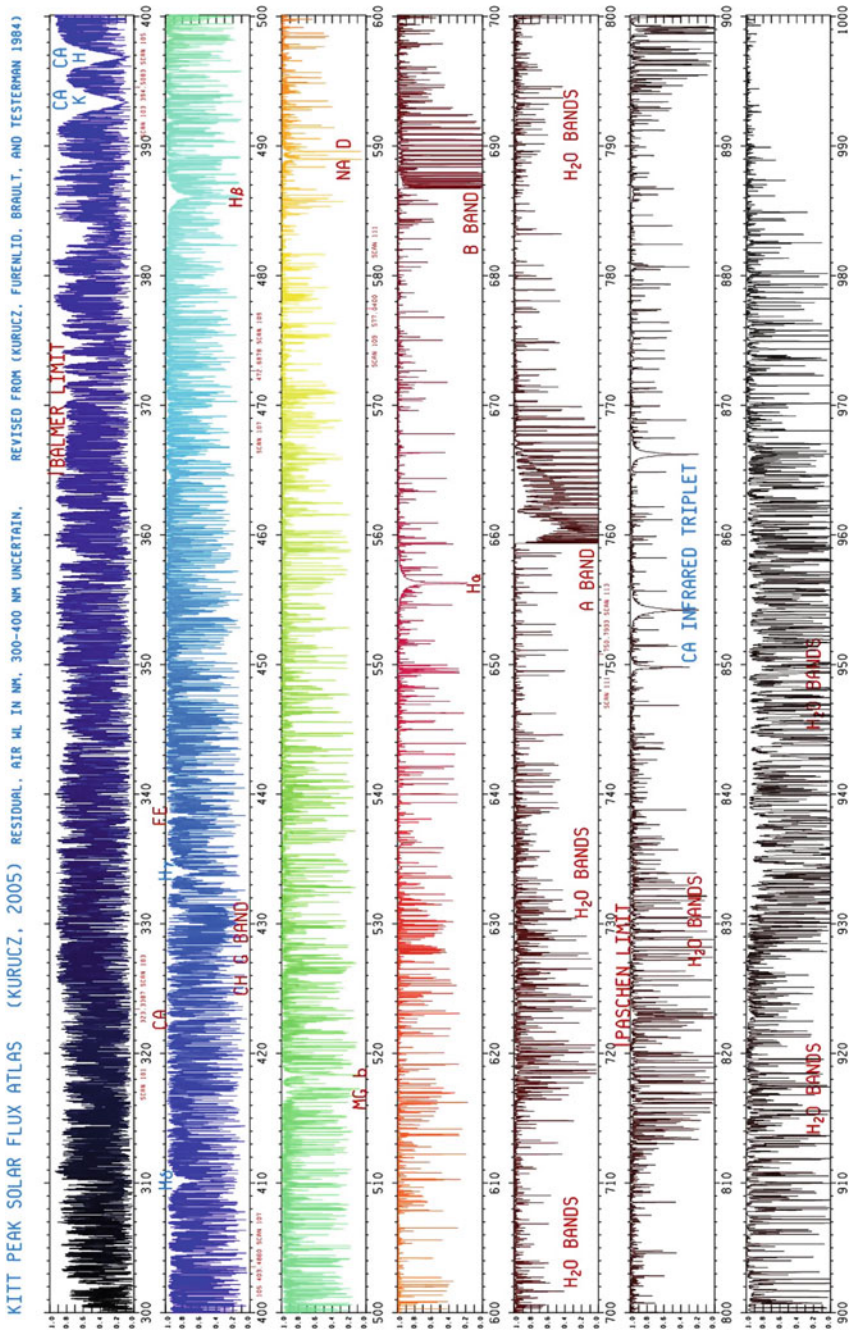

Fig. 1 The visible flux atlas from Kurucz (2005f)

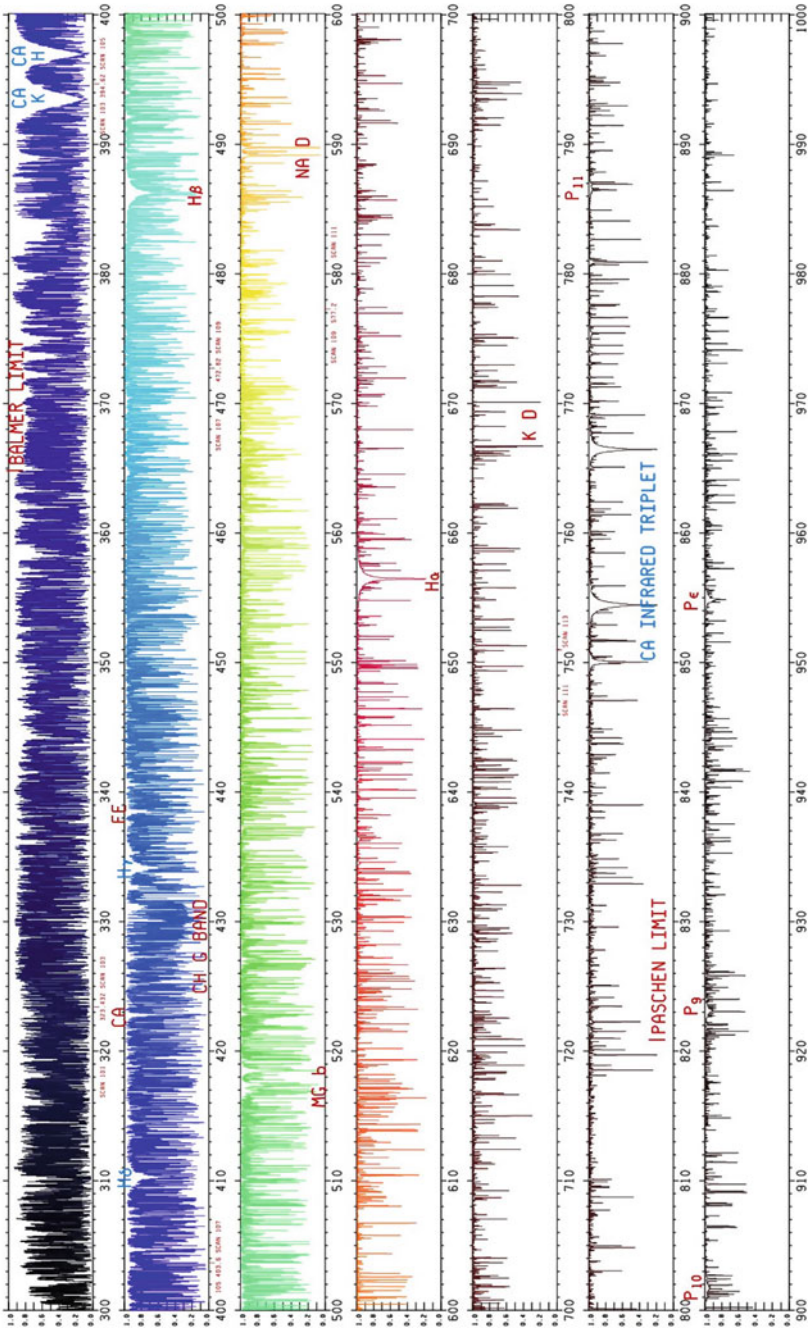

Fig. 2 The residual irradiance spectrum determined by removing the telluric lines from the flux spectrum (Kurucz 2005g)

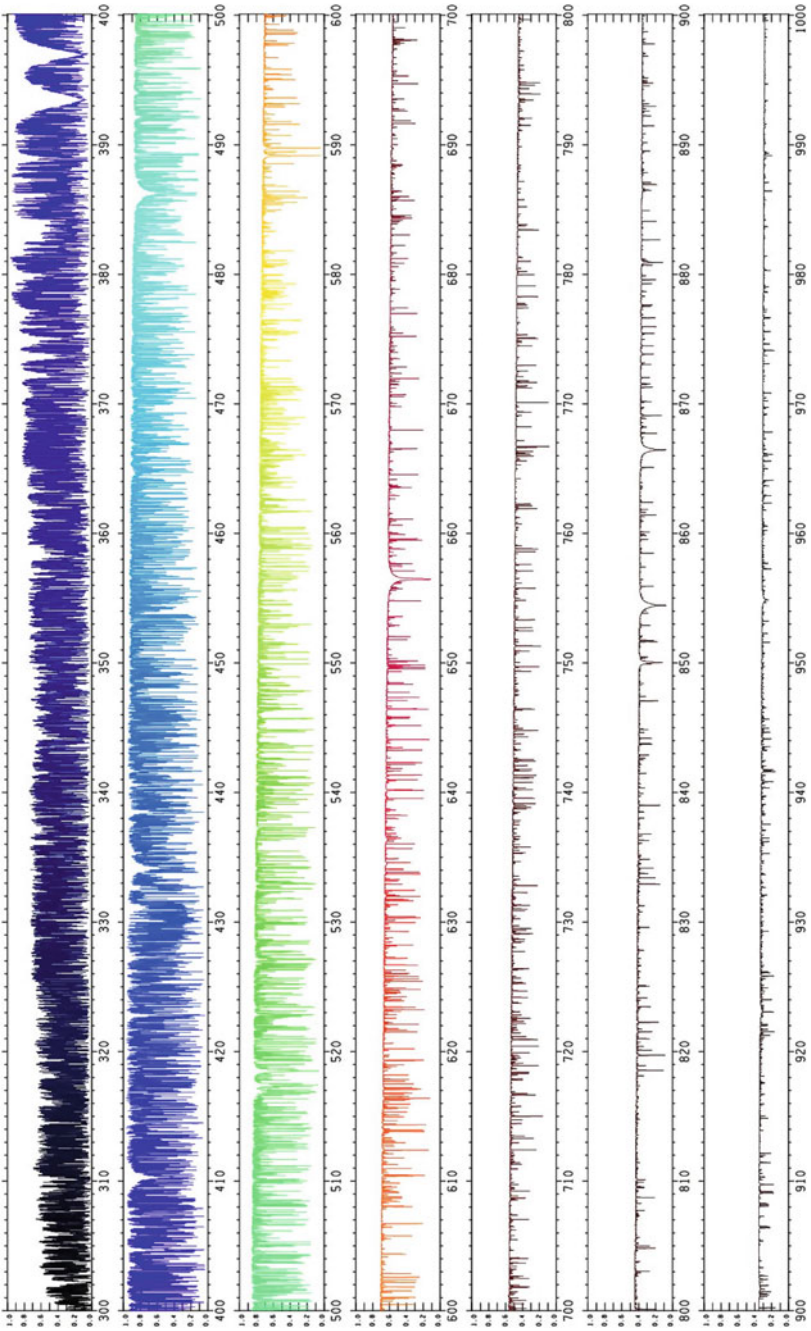

Fig. 3 The absolute irradiance spectrum determined by multiplying the residual irradiance times the continuum of the solar model ASUN seen from a distance of 1 AU (Kurucz 2005g)

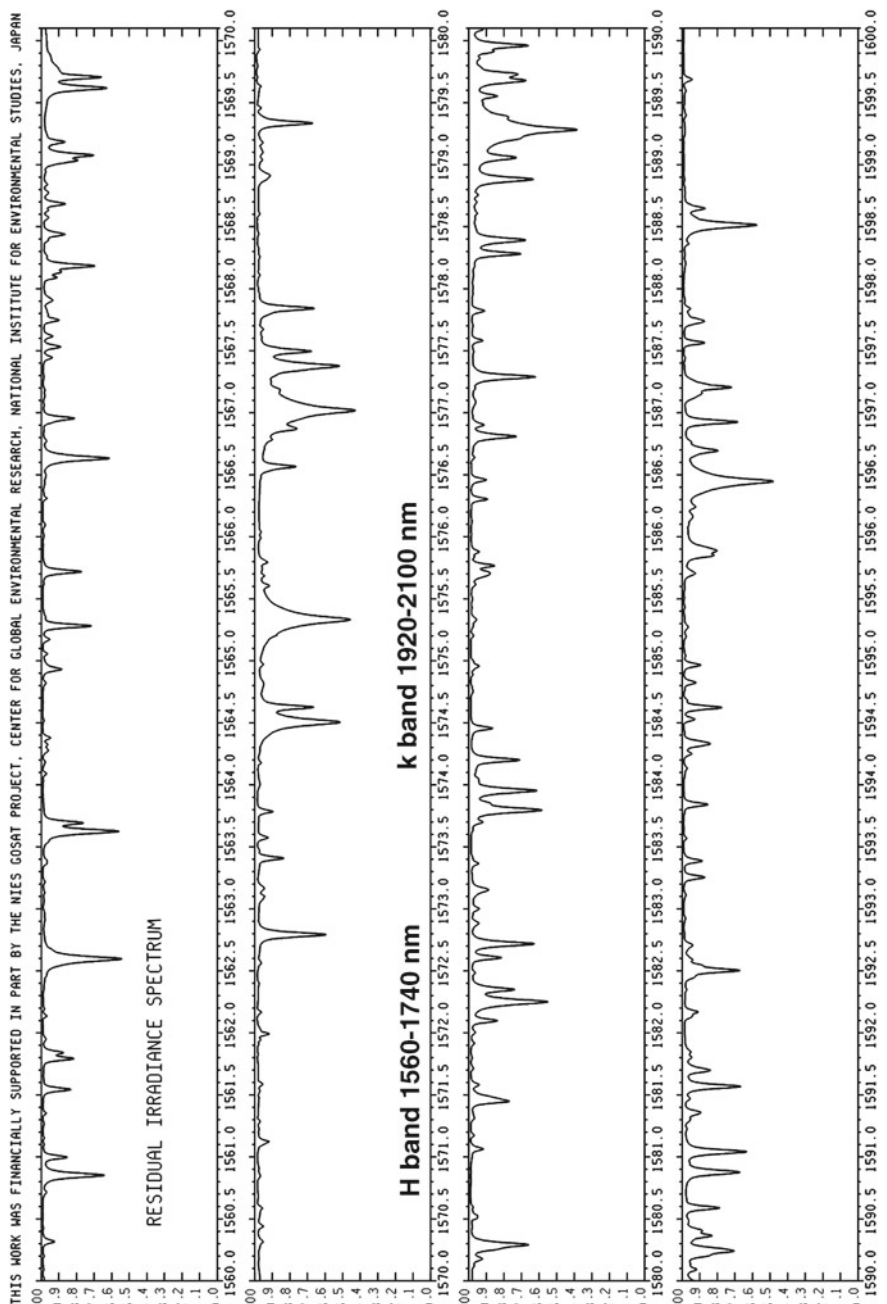

Fig. 4 A sample residual irradiance spectrum for part of the H and K bands (Kurucz 2008)

4 Validating Spectrum Calculations

Figure 5 shows a detailed comparison of the solar calculations to 0.15 nm of the flux atlas shown in Fig. 1 at 599.1 nm. I have 10 000 pages with comparisons like this. This is one of the least busy and best fitting. Each spectrum is plotted twice: at normal scale, and at 10 times scale to emphasize discrepancies. The observed FTS spectrum is plotted in black. The computed telluric spectrum broadened to the FTS resolution is plotted in cyan. The computed solar spectrum broadened to the FTS resolution is plotted in red. The product of the solar and telluric spectra broadened to the FTS resolution is plotted in magenta. Comparing the magenta spectrum to the black spectrum tests the wavelengths, gf values, and damping constants. The left feature at 599.13 nm with depth 0.26 is mainly Fe II with some blending with CN, Fe I, Yb II, and telluric H_2O. There are missing lines in both wings. The right feature at 599.185 nm with depth 0.05 is mostly 15 hyperfine components of a Co I line overlain by a telluric H_2O line. There are also blends with CN, Cr I, and Ca I. There are missing lines in both wings; several beyond 599.21 nm. There are probably additional missing lines included in both features. Overall the comparison shows a tremendous improvement in the treatment of the Co I feature over my earlier solar calculations.

In these plots we compare only the 1 % of my lines that have good wavelengths. Lines that are missing may be among the list of lines with predicted wavelengths. The predicted lines contribute statistically to the total opacity in model calculations.

Here are my conclusions from working with high-quality spectra:

- Abundances are generally determined from blended features that must be interpreted by synthesizing the spectrum including every significant blending line.
- In general, one half of the lines are missing from the list of lines with good wavelengths.
- Every line has to be adjusted in wavelength, damping constants, and gf value, and most are asymmetric from hyperfine and isotopic splitting. There are pressure shifts. There are depth-dependent Doppler shifts from motions.
- Most lines used in abundance analyses are not suitable.
- Including many lines reduces the accuracy.
- We do not know anything with certainty about the Sun except its mass.

5 ATLAS12

SYNTHE is the basis for ATLAS12. It provides the line and continuum opacity and the equation of state.

ATLAS12 can deal with more than 1 billion lines by sampling. It preselects into a smaller line list the lines that are relevant for the model and also saves them in a file. That file can be used as the input line list for similar models. It can treat arbitrary depth-dependent abundances, isotopes, and velocities. It defaults to 30 000

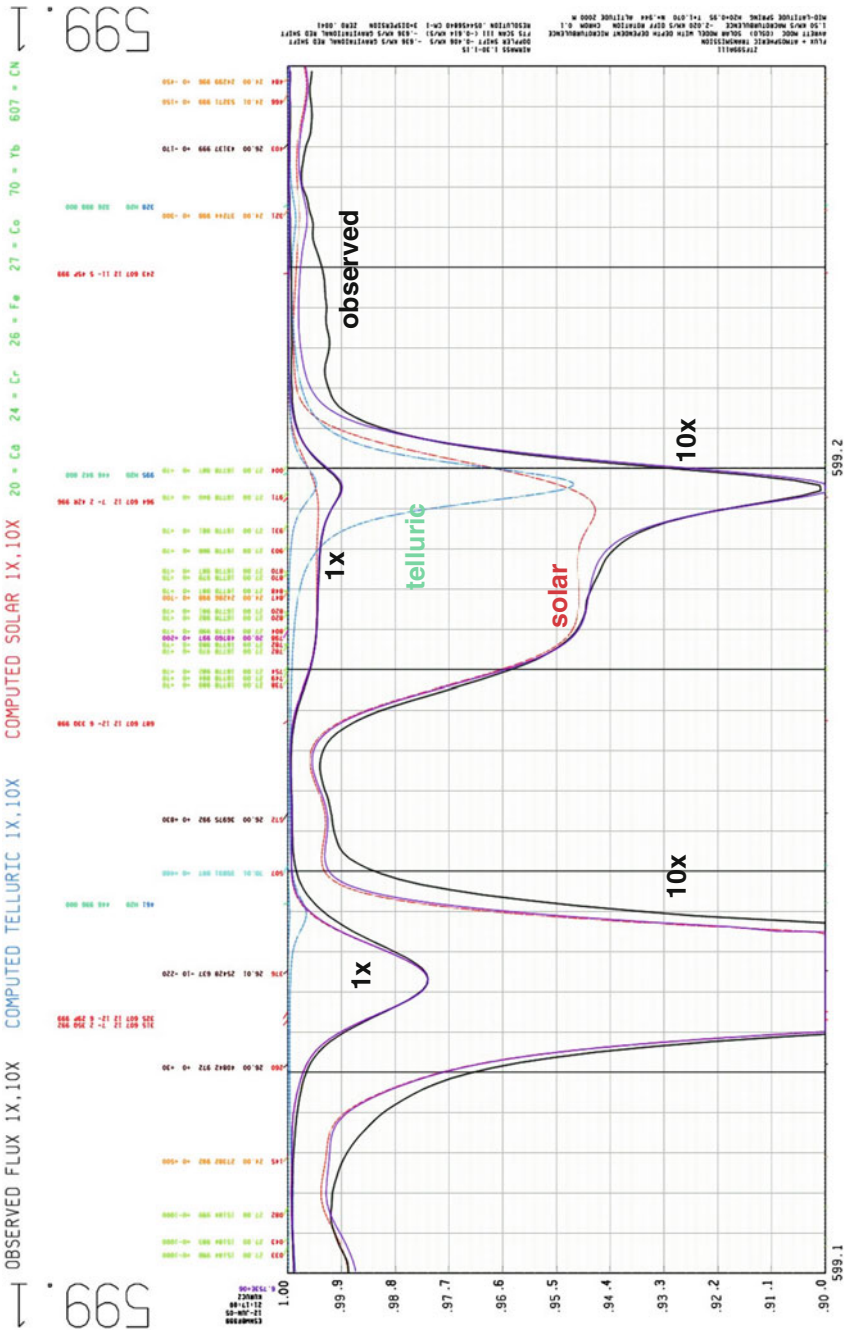

Fig. 5 A detailed comparison of the solar calculations to 0.15 nm of the flux atlas shown in Fig. 1 at 599.1 nm

sampling points but it could sample more than a million. The points shift with effective temperature to give good coverage of the flux maximum. 30 000 points are adequate for computing a flux-constant model but not for reliably predicting the SED over small intervals. For each model I make SYNTHE runs at resolving power 500 000 to compute the surface flux or intensities using the saved line file as input. I also compute spectra using only the lines with good wavelengths for comparison to observed spectra. Differences between the two computed spectra indicate how much more work needs to be done on the line list.

ATLAS12 is slow by design for treating individual stars with individually determined abundances and parameters. I compute a grid of models for each star I work on varying all the parameters. There is a big investment in quality.

6 DFSYNTHE and ODFs

If you are working on huge numbers of stars and want to interpolate in large grids of models to determine parameters, it is more efficient to pretabulate the opacities for a fixed set of abundances and then to compute the grid, or as many models as you need, using ATLAS9 because it is fast.

DFSYNTHE is the program you use to compute the line opacity spectra and from them to tabulate opacity distribution functions, ODFs.

First let me describe ODFs. Figure 6 shows a schematic line opacity profile and a schematic spectrum extending over an interval $\Delta\lambda$. An integral of some property of the radiation over that interval is independent of the wavelength order of the points in the spectrum as long as the source function, which is the Planck function B_ν, does not vary significantly over the interval. You can rearrange the line profile or spectrum in order of increasing opacity. If you then normalize by the width of the interval, you have a distribution function that tells you the fraction of the interval that has opacity less than a given value of the line opacity, ℓ_ν.

Figure 7 shows a set of distribution functions computed for the region on the blue side of the Balmer discontinuity for a range of electron number densities. The interval included about 10 000 wavelength points. In this case I approximated the distribution function with a 10 point step function. The average radiation field over this interval is then calculated at 10 distribution function points instead of 10 000 wavelength points, a saving of a factor of 1,000. Using a step function introduces some numerical error and some physical error. The smallest step represents the width of the line cores, so if the real line cores are narrower it smooths them and reduces the maximum optical depth. Fiorella Castelli (Castelli and Kurucz 2004) uses 12 steps to better represent the cores.

Another physical error is shown in Fig. 8. Using ODFs assumes that the opacity spectrum has similar appearance at every depth in the atmosphere as in the left panel. Then the optical depth is computed correctly even when the spectrum is rearranged in an ODF. But if the opacity spectrum significantly changes shape because of ionization or molecular bands that introduce a strong temperature dependence, the optical depth

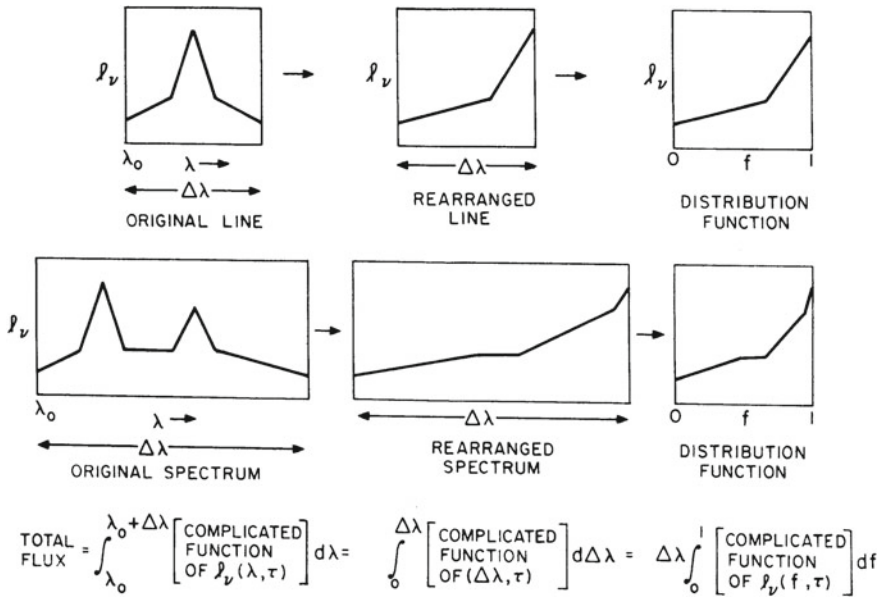

Fig. 6 Schematic opacity distribution functions, ODFs

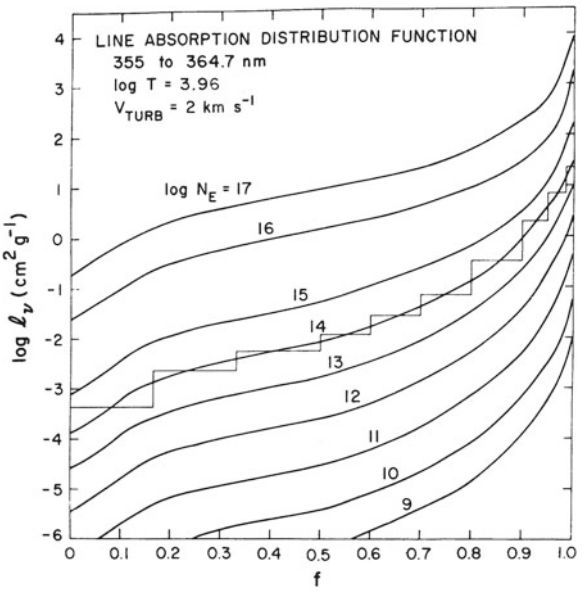

Fig. 7 Computed opacity distribution functions

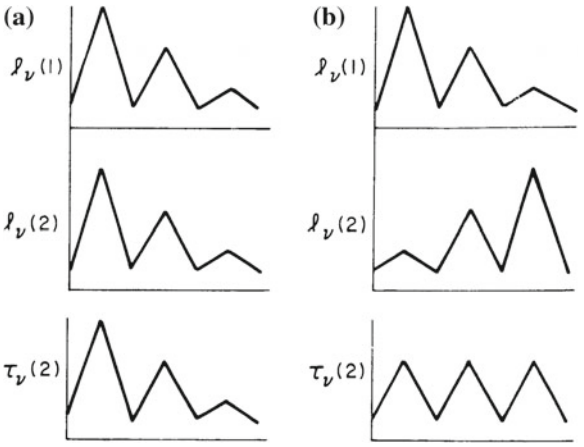

Fig. 8 ODFs can produce errors in optical depth; see text

will be underestimated and overestimated by the ODF. The spectra in the right panel have the same ODFs as those in the left but different optical depths. In practice, in general, ATLAS9 models with ODFs look the same as ATLAS12 models with sampling which do not have any rearrangement. It must be that the errors average out. However, no one has yet computed a complete ATLAS12 grid to compare to a complete ATLAS9 grid to look for peculiar cases.

DFSYNTHE is a version of SYNTHE that can compute the LTE opacity spectrum of more than 1 billion lines, at more than 4 million frequencies, for more than 1200 temperature-pressure pairs, for a range of V_{turb}, on a workstation (or a supercomputer). These spectra can be statistically processed into ODF tables as they are computed. Or the spectra can be saved directly if you have enough disk space. Then you can work out any kind of opacity representation you want with them.

7 ODFs and ATLAS9

ATLAS9 works with two different sets of ODFs. One with 337 "big" wavelength intervals covering the whole spectrum and one with 1221 "little" wavelength intervals covering the whole spectrum. The ODFs use a 12-step representation. There is one time-saving modification. The radiation field is computed starting with the highest step and working down. If a lower step does not matter because the line opacity is small relative to the continuum at all depths, all the lower steps are lumped together and not computed.

The big ODFs run faster while the little ODFs show more detail. I usually compute models with the big and then compute final fluxes with the little.

The original write-up for ATLAS, which describes ATLAS5, SAO Special Report 309 (Kurucz 1970), gives a general overview of other details of the program and how to compute models as of 40 years ago. It is on my website `/papers/SAO309`.

You can get the Castelli ODFs and grids of models computed with those ODFs from Fiorella Castelli's web site http://wwwuser.oat.ts.astro.it/castelli. She has the Linux versions of ATLAS9,ATLAS12, SYNTHE, and DFSYNTHE, and manuals. You may never have to compute the ODFs yourself unless you want your own personal set of abundances. Start with hers and then learn how to compute your own models. Szabolcs Mészáros has followed that path and computed ODFs and massive grids of models using the Linux versions (Mészáros et al. 2012) and put them on his website http://www.iac.es/proyecto/ATLAS-APOGEE.

References

Castelli F, Kurucz RL (2004) Arxiv:astro-ph/0405087
Hase F, Wallace L, McLeod SD, Harrison JJ, Bernath PF (2010) JQSRT 111:521
Kurucz RL (1970) SAO Spec Rep 309:291
Kurucz05a Kurucz RL (2005a) Mem Soc Astron Ital Suppl 8:10
Kurucz RL (2005b) Mem Soc Astron Ital Suppl 8:69
Kurucz RL (2005c) Mem Soc Astron Ital Suppl 8:72
Kurucz RL (2005d) Mem Soc Astron Ital Suppl 8:83
Kurucz RL (2005e) Mem Soc Astron Ital Suppl 8:158
Kurucz RL (2005f) Kitt peak solar Flux Atlas. http://kurucz.harvard.edu/sun/fluxatlas2005
Kurucz RL (2005g) Kitt peak solar irradiance Atlas. http://kurucz.harvard.edu/sun/irradiance2005
Kurucz RL (2008) Irradiance in the H and K bands. http://kurucz.harvard.edu/sun/irradiance2008
Kurucz RL, Avrett EH (1981) SAO Spec Rep 391:142
Kurucz RL, Furenlid I (1979) SAO Spec Rep 387:142
Mészáros Sz, Allende Prieto C, Edvardsson B, Castelli, F et al (2012) Astron J 144:120

Atomic Data: Where to Get Them, How to Use Them

Tatiana Ryabchikova

Abstract A short description of spectral line formation in stellar atmosphere is given to define a set of atomic parameters needed for stellar spectra calculations. The main sources of atomic parameters are different databases that collect laboratory or theoretical data from original publications. A brief review of spectroscopic databases, that are most important for stellar astrophysics is presented.

Keywords Atomic data · Molecular data · Line: profiles · Line: formation · Catalogues

1 Introduction

Most information about stellar atmosphere structure, chemistry and dynamics we extract from spectroscopic observations. Usually, we analyse spectra normalized to continuum level. In this case we remove the influence of Earth atmospheric extinction as well as all transfer functions of the instruments. As a result we have spectra, part of which are shown in Fig. 1 for two stars of different effective temperature. Our goal is to carry out atmospheric modelling of the star that allows us to reproduce the observed spectra as closely as possible. What information do we need for stellar spectrum analysis?

T. Ryabchikova (✉)
Institute of Astronomy, Russian Academy of Sciences, Pyatnitskaya 48,
Moscow, Russia 119017
e-mail: ryabchik@inasan.ru

E. Niemczura et al. (eds.), *Determination of Atmospheric Parameters of B-, A-, F- and G-Type Stars*, GeoPlanet: Earth and Planetary Sciences,
DOI: 10.1007/978-3-319-06956-2_5,

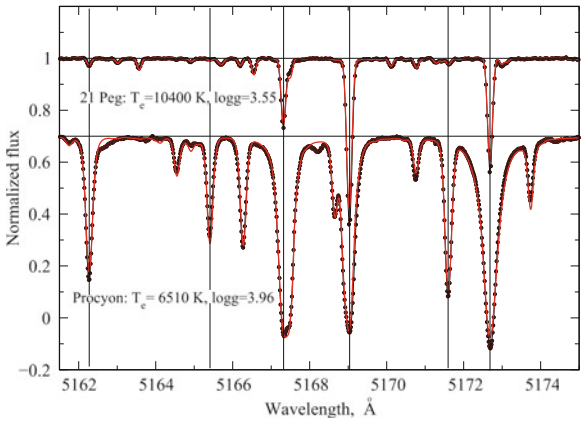

Fig. 1 Observed stellar spectra (*filled circles*) fitted with the best model calculations (*solid lines*). *Vertical lines* indicate position of the common features in spectra of both stars of different temperatures. The Procyon spectrum is shifted down by 0.3 for demonstration purposes

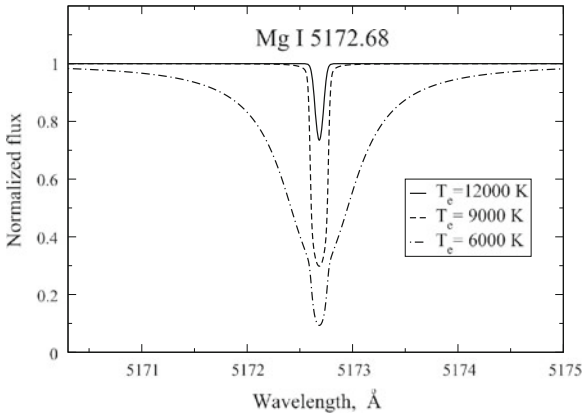

Fig. 2 Changes of line profile under different environment parameters, temperature and pressure defined by the effective temperature of the stellar atmosphere

2 Spectral Line Formation

The emergent stellar spectrum consists of a forest of spectral lines of different species, often overlapped with each other. An example of an individual line is shown in Fig. 2. This line produces an absorption defined by the line absorption coefficient

$$\kappa_\nu^l = n_i f_{ij} \frac{\pi e^2}{mc} \phi_\nu, \tag{1}$$

where n_i is the level population; f_{ij} is the oscillator strength and ϕ_ν is an absorption profile normalized to unity

$$\int_0^\infty \phi_\nu d\nu = 1. \tag{2}$$

In the approximation of local thermodynamic equilibrium (LTE) the level population n_i is defined by the Boltzmann and Saha equations

$$\frac{n_i}{N_n} = \frac{g_i}{u_n(T)} \mathrm{e}^{-\left(\frac{E_i}{kT}\right)}; \quad \frac{N_{n+1}}{N_n} = \frac{1}{N_e} \frac{2u_{n+1}}{u_n} \left[\frac{2\pi m_e kT}{h^2}\right]^{3/2} \mathrm{e}^{-\left(\frac{\chi_n}{kT}\right)}, \tag{3}$$

where $u_n(T) = \sum_j g_j \mathrm{e}^{-\frac{E_j}{kT}}$ is the partition function, N_n and N_e are number of atoms in n's ionization stage and electron number density, respectively. The absorption coefficient at the line center is defined by the following combination of atomic line parameters:

E_i, E_j	energy of the lower and upper levels of the transition,
χ_n	ionization potential,
$g_i = 2J_i + 1$	statistical weight of the level i;
J_i	total angular momentum,
$g_i f_{ij}$	$= 1.499 \times 10^{-16} g_i A_{ji} \lambda^2$,
A_{ji}	Einstein coefficient (spontaneous transition probability) in s^{-1},
λ	wavelength in Å.

In stellar atmospheres the absorption line profile is a product of the central line absorption and absorption profile ϕ_ν expressed by the Voigt-Hjerting function $H(u, a)$ for most but H and He lines

$$\phi_\nu = \frac{H(u,a)}{\sqrt{\pi}\Delta\nu_\mathrm{D}} = \frac{1}{\sqrt{\pi}\Delta\nu_\mathrm{D}} \frac{a}{\pi} \int_{-\infty}^{\infty} \frac{\mathrm{e}^{-y^2}}{(u-y)^2 + a^2} dy, \tag{4}$$

where $u = (\nu - \nu_0)/\Delta\nu_\mathrm{D}$ and $a = \gamma/(4\pi\Delta\nu_\mathrm{D})$.

This function is a result of Doppler and Lorentz profiles convolution, where the Doppler part $\Delta\nu_\mathrm{D} = \nu_0 \mathrm{v}/\mathrm{c}$ ($\mathrm{v}^2 = 2kT/m + \xi_t^2$), and the damping parameter in the Lorentz profile is $\gamma = \gamma_R + \gamma_4 + \gamma_6$, where

$\gamma_R = \sum_{k<j} A_{jk} + \sum_{l<k} A_{il}$ is the radiative (natural) damping constant;

γ_4 is the Stark damping constant (perturbation by charged particles—electrons, protons and ions), quadratic Stark effect;

γ_6 is the van der Waals damping constant (perturbation by neutral hydrogen and metals).

Unlike γ_R, γ_4 and γ_6 are not actually constants; they depend on temperature and pressure, that is, on the depth in the stellar atmosphere.

Laboratory measurements are scarce for γ_4 and γ_6. Stark and van der Waals damping constants are derived by quantum-mechanical calculations [see Kurucz' database for both γ_4 and γ_6 or (Barklem et al. 2000) for γ_6] or by semi-empirical (Griem 1968) and by semi-classical (Sahal-Bréchot 1969a, b) calculations as in case of γ_4.

For H and He lines a perturbation theory is used to represent line profiles which are available via numerical tables (Griem 1968; Vidal et al. 1973; Stehlé 1994a, b).

Besides Doppler and Lorentz broadening, few other mechanisms may affect the shape of a spectral line: hyperfine splitting of energy levels (hfs), isotopic shifts (IS) and Zeeman splitting of spectral lines in a magnetic field.

An isotope with odd atomic mass (for example, Sc, V, Mn, Co, etc.) has non-zero nuclear angular momentum and its levels are split due to multipolar interaction between magnetic momentum of the nucleus and the electron shell. In this case the angular momentum of the level $F = J + I$, where I is a nuclear angular momentum. The splitting of the levels is defined by the Casimir formula:

$$\Delta E = \frac{AK}{2} + \frac{3BK(K+1) - 4I(I+1)J(J+1)}{8I(2I-1)J(2J-1)}, \tag{5}$$

and each level splits in $2I + 1 (J > I)$ or $2J + 1 (J < I)$ sublevels. $K = F(F + 1) - J(J + 1) - I(I + 1)$. The relative strength of the hfs-components depends on F. A and B are hfs-constants. One needs to know I and J, A, B of the lower and upper levels to calculate the full hyperfine structure of a spectral line. An example of hfs-splitting is shown in Fig. 3.

Some of the chemical species have a few isotopes, which should be included in spectral synthesis to achieve an accurate presentation of line intensity and shape. To calculate correct line positions of the isotopes we need to know the isotopic splitting of the energy levels; to calculate correct intensities we need to know the isotopic composition.

In a magnetic field $\mathbf{B}$ the level with the total angular momentum J splits into $(2J + 1)$ Zeeman sublevels with magnetic quantum number $M = -J, \ldots, +J$ and energy level splitting $\Delta E \sim |\mathbf{B}|g$, where g is the Landé factor expressed as

$$g = \frac{3}{2} + \frac{S(S+1) - L(L+1)}{2J(J+1)} \tag{6}$$

in LS coupling scheme. The magnetic displacement is

$$\Delta\lambda = 4.67 \times 10^{-13} \lambda^2 |\mathbf{B}| g_{\rm eff}, \tag{7}$$

where $g_{\rm eff} = \frac{1}{2}(g_i + g_j) + \frac{1}{4}(g_i - g_j)(J_i(J_i + 1) - J_j(J_j + 1))$. An example of Zeeman splitting is shown in Fig. 4.

Summarizing all the information presented above we see that for accurate stellar spectroscopic analysis one needs about 15 parameters per line for a large number of spectral lines. Where can we find these data and how could we get them?

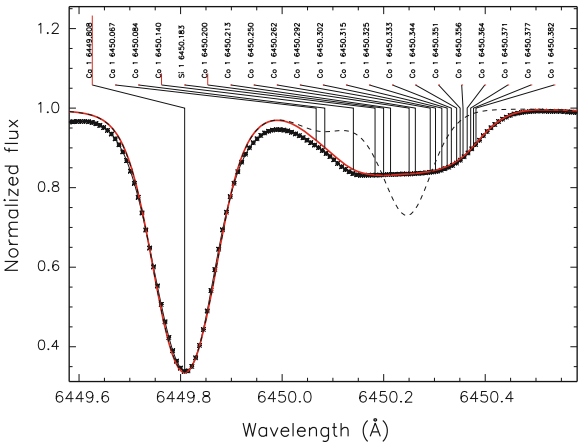

Fig. 3 Co I 6450.25 Å line in the solar spectrum (*asterisks*). Line profile synthesized with *hfs* effect taken into account is shown by a *solid line*, while theoretical spectrum without *hfs* is shown by a *dashed line*

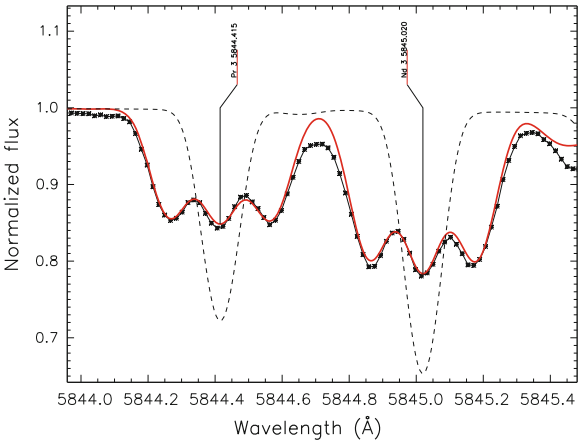

Fig. 4 Zeeman splitting in the spectrum of magnetic chemically peculiar star HD 144897 with surface magnetic field modulus 8.8 kG. Observations are shown by *asterisks*, magnetic model fit is shown by a *solid line*, and synthetic calculations without magnetic field are shown by a *dashed line*

3 Atomic Line Databases

Atomic line parameters come either from laboratory measurements or from theoretical calculations. Calculations for the transitions between experimentally known energy levels usually produce large amount of accurate data for wavelengths and are applicable for spectral synthesis of large spectral regions. For analysis of individual lines laboratory measurements are preferred. Theoretical calculations also provide

us with the data for hundreds million of the so-called predicted lines which cannot be used for precise spectral analysis but play a significant role in opacity calculations. Most parts of the atomic line parameters are collected in different databases. Below I give a short description of the most important databases for astrospectroscopy, starting with Robert Kurucz' database because it is the most complete line data collection for many astrophysical applications.

3.1 Robert Kurucz Database

Kurucz' collection of the atomic and molecular line parameters can be found on the website http://kurucz.harvard.edu/. It consists of three different parts: **Line lists, Atoms, and Molecules**.

Line lists is the older version of the data collection organized according to wavelengths. It consists of laboratory data and theoretical calculations for the transitions between experimentally known energy levels made before 1995 (see Kurucz 1975). Atomic and molecular data are separated.

Atoms is a collection of recent theoretical calculations based on advanced information about atomic energy levels and organized by atomic number and ion charge. Atomic parameters are given in text files with extension `*.lines` for all transitions including the predicted ones, and in files with extension `*.pos` for the transitions between experimentally known energy levels (observed lines). Predicted lines are indicated by negative energy for one or both levels. These data are needed for opacity calculations in stellar atmosphere modelling. For each spectral line Kurucz' calculations provide all important atomic parameters: wavelength, energy levels and level description, transition probability, damping parameters, Landé factors. Isotopic shifts and hfs data (if any) are included as well. The recent laboratory data for some ions are collected in separate files. For each ion, partition functions are given. Of course, calculated transition probabilities or damping parameters are not always accurate enough for the detailed analysis of individual lines in high-resolution, high signal-to-noise stellar spectra; however, Kurucz' calculations provide a unique possibility to search for possible blends in the vicinity of spectral lines of interest. They are very important in spectral synthesis. Kurucz' collection is the only database that provides all parameters needed to describe spectral lines of many species important in astrophysics: for example, hfs splitting in Sc, V, Mn, Co lines; hfs and *IS* splitting in Li I, Ba II, Eu II lines, etc.

A diagram of most recent Kurucz' calculations is shown in Fig. 5. Dashed regions indicate ions with *hfs* and/or *IS* information available.

The number of lines with accurate wavelengths (observed lines) for atoms in the first three ionizations stages exceeds one million, while the number of predicted lines for the same species exceeds 125 millions.

The **Molecules** directory contains data for diatomic molecules and H_2O from recent publications.

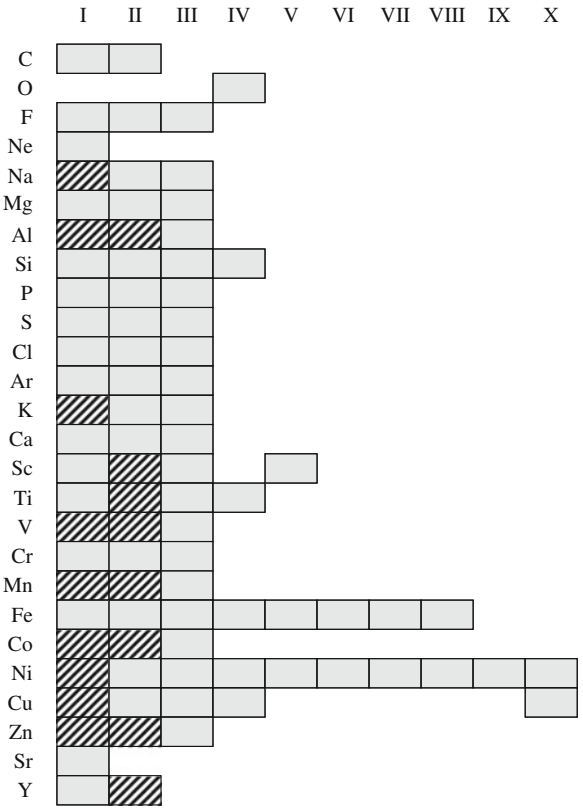

Fig. 5 Schematic presentation of Kurucz' recent calculations. The ions with *hfs* and/or *IS* data available are shown by *dashed* regions

3.2 NIST Atomic Spectra Database

NIST ASD[1] is a collection of critically evaluated data, accurate enough for detailed spectroscopy. For each transition NIST ASD (*Lines*) contains observed and Ritz wavelength, relative intensity, transition probability with the accuracy estimate, energy values and description of the lower and upper levels, transition type and references. Observed Landé factors of the lower and upper levels, if available, are given in a separate table *Levels*. The user defines search criteria and output options: HTML (formatted) or ASCII text. For many atomic species important in astrophysics such as lanthanides NIST ASD has little if any data on transition probabilities. Even for a very important element such as ionized Fe, NIST ASD Version 5 provides transition probabilities for 1,009 lines while the Kurucz DB contains 124,654 observed

[1] http://www.nist.gov/pml/data/asd.cfm.

lines. The NIST evaluation is based on the evaluation of the accuracy of experiments or theoretical calculation methods.

3.3 VALD3—Vienna Atomic Line Database, Third Release

VALD[2] was originally designed for stellar spectrum analysis that defines its functionality (Kupka et al. 1999). The VALD collection includes large parts of data from Kurucz's database (data for observed and predicted lines stored separately), and part of the data from NIST ASD and D.R.E.A.M. database transformed to VALD format. There are specific features in the VALD data structure:

- Data is sorted in wavelengths and stored in a special compressed format.
- Stored data include species, wavelength, levels energy (cm^{-1}) and angular momentum J, oscillator strength (transition probability) $\log(gf)$, Landé factors, damping constants, accuracy in $\log(gf)$, data reference, full level designation and term name. Also isotopic components for Li, Ca and Eu are available. No *hfs*-data.
- Publishing new dataset in VALD means adding a new data file saving all previous files.
- Data description is stored in various support files (list of species, configuration file).
- Configuration file stores ranks for every field in each file.

According to the user's request VALD returns data via e-mail or FTP; therefore, prior registration of the user is required. Registered users create a request with one of several VALD extraction tools:

- Show Line or Show Line ON-LINE.
- Extract All.
- Extract Element.
- Extract Stellar.

The last extraction tool is the most popular one among stellar spectroscopists. It returns a list of spectral lines whose contribution to the emergent flux for a chosen model atmosphere (detection threshold) is specified by the user. VALD output files may be directly used in synthetic spectrum calculations within some codes such as SYNTH3 and SYNTHV_NLTE.

The merging procedure is performed on the basis of ranking parameters for every field of each data file listed in the VALD configuration file. A default configuration file is provided by the VALD team, but a registered user can create a personal configuration file changing ranking parameters.

VALD has three mirror sites:

- Vienna http://vald.astro.univie.ac.at/~vald3/php/vald.php
- Uppsala http://vald.astro.uuu.se/~vald/php/vald.php
- Moscow http://vald.inasan.ru/~vald3/php/vald.php

[2] http://vald.astro.univie.ac.at/~vald3/php/vald.php.

where user finds all the information about VALD and the registration process. Some recent modifications in VALD content for Fe-peak elements are given in Ryabchikova et al. (2008). The VALD team evaluates data (first, transition probabilities) on the basis of line appearance and observed intensity in spectra of stars with different formation conditions (temperature and pressure).

3.4 D.E.S.I.R.E. and D.R.E.A.M. Databases at Mons University

D.E.S.I.R.E.—Database on Sixth Row Elements[3] consists of radiative transition database and Landé factors database for Ta I to Bi II.

D.R.E.A.M.—Database on Rare Earth's at Mons University[4] contains data for radiative transitions for lanthanides in the first three ionization stages from La III to Lu III and also for Th III. All included data come either from purely theoretical calculations or from semi-empirical calculations based on measured lifetimes and calculated branching ratios. Both databases contain wavelength, rounded energy value, parity and total angular momentum J of the lower and upper level, respectively, and transition probability. No level description (configuration or term) is given. Data are presented in ASCII text format.

3.5 STARK- B *Database*

STARK- B database[5] is a collection of calculated Stark widths and shifts for a set of atoms/ions from He to Pb. Perturbers are electrons, protons, ionized helium, magnesium, silicon, iron. Stark widths and shifts are given in Å in table format for a set of temperatures and perturber's number densities. In the reasonable density range, Stark widths and shifts have a linear dependence on density. STARK- B database also provides fitting coefficients for quadratic temperature dependence of damping parameters.

4 VAMDC—Virtual Atomic and Molecular Data Centre

VAMDC[6] is not a database; it is an international project aimed at the creation of a well documented interoperable interface to the differently organised existing Atomic and Molecular databases, financed by the European Union (EU). VAMDC

[3] http://w3.umons.ac.be/~astro/desire.shtml.

[4] http://w3.umons.ac.be/~astro/dream.shtml.

[5] http://stark-b.obspm.fr/index.php/home.

[6] http://www.vamdc.eu/.

consortium involves 15 administrative partners representing 24 teams from 6 EU member states (France, Austria, Germany, Italy, Sweden, United Kingdom), Serbia, the Russian Federation and Venezuela. The project lead institution is CNRS (France), and the project coordinator is Marie-Lise Dubernet (Dubernet et al. 2010). Currently, 29 databases enter the VAMDC test site,[7] where the user finds a short description of databases and working instructions.

VAMDC includes most of the above-mentioned databases of atomic and molecular line parameters and databases of the radiative and collisional cross-sections and reaction rate coefficients as well. A user makes a query by species (atom, molecule, particle), processes (radiative, collision) and/or environment (temperature, pressure, etc.). For example, to get atomic line parameters for a specific ion in a requested wavelength region one needs to specify the ion (atom symbol and ion charge) and the process (radiative). The primary advantage of VAMDC is a unified description for all parameters in all databases, so the user can get necessary information from VAMDC databases in a specific XSAMS format. This format is not convenient for immediate application. VAMDC, therefore, provides several conversion routines from XSAMS to table or csv formats.

Acknowledgments This work was partially supported by Praesidium RAS Program "Non-stationary Phenomena in Objects of the Universe" and by the Federal Agency for Science and Innovations (Grant No. 8529).

References

Barklem PS, Piskunov N, O'Mara BJ (2000) A&AS 142:467
Dubernet ML, Boudon V, Culhane JL et al (2010) JQSRT 111:2151
Griem HR (1968) Phys Rev 165:258
Kupka F, Piskunov N, Ryabchikova TA, Stempels HC, Weiss WW (1999) A&AS 138:119
Kurucz RL (1995) The Kurucz atomic and molecular database. In: Adelman SJ, Wiese WW (eds) Astronomical Society of the Pacific Conference Series, vol 78, pp 205
Ryabchikova T, Kildiyarova R, Piskunov N, Heiter U, Fossati L, Weiss WW (2008) JPhCS 130:012017
Sahal-Bréchot S (1969a) A&A 1:91
Sahal-Bréchot S (1969b) A&A 2:322
Stehlé C (1994a) A&A 292:699
Stehlé C (1994b) A&AS 104:509
Vidal CR, Cooper J, Smith EW (1973) ApJS 25:37

[7] http://portal.vamdc.eu/vamdc_portal_test/home.seam.

Problems with Atomic and Molecular Data: Including All the Lines

Robert L. Kurucz

Abstract The line data available on my web site for computing opacities, model atmospheres, and spectra were computed or collected from the literature more than 25 years ago. I am recomputing the existing line lists including many more configurations and energy levels and producing many more lines. I am collecting more recent data from the literature, and I am extending the calculation to heavier elements and higher stages of ionization. I will produce more than 10 times as many lines which will significantly increase the opacity in the models and produce improved fits to observed spectra. All the new data are available on my website http://kurucz.harvard.edu.

Keywords Atomic data · Molecular data · Opacity

1 Introduction

In 1965 I started collecting and computing atomic and molecular line data for computing opacities in model atmospheres and then for synthesizing spectra. I wanted to determine stellar effective temperatures, gravities, and abundances. I still want to.

I started using Cowan's atomic structure programs (Cowan 1968) and managed to get them to work on a CDC 6400 computer instead of a supercomputer. I also computed line lists for diatomic molecules.

For 23 years I put in more and more lines but I could never get a solar model to look right, to reproduce the observed energy distribution.

In 1985 Sugar and Corliss at the National Bureau of Standards (NBS, now NIST) published a compilation of energy levels for the iron group elements. They gave me

R. L. Kurucz (✉)
Harvard-Smithsonian Center for Astrophysics, 60 Garden Street, Cambridge, MA02138, USA
e-mail: rkurucz@cfa.harvard.edu

E. Niemczura et al. (eds.), *Determination of Atmospheric Parameters of B-, A-, F- and G-Type Stars*, GeoPlanet: Earth and Planetary Sciences,
DOI: 10.1007/978-3-319-06956-2_6,

Table 1 Iron group lines computed at San Diego Supercomputer Center 1988

	I	II	III	IV	V	VI	VII	VIII	IX
Ca	48573	4227	11740	113121	330004	217929	125560	30156	22803
Sc	191253	49811	1578	16985	130563	456400	227121	136916	30587
Ti	867399	264867	23742	5079	37610	155919	356808	230705	139356
V	1156790	925330	284003	61630	8427	39525	160652	443343	231753
Cr	434773	1304043	990951	366851	73222	10886	39668	164228	454312
Mn	327741	878996	1589314	1033926	450293	79068	14024	39770	147442
Fe	789176	1264969	1604934	1776984	1008385	475750	90250	14561	39346
Co	546130	1048188	2198940	1569347	2032402	1089039	562192	88976	15185
Ni	149926	404556	1309729	1918070	1971819	2211919	967466	602486	79627

the tape that they used to typeset the book. I was able to decode it. I then applied for time at the San Diego Supercomputer Center.

By 1988 I finally produced enough lines, I thought. I completed a calculation of the first 9 ions of the iron group elements shown in Table 1 (Kurucz 1988). There were data for 42 million lines that I combined with data for 1 million lines from my earlier list for lighter and heavier elements including all the data from the literature. In addition I had computed line lists for diatomic molecules including 15 million lines of H_2, CH, NH, OH, MgH, SiH, C_2, CN, CO, SiO, and TiO for a total of 58 million lines.

I then tabulated 2 nm resolution opacity distribution functions (ODFs) from the line list for temperatures from 2,000 to 200,000 K and for a range of pressure suitable for stellar atmospheres (Kurucz 1992a).

Using the ODFs I computed a theoretical solar model (Kurucz 1992b) with the solar effective temperature and gravity, the current solar abundances from (Anders and Grevesse 1989), mixing-length-to-scale-height ratio ℓ/H = 1.25, and constant microturbulent velocity 1.5 km s^{-1}. It generally matched the observed energy distribution from (Neckel and Labs 1984).

I computed thousands of model atmospheres that I distributed on magnetic tapes, then on CDs, and now on my web site, http://kurucz.harvard.edu. They made observers happy and they made galaxy modellers happy and they made me happy. However, agreement with low-resolution observations of integrated properties does not imply correctness.

2 Problems

In 1988 the abundances were wrong, the microturbulent velocity was wrong, the convection was wrong, and the opacities were wrong.

Since 1965 the Fe abundance has varied by over a factor of 10. In 1988 the Fe abundance was 1.66 times larger than today. There was mixing-length convection with

Table 2 Fe II in 1988. Based on Johansson (1978) and Sugar and Corliss (1985)

Even: 22 configurations; 5723 levels; 354 known levels; 729 Hamiltonian parameters, all CI; 46 free LS parameters; standard deviation 142 cm^{-1}

		d^7		
$d^6 4s$	$d^5 4s^2$	$d^6 4d$	$d^5 4s4d$	$d^4 4s^2 4d$ $d^5 4p^2$
$d^6 5s$	$d^5 4s5s$	$d^6 5d$	$d^5 4s5d$	$d^6 5g$
$d^6 6s$	$d^5 4s6s$	$d^6 6d$	$d^5 4s6d$	$d^6 6g$
$d^6 7s$		$d^6 7d$		$d^6 7g$
$d^6 8s$		$d^6 8d$		
$d^6 9s$				

Odd: 16 configurations; 5198 levels; 435 known levels; 541 Hamiltonian parameters, all CI; 43 free LS parameters; standard deviation 135 cm^{-1}

$d^6 4p$	$d^5 4s4p$	$d^6 4f$	$d^5 4s4f$	$d^4 4s^2 4p$
$d^6 5p$	$d^5 4s5p$	$d^6 5f$		
$d^6 6p$	$d^5 4s6p$	$d^6 6f$		
$d^6 7p$	$d^5 4s7p$			
$d^6 8p$	$d^5 4s8p$			
$d^6 9p$				

Total E1 lines saved	1254969
E1 lines with good wavelengths	45815

an exaggerated, constant microturbulent velocity. In the grids of models, the default microturbulent velocity was 2 km s^{-1}. My 1-D models still have mixing-length convection, but now with a depth-dependent microturbulent velocity that scales with the convective velocity. 3-D models with cellular convection do not have microturbulent velocity at all, but use the Doppler shifts from the convective motions.

In 1988 the line opacity was underestimated because not enough lines were included in the line lists. Table 2 is an outline for the Fe II line calculation then. The higher energy levels that produce series of lines that merge into ultraviolet continua were not included. Those levels also produce huge numbers of weaker lines in the visible and infrared that blend and fill in the spaces between the stronger lines. Also lines of heavier elements were not systematically included. And then the additional broadening from hyperfine and isotopic splitting was not included (In the following tables CI stands for configuration interaction and "good lines" are lines between measured levels).

In 1988 the opacities were low but were balanced by high abundances that made the lines stronger and high microturbulent velocity that made the lines broader.

Now the abundances, the convection, and the opacities are still wrong, but they have improved. I am concentrating on filling out the line lists.

3 Examples of New Calculations

Here I show sample statistics from my new semiempirical calculations for Fe II, Ni I, and Co I in Tables 3, 4 and 5 to illustrate how important it is to do the basic physics well and how much data there are to deal with. Ni, Co, and Fe are prominent in supernovae, including both radioactive and stable isotopes. There is not space here for the lifetime and gf comparisons. Generally, low configurations that have been well studied in the laboratory produce good lifetimes and gf values, while higher configurations that are poorly observed and are strongly mixed are not well constrained in the least-squares fit and necessarily produce poorer results and large scatter. My hope is that the predicted energy levels can help the laboratory spectroscopists to identify more levels and further constrain the least-squares fits. From my side, I check the computed gf values in spectrum calculations by comparing to observed spectra. I adjust the gf values so that the spectra match. Then I search for patterns in the adjustments that suggest corrections in the least-squares fits.

As the new calculations accumulate, I will put on my web site the output files of the least-squares fits to the energy levels, energy level tables, with E, J, identification, strongest eigenvector components, lifetime, A-sum, C_4, C_6, Landé g. The sums are complete up to the first (n = 10) energy level not included. There will be electric dipole (E1), magnetic dipole (M1), and electric quadrupole (E2) line lists. Radiative, Stark, and van der Waals damping constants and Landé g values are automatically produced for each line. Branching fractions are also computed. Hyperfine and isotopic splitting will be included when the data exist but not automatically. Eigenvalues are replaced by measured energies so that lines connecting measured levels have correct wavelengths. Most of the lines have uncertain wavelengths because they connect predicted rather than measured levels. Laboratory measurements of gf values and lifetimes will be included. Measured or estimated widths of autoionizing levels will be included when available. The partition function will be tabulated for a range of densities.

When computations with the necessary information are available from other workers, I am happy to use those data instead of repeating the work.

Once the line list for an ion or molecule is validated it will be incorporated into the wavelength sorted line lists on my website for computing opacities or detailed spectra. The web directories are http://kurucz.harvard.edu/atoms and http://kurucz.harvard/molecules for the details, and http://kurucz.harvard.edu/linelists for the completed line lists.

Table 6 presents line statistics from some of my recent calculations that show an order of magnitude increase over my earlier work because I am treating about 3 times as many levels. Considering only the ions in the table, there are about 257 million lines compared to 26 million in the 1988 calculation. Table 7 shows my estimate (individual ions only to astronomical accuracy) that my line lists will have several billion atomic and molecular lines if I can continue my work. I expect to update and replace all my previous calculations for lighter elements and for the iron group in the near future. Then I will concentrate on extending the work to heavier elements and higher ions.

Table 3 Fe II based on Nave and Johansson (2013) and Castelli and Kurucz (2010). ^{57}Fe has not yet been measured because it has hyperfine splitting. Rosberg et al. (1993) have measured ^{56}Fe–^{54}Fe in 9 lines and ^{58}Fe–^{56}Fe in one line. I split the computed lines by hand

Even: 46 configurations; 19771 levels; 466 known levels; 2645 Hamiltonian parameters, all CI; 57 free LS parameters; standard deviation 48 cm^{-1}

	d^7				
$d^6 4s$	$d^5 4s^2$	$d^6 4d$	$d^5 4s 4d$	$d^4 4s^2 4d$	$d^5 4p^2$
$d^6 5s$	$d^5 4s 5s$	$d^6 5d$	$d^5 4s 5d$	$d^6 5g$	$d^5 4s 5g$	$d^4 4s^2 5s$
$d^6 6s$	$d^5 4s 6s$	$d^6 6d$	$d^5 4s 6d$	$d^6 6g$	$d^5 4s 6g$	
$d^6 7s$	$d^5 4s 7s$	$d^6 7d$	$d^5 4s 7d$	$d^6 7g$	$d^5 4s 7g$	$d^6 7i$	$d^5 4s 7i$
$d^6 8s$	$d^5 4s 8s$	$d^6 8d$	$d^5 4s 8d$	$d^6 8g$	$d^5 4s 8g$	$d^6 8i$	$d^5 4s 8i$ $d^5 4s 9l$
$d^6 9s$	$d^5 4s 9s$	$d^6 9d$	$d^5 4s 9d$	$d^6 9g$	$d^5 4s 9g$	$d^6 9i$	$d^5 4s 9i$ $d^6 9l$

Odd: 39 configurations; 19652 levels; 643 known levels; 2996 Hamiltonian parameters, all CI; 47 free LS parameters; standard deviation 63 cm^{-1}

$d^6 4p$	$d^5 4s 4p$	$d^6 4f$	$d^5 4s 4f$	$d^4 4s^2 4p$	$d^4 4s^2 4f$	
$d^6 5p$	$d^5 4s 5p$	$d^6 5f$	$d^5 4s 5f$	$d^4 4s^2 5p$		
$d^6 6p$	$d^5 4s 6p$	$d^6 6f$	$d^5 4s 6f$	$d^6 6h$	$d^5 4s 6h$	
$d^6 7p$	$d^5 4s 7p$	$d^6 7f$	$d^5 4s 7f$	$d^6 7h$	$d^5 4s 7h$	
$d^6 8p$	$d^5 4s 8p$	$d^6 8f$	$d^5 4s 8f$	$d^6 8h$	$d^5 4s 8h$	$d^6 8k$	$d^5 4s 8k$
$d^6 9p$	$d^5 4s 9p$	$d^6 9f$	$d^5 4s 9f$	$d^6 9h$	$d^5 4s 9h$	$d^6 9k$	$d^5 4s 9k$

Total E1 lines saved	7834681 new	1254969 old ratio = 6.1
E1 lines with good wavelengths	124920 new	45815 old ratio = 2.3

Forbidden lines	M1 even	M1 odd	E2 even	E2 odd
Total lines saved	2702418	3651124	10856977	13551054
with good wavelengths	46846	80161	72075	131362
between metastable	1250	0	1853	0

Isotope	^{54}Fe	^{55}Fe	^{56}Fe	^{57}Fe	^{58}Fe	^{59}Fe	^{60}Fe
Fraction	.059	.0	.9172	.021	.0028	.0	.0

4 Molecules, TiO and H_2O

These are examples of incorporating data from other researchers.

Schwenke (1998) calculated energy levels for TiO including in the Hamiltonian the 20 lowest vibration states of the 13 lowest electronic states of TiO (singlets a, b, c, d, f, g, h and triplets X, A, B, C, D, E) and their interactions. He determined parameters by fitting the observed energies or by computing theoretical values. Using Langhoff (1997) transition moments he generated a line list for J = 0 to 300 for the isotopologues ^{46}Ti^{16}O, ^{47}Ti^{16}O. ^{48}Ti^{16}O, ^{49}Ti^{16}O, and ^{50}Ti^{16}O with fractional abundances .080, .073, .738, .055, and .054. My version has 37,744,499 lines.

Table 4 Ni I based on Litzén et al. (1993) with **isotopic splitting**

Total E1 lines saved	732160 new	149926 old	ratio = 4.9
E1 lines with good wavelengths	9663 new	3949 old	ratio = 2.4
Isotope ^{56}Ni ^{57}Ni ^{58}Ni ^{59}Ni ^{60}Ni ^{61}Ni ^{62}Ni ^{63}Ni ^{64}Ni			
Fraction .0 .0 .6827 .0 .2790 .0113 .0359 .0 .0091			

There are measured isotopic splittings for 326 lines from which I determined 131 energy levels relative to the ground. These levels are connected by **11670 isotopic lines**. Hyperfine splitting was included for ^{61}Ni but only 6 levels have been measured which produce 4 lines with 38 components. A pure isotope laboratory analysis is needed. Ni I lines are asymmetric from the splitting and they now agree in shape with lines in the solar spectrum

Table 5 Co I based on Pickering and Thorne (1996) and Pickering (1996) with **hyperfine splitting**

Total E1 lines saved	3771908 new	546130 old	ratio = 6.9
E1 lines with good wavelengths	15441 new	9879 old	ratio = 2.4
Isotope ^{56}Co ^{57}Co ^{58}Co ^{59}Co ^{60}Co			
Fraction .0 1. .0 .0 .0			

Hyperfine constants have been measured in 297 levels which produce **244264 component E1 lines**. The new calculation greatly improves the appearance of the Co I lines in the solar spectrum

Good analyses and a similar semiempirical treatment are needed for CaOH, ScO, VO, YO, ZrO, LaO, etc. I am adding line lists for VO, CaH, CrH, and FeH to extend my opacities through the M stars.

Partridge and Schwenke (1997) treated H_2O semiempirically. They included isotopologues $H_2{}^{16}O$, $H_2{}^{17}O$, $H_2{}^{18}O$, and $HD^{16}O$. My version has 65,912,356 lines.

Barber et al. (2006) have massively treated $H_2{}^{16}O$. My version of their line list has 335,767,086 lines. I left out the very weak lines and added in the Partridge and Schwenke isotopologues. Line lists for many molecules are available or referenced on their website http://www.exomol.com that I do not hesitate to appropriate.

5 Spectrum Analysis Using Stellar Atlases as the Laboratory Source

Chemically peculiar or CP stars are early type stars with large over- and underabundances. They can have very small projected rotation velocities, hence narrow lines. HR 6000 has $T_{\rm eff}$ = 13,450 K, log g = 4.3, and projected rotation velocity about 1.5 km s^{-1} from Castelli and Hubrig (2007). The abundances (log relative to solar) are Fe [+0.9], Xe [+4.6], P [>+1.5], Ti [+0.55], Cr [+0.2]. Mn [+1.5], Y [+1.2], Hg [+2.7], and He, C, N, O, Al, Mg, Si, S, Cl, Sc, V, Co, Ni, and Sr underabundant. With initial guidance from Johansson, Castelli analysed the Fe II lines and has determined 126 new 4d, 5d, 6d, and 4f energy levels (Castelli et al. 2008, 2009; Castelli and Kurucz 2010). These levels produce more than 18,000 lines throughout the spectrum

Table 6 Sample recent atomic calculations. This is one page worth. The current list including lighter and heavier elements is in http://kurucz.harvard.edu/atoms/completed

	Config.		Levels		E1 lines		
	Even	Odd	Even	Odd	Good wl	Total	Old
Sc I	61	61	2014	2318	15546	737992	191253
Sc II	61	61	509	644	3436	116491	49811
Sc III	39	38	134	147	1313	5271	1578
Ti I	61	61	6628	7350	33815	4758992	867399
Ti II	61	61	2096	2318	8188	835027	264867
Ti III	73	68	3636	3845	4090	499739	23742
V I	61	61	13767	15952	23342	7043556	1156790
V II	61	61	6740	7422	18389	3932853	925330
V III	61	61	2094	2318	9892	966528	284003
Cr I	47	40	18842	18660	35315	2582957	434773
Cr II	61	61	13767	15890	58996	6970052	1304043
Cr III	61	61	6580	7526	23150	5535931	990951
Mn I	44	39	18343	19652	16798	1481464	327741
Mn II	50	41	19686	19870	31437	4523390	878996
Mn III	61	61	13706	15890	17294	10525088	1589314
Fe I	61	50	18655	18850	93508	6029023	789176
Fe II	46	39	19771	19652	124654	7834553	1264969
Fe III	49	41	19720	19820	37199	9548787	1604934
Fe IV	61	54	13767	14211	8408	14617228	1776984
Fe V	61	61	6560	7526	11417	7785320	1008385
Fe VI	73	73	2094	2496	3534	9072714	475750
Fe VII	85	86	7132	7032	2326	2816992	90250
Fe VIII	52	52	1365	1244	233	220166	14561
Co I	61	61	10920	13085	15441	3771900	546130
Co II	61	50	18655	19364	23355	10050728	1361114
Co III	44	39	18343	19652	9356	11515139	2198940
Ni I	61	61	4303	5758	9663	732160	149925
Ni II	61	61	10270	11429	55590	3645991	404556
Ni III	61	50	18655	19364	21251	11120833	1309729
Ni IV	44	39	18343	19517	5659	15152636	1918070
Ni V	46	41	10637	19238	10637	15622452	1971819
Ni VI	61	61	13706	15792	12219	17971672	2211919
Ni VII	73	73	24756	19567	3502	28328012	967466
Ni VIII	73	73	12714	8903	758	12308126	602486
Ni IX	85	86	7132	7032	253	2671345	79627
Ni X	52	52	1365	1208	235	285029	
Cu I	61	61	920	1260	5720	28112	
Cu II	61	61	4303	5758	14959	622985	
Cu III	61	61	10270	11429	17539	5258607	

Table 7 Estimated lines in 3d and 4d group sequences (in millions)

	I	II	III	IV	V	VI	VII	VIII	IX	X	...
Ca	.05										
Sc	.7	.05									
Ti	5	.7	.05								
V	14	5	.7	.05							
Cr	10	14	5	.7	.05						
Mn	1.5	10	14	5	.7	.05					
Fe	6	7	10	14	5	.7	.05				
Co	4	10	7	10	14	5	.7	.05			
Ni	.7	4	10	7	10	14	5	.7	.05		
Cu	.03	.6	4	10	7	10	14	5	.7	.05	
Zn	.1	.03	.6	4	10	7	10	14	5	.7	...
Ga		.1	.03	.6	4	10	7	10	14	5	...
Ge			.1	.03	.6	4	10	7	10	14	...
As				.1	.03	.6	4	10	7	10	...
Se					.1	.03	.6	4	10	7	...
Br						.1	.03	.6	4	10	...
Kr							.1	.03	.6	4	...
Rb								.1	.03	.6	...
Sr	.05								.1	.03	...
Y	.7	.05								.1	...
Zr	5	.7	.05								
Nb	14	5	.7	.05							
Mo	10	14	5	.7	.05						
[Tc]	1.5	10	14	5	.7	.05					
Ru	6	7	10	14	5	.7	.05				
Rh	4	10	7	10	14	5	.7	.05			
Pd	.7	4	10	7	10	14	5	.7	.05		
Ag	.03	.6	4	10	7	10	14	5	.7	.05	
Cd	.1	.03	.6	4	10	7	10	14	5	.7	...
In		.1	.03	.6	4	10	7	10	14	5	...
Sn			.1	.03	.6	4	10	7	10	14	...
Sb				.1	.03	.6	4	10	7	10	...
Te					.1	.03	.6	4	10	7	...
I						.1	.03	.6	4	10	...
Xe							.1	.03	.6	4	...
Cs								.1	.03	.6	...
Ba									.1	.03	...

Total 3d > 500 million
Total 4d > 500 million
+lanthanide sequences > 1000 million
+all the other element sequences

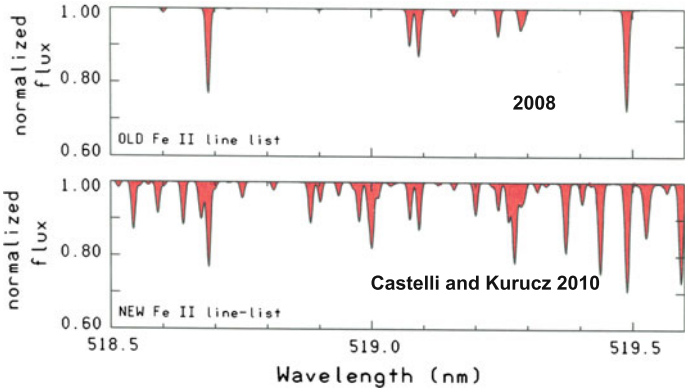

Fig. 1 The *upper panel* shows the Fe II spectrum computed for HR 6000 ($T_{\rm eff} = 13,450$ K, $\log g = 4.3$, $v \sin i = 1.5\,{\rm km\,s^{-1}}$, Fe = [+0.9]) using Kurucz data as of 2008. The *lower panel* is the same calculation using the current Kurucz Fe II line list

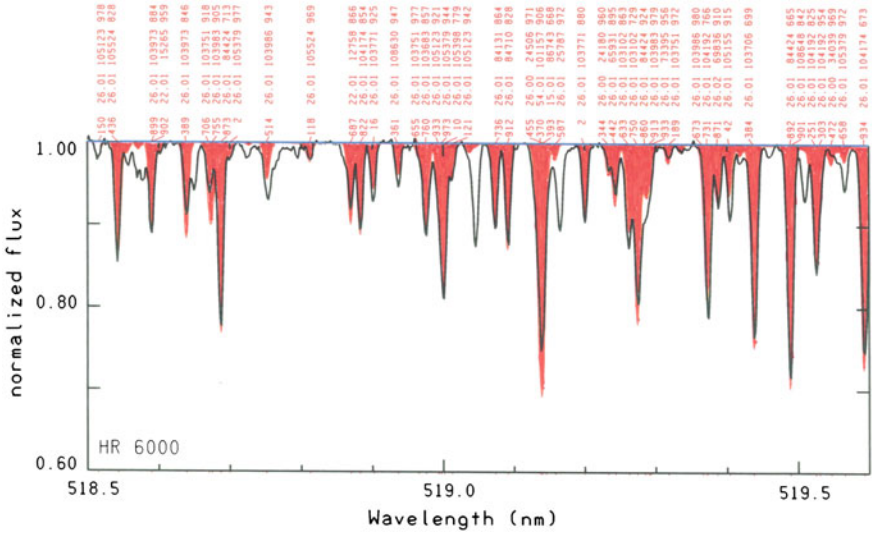

Fig. 2 The synthetic spectrum (in *red*) computed with a line list including the new Fe II lines compared to the observed spectrum of HR 6000 (in *black*). Note that many lines are missing and remain to be identified. The line identifications can be decoded as follows: for the first line, 150 = last 3 digits of the wavelength 518.5150; 26 = atomic number of Fe; .01 = charge/100. i.e. 26.01 identifies the line as Fe II; 105,123 is the energy of the lower level in $\rm cm^{-1}$; 970 is the residual central intensity in per mil

from ultraviolet to infrared. Figure 1 shows the improvement between Fe II computed with the 2008 Kurucz line list and the current line list. Figure 2 shows the improvement in the spectrum including all the lines. Note that many lines are still missing and remain to be identified.

In stars these Fe lines are seen in absorption and the Boltzmann factor for the lower level determines the line strength. Laboratory sources in emission have to populate the upper level. These lines appear in more "normal" stars as well but are smeared out and blended by rotation velocities 10–100 times higher.

Considerable telescope time should be allocated to making high-resolution, high-signal-to-noise atlases in the UV, visible, and IR of selected CP stars. These would be used as tools for extending laboratory spectrum analyses to higher energy levels for as many elements as possible.

Of course, high-quality solar atlases have been used to extend laboratory analyses for as long as they have existed (c.f. Geller 1992; Colin and Bernath 2010).

6 Conclusion

Inclusion of heavier elements, higher stages of ionization, additional molecules, and higher energy levels will increase the opacity in stellar atmosphere, pulsation, stellar interior, asteroseismology, nova, supernova, and other radiation hydrodynamics calculations. Detailed and more complete line lists will allow more accurate interpretation of features in spectra and the more accurate determination of stellar properties at any level from elementary 1-D approximations to the most sophisticated 3-D time-dependent treatments.

References

Anders E, Grevesse N (1989) Geochimica et Cosmochimica Acta 53:197
Barber RJ, Tennyson J, Harris GJ, Tolchenov RN (2006) Mon Not R Astron Soc 368:1087
Castelli F, Hubrig S (2007) Astron Astrophys 475:1041
Castelli F, Kurucz RL (2010) Astron Astrophys 520:A57
Castelli F, Johansson S, Hubrig S (2008) J Phys Conf Ser 130:012003
Castelli F, Kurucz RL, Hubrig S (2009) Astron Astrophys 508:401
Colin R, Bernath PF (2010) J Mol Spectros 257:120
Cowan RD (1968) JOSA 58:808
Geller M (1992) A high-resolution atlas of the infrared spectrum of the sun and earth atmosphere from space. Vol III. Key to identification of solar features, vol III. NASA Reference Pub. 1224, 456 pp
Johansson S (1978) Phys Scr 18:217
Kurucz RL (1988) In: McNally M (ed) Trans. internat. astronomical union XXB. Kluwer, Dordrecht, pp. 168–172
Kurucz RL (1992a) Revista Mexicana de Astronomia y Astrofisica 23:181
Kurucz RL (1992b) In: Barbuy B, Renzini A (ed) Stellar populations of galaxies. Kluwer, Dordrecht, pp. 225–232
Langhoff SR (1997) Astrophys J 481:1007
Litzén U, Brault JW, Thorne AP (1993) Phys Scr 47:628
Nave G, Johansson S, Astrophys J (2013) Supp 204:1
Neckel H, Labs D (1984) Solar Phys 90:205

Partridge H, Schwenke DW (1997) J Chem Phys 106:4618
Pickering JC (1996) Astrophys J Supp 107:811
Pickering JC, Thorne AP (1996) Astrophys J Supp 107:761
Rosberg M, Litzén U, Johansson S (1993) Mon Not Roy Astron Soc 262:L1
Schwenke DW (1998) Faraday Discuss 109:321
Sugar J, Corliss C (1985) J Phys Chem Ref Data 14 Suppl 2

Spectral Classification: The First Step in Quantitative Spectral Analysis

Richard Gray

Abstract Classification lies at the foundation of many sciences, and that is true for Astronomy as well. However, many stellar spectroscopists neglect this vital first step when carrying out a spectral analysis. This chapter discusses and illustrates the ways that spectral classification can contribute to spectroscopic analysis at every step of the process.

Keywords Methods: data analysis · Techniques: spectroscopic · Stars: fundamental parameters · Stars: abundances

1 Introduction

Morgan et al. (1943) introduced MK Spectral Classification seventy years ago and that system has a long list of important contributions to astronomy. Some of the highlights include the first demonstration that the Milky Way Galaxy is a spiral (Morgan et al. 1953); the identification of the critical link between stellar populations, kinematics, and elemental abundances (Roman 1950, 1952, 1954), which opened the door to modern theories of the chemical evolution of the Galaxy; the discovery and systemization of chemical peculiarities in the A- and B-type stars (see Titus and Morgan 1940); the discovery of the Humphreys-Davidson luminosity limit for the most massive stars (Humphreys and Davidson 1979); the identification of the most massive (O_2) main-sequence stars (Walborn et al. 2002); and, more recently, the discovery and characterization of the L- and T-type dwarfs (see Kirkpatrick et al. 1993, 1999; Burgasser et al. 1999; Geballe et al. 2002).

Classification is an essential activity of science, and serves as the beginning point for deeper analysis, and as such should not be neglected. It would be remiss, for

R. Gray (✉)
Appalachian State University, Boone, NC, USA
e-mail: grayro@appstate.edu

E. Niemczura et al. (eds.), *Determination of Atmospheric Parameters of B-, A-, F- and G-Type Stars*, GeoPlanet: Earth and Planetary Sciences,
DOI: 10.1007/978-3-319-06956-2_7,

instance, for a biologist to carry out a DNA study of a particular organism without first classifying it to the level of species, or to embark on a study of an ecosystem without identifying all of the associated organisms. Classification in both of those cases makes possible a more detailed study.

In stellar astronomy, spectral classification can play a similar role of laying the foundation for a more quantitative analysis of the stellar spectrum. Modern stellar astronomers unfortunately, often skip this step, but there are many reasons to classify before you analyse.

2 The Role of Classification in Spectral Analysis

The MK Spectral type is a *fundamental datum* of Astronomy if and only if (1) the spectral type is obtained solely through comparison with the MK spectral standards, and (2) theory and external sources of information are not used in the determination of the spectral type. By adhering to those two rules, the spectral type can serve as a starting point for further research. Why should the spectral type be independent of external sources of information? An simple example can help explain this: let us suppose that we admit photometric information into our determination of the spectral type (amazingly, I just recently had a referee who insisted that I should do exactly that), and so bias our spectral type to be in better accord with the observed colour of the star. If we do that, and then go on to use the spectral type to determine the interstellar reddening, our results will be unreliable. On the other hand, a spectral type derived solely through comparison with the MK standards will serve you at every point in your analysis; it can provide beginning points for stellar parameters, it can suggest interesting lines of inquiry, and at the end will provide a "reality check" for your results.

MK spectral classification has two goals that are of importance to spectral analysis. First, MK classification seeks to locate a star within the context of the broad population of stars—i.e. its location in the H-R diagram. Second, MK classification is extraordinarily good at identifying peculiar and therefore astrophysically interesting stars.

This means that spectral classification can be very useful in the early stages of spectral analysis. The first step in spectral analysis is the estimation of the basic physical parameters, $T_{\rm eff}$, $\log g$, and [M/H]. The spectral type, via calibrations, gives reddening-free estimates for those parameters, including the microturbulent velocity (c.f. Gray et al. 2001). In addition, in conjunction with photometry, spectral classification can help determine the interstellar reddening in a way that does not depend on a reddening model.

Spectral classification can identify peculiar and astrophysically interesting stars, and thus help in the selection of stars worthy of further analysis. Knowledge that a star is peculiar in some way can be of vital importance in spectral analysis. In addition to suggesting lines of inquiry, it is important to realize that some types of peculiar stars (for instance some Ap and Am stars) can have atmospheric structures

that deviate strongly from standard model atmospheres. If the researcher is unaware of this, either time will be wasted or incorrect results published.

At the end of your spectral analysis, the spectral type serves as a useful reference and check on your results. Is the spectral type in reasonable accord with your results? If not, then why not? Have you missed something important? Have you followed up all lines of inquiry suggested by your spectral type?

3 How are Spectral Types Determined?

3.1 Standard Stars

Spectral types are determined by direct comparison of the unknown with MK standard stars. The spectral criteria used in spectral classification were originally confined to the blue-violet part of the spectrum, but that is no longer the case, and spectral classification can be successfully carried out from the ultraviolet to the infrared. More details on spectral classification in general and the spectral criteria employed in that process can be found in *Stellar Spectral Classification* (Gray and Corbally 2009).

Standard stars are best observed with the same telescope/instrument combination used for obtaining the spectra of your program stars. Obtain spectra of enough standards to ensure that they bracket the range of possible spectral types of your program stars. Unfortunately, many telescope time allocation committees are reluctant to schedule adequate time to obtain observations of standards, and so in that case an alternative must be found. Published spectral libraries provide spectra that may be manipulated to conform to the spectral resolution (linespread function) of your program spectra. The web-based compilation *Librerias de espectros estelares* maintained by Daniel Montes at http://pendientedemigracion.ucm.es/info/Astrof/invest/actividad/spectra.html is an excellent source, but beware of the spectral types assigned in some of those libraries—they are often inaccurate or of uncertain provenance. Using only recognized MK standards is important in avoiding systematic errors in your spectral types. A number of tables of MK standards may be found in *Stellar Spectral Classification*. Another possibility is to ask a colleague who has the appropriate instrumentation to observe your star and a set of MK standards at typical MK resolutions (1–4 Å per two pixels, that is $R = 1{,}000 - 4{,}000$).

Then, classify your star *before* you begin your spectral analysis, not as an afterthought!

3.2 An Example of How to Classify a Star

There is not enough space to give examples of classification over the entire H-R diagram, but one example will illustrate the general principles. The book *Stellar Spectral*

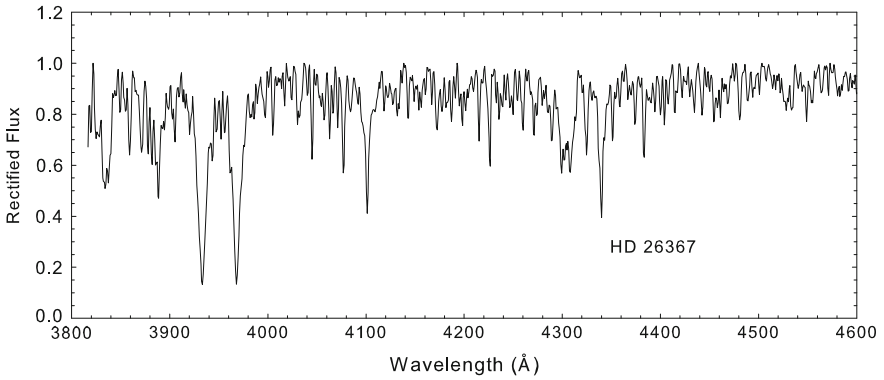

Fig. 1 The blue-violet spectrum of the peculiar F-dwarf, HD 26367. This spectrum has a resolution of 1.8 Å (per two pixels)

Classification is a useful general resource. Spectral classification on the MK System is two-dimensional, and so the spectral type of a normal star consists of a temperature type (say, A0), and a luminosity type (say, V), and is written A0 V. However, many spectral "peculiarities", such as non-solar metallicities, can be handled within the framework of the MK System.

As an example, consider the peculiar F dwarf, HD 26367 (see Fig. 1, Gray and Griffin 2007). Spectral classification begins with a rough estimate of the spectral type, often before detailed comparison with the standards takes place. This, of course, can take experience, but comparison of your program star with the spectral sequences in *Stellar Spectral Classification* can be helpful. This initial assessment suggests that HD 26367 is a late F-type (∼F8) dwarf with possible chemical peculiarities. The procedure is to first refine the temperature type (F8) by comparison with the spectra of MK standards of dwarfs of adjacent temperature types (Fig. 2), and then to refine the luminosity type by comparing with a sequence of standards (with the temperature type just determined) in the luminosity dimension. The process is iterated to convergence. The spectral features marked in Fig. 2 are useful in the temperature classification of late-type F dwarfs, and consist of the hydrogen lines (which weaken as the temperature decreases), the metallic-line spectrum in general, including the marked strong lines of Fe I and Ca I (which strengthen as the temperature decreases), and the G-band (which also strengthens as the temperature decreases).

It is important to keep in mind that the star might be metal-weak or metal-rich, in which case criteria based on the strength of the metallic-line spectrum or the G-band would lead to systematic errors in the spectral type. The classifier thus first concentrates on metallicity-independent temperature criteria. These consist of (1) the hydrogen lines, and (2) ratios of lines of different excitation energies of the iron-peak elements. A careful comparison of the strengths and profiles of the hydrogen lines of HD 26367 with the adjacent standards confirms a spectral type in the range

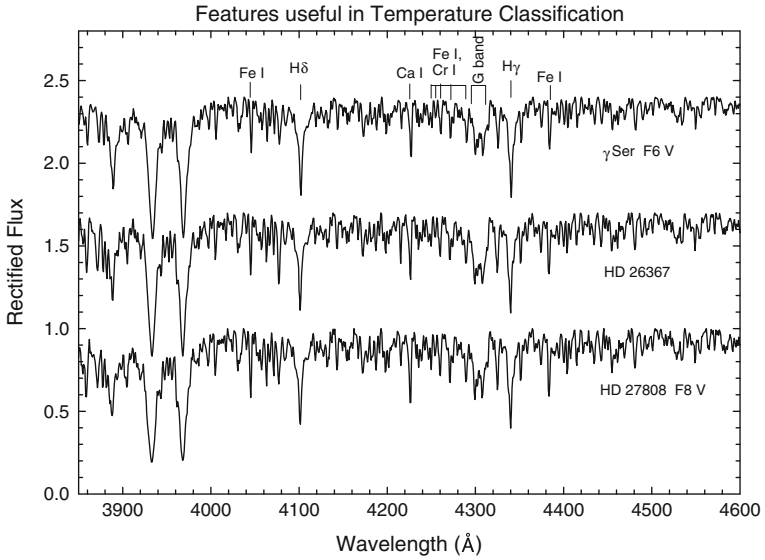

Fig. 2 The spectrum of HD 26367 is shown with the spectra of two adjacent MK standard dwarf spectra, γ Ser (F6 V) and HD 27808 (F8 V). Spectra criteria useful in the temperature classification of F- and G-type stars are marked on the top spectrum

F6–F8, but it is not possible to be more precise. Figure 3 indicates line ratios useful in temperature classification that are essentially independent of metallicity because they are based on iron-peak elements (which tend to have consistent abundance ratios). Fe I 4271 Å is a relatively low-excitation line (1.5 eV); it grows more rapidly with declining temperature than the adjacent higher excitation (2.4 eV) Fe I line at 4260 Å. Another ratio involving Fe I, Fe II 4233 Å and Fe I 4236 Å illustrated in the figure may also be used in the late F-type dwarfs. Caution, however, is required, as that ratio is also somewhat sensitive to gravity (luminosity) differences. For HD 26367 these two ratios give an average spectral type of F7. In the same region, a Cr I resonance line (4254 Å) may be rationed with Fe I 4260 Å to give a criterion that is very sensitive to the temperature in the G- and early K-type stars. It likewise is metallicity independent.

We now consider the metal-hydrogen ratios (Fe I 4046 Å/Hδ, Ca I 4226 Å/Hδ, Fe I 4383 Å/Hγ—Fig. 4). These are very sensitive discriminants of the temperature type in the late-F and G-type stars, but of course can be biased if the overall metallicity is not near solar. Those ratios indicate a temperature type of F7 for HD 26367, as they appear precisely intermediate to the ratios in γ Ser (F6) and HD 27808 (F8).

The overall strength of the metallic-line spectrum also places HD 26367 (assuming a 'V' luminosity type) intermediate to the F6 and F8 standards, and therefore at F7.

Thus the metallicity-independent temperature criteria (hydrogen-line strengths and the iron-peak line ratios) are in excellent agreement with the metallicity-dependent criteria (metal-hydrogen ratios and the overall strength of the metallic-line spectrum). This agreement indicates that HD 26367 has an overall metallicity that is

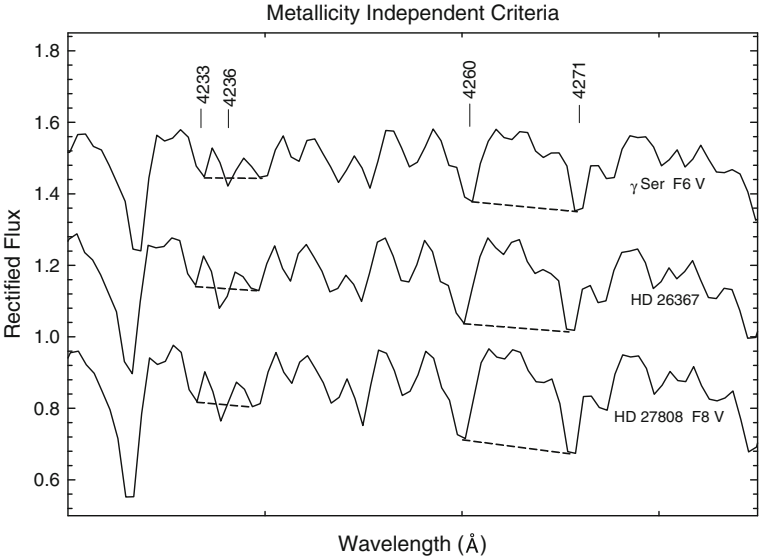

Fig. 3 The spectral lines marked in the figure may be used to estimate the spectral type independent of the metallicity of the star. Fe I 4271 Å is a low-excitation (1.5 eV) line which grows rapidly with declining temperature. It may be compared in ratio with Fe I 4260 Å, which has a higher excitation energy (2.4 eV) and so grows more slowly. The *dashed lines* joining the cores of the lines are meant to guide the eye; in this case, the ratio in HD 26367 agrees better with that in the F6 standard. The 4233 Å/4236 Å ratio may be used similarly but with some caution. The 4233 Å line is a blend of an Fe II and an Fe I line; the Fe II line fades while the Fe I line grows with declining temperature, yielding a blend that is nearly independent of temperature in the late F-type dwarfs. The 4236 Å line, however, is dominated by Fe I, and so grows with declining temperature. The ratio in HD 26367 suggests F8. The average spectral type based on these criteria is, therefore, F7

very nearly solar. If there is disagreement, then the temperature type is determined using only the metallicity-independent criteria.

The result, assuming that the luminosity class is 'V', is that the spectral type is firmly at F7. However, we have not yet considered the G-band, which is also a good temperature criterion in the F- and G-type stars. That comparison (see Fig. 5) indicates something is amiss—the G-band of HD 26367 is clearly stronger than the G-bands of both the F6 and the F8 V standards. This suggests that HD 26367 is carbon-rich, as the G-band is a molecular feature arising from CH.

We must now refine the luminosity class for HD 26367. Figure 6 shows a luminosity sequence of F8 standards (ideally we would use F7 standards for this purpose, but none exist, as F7 is not a "full" MK type). Lines of singly-ionized species, in particular Sr II, Fe II, and Ti II, in ratio with lines of neutral species (for instance the strong Fe I and Ca I lines marked in Fig. 2) make useful luminosity-sensitive criteria, with only a weak temperature sensitivity. The ratio Sr II 4077 Å/Fe I 4046 Å and especially the Sr II 4216 Å/Ca I 4226 Å ratio indicate a luminosity type between III and II (giant to bright giant), in gross disagreement with our original estimate of a

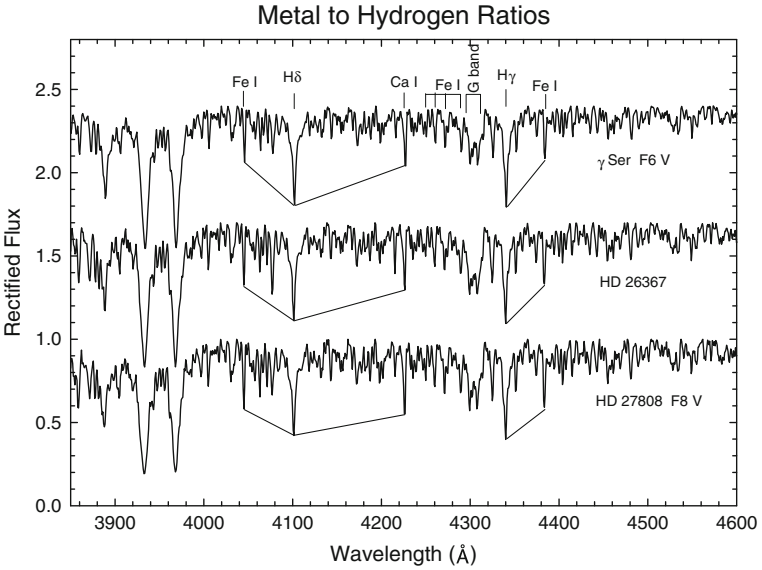

Fig. 4 The metal-to-hydrogen ratios shown in this figure may also be used to estimate the temperature type of the star, although these ratios are not reliable if the metallicity of the star is not nearly solar. Disagreement between the temperature type so determined and the metallicity-independent criteria described in the text will indicate that the star is either metal-weak or metal-rich. The lines drawn in the figure are to guide the eye only, and are not used in the actual determination of the temperature type

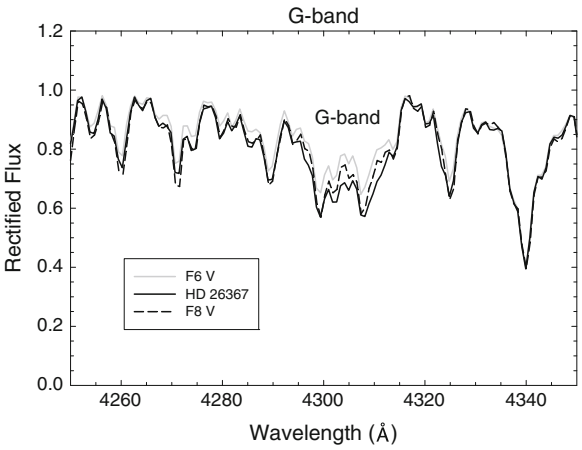

Fig. 5 The G-band strength of HD 26367 (*black*) in comparison with those of the F6 V standard (*grey*) and the F8 V standard (*dashed*). Note that the G-band of HD 26367 is stronger than either standard, indicating a possible carbon abundance enhancement

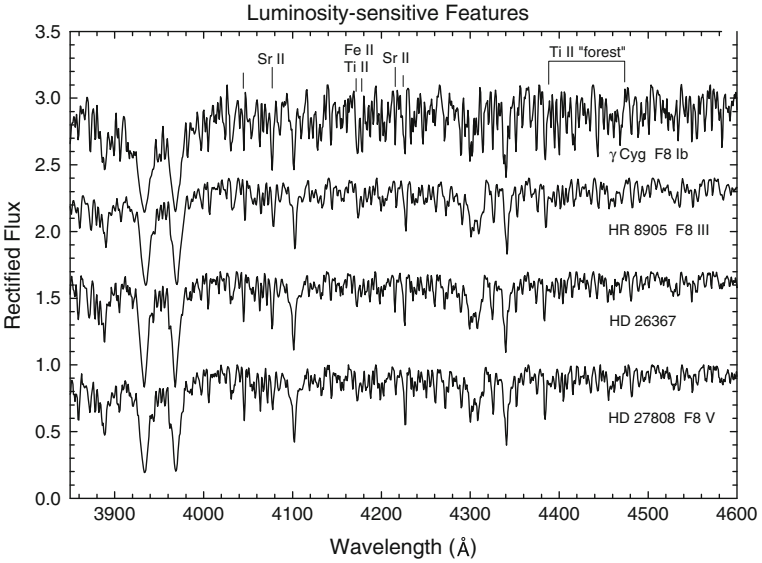

Fig. 6 Luminosity classification is carried out by comparing HD 26367 with dwarf, giant, and Ib supergiant F8 standards. Lines of ionized species such as Sr II, Fe II, and Ti II, usually in ratio with lines of neutral species constitute the luminosity criteria in F- and G-type stars. Here the Sr II lines give a discrepant luminosity class compared to the Fe II and Ti II lines, suggesting a strontium abundance anomaly

dwarf type. However, criteria based on Fe II and Ti II lines (for instance Fe II, Ti II 4172-78 Å in ratio with other nearby metallic-line blends, as well as the morphology of the so-called "Ti II forest" between 4400 and 4500 Å) places the luminosity class firmly at V (dwarf). This discrepancy in luminosity class suggests a strontium peculiarity; the significance of this abundance peculiarity will be explained below.

Thus, despite the strontium peculiarity, the conclusion is that HD 26367 is indeed a dwarf, consistent with the original assumption. If it had turned out that HD 26367 were a giant (III) or even a subgiant (IV), it would have been necessary to go back and redo the temperature classification with the appropriate standards and then iterate until consistency was obtained.

In conclusion, the final spectral type for HD 26367 is F7 V Sr CH+0.4. The CH+0.4 reflects the observation that the G-band is too strong for the spectral type; the index 0.4 is determined from the spectral type difference F9 – F7, where F9 is the spectral type with G-band strength in best agreement with the G-band of HD 26367. The formula used in the calculation of this index is

$$\mathrm{CH}_{\mathrm{index}} = 0.25\Delta,$$

where Δ is the spectral-type difference, in this case taken as $+1.5$, as F7 is a "half" spectral type. The index is rounded to the nearest tenth. Details on the calculation of abundance indices may be found in *Stellar Spectral Classification*.

The observation of a strontium and carbon over-abundance suggests that HD 26367 belongs to the group of "Barium Dwarfs" (see North et al. 1994). The leading theory explaining these abundance anomalies is that a barium dwarf was once in a close orbit with an AGB (carbon) star, and mass transfer from that star onto the present barium dwarf accounts for those anomalies. That AGB star is now a white dwarf. So, is HD 26367 a binary star? Yes, both Hipparcos and radial velocity measurements indicate the presence of an unseen companion with $M \sim 0.6 M_{\odot}$ (Gray and Griffin 2007), exactly what we would expect for a white dwarf arising from an AGB star. Indeed, GALEX photometry indicates a slight far-UV excess (Gray et al. 2011), which presumably arises from that hot companion.

4 Conclusions

The exercise classifying HD 26367 illustrates many of the points made in this discussion. HD 26367 was first identified as an interesting star via spectral classification in the Nearby Stars Project (Gray et al. 2003, 2006). That classification suggested HD 26367 was a new, bright member of the barium dwarfs, and that led to a radial-velocity program to determine its status as a binary, and high-resolution spectroscopic observations which revealed not only that strontium and carbon are overabundant, but that the s-process elements in general are overabundant. When we were satisfied that HD 26367 was indeed a barium dwarf and a binary, its brightness encouraged us to apply for time on the GALEX space telescope, and so obtained observations that constituted the first direct detection, via ultraviolet excesses, of the white-dwarf companion of a barium dwarf. The important point here is that experience shows that much of what you will ultimately learn about your star via detailed spectral analysis can be *anticipated* through spectral classification, and that that spectral type can therefore serve as a useful guide for your analysis from beginning to end. In conclusion, *classify before you analyse!* That may be the most important lesson you learn in this workshop!

References

Burgasser AJ et al (1999) ApJ 522:L65
Geballe TR et al (2002) ApJ 564:466
Gray RO, Corbally CJ (2009) Stellar spectral classification. Princeton University Press, Princeton
Gray RO, Griffin REM (2007) AJ 134:96
Gray RO, Corbally CJ, Garrison RF, McFadden MT, Robinson PE (2003) AJ 126:2048
Gray RO, Corbally CJ, Garrison RF, McFadden MT, Bubar EJ, McGahee CE (2006) AJ 132:161
Gray RO, Graham PW, Hoyt SR (2001) AJ 121:2159

Gray RO, McGahee CE, Griffin REM, Corbally CJ (2011) AJ 141:160
Humphreys RM, Davidson K (1979) ApJ 232:409
Kirkpatrick JD, Henry TJ, Liebert J (1993) ApJ 406:701
Kirkpatrick JD, Reid IN, Liebert J, Cutri RM, Nelson B, Beichman CA, Dahn CC, Monet DG, Gizis JE, Skrutskie MF (1999) ApJ 519:802
Morgan WW, Keenan PC, Kellman E (1943) An atlas of stellar spectra, with an outline of spectral classification. University of Chicago Press, Chicago
Morgan WW, Whitford AE, Code AD (1953) ApJ 118:318
North P, Berthet S, Lanz T (1994) A&AS 103:321
Roman NG (1950) ApJ 112:554
Roman NG (1952) ApJ 116:122
Roman NG (1954) AJ 59:307
Titus J, Morgan WW (1940) ApJ 92:256
Walborn NR, Howarth ID, Lennon DJ, Massey P, Oey MS, Moffat AFJ, Skalkowski G, Morrell NI, Drissen L, Parker JWM (2002) AJ 123:2754

Effective Temperature Determination

Barry Smalley

Abstract Effective temperature is the most important stellar atmospheric parameter. It is an essential prerequisite for detailed spectroscopic analyses. A discussion of the methods for determining effective temperature using stellar spectra is presented. The use of Balmer line profiles is explored and the role of spectral line depth ratios outlined. Equivalent width measurements are a powerful tool for determining effective temperature, via the excitation potential method. This is explored in detail including the sensitivity to surface gravity and metal abundance. The discussion leads to the use of spectrum synthesis fitting to determine effective temperature.

Keywords Line: profiles · Stars: atmospheres · Stars: fundamental parameters · Techniques: spectroscopic

1 Effective Temperature

The effective temperature ($T_{\rm eff}$) of a star is physically related to the total radiant power per unit area at stellar surface ($F_\star$):

$$\sigma {T_{\rm eff}}^4 = \int_0^\infty F_\lambda d\lambda = F_\star = \frac{L}{4\pi R^2}.$$

It is the temperature of an equivalent black body that gives the same total power per unit area, and is directly given by stellar luminosity (L) and radius (R).

Since there is not true 'surface' to a star, the stellar radius can vary with the wavelength of observation and nature of the star. Radius is taken as the depth of

B. Smalley (✉)
Astrophysics Group, Keele University, Keele, Staffordshire ST5 5BG, UK
e-mail: b.smalley@keele.ac.uk

E. Niemczura et al. (eds.), *Determination of Atmospheric Parameters of B-, A-, F- and G-Type Stars*, GeoPlanet: Earth and Planetary Sciences,
DOI: 10.1007/978-3-319-06956-2_8,

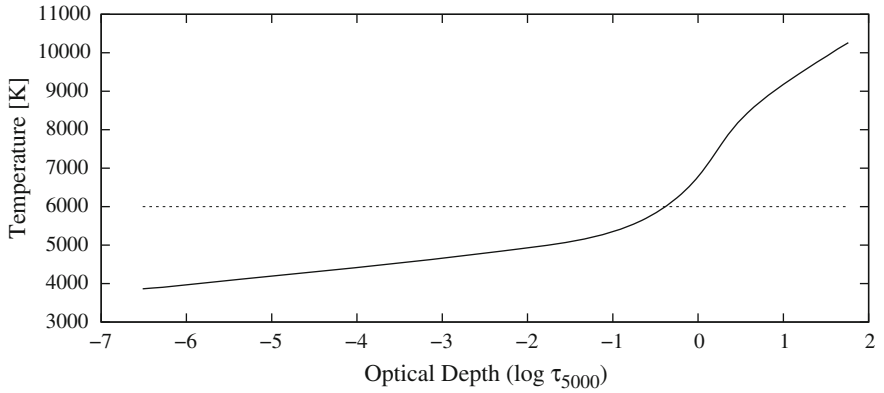

Fig. 1 The depth dependence of atmospheric temperature with monochromatic optical depth at 5,000 Å. Based on model atmosphere with $T_{\rm eff}$ = 6,000 K. The horizontal dashed line indicates a temperature of 6,000 K which intercepts the model at optical depth around $\log \tau_{5000} = -0.5$, corresponding the depth of formation of the continuum flux

formation of the continuum, which in the visible region is approximately constant for most stars (Gray 2008).

The effective temperature is broadly that of the atmospheric layer in which the continuum is formed. The temperature of line-forming region is lower than $T_{\rm eff}$ (Fig. 1). In addition, spectral lines are formed at differing depths and temperatures, making them useful as $T_{\rm eff}$ diagnostics.

2 The Paschen Continuum

The most direct method of determining stellar $T_{\rm eff}$ is by using absolute flux measurements. This requires moderate-resolution flux-calibrated spectra or spectrophotometry. However, even if only relative fluxes are available, they can be used to determine $T_{\rm eff}$, since the Paschen continuum is sensitive to temperature variations (Fig. 2). This is also the basis for $T_{\rm eff}$-colour calibrations. This is covered in more detail in Chap. 10

3 Temperatures from Balmer Line Profiles

The Balmer lines provide an excellent $T_{\rm eff}$ diagnostic for stars cooler than about 8,000 K due to their virtually null gravity dependence (Gray 2008; Heiter et al. 2002). By fitting theoretical profiles to observations, we can determine $T_{\rm eff}$. For stars hotter than 8,000 K, however, the profiles are sensitive to both temperature and gravity. For

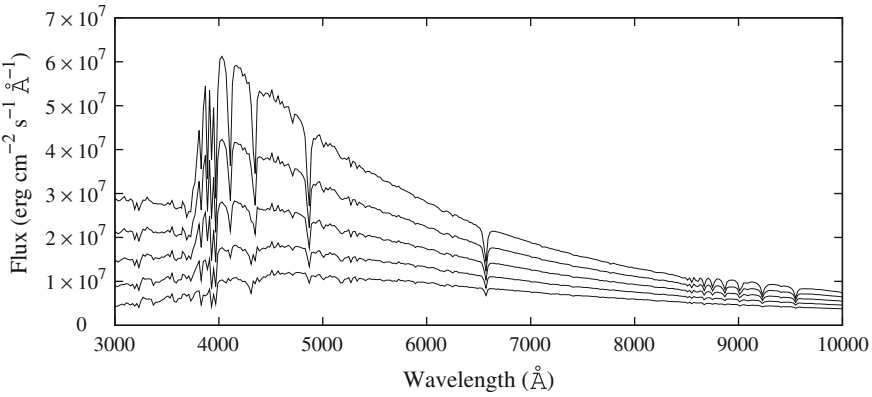

Fig. 2 The variation of stellar flux with $T_{\rm eff}$, ranging from 6,000 K (*bottom*) to 8,000 K (*top*) in steps of 500 K

these stars, the Balmer lines could be used to obtain values of surface gravity ($\log g$), provided that their $T_{\rm eff}$ can be determined from a different method.

The broad Balmer lines require careful continuum determination, because the true profile shape must be preserved (Smith and van't Veer 1988). Echelle spectra usually give poor profiles due to curved orders and the merging process in pipeline reductions (Bruntt et al. 2010). Hence, single-order medium-resolution spectra are preferred.

3.1 Examples of Balmer Line Fitting

Figure 3 shows a fit to the Solar Hα profile. Note that the core region (approximately ± 1 Å) is not used in the fitting, since it is formed high in the stellar atmosphere and subject to NLTE effects. On first inspection, the known $T_{\rm eff}$ for the Sun produces an acceptable fit. This would be especially true at higher noise levels. However, on closer inspection, the best fit is with a $T_{\rm eff}$ that is ~ 60 K lower than actual Solar value. Model deficiencies, for example the treatment of line-broadening or convection theory, can lead to temperature values that disagree with the true or fundamental value (see for example Cayrel et al. 2011). Hence, as with all model-dependent methods, they should be tested against stars with known model-independent $T_{\rm eff}$ values.

KIC 11772920 (TYC 3565-1235-1) is a slowly rotating G-type star (Appourchaux et al. 2012). Figure 4 shows a HERMES (Raskin et al. 2011) spectrum with the fit to the Hα profile. With the exception of the core, the profile is well fitted with a $T_{\rm eff}$ of 5,300 K.

KIC 11090405 (BD+48 2925) is a rapidly rotating A-type star exhibiting δ Sct type pulsations (Uytterhoeven et al. 2011). Figure 5 shows that the Hα profile indicates

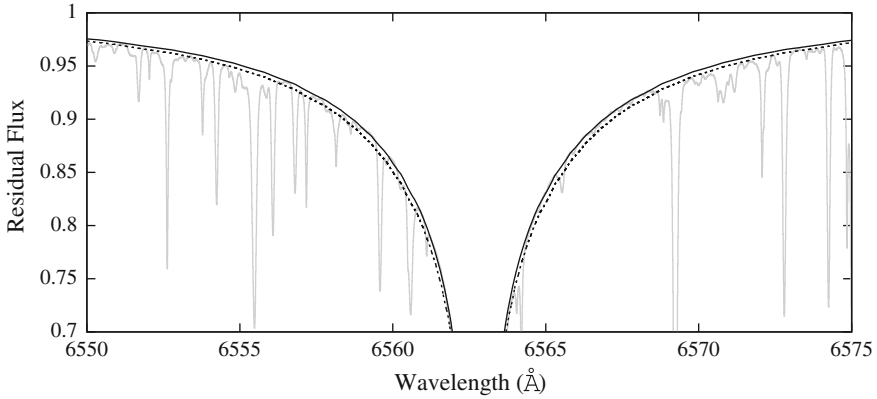

Fig. 3 The KPNO Solar Atlas Hα profile (*grey line*). The *dotted-line* is the fit using the parameters for the Sun ($T_{\rm eff}$ = 5,777 K and $\log g$ = 4.44), while the *black line* is the 'best-fitting' profile with $T_{\rm eff}$ = 5,720 K

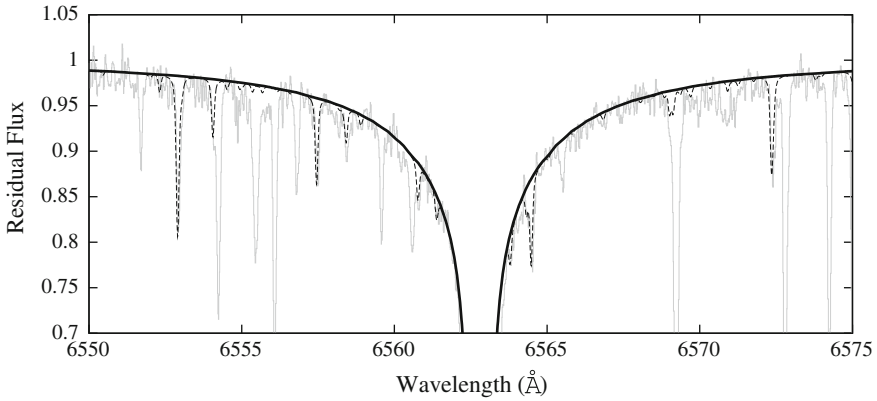

Fig. 4 The HERMES Hα profile of KIC 11772920 (*grey line*). The *black line* is the fit to the spectrum with $T_{\rm eff}$ = 5,300 K. Note that in addition to the presence of stellar absorption lines, there are several telluric lines arising due to water vapour in the Earth's atmosphere (*dashed-line*)

a $T_{\rm eff}$ of around 7,500 K. Note that rotation does not have a significant effect on the wings, only the core region, which as noted above we do not use in our fitting.

4 Spectral Line Depth Ratios

Spectral lines are sensitive to temperature variations within the line-forming regions. Line strength ratios can be used as temperature diagnostics, similar to their use in spectral classification. Gray and Johanson (1991) used line depth ratios to determine stellar effective temperatures with a precision of $\pm$10 K. While this method can

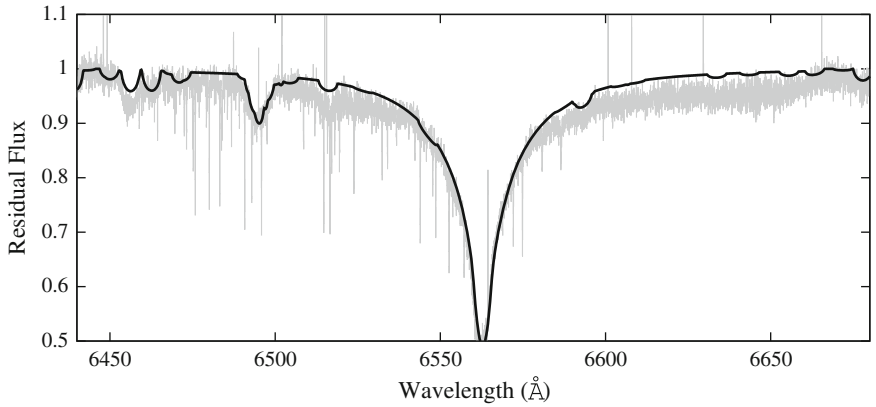

Fig. 5 The HERMES Hα profile of KIC 11090405 (*grey line*). The *black line* is the fit to the spectrum with $T_{\rm eff}$ = 7,500 K. Note the presence of sharp telluric absorption lines in the spectrum of this rapidly rotating star ($v \sin i = 120\,{\rm km\,s^{-1}}$).

yield very precise relative temperatures, the absolute calibration onto the $T_{\rm eff}$ scale is much less well determined (Gray 1994). This method is ideal for investigating stellar temperature variations (Gray and Livingston 1997).

5 Equivalent Width

The equivalent width (W_λ or just EW) is a widely-used measure of the strength of a spectral line:

$$W_\lambda = \int_0^\infty (1 - R_\lambda)\, d\lambda,$$

where R_λ is the residual flux at the given wavelength (λ). It is used in the determination of both stellar parameters and elemental abundances. It does, however, contain no information on shape of the line profile. While the truncation of strong wings can affect the measurement, as can uncertainties in the location of the continuum, it is line blending that is the most dominant source of uncertainties in EW measurements.

6 Metal Line Diagnostics

In a detailed spectral analysis, the equivalent widths of many lines are often measured. These can be used to determine the atmospheric parameters via metal line diagnostics:

- **Excitation Potential**
  Abundances from the same element must agree for all excitation potentials.

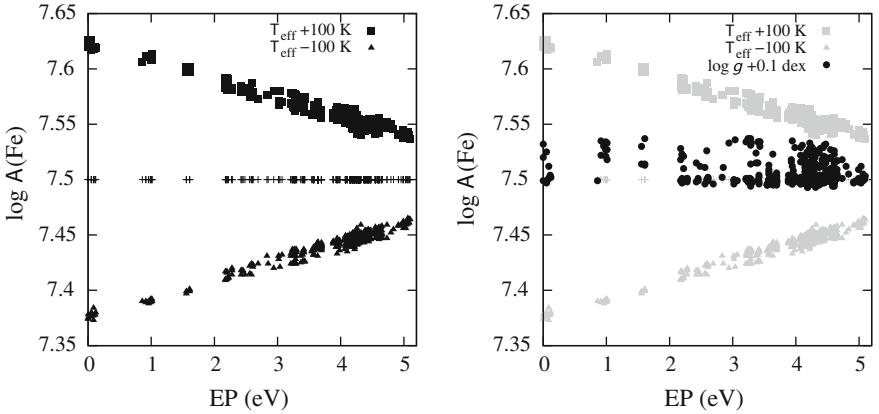

Fig. 6 The effect of changing $T_{\rm eff}$ (*left*) and changing $\log g$ (*right*) on the correlation between $\log A$(Fe) and EP

- **Ionisation Balance**
  The abundances obtained from differing ionisation stages of the same element must agree. The Fe I/Fe II ratio can be used as a $T_{\rm eff}$—$\log g$ diagnostic.

6.1 Exploring the Excitation Potential

When using the lower-level excitation potential (χ or just EP) to determine $T_{\rm eff}$ it is best to use lines that are not pressure sensitive. In the case of Solar-type stars use neutral metals, while in hotter stars use ionised metals. In both cases weak lines should be used to avoid the effects of saturation.

In order to investigate the use of excitation potential as a temperature diagnostic, a set of simulated 'observed' equivalent widths (W_0/λ) were generated using an ATLAS9 model with $T_{\rm eff}$ = 6,000 K, $\log g$ = 4.5 and $\log A$(Fe) = 7.50. The Fe I lines were taken from the Kurucz `gfall` line list in the wavelength range 5,000–6,000 Å. Only lines with calculated equivalent widths in the range 5–100 mÅ were retained.

Figure 6 shows that the change in slope caused by changing $T_{\rm eff}$ is clearly evident. However, variations in $\log g$ do not introduce a significant slope, but do increase the scatter in abundance. Of course, when using real data the observational uncertainties and errors in atomic data will introduce scatter into the trends.

The analysis method searches for null correlation between $\log A$(Fe) and EP (Santos et al. 2000). This can be by a linear regression fit and finding where the gradient is zero, or by finding where the linear-correlation coefficient is zero. Either method should yield the same result.

The uncertainty on $T_{\rm eff}$ can be taken to be the 1-σ error on gradient or correlation coefficient (Neuforge-Verheecke and Magain 1997). Another source of error is

uncertainties in equivalent widths, where in our example a 1% error in W_λ gives $\sim$10 K in $T_{\rm eff}$, 5 % 50 K and 10 % 100 K. In addition, there is a small but non-negligible influence by surface gravity, $\pm$0.1 dex in $\log g$ gives $\pm$20 K in $T_{\rm eff}$.

6.2 Equivalent Width Correlation

It could be argued that from a 'philosophical' viewpoint all the Fe I lines in an homogeneous stellar atmosphere must have the same abundance. Thus, we ought to use the differences in predicted line strengths as a diagnostic. Given that $\log\left(\frac{W_\lambda}{\lambda}\right) \propto \log A$ we can change the above procedure to use equivalent width differences. Let us use:

$$\log\left(\frac{W}{\lambda}\right) - \log\left(\frac{W_0}{\lambda}\right) = \log\left(\frac{W}{W_0}\right),$$

where W_0 is the observed equivalent width and W_λ is the calculated value for a given abundance.

The $T_{\rm eff}$ diagnostic is very similar, i.e. finding the lack of correlation between $\log\left(\frac{W_\lambda}{\lambda}\right)$ and EP. However, now we have to assume an abundance, which in our example is $\log A({\rm Fe}) = 7.50$.

The effects of changing $T_{\rm eff}$ and $\log g$ are very similar to previously, but with more scatter when varying $T_{\rm eff}$ and noticeably less scatter when varying $\log g$ (Fig. 7 top panels). However, since we have to assume an initial abundance, this value may not be correct. The lower-left panel of Fig. 7 shows the effect of changing $\log A({\rm Fe})$ by $\pm$0.1 dex; the overall trend is broadly horizontal, but the scatter is significantly enhanced. The scatter can be reduced by varying both $T_{\rm eff}$ and $\log A({\rm Fe})$ (Fig. 7 lower-right panel). In these cases, there is still a trend with EP, indicating that the parameters are not correct, but adding some noise and selecting less lines might give an acceptable result. Hence, using EW differences rather than calculating individual line abundances, appears to produce a slightly less acceptable procedure.

6.3 "Total" Equivalent Width

In order to abstract the method further, rather than using individual equivalent width differences, one could use the sum of the differences:

$$\sum \log\left(\frac{W}{W_0}\right).$$

In this case, rather than trend with EP, there is just one number per given $T_{\rm eff}$, $\log g$ and $\log A({\rm Fe})$ combination. The solution is now one of the combinations where the

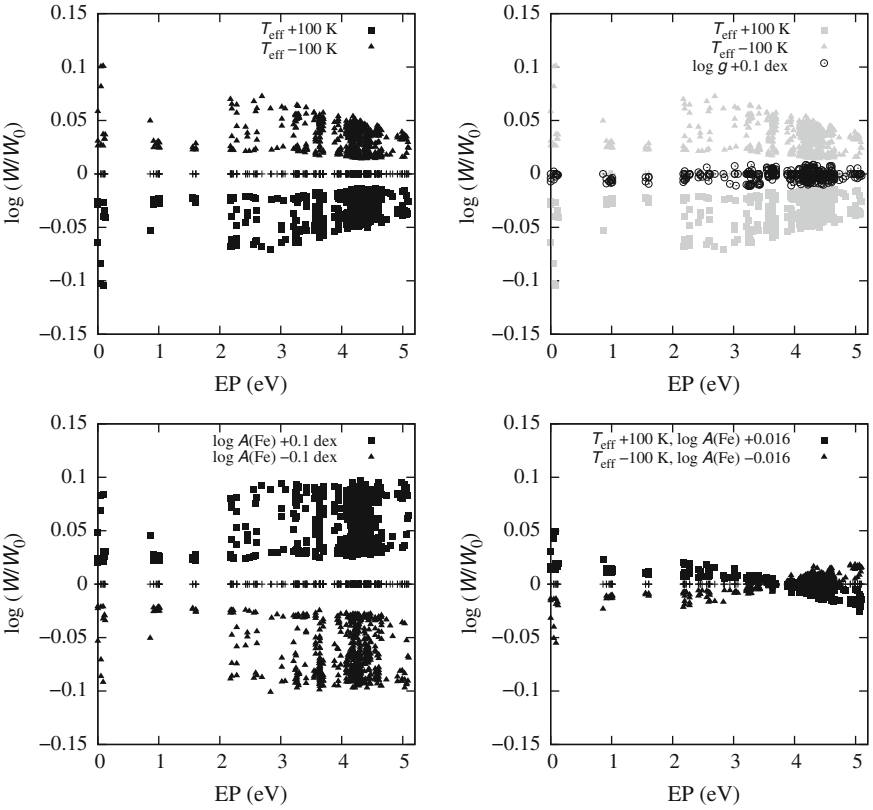

Fig. 7 The effects on the correlation between EP and $\log\left(\frac{W_\lambda}{\lambda}\right)$ of changing $T_{\rm eff}$ (*top left*), $\log g$ (*top right*), $\log A$(Fe) (*bottom left*), and both $T_{\rm eff}$ and $\log A$(Fe) (*bottom right*)

sum is zero, but which one? Thus, it would appear that using this method would result in a loss of information. However, Fig. 8 shows that while there is a trend with $\log A$(Fe), $T_{\rm eff}$ is virtually insensitive to $\log g$. Hence, provided a good value (or estimate) of $\log A$(Fe) is available, a sensible value of $T_{\rm eff}$ can be obtained.

6.4 Using χ^2

Measuring equivalent widths might not always be practical. For example, where there is severe line-blending, high rotation, etc. In these cases, we have to use spectrum synthesis methods in order to fit the spectrum to determine $T_{\rm eff}$.

Now consider $T_{\rm eff}$ determination using χ^2-fitting to spectrum. Using the same model as before, a synthetic 'observational' spectrum was generated using *all* spectral lines stronger than 5 mÅ in the wavelength range from 5,000 to 6,000 Å. In the χ^2

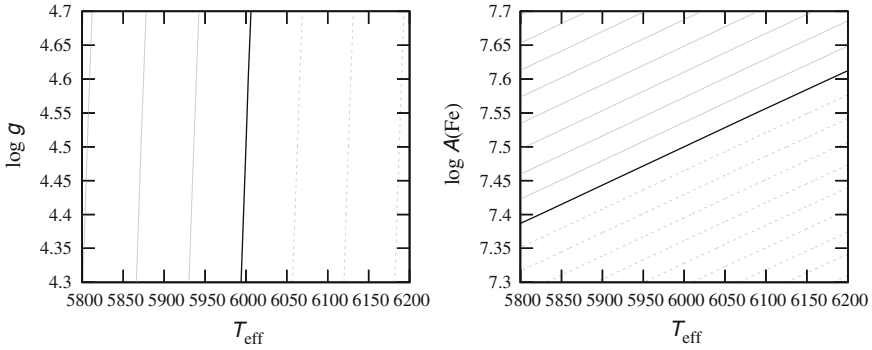

Fig. 8 The variation of "total" EW, $\sum \log(\frac{W}{W_0})$, for $\log g$ against $T_{\rm eff}$ (*left*) and $\log A$(Fe) against $T_{\rm eff}$ (*right*). While there is virtually no dependence on $\log g$, there is a strong correlation of $T_{\rm eff}$ with $\log A$(Fe)

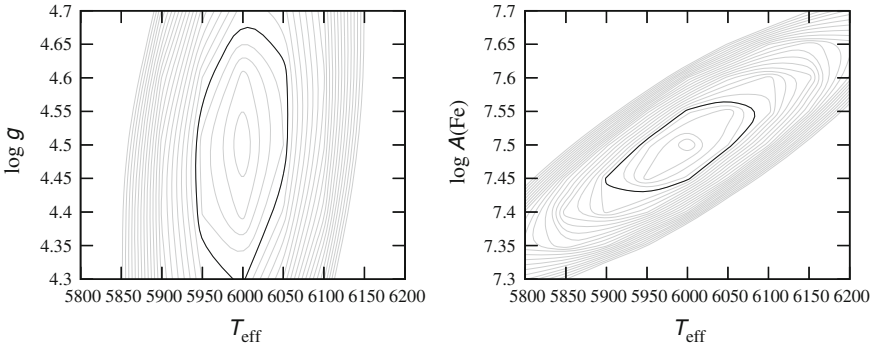

Fig. 9 χ^2 correlations, for $\log g$ against $T_{\rm eff}$ (*left*) and $\log A$(Fe) against $T_{\rm eff}$ (*right*). While there is virtually no dependence on $\log g$, there is a strong correlation of $T_{\rm eff}$ with $\log A$(Fe). The *darker line* gives the 1-σ error ellipse

calculation a signal-to-noise ratio of 100:1 was assumed, but no noise was added to the synthetic spectra.

As can be seen in Fig. 9, rather than a line in the diagrams, there is now a region of uncertainty—an error ellipse. As previously, there is a correlation between $\log A$(Fe) and $T_{\rm eff}$, but only a weak sensitivity to $\log g$. Further details on χ^2-fitting methods are given in Sect. 7.

6.5 Conclusions on Simulations

Using $\log A$(Fe) versus EP provides for a good determination of $T_{\rm eff}$, with low sensitivity to $\log g$. However, the other methods (EW, 'Total' EW, and χ^2) all have a $\log A$(Fe) complication, owing to the correlation between $T_{\rm eff}$ and $\log A$(Fe) and the

need to adopt or assume a value for log A(Fe). Nevertheless, using χ^2 gives regions of best fit, even though $T_{\rm eff}$ might be coupled with log A(Fe), but not (significantly) with log g. Adding noise and uncertainties in atomic data and model physics, will further complicate the analysis and, potentially, add unwanted systematics into the results.

7 Global Spectral Fitting

As mentioned in Sect. 6.4, an alternative to a detailed analysis of individual spectral line measurements, is to use the whole, or part, of the observed stellar spectrum and find the best-fitting synthetic spectrum. This is done by varying various input parameters, such as $T_{\rm eff}$, log g, metallicity ([M/H]), microturbulence ($\xi_{\rm t}$), and projected rotational velocity ($v \sin i$), etc., in order to find the combination that has the lowest χ^2 value. There are two commonly used procedures. The first is to take initial starting values for the input parameters and use a χ^2 minimization algorithm, such as Nelder-Mead downhill simplex or Levenberg-Marquardt, to find the best-fitting solution (e.g. Valenti and Piskunov 1996). The second is to take a large multi-dimensional grid of precomputed synthetic spectra for the various combinations of input parameters and search the whole grid to find the best-fitting solution (e.g. Lehmann et al. 2011).

The benefit of these methods is that they can be automated for vast quantities of stellar observations and can be used for spectra that are severely blended due to low resolution or rapid rotation (Hill 1995; Tkachenko et al. 2013).

Naturally, the final parameters are model-dependent and only as good as the quality of the model atmospheres used. The internal fitting errors only gives a measure of the precision of the result and is thus a lower-limit uncertainty on the parameters. Determination of the accuracy of the parameters requires the assessment of the results, using the exact same methods, to spectra of fundamental stars.

8 Do We Care About $T_{\rm eff}$?

It may appear strange, but the effective temperature of a star is not important; it is the T(τ_0) relationship that determines the spectral characteristics (Gray 2008). Hence, the parameters obtained from spectroscopic methods alone may not be consistent with the true values as obtained by model-independent methods. This is not necessarily important for abundance analyses of stars, but it is an issue when using the parameters to compare with fundamental values or to infer the physical properties of stars.

9 Conclusion

The effective temperature for a star can be obtained by several different techniques. By using a combination of these we can assess the quality of our parameter determinations. While some techniques can give precise $T_{\rm eff}$ values to ± 10 K, the overall accuracy of the values is significantly less and sometimes difficult to evaluate. At present $T_{\rm eff}$ determinations are generally accurate to no better than 1–2 % (50–100 K). Hence, always beware of $T_{\rm eff}$ values without error bars!

References

Appourchaux T, Chaplin WJ, García RA et al (2012) A&A 543:A54
Bruntt H, Bedding TR, Quirion P-O et al (2010) MNRAS 405:1907
Cayrel R, van't Veer-Menneret C, Allard NF, Stehlé C (2011) A&A 531:A83
Gray DF (2008) The observation and analysis of Stellar photospheres, 3rd edn. Cambridge University Press, Cambridge
Gray DF (1994) PASP 106:1248
Gray DF, Johanson HL (1991) PASP 103:439
Gray DF, Livingston WC (1997) ApJ 474:802
Heiter U, Kupka F, van't Veer-Menneret C et al (2002) A&A 392:619
Hill GM (1995) A&A 294:536
Lehmann H, Tkachenko A, Semaan T et al (2011) A&A 526:A124
Neuforge-Verheecke C, Magain P (1997) A&A 328:261
Raskin G, van Winckel H, Hensberge H et al (2011) A&A 526:A69
Santos NC, Israelian G, Mayor M (2000) A&A 363:228
Smith KC, van't Veer C (1998) Elemental abundance analyses. In: Adelman SJ, Lanz T (eds) Proceedings of the IAU working group on AP Stars Workshop, Institut d'Astronomie de l'Universite de Lausanne, p 133
Tkachenko A, Lehmann H, Smalley B, Uytterhoeven K (2013) MNRAS 431:3685
Uytterhoeven K, Moya A, Grigahcène A et al (2011) A&A 534:A125
Valenti JA, Piskunov N (1996) A&AS 118:595

How to Determine Surface Gravity from Stellar Spectra

Giovanni Catanzaro

Abstract One of the most important astrophysical parameters characterizing stellar atmosphere is the surface gravity. By a direct knowledge of mass and radius of a star it is straightforward to compute also the gravity, but unfortunately this is possible only in a few cases. For most stars, the only chance we have to infer the surface gravity is based on the analysis of spectral features: lines and continuum. In this lecture we describe some of these methods, dealing with those most commonly used in the literature.

Keywords Stars · Fundamental · Parameters · Techniques · Spectroscopic

1 Introduction: Generalities on Spectral Lines

An absorption line is produced in a stellar spectrum whenever photons of energy $E = h\nu$ are absorbed by an atom or ion causing an electron to jump from a lower to an upper energy level. The intensity of a spectral line is related to the number of absorbers, i.e. atoms or ions of the given elements at the lower level of the transition. In Local Thermodynamic Equilibrium (LTE), when only one ionization stage is available, the fraction of ions that can absorb is given by the Saha equation that regulates the ionization case

$$\frac{N_1}{N_0} P_e = \text{const}\, T^{\frac{5}{2}}\, \mathrm{e}^{-\frac{\Delta\varepsilon}{kT}}, \tag{1}$$

where N_0 is the number of neutral atoms, N_1 the number of ions, $\Delta\varepsilon$ is the ionization potential, T is the temperature, P_e the electronic pressure and k the Boltzmann

G. Catanzaro (✉)
INAF, Osservatorio Astrofisico di Catania, Catania, Italy
e-mail: giovanni.catanzaro@oact.inaf.it

E. Niemczura et al. (eds.), *Determination of Atmospheric Parameters of B-, A-, F- and G-Type Stars*, GeoPlanet: Earth and Planetary Sciences,
DOI: 10.1007/978-3-319-06956-2_9,

constant. When only excitation occurs, we can use the Boltzmann equation

$$\frac{N_n}{N_m} = \frac{g_n}{g_m} \mathrm{e}^{-\frac{\Delta\chi}{kT}}, \tag{2}$$

where N are the population of the levels, g are the statistical weights and $\Delta\chi$ is the excitation potential.

There are several mechanisms that broaden a spectral line, which is never a δ function, i.e. infinitely-narrow feature, but depending on the mechanism that dominates we can have a dispersion or Lorentzian profile

$$l(\lambda) = l_0 \frac{\gamma}{(\lambda - \lambda_0)^2 + \gamma}, \tag{3}$$

where γ is the damping constant, valid for natural atomic absorption and pressure broadening, or a Gaussian profile

$$g(\lambda) = g_0 \frac{1}{\Delta\lambda_D} \mathrm{e}^{\left(-\frac{\lambda-\lambda_0}{\Delta\lambda_D}\right)^2}, \tag{4}$$

that describes better the thermal Doppler and microturbulent broadening. The term $\Delta\lambda_D$ is given by

$$\Delta\lambda_D = \frac{\lambda}{c}\left(\sqrt{\frac{2kT}{m}} + \xi_\mathrm{t}\right), \tag{5}$$

where ξ_t stands for the microturbulence.

In this lecture we will explore pressure broadening, as this type of broadening is linked to the surface gravity of a star. Pressure broadening implies a collisional interaction between the atoms absorbing light and other particles: ions, electrons, atoms or even molecules in cool stars.

2 Measuring Gravity in Stars

In principle, the surface gravity of a star can be derived in a direct way, provided that we know its radius (R) and mass (M). The mass could be obtained in case of binary stars via the Doppler effect measured spectroscopically, and the radius by using interferometry, lunar occultation or analysing an eclipsing binary. When this tasks can be accomplished, and it is possible only for a few stars, then we can compute the gravity using the following relation

$$g = \frac{GM}{R^2}, \tag{6}$$

where G is the universal gravitational constant.

For the majority of cases, direct measurements are not feasible, and we must entrust in indirect measurements obtained thanks to spectroscopy. We know that pressure effects in stellar spectra are very weak if compared to temperature effects; in a few words we can say that, while temperatures span a factor of ten or so from O to M stars, pressure ranges over six orders from dwarfs to supergiants. Nevertheless, this is the only effect that we can measure if we want to have a determination of surface gravity.

Two contributions to the pressure are important in this context: electron and gas pressure. The interplay between P_e and P_g in a stellar atmosphere is fixed by the chemical composition, the temperature distribution, and hydrostatic equilibrium, but it is the surface gravity in the hydrostatic equation that controls the scale of the pressure distribution. Increasing gravity translates into a compression of the photosphere and therefore in an increase of all pressures.

The depth dependence of gas and electron pressures could be easily explained according to the temperature of the model. In the cooler models, electron pressure is orders of magnitude smaller than the gas pressure. Only in the deep layers the increased temperature boosts the ionization and hence the electron pressure. In contrast, the hotter models have temperature high enough to strongly ionize hydrogen, so the electron pressure is dominated by electrons from hydrogen and it is comparable with gas pressure. It is possible to approximate all these dependencies by

$$P_g \propto g^j, \tag{7}$$

where j ranges from approximately 0.64 to 0.54 from deeper to external layers in cooler models, and from 0.85 to 0.53 in hotter models. The electron pressure can be written as

$$P_e \propto g^i, \tag{8}$$

where i ranges from 0.33 to 0.48, going from deep to shallow layers in the case of cooler models, and from 0.82 to 0.53 for hotter models. For a detailed and thorough discussion we refer the reader to Gray (2005).

The pressure effects are visible in three ways:

- ionization equilibrium, that is, the change in the ratio of line absorbers to the continuum opacity;
- pressure sensitivity to damping constant for strong lines;
- pressure dependence of the linear stark broadening in hydrogen lines.

In the following sections we will see in detail how these effects are useful to derive information on stellar gravity. But, before proceeding, it is useful to make some general considerations on spectral lines. The strength of a spectral line is related to the ratio of the line and continuum absorption coefficients,

$$\frac{l_\nu}{\kappa_\nu}. \tag{9}$$

Moreover, we can write the Saha equation in a more schematic form

$$\frac{N_{r+1}}{N_r} = \frac{\Phi(T)}{P_e}, \tag{10}$$

where N_{r+1} is the number of atoms/ions in the $r+1$ ionization stage, N_r is the number of atoms/ions in the r ionization stage, $\Phi(T)$ is a function that includes all terms not dependent on pressure, and it is a constant once we fixed the temperature. Also, remember that the following relation of proportionality is still valid,

$$l_\nu \propto N_r. \tag{11}$$

3 Weak Lines in Cool Stars

Let us start by examining the behaviour of weak lines in cool stars (lines with no strong wings). We consider a spectral line generated by a particular atom in a neutral or ionized state. According to the ionization stage of most of this element in the stellar atmosphere, we can distinguish three different cases (Gray 2005):

1. weak lines formed by an element where most of it is in the next higher ionization stage;
2. weak lines formed by an element where most of it is in the same ionization stage;
3. weak lines formed by an element where most of it is in the next lower ionization stage.

Case 1 In this case, since most of an element is in the next higher ionization stage, we can write

$$N_{r+1} \approx N_{tot} = \text{const.} \tag{12}$$

Then, using Eqs. 10 and 11, we have

$$l_\nu \propto N_r \propto \text{const}\, P_e. \tag{13}$$

In cool stars the most important source of continuum opacity is the negative hydrogen ion (H^-), so we have

$$\kappa_\nu \propto \text{const}\, P_e. \tag{14}$$

Then, substituting the expressions for the absorption coefficients in Eq. 9, we obtain

$$\frac{l_\nu}{\kappa_\nu} = \text{const.} \tag{15}$$

This simply shows that *these lines are insensitive to gravity*, but are of course useful to determine the abundance of that element.

Case 2 In this case, when most of an element is in the same ionization stage, following the same reasoning as before, we have

$$N_r \approx N_{tot} = \text{const.} \tag{16}$$

Then, using again Eqs. 10 and 11, we can write

$$l_\nu \propto N_r \propto \text{const.} \tag{17}$$

As we are still in the cool star case, Eq. 14 holds, and we have

$$\frac{l_\nu}{\kappa_\nu} = \frac{const}{P_e} \approx \text{const}\, g^{-\frac{1}{3}}. \tag{18}$$

Hence, *these lines are sensitive to gravity*. Therefore, they are useful as a gravity diagnostic.

Case 3 With similar arguments it can be shown that in the case in which most of the element is in the next lower ionization stage, we obtain

$$\frac{l_\nu}{\kappa_\nu} \approx \text{const}\, g^{-\frac{2}{3}}. \tag{19}$$

Then, *these lines are very sensitive to gravity*.

Let us consider, as an example, weak lines generated from iron in F-type stars. Iron is mostly ionized in this spectral type, so lines from Fe I are insensitive to gravity (Case 1), while those from Fe II are very useful indicators (Case 2). Also lines of O I are good diagnostic of gravity, because oxygen is neutral at these temperatures (Case 2).

4 Broad Wings of Strong Lines in Cool Stars

Following the outline of the previous section, we analyse here the behaviour of strong lines as a function of gravity in cool stars. Since strong lines are saturated, we concentrate our attention to the broad wings of these lines, and we deal separately the case of neutral and ionic lines (Gray 2005).

4.1 Neutral Lines

In case of wings of strong lines, the line absorption coefficient is proportional to the damping constant, according to the relation

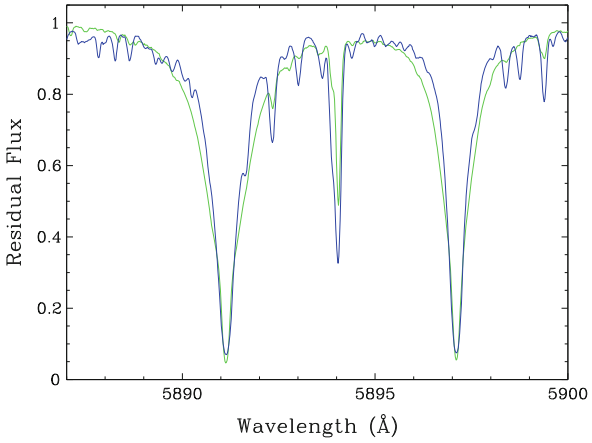

Fig. 1 Profiles of the Na D lines of HD 100623 (K0 V, *green*) and HD 99322 (K0 III, *blue*) taken from the UVES-POP database (Bagnulo et al. 2003). The effect of different gravity can clearly be seen, the lines of the giant are narrower than the lines of the dwarf

$$l_\nu \propto N\,\gamma, \tag{20}$$

where N is the number of absorbers and γ is given by three contributions, γ_{nat}, γ_6, and γ_4 for natural, van der Waals and quadratic Stark broadening, respectively. The general damping constant can be written as the sum of these contributions

$$\gamma = \gamma_{nat} + \gamma_6 + \gamma_4 = \gamma_{nat} + \Phi_6(T)\,P_g + \Phi_4(T)\,P_e, \tag{21}$$

where the functions $\Phi_6(T)$ and $\Phi_4(T)$ are shorthand for the pressure independent terms. In a cool star where continuum absorption coefficient κ_ν, is dominated by the negative hydrogen ion, i.e. $\kappa_\nu \propto P_e$, the wings of a strong line for a neutral atom, where most of the element is ionized, are proportional to

$$\frac{l_\nu}{\kappa_\nu} \approx \text{const}\,\gamma = \text{const}\left[\gamma_{nat} + \Phi_6(T)\,P_g + \Phi_4(T)\,P_e\right]. \tag{22}$$

Substituting Eqs. 7 and 8, we obtain

$$\frac{l_\nu}{\kappa_\nu} \approx \text{const}\,g^{\frac{2}{3}} + \text{const}\,g^{\frac{1}{3}} + \text{const}. \tag{23}$$

The relative sizes of the damping constants can span from no gravity dependence (when natural damping constant is dominant) to a maximum dependence (when $g^{\frac{2}{3}}$ van der Waals term is dominant). In solar-type stars, the sodium doublet at 5,890 Å is an important diagnostic of gravity (see Fig. 1), as van der Waals term of damping

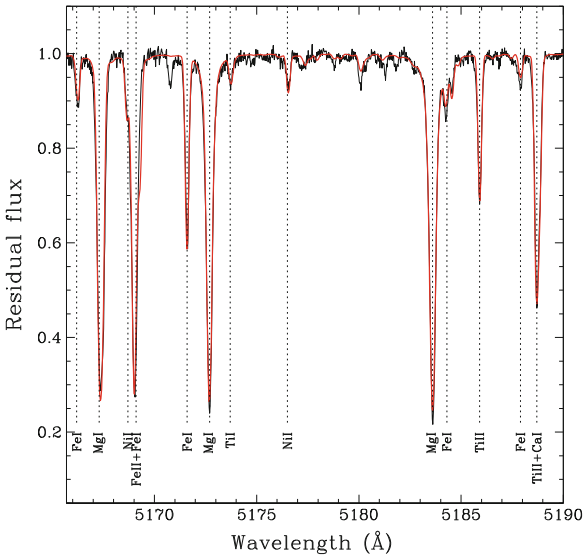

Fig. 2 Example of fitting of the Mg I triplet. Credit: Catanzaro et al. (2013, Fig. 3) (By permission of Oxford University Press on behalf of The Royal Astronomical Society.)

constant dominates, while Mg I at 8,806 Å has little gravity dependence, since the natural damping constant is very large (e.g. Fig. 2).

4.2 Ionic Lines

For ionic lines, considering that the element is always mostly ionized, we have

$$\frac{l_\nu}{\kappa_\nu} \approx \text{const}\,\frac{\gamma}{P_e}. \tag{24}$$

Using Eq. 22 we obtain

$$\frac{l_\nu}{\kappa_\nu} \approx const\, g^{-\frac{1}{3}} + const + const\, g^{\frac{1}{3}}. \tag{25}$$

Typical cases are the Ca II H and K lines that show an inverse gravity dependence. For the sake of clarity, we show in Fig. 3 the observed Ca II H line in HD 152311 (from the UVES-POP archives Bagnulo et al. 2003), with stellar parameters: $T_{\rm eff} = 5,597$ K, $\log g = 3.97$, [Fe/H] = 0.10, and $v \sin i = 4$ km s^{-1}

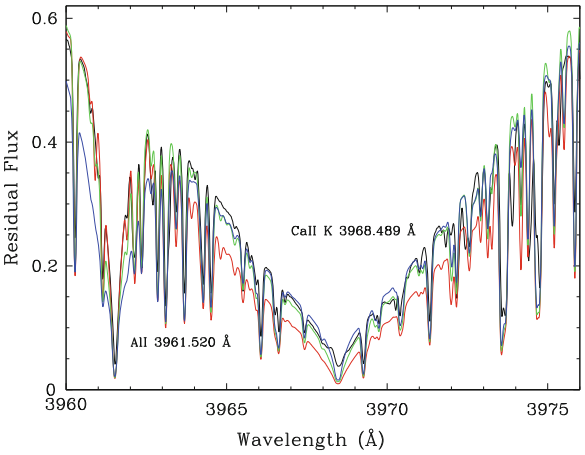

Fig. 3 *Black line* is the observed Ca II H line in HD 152311, the *red*, *green*, and *blue lines* are the computed ones for $\log g = 3.0, 4.0,$ and 5.0, respectively

(Ramirez et al. 2007). Over-imposed on this line are three theoretical lines computed by varying $\log g$ (details are reported in the caption of the figure) and keeping other parameters unchanged.

5 Broad Wings of Balmer Lines in Hot Stars

In hot stars, where the excitation of the hydrogen atom becomes important, the most prominent spectral feature in the visible range are the Balmer lines. These lines are different from other spectral lines because the atomic structure of hydrogen is particularly subject to the linear Stark effect. The corresponding broadening can be enormously larger than typical broadening of metal lines. Struve (1929) gave the first convincing argument that the broad wings of hydrogen lines in hot stars are due to linear Stark effect. The spatial distribution of ions gives a non-zero electric field at the position of the atom, causing a perturbation and splitting of the energy levels.

If we call by R the separation of some ion from the hydrogen atom, then the splitting of the energy levels can be expressed as the wavelength shift of the spectral components

$$\Delta\lambda_j = c_j E = c_j \frac{e}{R^2}, \tag{26}$$

where E is the electric field at the hydrogen atom position due to the disturbing ion, and c_j is the proportionality constant of the jth spectral component. So, a greater compression of the atmosphere results in a greater E, which is the reason why Balmer lines increase in strength toward lower luminosity.

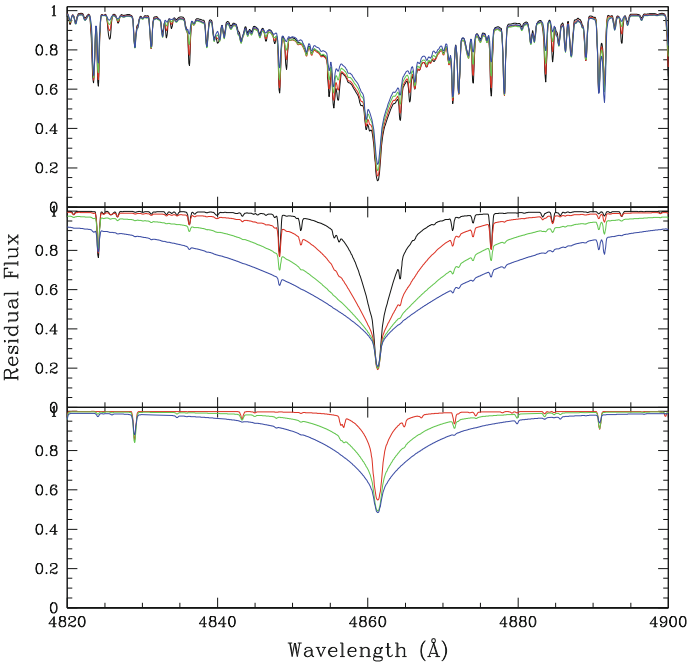

Fig. 4 *Upper panel* Hβ computed for $T_{\rm eff} = 7{,}000$ K and $\log g = 2.0$ (*black*), 3.0 (*red*), 4.0 (*green*), and 5.0 (*blue*). *Middle* and *bottom panels* Hβ computed for $T_{\rm eff} = 10{,}000$ K and $T_{\rm eff} = 25{,}000$ K, respectively, and same gravities as before

The line absorption in the wings (very prominent in the profile) is proportional to P_e because the Stark effect is proportional to the microscopic electric field. In this case the continuum absorption coefficient is dominated by the neutral hydrogen absorption, so κ_ν is proportional to the number of neutral hydrogen atom and we can write

$$\frac{l_\nu}{\kappa_\nu} \propto \text{const}\, P_e. \tag{27}$$

In Fig. 4, we show some computed Hβ for three different $T_{\rm eff}$, namely 7,000, 10,000, and 25,000 K. It is evident that for low temperatures (upper panel) the Balmer line profile is not a good diagnostic, while for hot stars it becomes extremely sensitive to the gravity.

Several studies have shown that a non-standard chemical composition of the stellar atmosphere alters the profiles of the Balmer lines (Leone and Manfrè 1997; Catanzaro et al. 2004). In such stars, gravity determination should be performed simultaneously with $T_{\rm eff}$ and chemical composition. In Fig. 5, we show an example of fitting the Hγ of the chemically peculiar star HR 6000 (Catanzaro et al. 2004). The three panels show different synthetic profiles obtained for different combinations of atmospheric

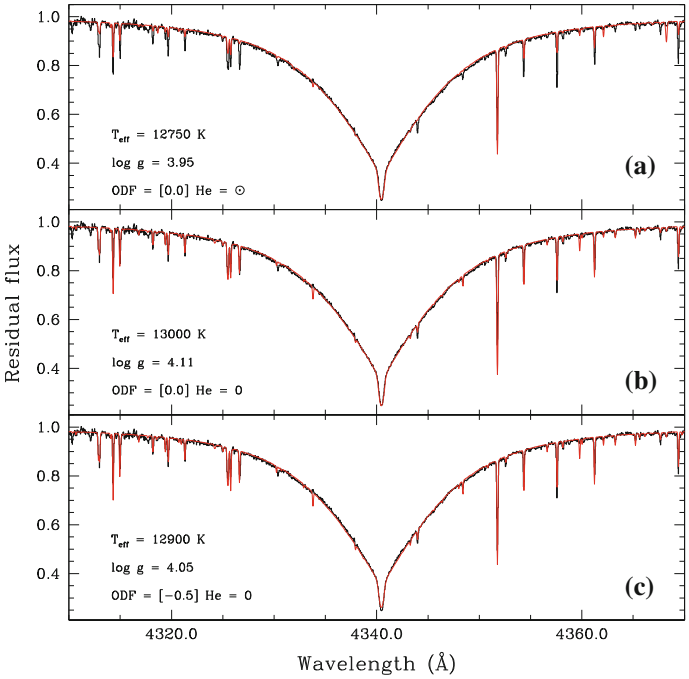

Fig. 5 Fitting of Hγ observed in the chemical peculiar star HR 6000. Each profile has been calculated using models with different opacity distribution functions (*ODF*), i.e. different metallicities. Credit: Catanzaro et al. (2004), reproduced with permission ©ESO

parameters, such as effective temperature, gravity and chemical composition. Only with an accurate iterative procedure we can fix consistently all these parameters, gravity in particular.

6 The Gravity–Temperature Diagram

So far we have looked at spectral lines only as indicators of surface gravity. But we must not forget that they are also indicators of effective temperature, and therefore it is useful to discuss a method that provides a simultaneous solution for both quantities, the so-called gravity–temperature diagram. The method works well if we use lines having different response to the variables, through different excitation potentials, for example.

For the sake of clarity, let us consider in Fig. 6 two lines of Fe II with different excitation potentials, each curve is computed for a constant iron abundance, while varying $\log g$ for a given $T_{\rm eff}$ (or vice versa) to recover the observed equivalent widths. The crossing point is obviously the solution, that is, the right temperature and

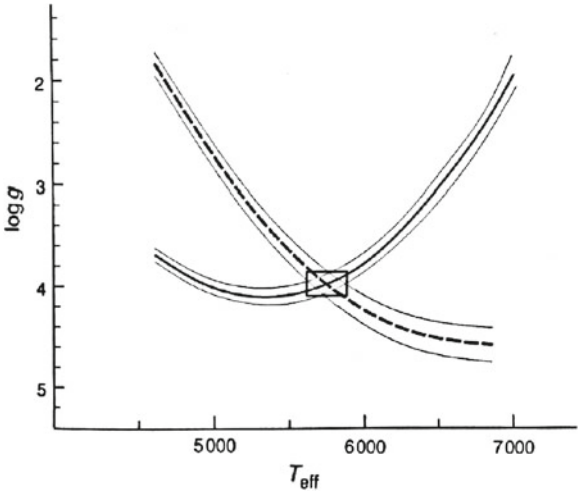

Fig. 6 This log g–T_{eff} diagram shows the curves obtained for two Fe II lines with different excitation potential, 5 eV (*dashed line*) and 0 eV (*solid line*). Typical measurement errors are indicated by the *lighter lines*. The solution is then indicated by the locus where the lines cross [adapted from Gray (2005)]

gravity. The uncertainties can be estimated evaluating the locus created by changing the observed equivalent width by an amount equal to $\pm \delta\, EW$, where $\delta\, EW$ is the measurement error on the equivalent width (the box in Fig. 6).

Any number of diagnostics can be placed on such a diagram: Balmer jump, hydrogen lines, strong metal lines, weak metal lines of various excitation potentials and so on. Of course, relations are expected to cross each other, and the more orthogonal the crossing, the more precisely the intersection and the solution is established. Some examples are reported in Fig. 7, taken from Lyubimkov et al. (2002) and Lehner et al. (2000), left and right panels, respectively.

7 Balmer Jump as log g Indicator

The Balmer jump, i.e. the ratio between the flux at 3,660 Å to that at 3,640 Å, is the only continuum feature sensitive enough to the gravity. The best sensitivity occurs at around 7,500 K. The usefulness of this indicator does not extend to stars as cool as late F stars, because the multitude of metal lines that already appears at this temperature contributes to mask the Balmer jump. Moreover, at lower temperatures negative hydrogen ion grows, while neutral hydrogen diminishes from lack of excitation. At the higher temperature, the Balmer jump becomes smaller as the hydrogen absorption fades with increasing ionization of hydrogen.

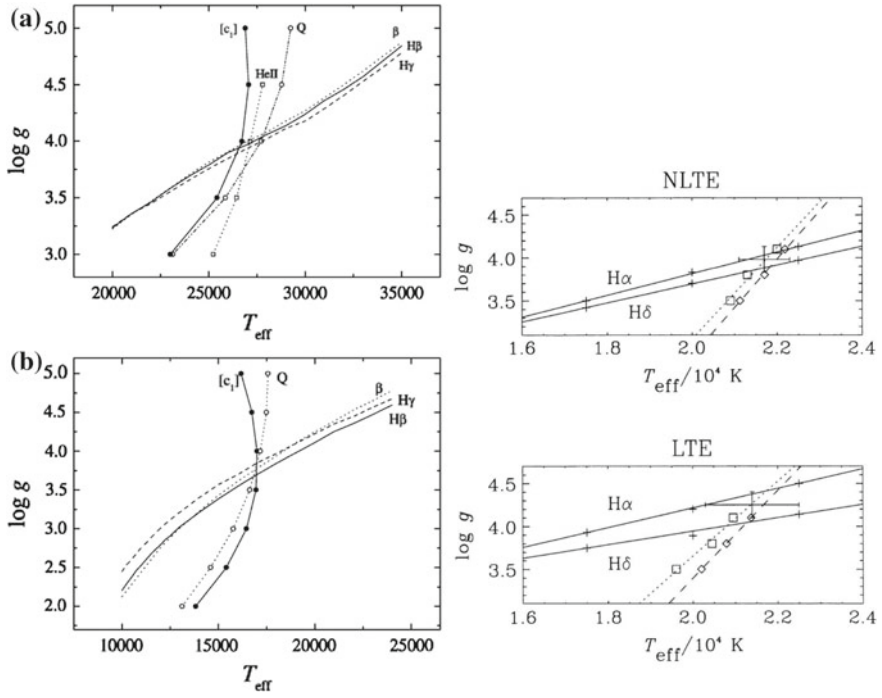

Fig. 7 *Left panel* this figure shows an example of $\log g$–$T_{\rm eff}$ diagram. The authors used as diagnostics several quantities, such as: photometric indices Q, $[c_1]$, and β and equivalent widths of Hβ and Hγ. The various lines are the loci from the theoretical models which predict the observed value for each of the considered parameters. *Upper panel* is for HD 8797 (B0.5 IV) and *bottom panel* is for HR 6588 (B3 IV). Credit: (Lyubimkov et al. 2002, Fig. 3) (By permission of Oxford University Press on behalf of The Royal Astronomical Society). *Right panel* this example shows an estimation of atmospheric parameters for LTE and non-LTE cases. *Solid lines* are the loci of fits to the Hα and Hδ lines. *Dotted lines* (profile-fitting method) and *dashed lines* (equivalent widths method) result from a Si II/Si III ionization balance. Adopted parameters are also displayed with respective *error bars*. Credit: (Lehner et al. 2000, Fig. 1) (By permission of Oxford University Press on behalf of The Royal Astronomical Society.)

In Fig. 8, we show the behaviour of Balmer jump with temperature and gravity (left panel) and an example of this method (right panel).

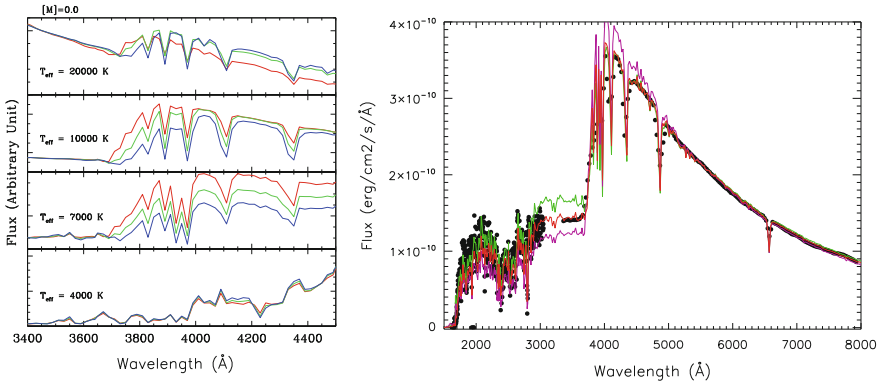

Fig. 8 *Left panel* four different behaviours of the Balmer jump computed for $T_{\rm eff} = 4{,}000, 7{,}000, 10{,}000$, and $20{,}000$, $\log g = 3.0$ (*red*), 4.0 (*green*), and 5.0 (*blue*). All the models have been calculated for solar chemical composition. *Right panel* spectral energy distribution observed in γ Boo fitted with a model computed for $T_{\rm eff} = 7{,}600$ K and $\log g = 3.7$ (Ventura et al. 2007). We overimposed two models computed with the same temperature but with two different gravities: $\log g = 3.00$ (*purple*) and 4.40 (*green*)

References

Bagnulo S, Jehin E, Ledoux C et al (2003) The UVES Paranal Observatory Project: A Library of High-Resolution Spectra of Stars across the Hertzsprung-Russell Diagram. The Messenger 114:10

Catanzaro G, Leone F, Dall TH (2004) Balmer lines as Teff and log g indicators for non-solar composition atmospheres. An application to the extremely helium-weak star HR 6000. A&A 425:641

Catanzaro G, Ripepi V, Bruntt H (2013) Testing different methods for atmospheric parameters determination. The case study of the Am star HD 71297. MNRAS 431:3258

Gray DF (2005) The Observation and analysis of Stellar Photospheres. Cambridge University Press, New York

Lehner N, Dufton PL, Lambert DL, Ryans RSI, Keenan FP (2000) High-resolution optical spectroscopy of the sharp-lined B-type star HD83206. MNRAS 314:199

Leone F, Manfrè M (1997) The importance of a correct abundance assumption in determining the effective temperature and gravity of stars. A spectroscopic study of the helium weak stars HD 5737, HD 175362 and HD 202671. A&A 320:257

Lyubimkov LS, Rachkovstaya TM, Rostopchin SI, Lambert DL (2002) Surface abundances of light elements for a large sample of early B-type stars-II. Basic parameters of 107 stars. MNRAS 333:9

Ramirez I, Allende Prieto C, Lambert DL (2007) Oxygen abundances in nearby stars. Clues to the formation and evolution of the Galactic disk. A&A, 465:271

Struve O (1929) The Stark Effect in Stellar Spectra. ApJ 69:173

Ventura R, Catanzaro G, Christensen-Dalsgaard J, di Mauro MP, Paternò L (2007) A spectroscopic search for non-radial pulsations in the δ Scuti star γ Bootis. MNRAS 381:1647

Stellar Parameters from Photometry

Barry Smalley

Abstract Stellar photometry is a powerful tool for determining stellar parameters, especially effective temperature. The role of fundamental stars is discussed, along with the accuracy of values for the Sun, Vega and Procyon. Absolutely calibrated flux measurements enable the direct determination of effective temperature for stars with known angular diameters, and indirectly via the Infrared Flux Method and model flux-fitting. Broad- and intermediate-band photometric systems are also discussed.

Keywords Techniques: photometric · Stars: atmospheres · Stars: fundamental parameters · Stars: individual Vega · Stars: individual: Procyon

1 Fundamental Stars

A fundamental star has at least one of its atmospheric parameters obtained without reference to model atmospheres. An ideal fundamental star will have both effective temperature ($T_{\rm eff}$) and surface gravity ($\log g$) measured. These stars are vital for the quality assurance of model predictions. Unfortunately, the number of fundamental stars is relatively limited by the lack of suitable measurements.

1.1 Effective Temperature

The effective temperature of a star is physically related to the total radiant power per unit area at stellar surface ($F_\star$):

B. Smalley (✉)
Astrophysics Group, Keele University, Staffordshire ST5 5BG, UK
e-mail: b.smalley@keele.ac.uk

E. Niemczura et al. (eds.), *Determination of Atmospheric Parameters of B-, A-, F- and G-Type Stars*, GeoPlanet: Earth and Planetary Sciences,
DOI: 10.1007/978-3-319-06956-2_10,

$$\sigma T_{\rm eff}^4 = F_\star = \frac{\theta^2}{4} f_\oplus.$$

Providing there is no interstellar reddening (or due allowance for it is made), the total observed (bolometric) flux at the Earth ($f_\oplus$) can be used to determine the total flux at the star:

$$F_\star = \frac{\theta^2}{4} f_\oplus.$$

The only additional requirement is a determination of the stellar angular diameter (θ). This can be obtained directly using techniques such as speckle photometry, interferometry and lunar occultations (McAlister 1985; Quirrenbach 2001), and indirectly from eclipsing binary systems with known distances (Smalley et al. 2002). We must, however, be aware that some of these methods require the (not always explicit) use of limb-darkening corrections.

1.2 Surface Gravity

The surface gravity of a star is directly given by the stellar mass and radius (in solar units):

$$g = g_\odot \frac{M}{R^2} \qquad \text{or, logarithmically,} \qquad \log g = \log M - 2\log R + 4.437.$$

Surface gravity is a measure of the photospheric pressure of the stellar atmosphere, where pressure is the total pressure including gas, radiation and, if present, magnetic pressures. Direct measurements are possible from eclipsing spectroscopic binaries (Torres et al. 2010), but again be aware of hidden model atmosphere dependencies. It is also possible to obtain $\log g$ from the analysis of planetary transits and asteroseismology (Winn 2011; Verner et al. 2011).

2 Accuracy of Direct Measurements

2.1 The Sun

Our nearby stellar companion, the G2 V-type Sun, has the most accurately known stellar parameters. The measured total solar flux at the Earth, the Solar Constant, is $f_\oplus = 1{,}367 \pm 4\,\mathrm{W\,m^{-2}}$ (Mendoza 2005). Variations due to the Solar Cycle and rotation, contribute 0.1 and 0.2 %, respectively (Zahid et al. 2004). This equates to ± 4 K in the Solar effective temperature. A value of $T_{\rm eff} = 5{,}777 \pm 10$ K is obtained from the Solar Constant and the measured Solar radius, including calibration

uncertainties. The Solar surface gravity is exceedingly well known; $\log g = 4.4374 \pm 0.0005$ (Gray 2008).

2.2 Vega

The bright A0 V star Vega is our primary stellar flux calibrator (Hayes and Latham 1975; Bohlin and Gilliland 2004). The measured total flux at the Earth is $f_{\oplus} = 29.83 \pm 1.20 \times 10^{-9}\,\mathrm{W\,m^{-2}}$ (Alonso et al. 1994), which is an uncertainty of some 4 %. Using the interferometric angular diameter of Ciardi et al. (2001), $\theta = 3.223 \pm 0.008$ mas, we obtain $T_{\rm eff} = 9{,}640 \pm 100$ K. Most of the uncertainty ($\sim$95 K) is due to the uncertainties in the measured fluxes, while the error in the angular diameter only contributes $\sim$10 K.

Since Vega is a single star, there is no direct fundamental $\log g$ measurement. Thus any calibration which uses Vega as a zero-point must assume a value for $\log g$. Detailed model atmosphere analyses give a value of $\log g = 3.95 \pm 0.05$ (Castelli and Kurucz 1994). However, since Vega is a rapidly-rotating pole-on star, the temperature and gravity varies across the surface (Hill et al. 2010). It is also a metal-poor λ Boo-type star (Ilijic et al. 1998).

Uncertainties in $T_{\rm eff}$ are mostly due to uncertainty in stellar fluxes. An interesting discussion on the accuracy of the visible and near-infrared absolute flux calibrations is given by Mégessier (1995). These uncertainties place a limit on our current direct determinations of stellar fundamental parameters. See also Gray (2007) for a discussion as to why Vega should not be a fundamental calibrator.

2.3 Procyon

Procyon is a spectroscopic binary, with a period of 40 years. The companion is a white dwarf. This bright F5 IV-V star is a very useful fundamental star. Using bolometric flux values and interferometric angular diameter measurements, many direct determinations of its $T_{\rm eff}$ have been obtained, ranging from $6{,}516 \pm 87$ K (Aufdenberg et al. 2005) to $6{,}591 \pm 43$ K (Chiavassa et al. 2012). Using the HIPPARCOS parallax, Aufdenberg et al. (2005) determined a radius of $2.031 \pm 0.013\,R_{\odot}$. The mass of Procyon has been determined using the astrometric orbit, but with some debate as to the actual value (Girard et al. 2000; Gatewood and Han 2006; Liebert et al. 2013). Combining the two gives the surface gravity; Kervella et al. (2004) found $\log g = 3.96 \pm 0.02$, while Chiavassa et al. (2012) obtained $\log g = 4.01 \pm 0.03$.

3 Indirect Methods

The direct determination of $T_{\rm eff}$ and $\log g$ is not possible for most stars. Hence, we have to use indirect methods. In this section we discuss the use of various techniques used to determine the atmospheric parameters. When determining $T_{\rm eff}$ and $\log g$, using model-dependent techniques, we must not neglect metallicity ([M/H]). An incorrect metallicity can have a significant effect on perceived stellar parameters (Smalley and Dworetsky 1993).

3.1 Photometric Systems

There have been many photometric systems developed to describe the shape of stellar flux distributions via magnitude differences (colours). Since they use wide band passes, observations can be obtained in a fraction of the time required by spectrophotometry and can be extended to fainter stars. The use of standardized filter sets allows for the quantitative analysis of stars over a wide magnitude range.

Theoretical photometric indices from Kurucz ATLAS flux calculations are normalized using the observed colours and known atmospheric parameters of Vega. Vega was originally chosen because it is the primary flux standard with the highest accuracy spectrophotometry, but recall it does not have a fundamental $\log g$ value.

An alternative, semi-empirical approach, is to adjust the theoretical photometry to minimize the discrepancy with observations of stars with known parameters. Moon and Dworetsky (1985) used stars with fundamental values to shift the grids in order to reduce the discrepancy between the observed and predicted colours. In contrast, Lester et al. (1986) treated the raw model colours in the same manner as observed stellar photometry. The model colours were placed on the standard system using the usual relations of photometric transformation. However, both these approaches have the potential to mask physical problems with models.

Overall, photometry can give very good first estimates of atmospheric parameters. In the absence of any other suitable observations, the values obtainable from photometry are of sufficient accuracy for most purposes, with typical uncertainties of not better than ± 200 K and ± 0.2 dex in $T_{\rm eff}$ and $\log g$, respectively. A good review of photometric systems is given by Bessell (2005).

3.2 $T_{\rm eff}$-Colour Relationships

Effective temperatures can be estimated from photometric colour indices. Empirical calibrations are based on stars with known temperatures, often obtained using the InfraRed Flux Method (see Sect. 4.1). There are many examples in the literature, for example: Alonso et al. (1996), VandenBerg and Clem (2003), Clem et al. (2004), Casagrande et al. (2010).

Particularly useful are $(V-K)$ calibrations, since this index is much less sensitive to metallicity than $(B-V)$ (Alonso et al. 1994; Kinman and Castelli 2002; Ramírez and Meléndez 2005). However, this index is more sensitive to the presence of a cool companion.

Often, there are several steps involved in obtaining the calibrations. The uncertainties and final error on the parameters obtained are not always immediately obvious.

3.3 Strömgren *uvbyβ* Photometry

The four intermediate-band filters (Strömgren 1966), plus a pair Hβ filters (Crawford 1958), yield four indices: $b-y$, c_1, m_1, β. These have been constructed to allow for the discrimination between $T_{\rm eff}$, $\log g$ and [M/H]. A dereddening routine UVBYBETA was written in FORTRAN by Moon (1985), which is now available in the IDL Astronomy Library: http://idlastro.gsfc.nasa.gov/ftp/pro/astro/uvbybeta.pro.

Parameter determination can be done using model atmosphere photometry grid calibrations. For example, the FORTRAN code TEFFLOGG (Moon 1985) based on Moon and Dworetsky (1985). While this is now somewhat dated, it does provide a quick and reasonably accurate parameter values. Small corrections to $\log g$ were made by Napiwotzki et al. (1993). Other calibrations are available in the literature (e.g. Smalley and Dworetsky 1995; Önehag et al. 2009).

3.4 Geneva Photometry

The seven-colour Geneva system has been used since around 1960 at the Geneva Observatory. Using a mixture of intermediate and wide passbands, it has similar efficiency to *uvbyβ*. However, for A-type stars and later Geneva photometry is unable to discriminate between reddening and temperature effects (Nicolet 1981). Calibrations include that of Künzli et al. (1997).

3.5 KIC Photometry

The *Kepler* Input Catalogue (KIC) gives photometric measurements and estimated stellar parameters (Brown et al. 2011). The overall accuracy is $T_{\rm eff} \pm 300\,{\rm K}$ and $\log g \pm 0.5$ dex for dwarfs, but larger for giants. Metallicity ([M/H]) estimates can be off by over 1 dex! A revised $T_{\rm eff}$ scale was determined by Pinsonneault et al. (2012) making dwarf stars approximately 200 K hotter.

4 Spectral Energy Distributions

For many bright stars we have flux-calibrated spectrophotometry, but for fainter stars we have to construct a spectral energy distribution (SED) from available broad-band photometry:

- **Ultraviolet** For the brightest stars TD-1 (Carnochan 1979) and IUE final archive (Wamsteker et al. 2000) can be a source, while GALEX with its two broad UV bands can be useful for fainter stars (Morrissey et al. 2007). Another source is FUSE spectra (Dixon et al. 2007) which are indeed very useful, for example to check the adopted reddening.
- **Optical** In the absence of flux-calibrated spectrophotometry, broad-band photometry can be used, for example $UBVRI$, SDSS (Ahn et al. 2012), Tycho B and V (Hoeg et al. 1997), TASS I (Droege et al. 2006).
- **Infrared** 2MASS is a good source of all-sky JHK photometry (Skrutskie et al. 2006), while DENIS can be used in the southern sky (Epchtein et al. 1999). Further into the infrared, WISE photometry can be considered (Wright et al. 2010).

4.1 InfraRed Flux Method

The InfraRed Flux Method (IRFM), developed by Blackwell and Shallis (1977), can be used to determine $T_{\rm eff}$. The method relies on the fact that the stellar surface flux at an infrared wavelength (λ_0) is relatively insensitive to temperature. The method is almost model independent (hence near fundamental), with only the infrared flux at the stellar surface, $\phi(T_{\rm eff},\ \log g,\ \lambda_0)$, requiring the use of model calculations (Blackwell and Lynas-Gray 1994; Mégessier 1994):

$$\frac{f_\oplus}{f_{\lambda_0}} = \frac{F_\star}{F_{\lambda_0}} = \frac{\sigma {T_{\rm eff}}^4}{\phi(T_{\rm eff}, \log g, \lambda_0)}.$$

The method requires a complete flux distribution in order to obtain the total integrated ($f_\oplus$) stellar flux. In practice, however, all of the flux is not observable, especially in the far-ultraviolet. But, this is only a serious problem in the hottest stars, where model atmospheres can be used to insert the missing flux, in order to obtain the total integrated flux. Accurate infrared fluxes are, of course, essential for this method to produce reliable results.

The method is sensitive to the presence of any cooler companion stars. The effect of the companion is to lower the $T_{\rm eff}$ derived for the primary. A modified method was proposed and discussed by Smalley (1993). This method relies on the relative radii of the two components in the binary system. The effect of allowing for the companion can be dramatic; the $T_{\rm eff}$ determined for the primary can be increased by 200 K or more.

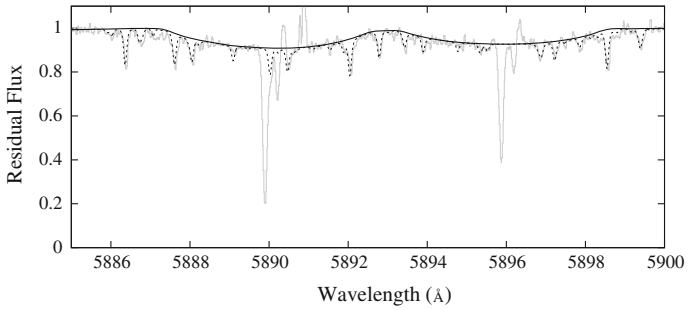

Fig. 1 The Na D lines of KIC 11090405 are washed out due to rapid rotation (*solid line*), while sharp interstellar lines are clearly present in the observations (*grey line*). This region is also affected by telluric water lines (*dashed line*) which can interfere with the measurements

Given good spectrophotometry, the IRFM should give values of $T_{\rm eff}$ which are close to the 'true' fundamental value. In fact it has been used as the basis of other calibrations (e.g. Ramírez and Meléndez 2005; Casagrande et al. 2010). Typically we can obtain temperatures to an accuracy of 1–2 % (Blackwell et al. 1990). The IRFM results for Vega have an uncertainty of ∼150 K.

Uncertainties in absolute calibration of IR photometry are important. For example, for 2MASS an error of ∼50 K, for a $T_{\rm eff}$ of 6,500 K, arises from the uncertainty in the absolute calibration alone (Cohen et al. 2003). However, the use of solar twins circumvents the uncertainties in the absolute flux scale and has enabled the temperature uncertainty to be reduced to around 20 K (Casagrande 2009).

4.2 Flux Fitting

The emergent flux distribution of a star is related to its atmospheric parameters. We can determine values for these parameters, by fitting model atmosphere fluxes to the observed SED (stellar energy distribution). However, interstellar reddening must be allowed for, since it can have a significant effect on the observed flux distribution and derived parameters.

If suitable spectra are available, reddening can be estimated using interstellar Na D lines. Munari and Zwitter (1997) presented a calibration using the equivalent width (EW) of the 5,890 Å line. For example, the star KIC 11090405 has an interstellar Na D EW ∼0.10 Å which gives $E(B-V)$ ∼0.03 (Fig. 1). Alternatively, if $uvby\beta$ photometry is available, this can be used to obtain a value of $E(B-V)$ (see for example Moon 1985). Also, for B-type stars with UBV photometry, the Q-Method (Johnson and Morgan 1953; Heintze 1973; Mayne and Naylor 2008) can be used to obtain $E(B-V)$.

Figure 2 shows the SEDs and fits for two *Kepler* stars. KIC 11772920 is fitted by a model with $T_{\rm eff} = 5{,}410$ K and $\log g = 4.5$, which agrees with that of ∼5,300 K obtained by the Hα profile (see Lecture on Stellar Parameters from Spectroscopy,

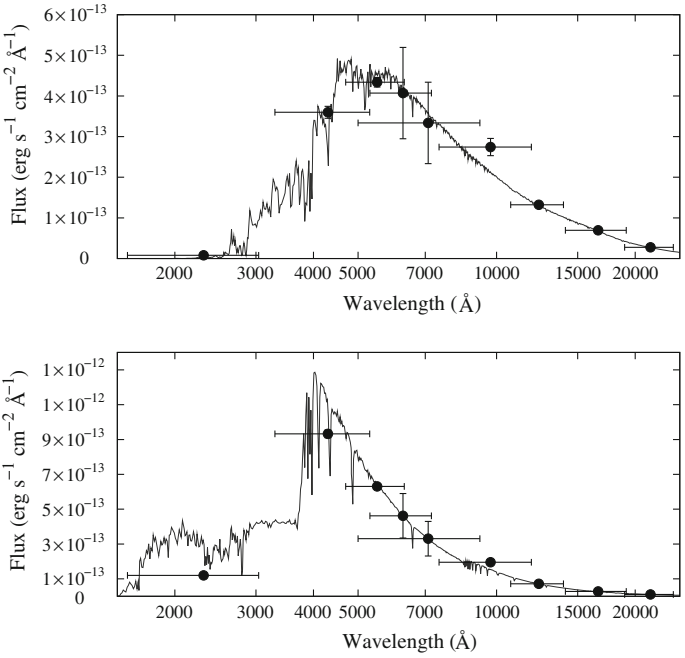

Fig. 2 Spectral energy distributions created from broad-band photometry (*filled circles*) and the best-fitting models flux distributions (*line*). The top panel is KIC 11772920 and the lower panel KIC 11090405. Note that the x error bar indicates the band-width of the photometry

this volume). The dereddened SED of KIC 11090405 is fitted by a model with $T_{\rm eff} = 7{,}980$ K and $\log g = 3.5$, which is slightly hotter than that found from the Hα profile ($T_{\rm eff} \sim 7{,}500$ K).

4.3 Metallicity

Stellar metallicity can affect the parameters determined from flux-fitting and broad-band photometry, but it is not normally obtainable from these methods. However, the Strömgren δm_0 index can be used to estimate metallicity in A-stars (Smalley 1993) and F and G stars (Nissen 1988; Önehag et al. 2009).

5 Conclusion

Photometry can provide very valuable input to the determination of stellar parameters. Stellar fluxes and the IRFM can give *near-fundamental* values of effective temperature that are good to 1 or 2 %. Intermediate-band photometry (e.g. $uvby\beta$) can yield values of $T_{\rm eff}$, $\log g$ and [M/H], and also estimates of interstellar reddening.

References

Ahn CP, Alexandroff R, Allende Prieto C et al (2012) ApJS 203:21
Alonso A, Arribas S, Martinez-Roger C (1996) A&A 313:873
Alonso A, Arribas S, Martinez-Roger C (1994) A&A 282:684
Aufdenberg JP, Ludwig H-G, Kervella P (2005) ApJ 633:424
Bessell MS (2005) Ann Rev A&A 43:293
Blackwell DE, Lynas-Gray AE (1994) A&A 282:899
Blackwell DE, Petford AD, Arribas S, Haddock DJ, Selby MJ (1990) A&A 232:396
Blackwell DE, Shallis MJ (1977) MNRAS 180:177
Bohlin RC, Gilliland RL (2004) AJ 127:3508
Brown TM, Latham DW, Everett ME, Esquerdo GA (2011) AJ 142:112
Carnochan DJ (1979) Bulletin d'Information du Centre de Donnees Stellaires 17:78
Casagrande L (2009) Mem Soc Astron Ital 80:727
Casagrande L, Ramírez I, Meléndez J, Bessell M, Asplund M (2010) A&A 512:A54
Castelli F, Kurucz RL (1994) A&A 281:817
Chiavassa A, Bigot L, Kervella P et al (2012) A&A 540:A5
Ciardi DR, van Belle GT, Akeson RL et al (2001) ApJ 559:1147
Clem JL, VandenBerg DA, Grundahl F, Bell RA (2004) AJ 127:1227
Cohen M, Wheaton WA, Megeath ST (2003) AJ 126:1090
Crawford DL (1958) ApJ 128:185
Dixon WV, Sahnow DJ, Barrett PE et al (2007) PASP 119:527
Droege TF, Richmond MW, Sallman MP, Creager RP (2006) PASP 118:1666
Epchtein N, Deul E, Derriere S et al (1999) A&A 349:236
Gatewood G, Han I (2006) AJ 131:1015
Girard TM, Wu H, Lee JT et al (2000) AJ 119:2428
Gray DF (2008) The observation and analysis of stellar photospheres, 3rd edn. Cambridge University Press, Cambridge
Gray RO (2007) In: Sterken C (ed) The future of photometric, spectrophotometric and polarimetric standardization, ASP conference series, vol 364, p 305
Hayes DS, Latham DW (1975) ApJ 197:593
Heintze JRW (1973) In: Hauck B, Westerlund BE (eds) Problems of calibration of absolute magnitudes and temperature of stars, proceedings of IAU symposium, vol 54, p 231
Hill G, Gulliver AF, Adelman SJ (2010) ApJ 712:250
Hoeg E, Bässgen G, Bastian U et al (1997) A&A 323:L57
Ilijic S, Rosandic M, Dominis D, Planinic M, Pavlovski K (1998) Contrib Astron Observatory Skalnate Pleso 27:467
Johnson HL, Morgan WW (1953) ApJ 117:313
Kervella P, Thévenin F, Morel P et al (2004) A&A 413:251
Kinman T, Castelli F (2002) A&A 391:1039
Künzli M, North P, Kurucz RL, Nicolet B (1997) A&AS 122:51
Lester JB, Gray RO, Kurucz RL (1986) ApJS 61:509
Liebert J, Fontaine G, Young PA, Williams KA, Arnett D (2013) ApJ 769:7
Mayne NJ, Naylor T (2008) MNRAS 386:261
McAlister HA (1985) Ann Rev A&A 23:59
Mégessier C (1995) A&A 296:771
Mégessier C (1994) A&A 289:202
Mendoza B (2005) Adv Space Res 35:882
Moon TT (1985) Comm Univ Lond Obs 78
Moon TT, Dworetsky MM (1985) MNRAS 217:305
Morrissey P, Conrow T, Barlow TA et al (2007) ApJS 173:682
Munari U, Zwitter T (1997) A&A 318:269
Napiwotzki R, Schoenberner D, Wenske V (1993) A&A 268:653

Nicolet B (1981) A&A 104:185
Nissen PE (1988) A&A 199:146
Önehag A, Gustafsson B, Eriksson K, Edvardsson B (2009) A&A 498:527
Pinsonneault MH, An D, Molenda-Żakowicz J et al (2012) ApJS 199:30
Quirrenbach A (2001) Ann Rev A&A 39:353
Ramírez I, Meléndez J (2005) ApJ 626:465
Skrutskie MF, Cutri RM, Stiening R et al (2006) AJ 131:1163
Smalley B (1993) MNRAS 265:1035
Smalley B (1993) A&A 274:391
Smalley B, Dworetsky MM (1995) A&A 293:446
Smalley B, Dworetsky MM (1993) A&A 271:515
Smalley B, Gardiner RB, Kupka F, Bessell MS (2002) A&A 395:601
Strömgren B (1966) Ann Rev A&A 4:433
Torres G, Andersen J, Giménez A (2010) A&A Rev 18:67
VandenBerg DA, Clem JL (2003) AJ 126:778
Verner GA, Elsworth Y, Chaplin WJ et al (2011) MNRAS 415:3539
Wamsteker W, Skillen I, Ponz JD et al (2000) Ap&SS 273:155
Winn JN (2011) In: Seager S (ed) Exoplanets. University of Arizona Press, Arizona, p 55
Wright EL, Eisenhardt PRM, Mainzer AK et al (2010) AJ 140:1868
Zahid HJ, Hudson HS, FrÖhlich C (2004) Sol Phys 222:1

Spectral Lines Analysis: Rotational Velocity and Velocity Fields

Giovanni Catanzaro

Abstract From an analysis of spectral line profiles we can obtain information on the physical structure of the star. In particular, in this lecture we focus on the determination of stellar rotational velocity and velocity fields, such as macroturbulence and microturbulence.

Keywords Stars: rotation · Techniques: spectroscopic

1 Introduction on Stellar Rotation

Since stars rotate around an axis, we expect to see the effects of rotation on the observed spectrum. These effects are small on the continuum, except when the star rotates close to the break-up limit. On the other hand, the spectral lines are strongly changed by the relative Doppler shifts of the light coming from different parts of the stellar disk. The approaching limb corresponds to the blue-shifted portion of a rotation-broadened line profile and the receding limb to the red-shifted portion (see Fig. 1 for clarity).

The characteristic shape of a spectral line when the rotation is much greater than all other Doppler shifts, can be calculated assuming a spherical and rotating star around its axis as a rigid body. Following Gray (2005) the rotation profile can be written as

$$G(\Delta\lambda) = c_1 \left[1 - \left(\frac{\Delta\lambda}{\Delta\lambda_L}\right)^2\right]^{1/2} + c_2 \left[1 - \left(\frac{\Delta\lambda}{\Delta\lambda_L}\right)^2\right], \qquad (1)$$

G. Catanzaro (✉)
INAF, Osservatorio Astrofisico di Catania, Catania, Italy
e-mail: Giovanni.Catanzaro@oact.inaf.it

E. Niemczura et al. (eds.), *Determination of Atmospheric Parameters of B-, A-, F- and G-Type Stars*, GeoPlanet: Earth and Planetary Sciences,
DOI: 10.1007/978-3-319-06956-2_11,

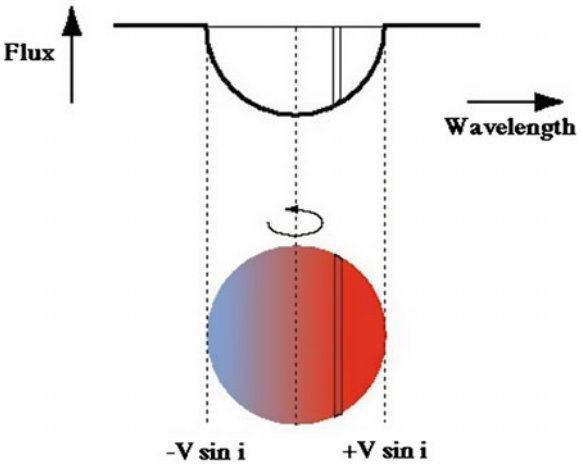

Fig. 1 Schematic view of the Doppler broadening of a spectral line due to rotation

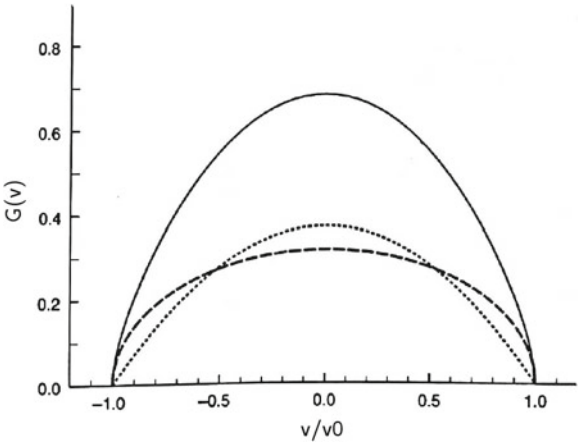

Fig. 2 Schematic view of the Doppler broadening of a spectral line due to rotation. The *dashed line* represents the first term of Eq. 1, the *dotted line* the second term, and the *solid* one represents the total. Both terms have been plotted considering $\varepsilon = 0.6$

where c_1 and c_2 are functions of the limb-darkening coefficient ε, $\Delta\lambda$ is the Doppler width relative to a generic point of the star and $\Delta\lambda_L$ is the maximum shift corresponding to the disk points on the limb at the stellar equator. The two terms of Eq. 1 and the total function are plotted in Fig. 2 (from Gray 2005).

The rotational axis has an arbitrary orientation with respect the line-of-sight of the observer, but because of the Doppler effect we can see only the component of the equatorial velocity parallel to the line-of-sight. Referring to Fig. 3, we call i the angle between the rotational axis and the line-of-sight (coincident with the x axis); we can measure only the projection of the vector velocity along the x axis, $v_0 \sin i$, where v_0

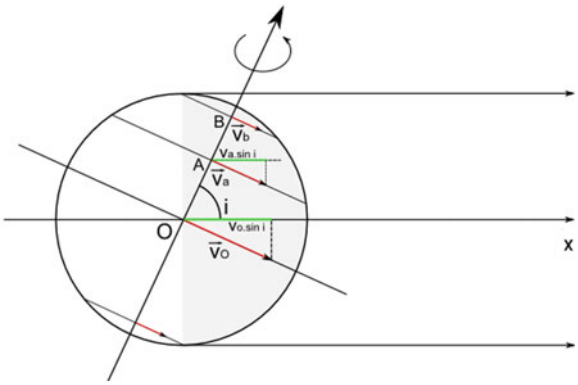

Fig. 3 In this figure x-axis is parallel to the line-of-sight. Because of the Doppler effect, an observer can see only the component projected along this axis, i.e. $v \sin i$

is the equatorial velocity. Two special cases occur for $i = 90°$, when vector velocity is parallel to the line-of-sight and star appears to rotate with v_0, and $i = 0°$, when velocity is perpendicular to line-of-sight and star appears not to rotate. In the latter case, the rotational broadening of the spectral line is null.

2 Determination of $v \sin i$

When the rotational broadening is large compared to all other broadening mechanisms, the profiles of spectral lines will be dominated by the shape of $G(\lambda)$, expressed as in Eq. 1. In such cases, including also the convolution with the instrumental profile, we can write the observed data as

$$D(\lambda) = H(\lambda) * G(\lambda) * I(\lambda), \tag{2}$$

where $D(\lambda)$ is the final spectrum, $I(\lambda)$ is the instrumental profile, $G(\lambda)$ is the rotational profile, and $H(\lambda)$ is the actual stellar flux. In the following sections we will discuss two methods commonly used in the literature to infer the rotational velocity of stars.

2.1 Profile Fitting Method

The $v \sin i$ can be determined by comparing the line profiles of the star to synthetic rotational profiles. The lines chosen should be free of strong pressure broadening, and must be strong enough so the rotation-broadened profile can still be seen and measured. In Gray (2005) the reader can find an extensive list of spectral lines useful for this purpose both for hot and cool stars.

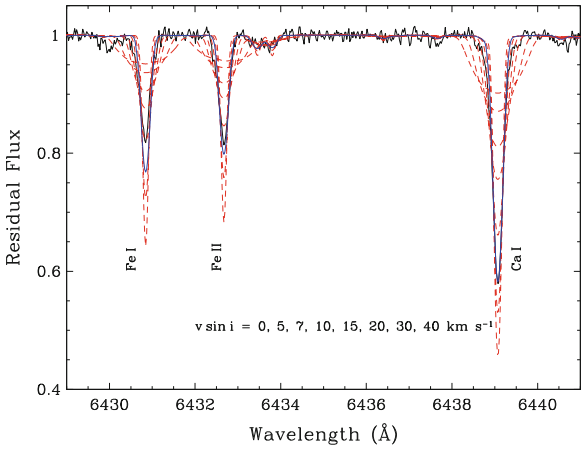

Fig. 4 Part of an observed spectrum with several synthetic spectra overimposed. Each synthetic spectrum was computed for different value of rotational velocity. The best fit is achieved for $v \sin i = 7\,\mathrm{km\,s^{-1}}$

In Fig. 4, we show a typical example of spectral synthesis, where we reproduced the spectral range between 6,429 and 6,441 Å, containing three important lines: Fe I λ6,431 Å, Fe II λ6,432 Å, and Ca I λ6,439 Å. On the observed spectrum, we overplotted several synthetic spectra computed for the same $T_{\rm eff}$, $\log g$, and abundances (previously determined), but with different values of $v \sin i$, the best fit can be evaluated using a minimization algorithm. The adopted value for the projected rotational velocity is $7\,\mathrm{km\,s^{-1}}$.

It is important to realize that rotational broadening does not alter the total absorption of the lines. In fact, lines with larger $v \sin i$ are wider and shallower, in such a way that the equivalent width is conserved.

Actually, before comparing observation with theory, we must take into account the instrumental profile, that is, the artificial broadening of the spectral lines induced by the spectrograph. From Eq. 2, the computed stellar flux must be convolved with the instrumental profile and then compared with the observation. As a measure of the instrumental profile we commonly use the resolving power (or resolution) of the spectrograph, the greater is the resolving power the narrower are the spectral lines. In the case of the spectrum shown in Fig. 4 the resolving power is $\mathrm{R} = \frac{\lambda}{\Delta\lambda} = 57{,}000$.

The correct assumption of the resolving power is of fundamental importance in the final results of our fitting procedure. Let us explore what happens when we make a mistake in choosing the correct resolution. In Fig. 5 we show the observed Fe II λ5,316 Å line of the star KIC 04077032, observed with HERMES with R = 85,000. Using this value, we obtain the fit shown as a red line, computed for $v \sin i = 18\,\mathrm{km\,s^{-1}}$ and $\log \frac{N_{\rm Fe}}{N_{\rm Tot}} = -4.48$. If we repeat the same procedure but considering an incorrect resolution of R = 20000, we obtain again a good fit (green line) but with different parameters: $v \sin i = 14\,\mathrm{km\,s^{-1}}$ and $\log \frac{N_{\rm Fe}}{N_{\rm Tot}} = -4.30$.

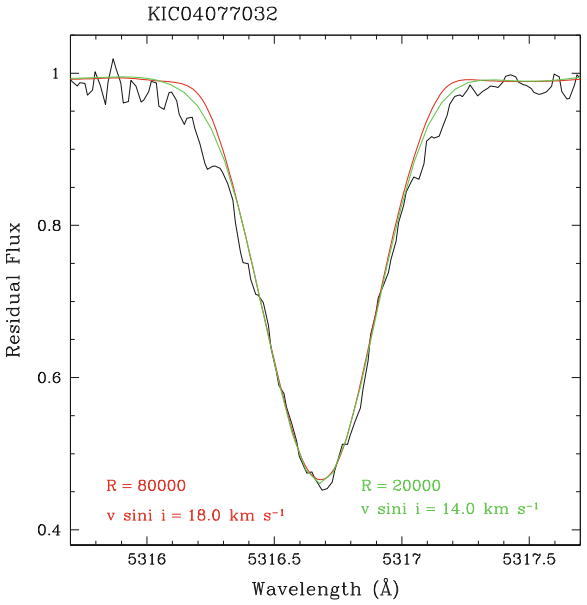

Fig. 5 Observed Fe II λ5,316 Å in KIC 04077032 (*black line*) with overimposed two synthetic lines computed for two different resolving powers (see description in the text)

2.2 Fourier Analysis Method

The information about $G(\lambda)$, defined as in Eq. 1, could be achieved also in the Fourier domain, that in some respects is more favourably distributed than in wavelength space. In Fig. 6 we show in the log-log plane the transforms of $G(\lambda)$, which we call $g(\sigma)$, for two spectral lines of two stars with different rotational velocities. The horizontal scale of the rotation profile is proportional to $v \sin i$, so the scale of $g(\sigma)$ is inversely proportional to $v \sin i$. In Fig. 6 green line refers to a star that rotates faster with respect to the blue one.

If we compare the transform of a $G(\lambda)$ computed for $v \sin i = 1\,\mathrm{km\,s^{-1}}$ with the transform of stellar line profile, the $\log \sigma$-scale difference between them gives $v \sin i$ directly.

3 Velocity Fields

Stellar atmospheres consist of layers in which the gas is in continuous movement. Motions of photospheric gases, called turbulence, introduce Doppler shifts that shape the profiles of most spectral lines. They have been observed to exist in hot as well as in cool stars. If we compare the size of the turbulent element to the unit optical depth (or in other word, to the mean free path of a photon), we can make two approximations:

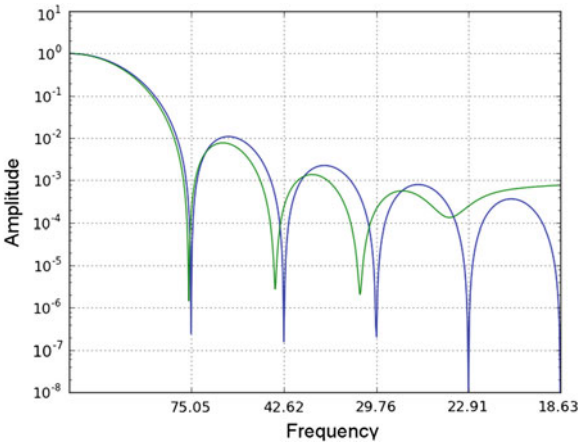

Fig. 6 A log-log plot of the Fourier transform of the rotational profiles of two different spectral lines. The abscissa scales inversely as with $v \sin i$

- **macroturbulent limit**, when the size of the turbulent element is large compared to the unit optical depth;
- **microturbulent limit**, when the size of the turbulent element is smaller than the unit optical depth.

3.1 Macroturbulence

In case of macroturbulence, turbulent cells are large enough so that photons remain trapped in them from the time they are created until they escape from the star. Lines are Doppler broadened: each cell produces a complete spectrum that is displaced by the Doppler shift corresponding to the velocity of the cell. In general we can write the following equation

$$I_\nu = I_\nu^0 * \Theta(\lambda), \tag{3}$$

where I_ν^0 is the intensity spectrum without macroturbulence and the function $\Theta(\lambda)$ is the macroturbulent velocity distribution (see Gray 2005). Observational evidence has shown that macroturbulence could not be represented by an isotropic Gaussian function, even if in the past decades this model was successfully used to compute spectral lines. At that time, the signal-to-noise ratios of the spectra were too poor to supply refuting evidence.

We know that atmospheric gases, especially when convection dominates the photosphere, are organized in convective cells which rise and fall, and there is also horizontal motion between the rising and falling areas. Thus, we can think to motions with velocity vectors restricted to being either along stellar radii or tangential to the surface but having a Gaussian distribution of speeds. This is the so-called "radial-

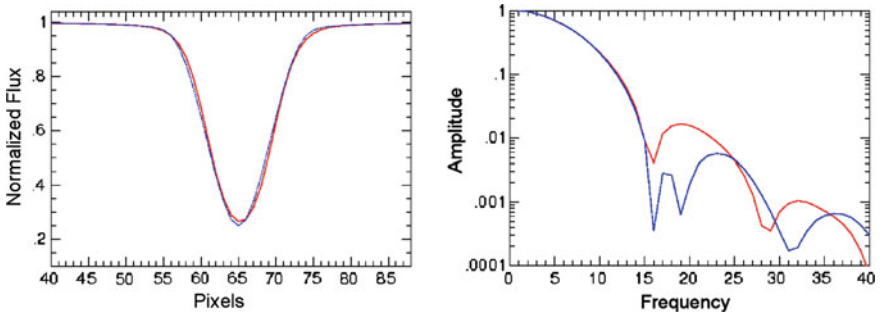

Fig. 7 *Left panel* spectral line reproduced with two different combinations of $v \sin i$ and macroturbulence ζ_{RT}: $v \sin i = 3\,\mathrm{km\,s^{-1}}$ and $\zeta_{RT} = 0\,\mathrm{km\,s^{-1}}$ (*red line*) and $v \sin i = 0\,\mathrm{km\,s^{-1}}$ and $\zeta_{RT} = 3\,\mathrm{km\,s^{-1}}$ (*blue line*). *Right panel* same lines in the Fourier domain

tangential" model, that has been introduced by Gray (1975). We can suppose that a certain fraction of stellar surface area is presumed to have radial motion, A_R, and the rest tangential motion, A_T. Then we can write $\Theta(\lambda)$ as:

$$\Theta(\lambda) = A_R \Theta_R(\lambda) + A_T \Theta_T(\lambda). \tag{4}$$

It is interesting to focus on the shape of the radial-tangential Doppler-shift distribution after the integration of Eq. 3 on the visible disk. This integration, performed to compute the emergent flux, has a very important effect. Even though the velocity distributions are Gaussian, the net result is a cuspid with a markedly sharper peak and wider wings.

An important characteristic of macroturbulence is that it does not alter the total absorption of the lines, or in other words it conserves the equivalent width of the lines. Lines broadened by macroturbulence are also made shallower.

There is an important trade-off between rotation and macroturbulent velocities, that is important to be stressed. It is possible to compensate a decrease in rotation by increasing the macroturbulent velocity. In Fig. 7 left panel, the spectral line can be reproduced with two different combinations of $v \sin i$ and macroturbulence ζ_{RT}: $v \sin i = 3\,\mathrm{km\,s^{-1}}$ and $\zeta_{RT} = 0\,\mathrm{km\,s^{-1}}$ (red line) and $v \sin i = 0\,\mathrm{km\,s^{-1}}$ and $\zeta_{RT} = 3\,\mathrm{km\,s^{-1}}$ (blue line). While in the wavelength space the differences between these two lines are barely noticeable, in Fourier space (right panel of Fig. 7) the differences are larger.

3.2 Microturbulence

In contrast to macroturbulence, we deal with microturbulent velocity when turbulent cells have sizes small compared to the mean free path of a photon. Then the line-of-sight penetrates through many cells of motion in the atmosphere and the

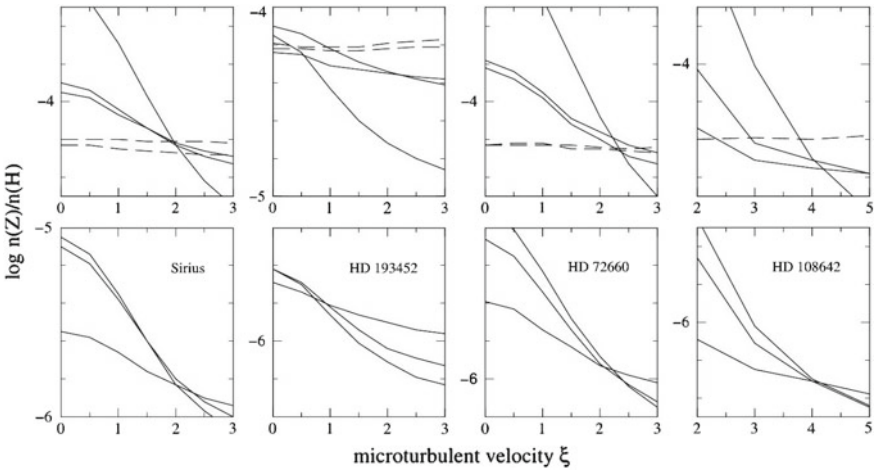

Fig. 8 Blackwell diagrams for Sirius, HD 193452, HD 72660, and HD 108642 (from *left* to *right*). The upper panels are for Fe II λλ 4,620, 4,625, 4,629, 4,635, and 4,631 Å; the lower panels are for Cr II λλ 4,616, 4,618, and 4,634 Å. Each panel is 1.0 dex high. *Dashed curves* indicate spectral lines with astrophysical gf values (Credit: J. Landstreet, A&A, 425, 641, 2004, reproduced with permission ©ESO)

distribution of cells velocities behaves like the particle velocity distribution. As a consequence, we can write the line absorption coefficient as the following convolution:

$$\alpha = \alpha' * N(\Delta\lambda), \tag{5}$$

where α and α' are the absorption coefficient with and without broadening, respectively, and $N(\Delta\lambda)$ is the distribution of velocity. Since typical values for microturbulent velocities are of the order of 1–2 km s^{-1} (Landstreet et al. 2009), small enough compared to the other components of line broadening, it is quite impossible to measure the shape of $N(\Delta\lambda)$. It has become standard practice to assume $N(v)$ to be an isotropic Gaussian of the form

$$N(v)\,dv = \frac{1}{\pi^{1/2}\,\xi_t} e^{-\left(\frac{v}{\xi_t}\right)^2} dv. \tag{6}$$

The convolution of α' with $N(v)$ can be included by a simple modification of the thermal broadening in α which is also Gaussian. The convolution of two Gaussians is still a Gaussian with a total dispersion parameter given by the quadratic sum

$$v^2 = v_0^2 + \xi_t^2. \tag{7}$$

Therefore, we can simply write

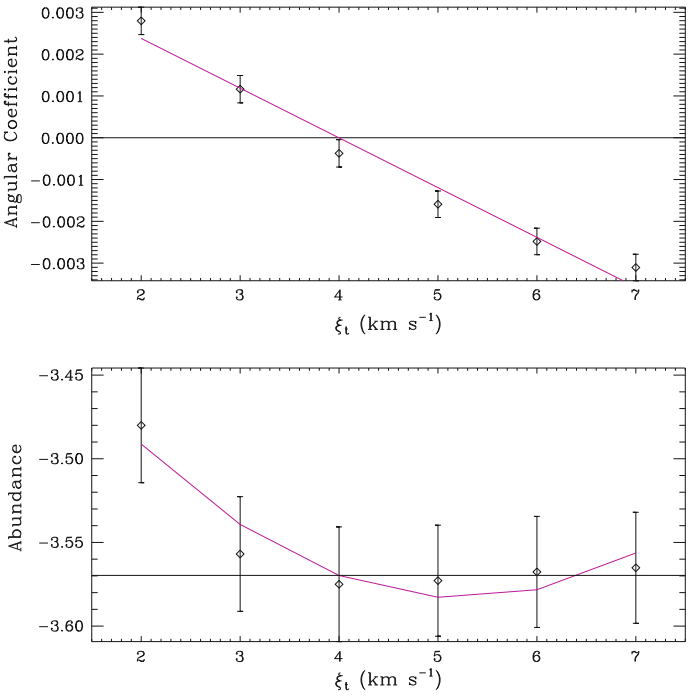

Fig. 9 *Upper panel* we show the behaviour of the angular coefficient versus the microturbulence; *bottom panel* iron abundance as a function of microturbulence. The results are: $\xi_t = 4.0 \pm 0.4\,\mathrm{km\,s^{-1}}$, $\log \frac{N_{Fe}}{N_{tot}} = -3.57 \pm 0.01$

$$\Delta\lambda = \frac{\lambda}{c}\left(\frac{2kT}{m} + \xi_t^2\right)^{1/2}, \tag{8}$$

where the dispersion parameter ξ_t is what we call microturbulence.

We stated before that typical values of ξ_t are of the order of 1 or $2\,\mathrm{km\,s^{-1}}$, so it is very hard to distinguish this broadening in the shape of the line profile. Let us look at two common methods used in literature to derive the microturbulence. The idea which underlies such methods is that the broadening due to the microturbulence has no effect on the abundance of the chemical element that has generated the line itself. This means that, for a fixed set of T_{eff}, $\log g$ and microturbulence, lines of the same element must give the same abundance, otherwise we have to tune the microturbulence until the equality is established again.

One of these methods is the Blackwell diagram. For a chosen set of lines belonging to the same element, one can calculate the abundance for several values of ξ_t, and plot the abundances versus ξ_t. The loci in common with all the lines is the microturbulence we searched for. In Fig. 8, we show an example of such diagram taken from Landstreet (1998). The authors derived ξ_t for four stars by using iron and chromium lines.

Of course there is agreement between the result obtained from iron lines and that obtained from chromium lines.

Another type of diagram useful for this purpose is to plot abundances versus equivalent widths, and requiring that the inferred abundance not depend on them. In other words we require that the slope of the best fit line is null. In Fig. 9, we show an example of this method, applied to the Am star HD 27411 (Catanzaro and Balona 2012). The authors computed, for various ξ_t, the abundances of 71 FeI lines, than they fitted those abundances against the equivalent width, and they plotted the angular coefficient versus ξ_t (upper panel). The value of ξ_t for which the angular coefficient goes to zero is the adopted microturbulence.

References

Catanzaro G, Balona L (2012) Abundances in HD 27411 and the helium problem in Am stars. MNRAS 421:1222

Gray DF (2005) The observation and analysis of stellar photospheres. Cambridge University Press, New York

Gray DF (1975) Atmospheric turbulence measured in stars above the main sequence. ApJ 202:148

Landstreet JD, Kupka F, Ford HA, Officer T, Sigut TAA et al (2009) Atmospheric velocity fields in tepid main sequence stars. A&A 503:973

Landstreet JD (1998) Detection of atmospheric velocity fields in A-type stars. A&A 338:1041

Convection and Turbulence

Barry Smalley

Abstract Convection and turbulence in the atmospheres of A-types and cooler stars produce observable effects. A discussion of the 1-D parameterization via mixing-length, microturbulence and macroturbulence is presented, along with a comparison of various calibrations. Overcoming some of the limitations of 1-D model atmospheres, 2-D and 3-D hydrodynamic simulations can yield improved fits to observed line profiles without the need for these parametrisations.

Keywords Convection · Turbulence · Line: profiles · Stars: atmospheres

1 Introduction

Convection and turbulence produce observable effects in the atmospheres of A-type stars and cooler. These are directly seen as granulation on the Sun due to surface convection cells. We indirectly infer their presence by the need for microturbulence and macroturbulence in 1-D spectrum syntheses, as well as curvatures observed in spectral line bisectors. As we shall see, convection and turbulence are characterised by free parameters in 1-D model atmospheres. These parameters can vary with depth in the atmosphere. The use of the more-realistic 2-D and 3-D models do not need these ad hoc parameters and imply that their use in 1-D models should be properly constrained.

B. Smalley (✉)
Astrophysics Group, Keele University, Staffordshire ST5 5BG, UK
e-mail: b.smalley@keele.ac.uk

E. Niemczura et al. (eds.), *Determination of Atmospheric Parameters of B-, A-, F- and G-Type Stars*, GeoPlanet: Earth and Planetary Sciences,
DOI: 10.1007/978-3-319-06956-2_12,

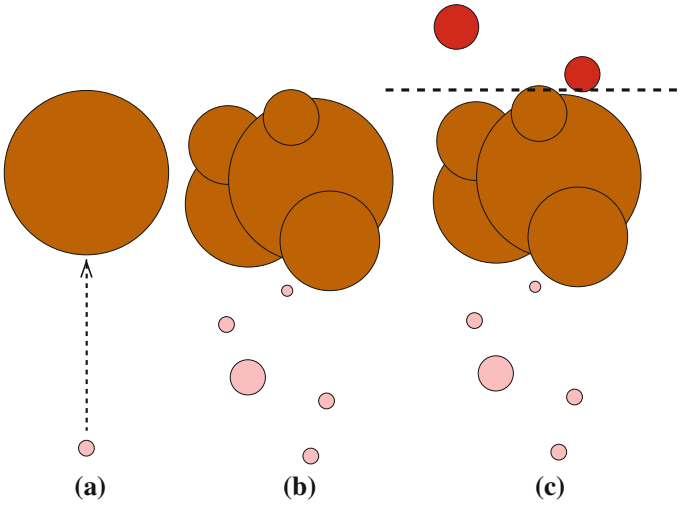

Fig. 1 Schematic bubble representations of convection treatments. In mixing-length theory (**a**), a single bubble rises within the atmosphere, while in turbulent convection bubbles of varying sizes rise (**b**). In (**c**) we have overshooting above the convection zone

2 Convection Theory

2.1 Mixing-Length Theory

Convection in stellar atmospheres is usually based on the mixing-length theory (MLT) (Böhm-Vitense 1958; Kippenhahn et al. 2013). In this model, a single bubble of gas rises a certain length l, relative to the pressure scale height H, before dispersing (Fig. 1a) and l/H is called the mixing-length. The problems with this theory is that it is clearly far too simple and that mixing-length is a totally free parameter. There is no prescription for mixing-length.

2.2 Turbulent Convection

Canuto & Mazzitelli (1991, 1992) proposed a model of turbulent convection in order to overcome one of the most basic short-comings of MLT, namely that a single convective element (or "bubble" or "eddy") is responsible for the transport of all the energy due to convection. This new model (CM) accounts for eddies of various sizes that interact with each other (Fig. 1b). The CM convection model was implemented in the ATLAS9 code by Kupka (1996) and is included in the LLMODELS9 (Shulyak et al. 2004). The CM model has no user adjustable free parameters. An improved variant is the self-consistent (CGM) method of Canuto et al. (1996).

2.3 Convective Overshooting

Convective bubbles rise above the convection zone into the stable regions (Fig. 1c). This is called overshooting, and should be present in our model atmosphere calculations. The ATLAS9 models introduced an "approximate overshooting" which has not been without its critics (see Castelli et al. 1997 for full details). The following quote from Kurucz' web site (http://kurucz.harvard.edu) aptly summarises the situation:

> Convective models use an overshooting approximation that moves flux higher in the atmosphere above the top of the nominal convection zone. Many people do not like this approximation and want a pure unphysical mixing-length convection instead of an impure unphysical mixing-length convection.

2.4 Atmospheric Structure

Figure 2 gives a comparison of the various convective models for $T_{\rm eff} = 7{,}000\,{\rm K}$ and $\log g = 4.0$. The CM model remains close to the radiative temperature gradient. MLT gives more convective flux than CM, even when $l/H = 0.5$. Overshooting produces an excess of convective flux in higher layers, which produces a noticeable bump in the temperature-depth relation compared to MLT without overshooting. At $T_{\rm eff} = 8{,}000\,{\rm K}$, CM gives essentially radiative temperature gradient with significantly less convective flux than MLT, while approximate overshooting introduces flux into higher layers (Heiter et al. 2002). There is a rapid decline of heat transport in the atmosphere and the layers immediately below as $T_{\rm eff}$ increases. This results in convection becoming unimportant for obtaining the atmospheric temperature structure above $T_{\rm eff} = 8{,}000\,{\rm K}$, but well below $T_{\rm eff} \sim 10{,}000\,{\rm K}$ where the atmosphere becomes (nearly) radiatively stable according to the Schwarzschild criterion (Landstreet 1998, Fig. 7).

2.5 Balmer Profile Variations

The temperature sensitivity of Balmer lines makes them an excellent diagnostic tool for late A-type stars and cooler. However, as emphasised by van't Veer-Menneret & Mégessier (1996), Hα and Hβ profiles behave differently due to convection: Hα is significantly less sensitive to mixing-length than Hβ. Both profiles are, nevertheless, affected by the presence of overshooting, with Hβ being more influenced than Hα (Fig. 3). Since Hα is formed higher in the atmosphere than Hβ, Balmer lines profiles are a very good depth probe of stellar atmospheres. Naturally, Balmer profiles are also affected by microturbulence, metallicity and, for the hotter stars, surface gravity (Heiter et al. 2002).

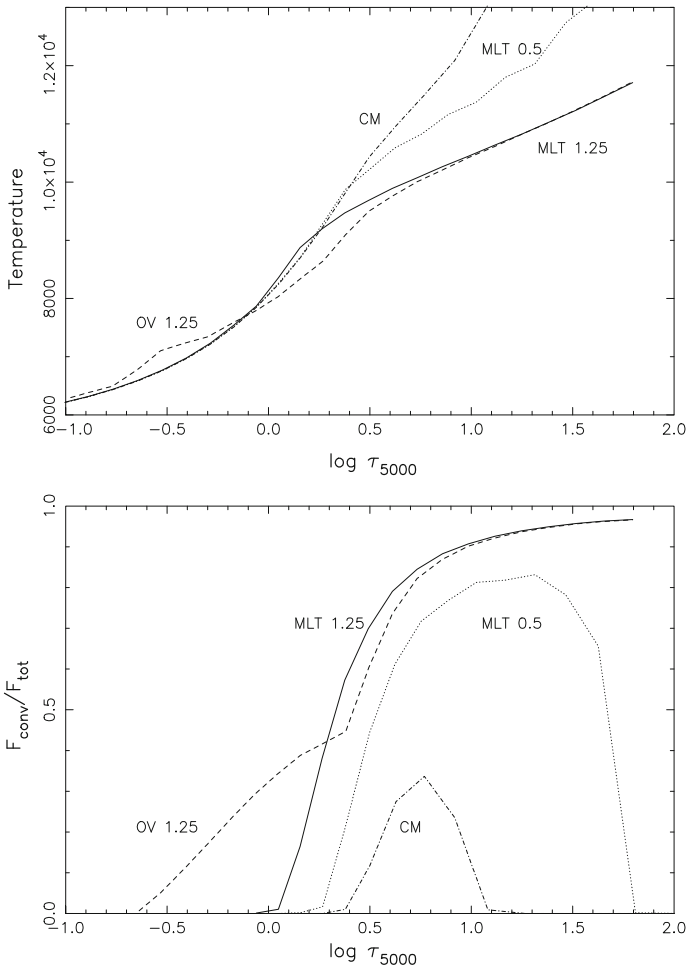

Fig. 2 Models with $T_{\rm eff} = 7{,}000$ K and $\log g = 4.0$ showing differences arising from changing the treatment of convection. The *upper panel* shows the variation of temperature with optical depth, while the *lower panel* shows the ratio of convective flux to total flux as function of optical depth. The *filled circles* in the *upper panel* show the temperature structure of a fully radiative model

2.6 *What to Use in* ATLAS *Models?*

In their studies of Hα and Hβ profiles of A and F stars (Gardiner et al., 1999; Smalley et al., 2002) found good agreement with fundamental stars for CM and MLT ($l/H \sim 0.5$) without approximate overshooting. However, Gardiner et al. (1999) found that $l/H = 1.25$ gave better results for stars in the temperature range $6{,}000 < T_{\rm eff} < 7{,}000$ K. Overall, the ATLAS models with no overshooting and $l/H = 1.25$ given by Castelli et al. (1997) are a good choice for use in stellar parameter determinations.

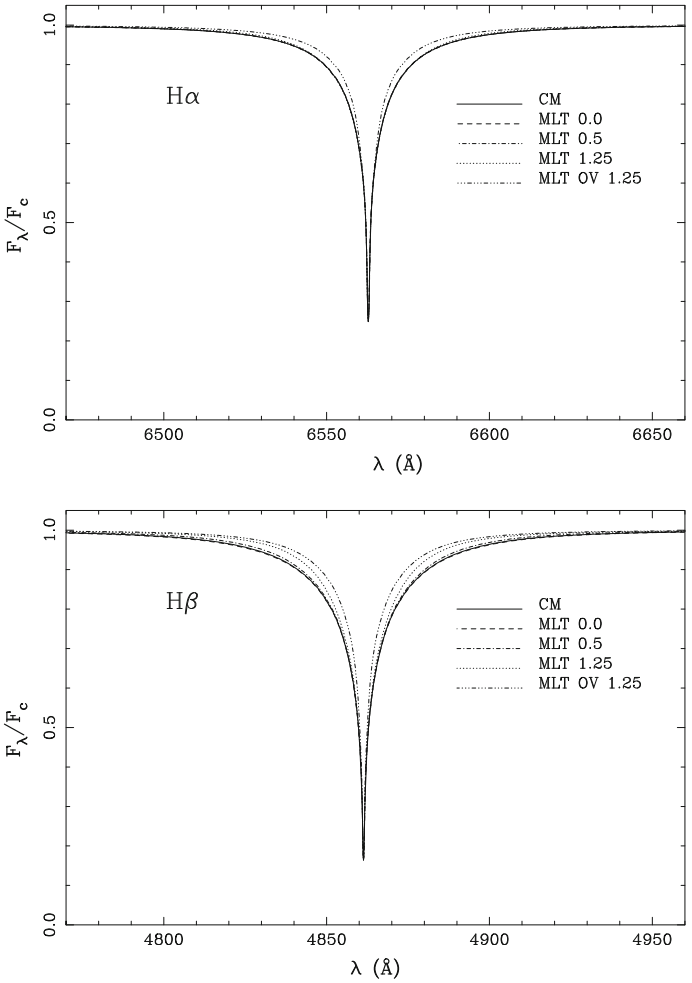

Fig. 3 The effects of convection on the predicted shape of Balmer profiles for models with $T_{\rm eff} = 7{,}000\,{\rm K}$, $\log g = 4.0$, [M/H] = 0.0 and $\xi_{\rm t} = 2\,{\rm km\ s^{-1}}$. H$\alpha$ (*upper panel*) is unaffected by the values of l/H, but sensitive to "approximate overshooting", while Hβ (*lower panel*) is sensitive to both

3 Microturbulence

Microturbulence ($\xi_{\rm t}$) is a free parameter introduced to allow abundances from weak and strong lines to agree. It is an extra source of broadening, which is added to thermal broadening of stellar lines (Struve & Elvey 1934). Physically, it is postulated as small-scale turbulent motions within the atmosphere, where the size of the turbulent elements is less than the unit optical depth (Gray 2008).

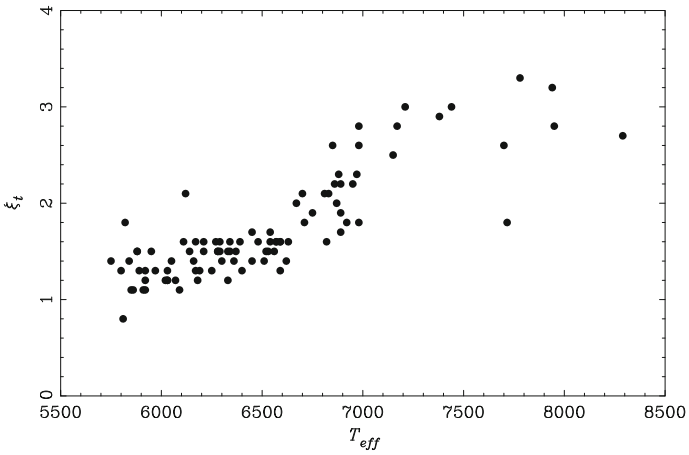

Fig. 4 The variation of microturbulence with effective temperature. Based on results of Gray et al. (2001) for stars near the main sequence (Smalley 2004). Note the apparent relatively abrupt change in behaviour between 6,500 and 7,000 K

Observations show that microturbulence does vary systematically with effective temperature (Chaffee 1970; Nissen 1981; Coupry & Burkhart 1992; Gray et al. 2001). Figure 4 shows the variation of $\xi_{\rm t}$ with $T_{\rm eff}$ for near main-sequence stars ($\log g > 4.0$) based on the results given by Gray et al. (2001). There is a relatively abrupt change in behaviour between 6,500 and 7,000 K, which is related to the change from weak subsurface convection to the fully convective atmospheres of cooler stars. Microturbulence increases with increasing $T_{\rm eff}$, peaking around mid-A type, before falling away to zero for B-type stars (Landstreet et al. 2009, Fig. 2).

The microturbulence of 1-D modelling is not turbulent motions, but rather velocity gradients within the atmosphere. Hence, microturbulence should no longer be a free parameter, but ought to be constrained within model atmosphere calculations. Indeed, Kurucz presented an empirical method for constraining depth-dependent microturbulence within ATLAS (Kurucz 2005).

3.1 Microturbulence Calibrations

Unless determined during an analysis, a value of microturbulence needs to be adopted in spectrum syntheses. As we have seen there is clear evidence that microturbulence varies with $T_{\rm eff}$.

During this workshop we have seen SME (Valenti & Piskunov 1996) in action. Valenti & Fischer (2005) found a *"strongly correlated values of* $\xi_{\rm t}$ *and* $[M/H]$, *suggesting that* $\xi_{\rm t}$ *and* $[M/H]$ *are partially degenerate."*, but since their analysis found no significant dependence with $T_{\rm eff}$ they adopted a fixed value. Indeed, inspection

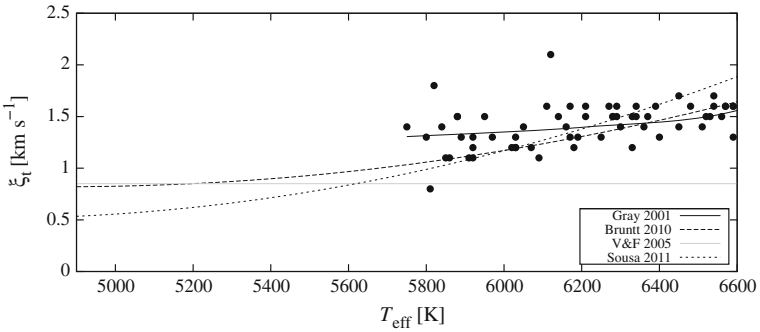

Fig. 5 Comparison of microturbulence values from the four different sources discussed in the text. The points are those from Gray et al. (2001) with the fit as given by Smalley (2004) (*solid line*), the *dashed-line* is the calibration of Bruntt et al. (2010), the constant value adopted by Valenti & Fischer (2005) is given as a *grey line*, and the *dotted-line* gives the fit to the Sousa et al. (2011) values by Gómez Maqueo Chew et al. (2013)

of Fig. 4 does show that for Solar-type stars the variation with $T_{\rm eff}$ is quite small. However, analyses using EW-based methods do find a significant variation with $T_{\rm eff}$. Examples are Sousa et al. (2011) using the ARES/MOOG combination we have also used at this workshop and the VWA-based results of Bruntt et al. (2010). A calibration based on the Sousa et al. (2011) results was presented in Gómez Maqueo Chew et al. (2013). Figure 5 compares the microturbulence values from these analyses.

4 Macroturbulence

Observations of spectral lines in Solar-type stars show extended shallow wings, which are the manifestation of granulation. The effect can be strong in giants and supergiants. It is seen in A-type stars, and even B-type supergiants (Przybilla et al. 2006). These large-scale velocities within atmosphere are what we call macroturbulence.

Macroturbulence is commonly implemented using the Radial-Tangential Model (Gray 1975, 2008). The model considers Doppler broadening in both the radial and tangential directions within the atmosphere, usually assuming that half the surface is radial and the other half is tangential, and that both have the same velocity ($\zeta_{\rm RT}$). It is another free parameter and the model is an ad hoc function convolved with the disk-integrated stellar spectrum. It is not even a local model in the way that microturbulence is, where it is incorporated into atmospheric radiative transfer.

Figure 6 compares calibrations of Gray (1984), Valenti & Fischer (2005) and Bruntt et al. (2010). There are noticeable differences, which would affect the determination of $v \sin i$ for example. It is worth noting that the often used calibration of Valenti & Fischer (2005) is, as clearly stated in their paper, an *upper limit*, since macroturbulence was determined by assuming $v \sin i = 0\,{\rm km\,s^{-1}}$. They also warn that their calibration might underestimate macroturbulence above ~5,800 K.

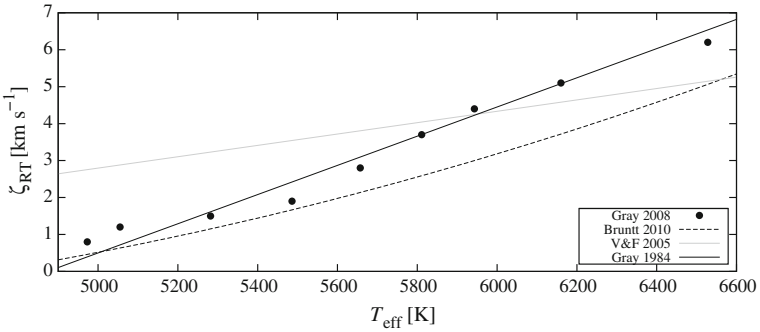

Fig. 6 Comparison of macroturbulence calibrations. The points are from the tabulation in Gray (2008), the *dashed line* from Bruntt et al. (2010), the Valenti & Fischer (2005) upper limit is given as the *grey line*, and the *black line* is Gray (1984)

5 Line Asymmetries

Velocity fields are present in stellar atmospheres which can be measured using line bisectors (Dravins 1987). Compared to Solar-type stars, the line bisectors in A-type stars are reversed, indicating small rising columns of hot gas and larger cooler downdrafts (Landstreet 1998). It is these motions that are thought to be responsible, at least in part, for the existence of microturbulence. In addition, since macroturbulence is linked to granulation, the line asymmetries can be represented by a mixture of both micro- and macroturbulence in the classical, 1-D framework. The results from 3-D numerical simulations of solar granulation can account for observed line profiles without the need for any microturbulence or macroturbulence (Asplund et al. 2000). Similar results have been found for Procyon (Gray 1982; Allende Prieto et al. 2002), which is also a star with well-known physical parameters (e.g. Kervella et al. 2004). However, hydrodynamic models of A-type stars do not yet reproduce the 'reversed' bisectors (Steffen et al. 2005).

6 Realistic Convection Models

None of the current 1-D models of convection are totally satisfactory, so what do 2-D and 3-D hydrodynamic simulations reveal?

A 2-D calibration of mixing-length was given by Ludwig et al. (1999), which was broadly in agreement with that found by the observational studies of convection mentioned earlier. Allende Prieto et al. (2002) presented line profile calculation in both 1-D and 3-D for Procyon, finding that the 3-D profiles were a better fit to the observations. Recently, 3-D simulations of mass mixing-length variations (Trampedach & Stein 2011) and granulation sizes and contrasts (Trampedach et al. 2013) show similar variations with $T_{\rm eff}$ and $\log g$.

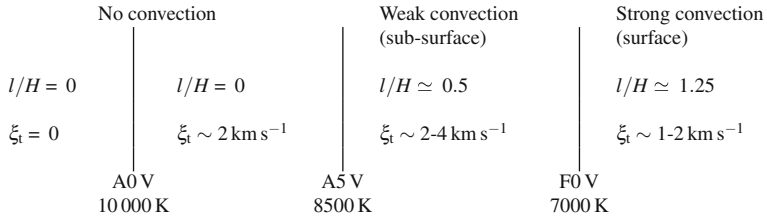

Fig. 7 The Convection Recipe for main-sequence stars from Smalley (2004)

Microturbulence and macroturbulence predictions from CO5BOLD 3-D stellar atmospheres (Steffen et al. 2009, 2013) give overall turbulence values close to the observed values for the Sun and Procyon, but microturbulence is slightly underestimated and macroturbulence is slightly overestimated.

Asteroseismology also has a role in improving our understanding of convection and turbulence. For example, Bonaca et al. (2012) in their analysis of *Kepler* data found a mixing-length lower than the Sun and that it increased with increasing [M/H]. Evidence has also been found for granulation in A-type stars (Kallinger & Matthews 2010; Balona 2011).

7 A Convection Recipe

Smalley (2004) presented a schematic variation of microturbulence and mixing length with T_{eff} for stars near the main sequence (Fig. 7). For stars hotter than A0 there is no convection or significant microturbulence. For early A-type stars the atmospheric temperature gradient is radiative, not because convection is absent, but because the convection simply carries almost none of the flux. There are velocity fields as indicated by the modest microturbulence values. These velocity fields increase as we go through mid to late A-type stars, and inefficient convection is required within the atmosphere. Once convection becomes efficient (F-type and later) the value of microturbulence is found to drop, while the mixing-length increases.

8 Summary

Convection and turbulence are parameterized in 1-D models via mixing-length, microturbulence and macroturbulence. While these are free parameters, they should not be and calibrations ought to be used in spectral analyses. Hydrodynamic 3-D models and detailed observations should be able to provide suitable prescriptions for these 1-D parameters.

References

Allende Prieto, C., Asplund, M., García López, R. J., & Lambert, D. L., ApJ, 567, 544 (2002).
Asplund, M., Nordlund, Å., Trampedach, R., Allende Prieto, C., & Stein, R. F., A&A, 359, 729 (2000).
Böhm-Vitense E (1958) Zeitschrift für Astrophysik 46:108
Balona LA (2011) MNRAS 415:1691
Bonaca A, Tanner JD, Basu S et al (2012) ApJL 755:L12
Bruntt H, Bedding TR, Quirion P-O et al (2010) MNRAS 405:1907
Canuto VM, Goldman I, Mazzitelli I (1996) ApJ 473:550
Canuto VM, Mazzitelli I (1996) ApJ 389:724
Canuto VM, Mazzitelli I (1991) ApJ 370:295
Castelli F, Gratton RG, Kurucz RL (1997) A&A 318:841
Chaffee FH Jr (1970) A&A 4:291
Coupry MF, Burkhart C (1992) A&AS 95:41
Dravins D (1987) A&A 172:200
Gómez Maqueo Chew, Y., Faedi, F., Cargile, P., et al., ApJ, 768, 79 (2013).
Gardiner RB, Kupka F, Smalley B (1999) A&A 347:876
Gray DF (1984) ApJ 281:719
Gray DF (1982) ApJ 255:200
Gray DF (1975) ApJ 202:148
Gray DF (2008) 2008 , 3rd edn. The Observation and Analysis of Stellar Photospheres, Cambridge University Press
Gray RO, Graham PW, Hoyt SR (2001) AJ 121:2159
Heiter, U., Kupka, F., van't Veer-Menneret, C., et al., A&A, 392, 619 (2002).
Kallinger T, Matthews JM (2010) ApJL 711:L35
Kervella P, Thévenin F, Morel P et al (2004) A&A 413:251
Kippenhahn R, Weigert A, Weiss A (2013) Stellar Structure and Evolution. Astronomy and Astrophysics Library, Springer-Verlag, Berlin Heidelberg
Kupka, F. In: Model Atmospheres and Spectrum Synthesis (Adelman, S. J., Kupka, F., Weiss, W. W. Eds.), ASP Conference Series, 108, p. 73 (1996).
Kurucz RL (2005) Mem. Soc. Astron. Ital. Suppl. 8:14
Landstreet JD (1998) A&A 338:1041
Landstreet JD, Kupka F, Ford HA et al (2009) A&A 503:973
Ludwig H-G, Freytag B, Steffen M (1999) A&A 346:111
Nissen PE (1981) A&A 97:145
Przybilla N, Butler K, Becker SR, Kudritzki RP (2006) A&A 445:1099
Shulyak D, Tsymbal V, Ryabchikova T, Stütz C, Weiss WW (2004) A&A 428:993
Smalley B, Gardiner RB, Kupka F, Bessell MS (2002) A&A 395:601
Smalley, B., In: The A-Star Puzzle (Zverko J., Žižnovský, J., Adelman, S. J. Eds.) Proc. IAU Symposium 224, p. 131 (2004).
Sousa SG, Santos NC, Israelian G et al (2011) A&A 526:A99
Steffen M, Caffau E, Ludwig H-G (2013) Mem. Soc. Astron. Ital. Suppl. 24:37
Steffen, M., Freytag, B., & Ludwig, H.-G., Proc. 13th Cambridge Workshop on Cool Stars, Stellar Systems and the Sun (Favata, F., Hussain, G. A. J., Battrick B. Eds.), ESA SP-560, p. 985 (2005).
Steffen M, Ludwig H-G, Caffau E (2009) Mem. Soc. Astron. Ital. 80:731
Struve O, Elvey CT (1934) ApJ 79:409
Trampedach R, Asplund M, Collet R, Nordlund Å, Stein RF (2013) ApJ 769:18
Trampedach R, Stein RF (2011) ApJ 731:78
Valenti JA, Piskunov N (1996) A&AS 118:595
Valenti JA, Fischer DA (2005) ApJS 159:141
van't Veer-Menneret, C., & Mégessier, C., A&A, 309, 879 (1996).

Diffusion and Its Manifestation in Stellar Atmospheres

Tatiana Ryabchikova

Abstract A short introduction to the diffusion process under mutual action of radiation acceleration and gravitational settling is given. In a stable stellar atmosphere diffusion develops significant abundance gradients (chemical stratification). The effects of stratification appear as changes in the observed spectral characteristics that are considered in the lecture.

Keywords Diffusion · Stars: atmospheres · Stars: fundamental parameters · Stars: abundances · Stars: chemically peculiar

1 Introduction

In a stellar atmosphere the atomic/molecular species absorb radiation and get the momentum characterized by radiative acceleration ($g_{\rm rad}$) that can be written as follows:

$$g_{\rm rad}(A_i) = \frac{4\pi}{c}\frac{1}{X_{A_i}}\int_0^\infty \kappa_\lambda(A_i) H_\lambda d\lambda \qquad (1)$$

where X_{A_i} is the mass fraction of ion A, $\kappa_\lambda(A_i)$ is the absorption coefficient of the species and H_λ is the monochromatic (Eddington) radiation flux. The line and continuum opacities are considered separately. There are other forces acting on species – gravitation, concentration gradients, etc. Trace elements diffuse in the atmosphere with the diffusion velocity approximated by the formula (see Burgers 1960):

T. Ryabchikova (✉)
Institute of Astronomy, Russian Academy of Sciences, Pyatnitskaya 48,
119017 Moscow, Russia
e-mail: ryabchik@inasan.ru

E. Niemczura et al. (eds.), *Determination of Atmospheric Parameters of B-, A-, F- and G-Type Stars*, GeoPlanet: Earth and Planetary Sciences,
DOI: 10.1007/978-3-319-06956-2_13,

$$V_i = D_i \left\{ \frac{\partial \ln c_i}{\partial r} + \frac{m_i}{kT} \left[g^i_{\rm rad} - \left(\frac{2A_i - Z_i - 1}{2A_i} \right) g \right] + (3.45 Z_i^2 - 0.82) \frac{\partial \ln T}{\partial r} \right\} \quad (2)$$

we consider here diffusion of trace elements relative to hydrogen in the stellar atmosphere and neglect the drag part between different kinds of particles. A_i, m_i, Z_i are the atomic weight, the mass, and the charge of the ion, g is the local gravity. The part in quadratic parentheses is called the effective acceleration $g^i_{\rm eff}$ and represents the combined effect of radiative, gravitational and electric forces on ion i. At different parts of the stellar atmosphere and envelope atom may be in different ionization stages, so the mean radiative acceleration is usually defined as a weighted mean:

$$g_{\rm rad} = \frac{\sum_i N_i D_i g^i_{\rm rad}}{\sum_i N_i D_i}, \quad (3)$$

where N_i and D_i are relative population of the ion i and its diffusion coefficient. One has to keep in mind that $g_{\rm rad}$ from Eq. 3 can be overestimated unless redistribution processes are taken into account (see Fig. 6 in Gonzalez et al. 1995). Depending on the competition between the gravitational and radiative accelerations an element either sinks or is pushed up in the stellar atmosphere.

2 Abundance Stratification in Stellar Atmospheres

The diffusion velocities are very small, $<1\,{\rm cm\,s^{-1}}$ (Michaud 1970); therefore, any mixing processes such as convection, meridional circulation, etc. easily prevent diffusion from creating abundance gradients. In what type of stars can we see the results of diffusion process? It may be observed in single white dwarfs where radiative levitation competes with the gravitational settling (Dreizler and Wolff 1999). In the cooler part of the Main Sequence (MS), stars have convective atmospheres; therefore, we cannot expect to see any traces of diffusion at work. Hotter MS stars have radiative atmospheres but they are usually fast rotators, which also destroys possible diffusion separation by meridional circulation. However, a fraction of A- and B-type stars have radiative atmospheres and slow rotation. These stars usually show abundance anomalies of different elements. In particular, chemically peculiar stars with global magnetic field (Ap stars) have the highest atmospheric anomalies observed. Magnetic fields seem to play a significant role in stabilizing the stellar atmosphere.

The first diffusion calculations (Michaud 1970; Michaud et al. 1976) predicted the overall abundance anomalies created by diffusion in stable atmospheres: underabundances of some light elements He, C, N, O, and overabundances of the elements with atomic mass >60. Later on, the calculations of equilibrium distributions of some elements through the atmosphere were carried out (see, for example, Borsenberger et al. 1981; Babel 1992, for Ca). Equilibrium distributions become established when diffusion velocities are zero for all elements. Time-dependent diffusion is not considered. The calculations show strongly inhomogeneous element

distribution produced by diffusion process. However, the model atmospheres were calculated with homogeneous abundances, although different from the solar ones. The first self-consistent diffusion models appeared at the turn of the 20th century (Dreizler and Wolff 1999; Hui-Bon-Hoa 2000). Stratifications of up to 39 chemical elements were calculated and included in iterative atmospheric modelling. The iterations continue until the model is converged. Magnetic field effects were also taken into account in diffusion calculations (Alecian and Stift 2010; Stift et al. 2012; Leblanc et al. 2009).

As mentioned above, theoretical calculations show an inhomogeneous abundance distribution in the stellar atmosphere. The predicted abundance profile depends on the effective temperature of the star and on the chemical element. An example of abundance profiles for models with effective temperatures of 8,000 and 12,000 K is shown in Fig. 1. The figure is analogous to Fig. 9 of Leblanc et al. (2009) and is produced from the models kindly presented to us by one of the co-authors, F. LeBlanc.

Figure 1 shows the equilibrium abundance distribution for two models with the effective temperatures of 8,000 and 12,000 K, which roughly limit the temperature region of Ap stars. For cooler stars an abundance profile for all considered elements has a step-like shape with a predominant concentration of the elements near the photosphere, sharp abundance decrease in narrow range of optical depths $-1 \leq \log \tau_{5000} \leq 0$, and strong depletion of the element in the upper atmospheric layers. In such a chemically inhomogeneous atmosphere we would derive different abundances from spectral lines formed at different optical depths, when performing a classical abundance analysis based on a chemically homogeneous model atmosphere. According to self-consistent diffusion calculations (see Fig. 1 in Ryabchikova 2008), the abundance jump decreases and moves towards the upper layers with the rise of effective temperature. At certain temperatures an element distribution tends to become quasi-homogeneous with high element overabundance at least in the line formation region (see bottom panel of Fig. 1). For elements like Cr and Ti, with relatively low cosmic abundance, diffusion calculations simply show maximal supported abundance allowed in calculations. Therefore, in hot Ap stars classical abundance analysis gives the same high element abundance for all individual lines independent of their formation depth. Strong lines with the developed wings, like Ca II resonance lines and IR-triplet lines in cool stars, would show a significant distortion of line profile because they are formed over the large part of the stellar atmosphere. Do we observe such effects in Ap stars?

3 Manifestation of Abundance Stratification in Stellar Atmospheres

First, let us consider the temperature behaviour of the average abundances for chemically peculiar and normal stars. Ryabchikova (2005) collected data for elements Si, Ca, Cr, and Fe for a set of stars in the temperature range 6,500–16,000 K. Data for Cr and Fe taken from Ryabchikova (2005) and supplemented by a few more

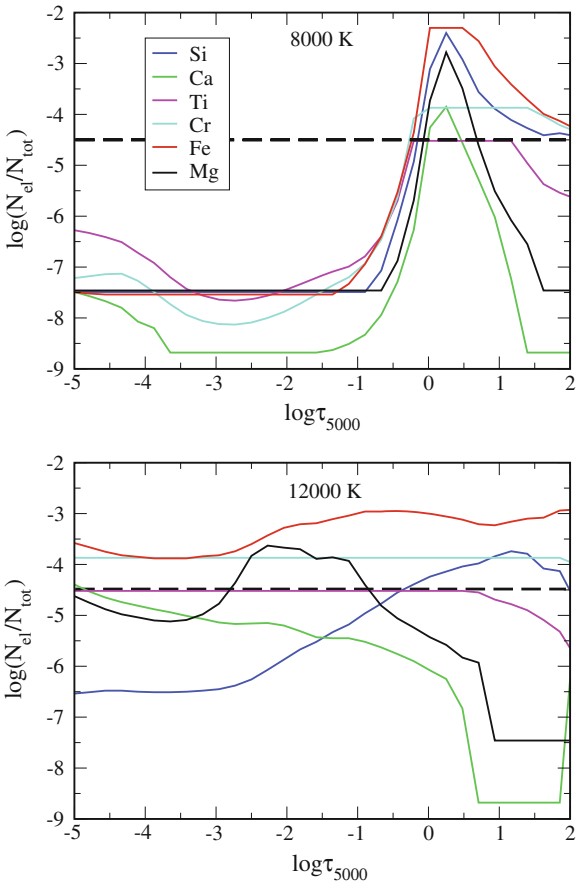

Fig. 1 The abundances of elements Mg, Si, Ca, Ti, Cr, Fe as a function of optical depth for self-consistent diffusion models with effective temperatures of 8,000 K (*top panel*) and 12,000 K (*bottom panel*). Surface gravity $\log g = 4.0$ was used in both models. *Dashed lines* indicate the solar Fe abundance

points from recent analyses are plotted versus effective temperature in Fig. 2 using black filled circles (Ap stars) and asterisks (normal and superficially normal stars). On the same plot we put theoretical points (open red squares) derived in the following way. We take a set of self-consistent diffusion models, kindly provided to us by Leblanc (see Leblanc and Monin 2004), and calculate synthetic spectra. Then, using these spectra as the observations, we carry out a classical abundance analysis based on equivalent widths/spectral synthesis and on the model atmosphere with the same parameters as diffusion model but calculated with homogeneous abundances (e.g., ATLAS9). One can see that the resulting average abundances and their dispersions are equivalent to those observed in real stars. We obtain the same rapid increase of average abundances with effective temperature, that gives us strong support for diffusion process operating in Ap star atmospheres.

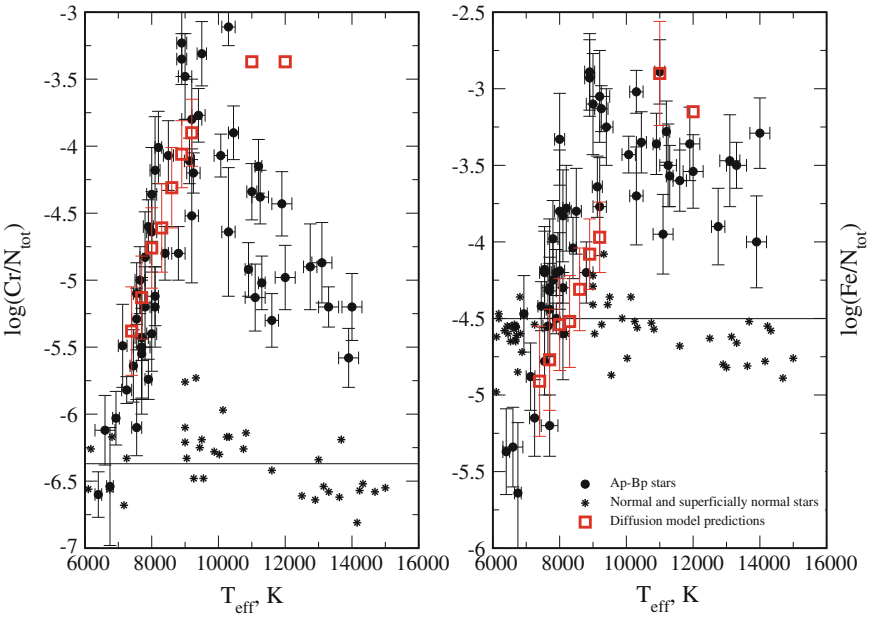

Fig. 2 Observed average Cr and Fe abundances in Ap (*black filled circles*) and normal (*asterisks*) stars as a function of $T_{\rm eff}$. Solar abundances are shown by *horizontal lines*. Calculated average abundance for a set of self-consistent diffusion models (see text) are shown by *open red squares*

While in hotter Ap stars element stratification results in the observed strong average overabundance of Cr and Fe, in cooler stars the inhomogeneous abundances distribution shown in Fig. 1 (upper panel) causes changes in the profile of strong spectral lines with developed wings. Different parts of a strong line are formed at different atmospheric layers with very different abundances created by diffusion. As a result we cannot fit the full observed line profile in Ap stars with the homogeneous abundance distribution. The best case for illustration is the resonance Ca II 3,933 Å line. Observations of this line in spectra of two stars of the same effective temperature of 7,650 K are shown in Fig. 3. In the spectrum of Am star HD 24711 the Ca II 3,933 Å line is perfectly fitted by theoretical calculations with the homogeneous Ca abundance, while in the Ap star HD 176232 (10 Aql) it is not. The observed line core is much narrower and the observed wings are much stronger compared to the theoretical line profile (blue dashed line). The observed line profile is perfectly represented by the theoretical one calculated with the Ca abundance distribution derived in course of stratification analysis (see Fig. 4, right plot).

4 Methods of Stratification Analysis

There are a few practical methods of stratification analysis. One may calculate the depth of formation of spectral lines in a chemically homogeneous atmosphere and look at the dependence of individual abundances on optical depth. In a stratified

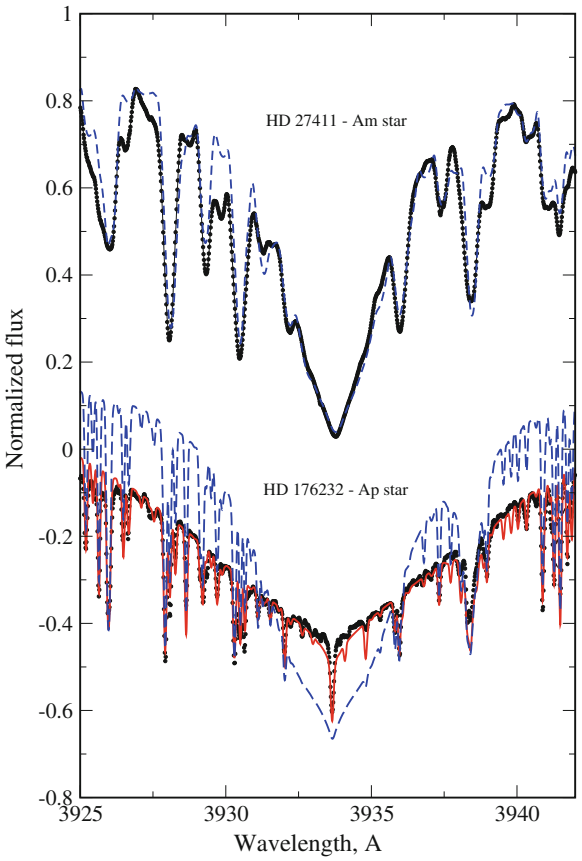

Fig. 3 Ca II 3,933 Å line profile in the spectra of Am (*top*) and Ap (*bottom*) stars with the similar $T_{\rm eff} = 7{,}650$ K. Observations are shown by *black filled circles*, theoretical line profile with homogeneous Ca abundance is shown by the *blue dashed-line*, and theoretical line profile calculated with Ca stratification is shown by the *solid red line*

atmosphere a trend will appear, which may be estimated and compared to the theoretical predictions. This approach was employed for iron stratification analysis in the atmospheres of blue horizontal-branch stars (Khalack et al. 2010; Leblanc et al. 2010).

A more general approach is based on the theoretical shape of the abundance profile. Babel (1992) showed that, as predicted by diffusion, Ca abundance distribution has step-like form. This step-function approximation for stratification analysis was implemented in a special code DDAFIT written by O. Kochukhov in IDL language (see Ryabchikova et al. 2005). For a carefully chosen set of observed spectral lines formed at different optical depths, the code searches for an abundance distribution that provides the best fit to all observed lines. Vertical abundance distribution is described with four parameters: chemical abundance in the upper atmosphere,

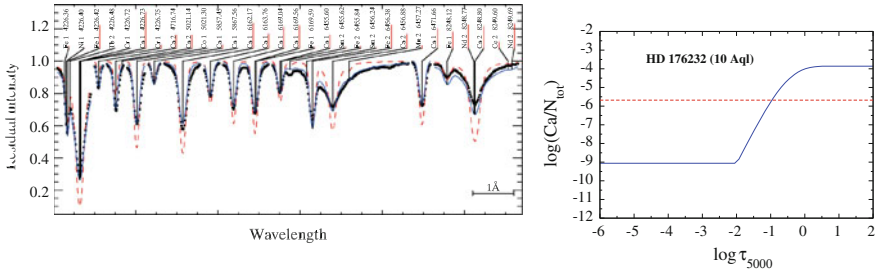

Fig. 4 Comparison of the observed Ca line profiles in spectrum of Ap star HD 176232 (10 Aql) and calculated with homogeneous (*red dashed-line*) and stratified (*blue solid-line*) Ca distribution. Homogeneous and stratified Ca abundance is shown in *right panel*. Stratification solution is obtained with DDAFIT code

abundance in deep layers, the depth position of abundance step in the atmosphere and the width of the transition region where chemical abundance changes between the two values. All four parameters are optimized simultaneously with the least-squares fitting routine. DDAFIT is successfully applied to stratification analysis of different chemical elements in the atmospheres of Ap stars. For example, it was employed in the Ca distribution study in the atmospheres of 23 Ap stars (Ryabchikova et al. 2008), where not only general Ca stratification but also an isotopic separation was found. It was shown that while the main ^{40}Ca isotope is accumulated near the photospheric layers, the heavier isotopes replace it in the upper atmospheric layers. One of the examples of Ca abundance distribution derived in Ryabchikova et al. (2008) is presented in Fig. 4. Note that a fit to the Ca II 3,933 Å line in the spectrum of 10 Aql shown in Fig. 3 is obtained with this Ca distribution.

An important application of stratification analysis is the construction of self-consistent empirical atmospheric models of Ap stars. An initial element stratification is derived from the observations using the chemically homogeneous models. This stratification is considered as an input parameter for further iterations. The next step is model calculation with the initial element stratification, performed with model atmosphere code LLMODELS (Shulyak et al. 2004). A recalculated model is employed for the second stratification iteration and so on. The procedure repeats until convergence is achieved. The self-consistent empirical modelling allows to improve significantly the atmospheric parameters and to derive rather accurate fundamental parameters of cool bright roAp stars from the comparison between theoretical and observed energy distributions (see, for example, Shulyak et al. 2013).

Acknowledgments This work was partially supported by Praesidium RAS Program "Non-stationary Phenomena in Objects of the Universe".

References

Alecian G, Stift MJ (2010) A&A 516:A53
Babel J (1992) A&A 258:449
Borsenberger J, Michaud G, Praderie F (1981) ApJ 243:533
Burgers JM (1960) Plasma dynimics. In: Clauser FH (ed) Addison-Wesley Publishing Company, Boston, p 119
Dreizler S, Wolff B (1999) A&A 348:189
Gonzalez J-F, LeBlanc F, Artru M-C, Michaud G (1995) A&A 297:223
Hui-Bon-Hoa A, LeBlanc F, Hauschildt PH (2000) ApJ 535:L43
Khalack VR, Leblanc F, Behr BB (2010) MNRAS 407:1767
Leblanc F, Hui-Bon-Hoa A, Khalack VR (2010) MNRAS 409:1606
Leblanc F, Monin D (2004) Modelling of stratified atmospheres of CP-stars. In: Zverko J, Ziznovsky J, Adelman SJ, Weiss WW (eds) IAU symposium 224, The A-Star Puzzle Proceedings, Cambridge University Press, p 193
Leblanc F, Monin D, Hui-Bon-Hoa A, Hauschildt PH (2009) A&A 495:937
Michaud G (1970) ApJ 160:641
Michaud G, Charland Y, Vauclair S, Vauclair G (1976) ApJ 210:447
Ryabchikova TA (2005) Astron Lett 31:388
Ryabchikova TA (2008) Contrib Astron Obs Scalnate Pleso 38:257
Ryabchikova T, Leone F, Kochukhov O (2005) A&A 438:973
Ryabchikova T, Kochukhov O, Bagnulo S (2008) A&A 480:811
Shulyak D, Tsymbal V, Ryabchikova T, Stütz Ch, Weiss WW (2004) A&A 428:993
Shulyak D, Ryabchikova T, Kochukhov O (2013) A&A 551:A14
Stift MJ, Alecian G (2012) MNRAS 425:2715

Basics of the NLTE Physics

Jiří Kubát

Abstract The basic assumptions of the NLTE approximation in stellar atmospheres are summarized. The assumptions of thermodynamic equilibrium, local thermodynamic equilibrium (LTE), and non-LTE (NLTE) are compared. It is emphasized that LTE is a poor approximation if radiative transitions dominate in stellar atmospheres. The equations of kinetic equilibrium and methods of their solution are discussed.

Keywords Radiation mechanisms: general · Radiation mechanisms: non-thermal · Atomic processes · Radiative transfer · Stars: atmospheres

1 Introduction

Let us assume that using some spectrograph and telescope we have observed a stellar spectrum, and that we have reduced it using some data reduction software. Such spectrum is ready for its analysis. If we decide to do a model atmosphere analysis of this spectrum, we need to proceed in several steps using different kinds of software. First, we have to calculate a model atmosphere (spatial distribution of temperature, density, and occupation numbers), which can be done using the assumption of local thermodynamic equilibrium (LTE), for example using the popular code ATLAS9 (Kurucz 1993), or without this restrictive assumption allowing the atomic level population to differ from their equilibrium values (the so-called NLTE), which can be done using the code TLUSTY (Hubeny 1988). With the model atmosphere calculated we then have to determine the detailed emergent spectrum. This can be done using spectral synthesis codes (like SYNTHE associated with ATLAS9 or SYNSPEC associated with TLUSTY), which calculate the formal solution of the radiative transfer equation for

J. Kubát (✉)
Astronomický ústav AV ČR, Fričova 298, 251 65 Ondřejov, Czech Republic
e-mail: kubat@sunstel.asu.cas.cz

E. Niemczura et al. (eds.), *Determination of Atmospheric Parameters of B-, A-, F- and G-Type Stars*, GeoPlanet: Earth and Planetary Sciences,
DOI: 10.1007/978-3-319-06956-2_14,

as many frequencies as we need, so that an accurate theoretical emergent stellar radiation is obtained. The final step of the analysis is a comparison of the theoretical spectrum with observations, which can also be done using a computer code.

It is clear that for each step of this procedure different computer codes are used. Unfortunately, some users focus mostly to the last step (comparison of observations with the theoretical spectrum) and they are satisfied when any theoretical spectrum fits observations. They do not care about the details of model atmosphere calculations and associated assumptions. However, a good fit of a simplified model does not necessarily mean that the simplification is acceptable. Taking into account more accurate physics generally leads to better models. Switching from the assumption of LTE to the assumption of NLTE is such a step towards better models. Particular steps in the above mentioned spectrum analysis are influenced differently if LTE or NLTE are assumed. The initial step of model atmosphere calculation strongly depends on the assumption of LTE or NLTE. Spectral synthesis is dependent on the initial step, since data input to the code is more complex for the NLTE case. The comparison step is the same if we used the NLTE model or not.

In this chapter we shall discuss the physical and microscopic bases of the assumption of NLTE in greater detail.

2 Microscopic Distributions

Solution of the stellar atmosphere problem can be considered as the determination of spatial dependence of basic macroscopic quantities (see e.g. Mihalas 1978; Hubeny and Mihalas 2014 and references therein). It can also be understood (following Hubený 1976) as searching for basic microscopic distributions, namely, the momentum distribution (which is equivalent to the distribution of velocities of all particles), distribution of particle internal degrees of freedom (i.e. populations of atomic excitation stages), and distribution of internal degrees of freedom of the electromagnetic field (which is the radiation field for all frequencies and directions). Several different approximations may be applied to determination of these distributions.

2.1 Thermodynamic Equilibrium

In thermodynamic equilibrium, all these three distributions have their equilibrium values. A system in thermodynamic equilibrium experiences no changes when it is isolated. By relaxation time we understand time necessary for the system to return back to equilibrium from a perturbed state. Macroscopic changes have to be slower with respect to relaxation time.

In thermodynamic equilibrium, the radiation field has the Planck distribution and velocities of particles follow the Maxwell distribution. Individual atomic energy levels (states) are populated according to the Boltzmann distribution

$$\frac{n^*_{i,j}}{n^*_{0,j}} = \frac{g_{i,j}}{g_{0,j}} \mathrm{e}^{-\frac{\chi_{0i,j}}{kT}}. \tag{1}$$

When Eq. (1) is applied to the ground levels of two successive ions, it describes the ionization equilibrium (the Saha equation),

$$\frac{n^*_{0,j+1}}{n^*_{0,j}} = \frac{2g_{0,j+1}}{g_{0,j}} \frac{1}{n_\mathrm{e}} \left(\frac{2\pi m_\mathrm{e} kT}{h^2} \right)^{\frac{3}{2}} \mathrm{e}^{-\frac{\chi_{I,j}}{kT}}. \tag{2}$$

In these equations, T is temperature, m_e is the electron mass, n_e is the electron number density, $n^*_{i,j}$ is the equilibrium population and $g_{i,j}$ is the statistical weight of the level i of the ion j (similarly for $i = 0$, the ground level), $\chi_{0i,j}$ is the excitation energy of the level i from the ground level, $\chi_{I,j}$ is the ionization energy of the ground state of the ion j, h is the Planck constant, and k is the Boltzmann constant. Expressions for these distributions, as well as discussion about influence of individual processes on maintenance of equilibrium distributions, are presented also in Kubát (2010), together with references to literature.

However, thermodynamic equilibrium cannot be used for a description of the stellar atmosphere. As it is evident from observations of stellar spectra, the stellar radiation does not obey the Planck distribution.

2.2 Local Thermodynamic Equilibrium

To describe the stellar atmosphere, which is the transition from the dense and hot star to almost void and cold interstellar medium, we have to introduce the possibility of depth-dependent density and temperature in the stellar atmosphere. This also allows the radiation to escape from the stellar atmosphere.

To preserve the advantages of the thermodynamic equilibrium, we introduce the *local thermodynamic equilibrium*, where we assume a Maxwell distribution of particle velocities and a Saha-Boltzmann distribution of excitation and ionization states to be valid locally using local values of temperature T and electron density n_e. Thus the atomic energy level populations are calculated after Eqs. (1) and (2). The radiation field is no longer in equilibrium (does not have Planck distribution). It has to be determined by solution of the radiative transfer equation. However, the assumption of local thermodynamic equilibrium allows to use the equilibrium source function, which is equal to the Planck function.

2.3 Kinetic Equilibrium (NLTE or non-LTE)

The assumption of kinetic equilibrium (see Hubeny and Mihalas 2014) is more general than the assumption of local thermodynamic equilibrium. In kinetic equilibrium

we determine the radiation field by solution of the radiative transfer equation and we use the exact source function. Populations of individual atomic levels are calculated using equations of kinetic equilibrium (which include the non-local influence of radiation on level populations), and the particle velocities are assumed to be in equilibrium (Maxwell distribution). This approximation is usually called non-LTE or NLTE, which looks like negation of equilibrium. This is evidently not true, since in this "non-equilibrium" there are still particle velocities in equilibrium. Even more confusing is the expansion of the acronym LTE, which gives "non-local thermodynamic equilibrium", which is also far from the reality. More exactly, by non-LTE we understand *any* state that departs from LTE. Therefore, it is better to follow Hubeny and Mihalas (2014) and call this approximation *kinetic equilibrium*, in contrast to the commonly used (but inexact) term *statistical equilibrium*. Since the acronym NLTE is commonly used for this approximation, we shall use it also in this chapter.

How close the distribution of excitation states comes to the equilibrium one, depends on a balance between radiative and collisional processes. If the collisional processes dominate, then the distribution is close to the equilibrium one. On the other hand, if radiation processes dominate, then the distribution may differ from the equilibrium one significantly. In NLTE, no assumption is made about the source function, which is consistently calculated from actual opacities and emissivities.

Generally, collisional processes tend to establish equilibrium (since particles have equilibrium velocity distributions), while radiative processes tend to destroy it if radiation field is not in equilibrium (which is the case in stellar atmospheres).

A detailed discussion of individual processes may be found in Kubát (2010, see Table 1).

2.4 Basic Comparison of LTE and NLTE

Both in the local thermodynamic equilibrium (LTE) and in the kinetic equilibrium (NLTE) cases the Maxwellian (equilibrium) distribution of particle velocities is assumed. Frequent elastic collisions between particles preserve the equilibrium velocity distribution. Inelastic collisions tend to destroy it; however, if the number of elastic collisions between two inelastic collisions is very large, any deviation from equilibrium caused by inelastic collision is quickly compensated and equilibrium is preserved. In other words, for an equilibrium velocity distribution it is necessary that the relaxation time be much shorter than the time between inelastic collisions. Since this condition is fulfilled in most cases in stellar atmospheres, we assume in the following that the particle distribution is Maxwellian (equilibrium).

The basic difference between LTE and NLTE is the behaviour of calculated atomic level populations. The approximation of LTE allows their relatively very simple and fast calculation using the Saha-Boltzmann distribution (Eqs. 1 and 2). The NLTE approximation takes into account the fact that the level populations are influenced by the radiation field. In this case, the populations have to be determined by the equations of kinetic equilibrium (Eqs. 3 or 4 later in this chapter).

It is the balance between several types of microscopic processes, which tells us how exact (or inexact) the assumption of LTE is. The validity of the LTE approximation is determined by a competition between collisional and radiative processes. The radiative processes tend to destroy the equilibrium distributions (if the radiation field is not in equilibrium), while the inelastic collisions tend to establish an equilibrium distribution of excitation states, however, provided that the elastic collisions are even more frequent than the inelastic ones. As collisional processes we may consider processes where more than one particle (electron, ion, but not a photon) take part. A special case is radiative recombination, which is a radiative process (radiation is emitted), but a collision of two particles (namely an ion and an electron) must happen. For a more detailed list of microscopic processes see Table 1 in Kubát (2010).

The necessary microscopic condition for the validity of LTE is the condition of *detailed balance*, which means that rates of all processes are balanced by rates of their reverse processes. If the equilibrium particle velocities distribution holds, then also collisional excitation and ionization processes are in detailed balance. However, the radiative processes are in detailed balance only if the radiation field is in equilibrium, i.e. if it obeys the Planck distribution. If the mean intensity of the radiation field $J(\nu) \neq B(\nu)$, we can not reach detailed balance in radiative transitions. Since in stellar atmospheres the radiation field *is generally not* in equilibrium, detailed balance cannot be achieved if radiative transitions dominate, and, consequently, LTE is a poor approximation there. Illustrative discussion may be found in Mihalas and Athay (1973).

3 Equations of Kinetic Equilibrium

The general form of kinetic equilibrium equations for the state (energy level) i is (Mihalas 1978, Eq. (5–48), see also Hubeny and Mihalas 2014)

$$\frac{\partial n_i}{\partial t} + \nabla \cdot (n_i \mathbf{v}) = \sum_{\substack{l=1 \\ l \neq i}}^{L} (n_l P_{li} - n_i P_{il}) \,, \tag{3}$$

$(i = 1, \ldots, L)$, where L is the total number of energy levels considered, and $n_i P_{il}$ is the number of transitions per time unit from the state i to the state l (which includes both line and continuum transitions). The quantity P_{il} is the transition rate.[1] It can be expressed as a sum, $P_{il} = R_{il} + C_{il}$, where R_{il} is the rate of the transition caused by absorption or emission of radiation, and C_{il} is the rate of the transition caused by a collision with a neighbouring particle, mostly with an electron. While the

[1] Note that sometimes $n_i P_{il}$ is called the rate. Here we prefer to use the notation consistent with the textbook of Hubeny and Mihalas (2014).

collisional rates depend only on local values of electron density n_e and temperature T, the radiative rates depend also on the radiation field, which is non-local. Detailed expressions for both collisional and radiative rates are listed in Chap. 16. Multiplying Eq. (3) by mass of the corresponding particle and summing all such equations over all energy levels of all species we obtain the continuity equation $\partial\rho/\partial t + \nabla\cdot(\rho\mathbf{v}) = 0$.

For the case of a static atmosphere ($\mathbf{v} = 0$) in a steady state ($\partial/\partial t \to 0$), we may neglect both the time derivative and the advective term in Eq. (3) and we obtain the time independent set of the kinetic equilibrium equations for a static medium,

$$\sum_{\substack{l=1\\ l\neq i}}^{L} (n_l P_{li} - n_i P_{il}) = 0. \tag{4}$$

However, this equation is commonly used not only for static atmospheres, but the advective term is very often neglected also for expanding stellar envelopes.

3.1 Equilibrium Level Populations

If we want to measure how much the population numbers differ from their LTE values, we use the departure coefficients (b-factors) $b_{i,j} = n_{i,j}/n^*_{i,j}$ (Menzel 1937), which relate actual ($n_{i,j}$) and equilibrium ($n^*_{i,j}$) populations of the level i of the ion j.

There are two ways how to define the equilibrium populations. The first one is the natural one. The equilibrium populations in the whole stellar atmosphere are calculated using Saha-Boltzmann distributions using temperature and density distributions obtained also for the assumption of local thermodynamic equilibrium.

On the other hand, Mihalas (1978) uses the quantity $n^*_{i,j}$ in a different meaning. The LTE populations are calculated with respect to the population of the ground level of the next higher ion using the Eq. (5-14) in Mihalas (1978), which follows from Eqs. (1) and (2),

$$n^*_{i,j} = n_{0,j+1} n_e \frac{g_{ij}}{g_{0,j+1}} \frac{1}{2} \left(\frac{h^2}{2\pi mkT}\right)^{\frac{3}{2}} \mathrm{e}^{-\frac{\chi_{Ij}-\chi_{ij}}{kT}}. \tag{5}$$

Here $n_{0,j+1}$ is the *actual* population of the ground level of the next higher ion, which does not need to be an LTE value. This definition of the LTE value of population numbers reflects the fact that the radiative recombination is an equilibrium process, because the ionization transitions from the highest levels of each ion j are close to detailed balance.

3.2 System of Kinetic Equilibrium Equations

For each atom, the kinetic equilibrium Eq. (4) can be written as

$$n_i \sum_{\substack{l=1 \\ l \neq i}}^{L} (R_{il} + C_{il}) - \sum_{\substack{l=1 \\ l \neq i}}^{L} n_l \, (R_{li} + C_{li}) = 0, \tag{6}$$

where $i = 1, \ldots, L$ and L is the total number of atomic energy levels considered. For each atom, the system of equations is linearly dependent. We have to replace one of the equations by a 'closing equation', which sets the total atom particle density and thus makes the system linearly independent. For model atmosphere calculations we can use the charge conservation equation, which compares the total charge of all ions included in kinetic equilibrium with the charge of electrons. Alternatively, the particle conservation equation may be used. This equation uses the total number density and thus fixes the total number of particles involved. If more atoms are included in the equations of kinetic equilibrium, an additional abundance equation is used as a closing equation. Kinetic equilibrium equations for each independent atom have to be closed by one such equation. These equations are listed in Kubát (2010).

The full set of kinetic equilibrium equations can be formally written as

$$\mathscr{A} \cdot \mathbf{n} = \mathscr{B}, \tag{7}$$

where $\mathbf{n} = (n_1, \ldots, n_L)$ is a vector of all populations, the matrix $\mathscr{A}$ contains all the rates included (it is called the rate matrix) and the right hand side vector $\mathscr{B}$ is 0 except rows with conservation laws.

3.3 Solution of the System of Kinetic Equilibrium Equations

For given $\mathscr{A}$ and $\mathscr{B}$, Eq. (7) is a set of linear equations with a straightforward solution. However, the rate matrix $\mathscr{A}$ depends on the radiation field. As a consequence, we have to solve the set of equations of kinetic equilibrium *simultaneously* with the radiative transfer equation for all frequencies considered. This is a non-linear system of equations. There is a simple iteration scheme, which consists of subsequent solution of the radiative transfer equation for given opacity and emissivity (the formal solution of the radiative transfer equation) and solution of the equations of kinetic equilibrium for given radiation field. However, this iteration scheme, known as the Λ-iteration, does not work for stellar atmospheres. More precisely, it converges so slowly that it is unusable for media which are optically thick at some frequency. Illustrative examples can be found in Auer (1984). Consequently, different iteration schemes must be used. It may be either the multidimensional Newton-Raphson method (introduced to mode ling of stellar atmospheres by Auer and Mihalas (1969), and usually referred to as the

complete linearisation method) or the *accelerated* Λ*-iteration technique* (introduced to radiative transfer by Cannon 1973a, b), which differs from the ordinary lambda iteration by using the approximate lambda operator. This operator allows simultaneous solution of the equations of kinetic equilibrium together with the approximate radiative transfer equation with a subsequent exact solution of the radiative transfer as a correction term. Useful reviews of accelerated lambda iteration methods were published by Hubeny (1992, 2003). These solution methods may be used also for the generalized problem of calculation of a full NLTE model atmosphere, where additional equations of radiative and hydrostatic equilibrium are simultaneously solved.

4 Summary

The acronym NLTE (or non-LTE) denotes deviation from LTE which in stellar atmospheres means that:

- the radiation field is not in thermodynamic equilibrium; its intensity has to be determined from the radiative transfer equation,
- excitation and ionization state of matter is not in thermodynamic equilibrium; the level populations have to be determined from equations of kinetic equilibrium,
- equations of radiative transfer and kinetic equilibrium have to be solved *simultaneously* because they are coupled,
- particle velocities are in thermodynamic equilibrium; they obey Maxwell distribution.

This approximation gives significantly better and more exact description of reality than the "standard" approximation of LTE.

Acknowledgments The author would like to thank Dr. Ewa Niemczura for inviting him to the Spring School of Spectroscopic Data Analyses in Wrocław. He is also grateful to both referees (Ivan Hubeny and the anonymous one) for their invaluable comments. This work was partly supported by the project 13-10589S of the Grant Agency of the Czech Republic (GA ČR).

References

Auer LH (1984) Difference equations and linearisation methods for radiative transfer. In: Kalkofen W (ed) Methods in radiative transfer. Cambridge University Press, Cambridge, p 237

Auer LH, Mihalas D (1969) ApJ 158:641

Cannon CJ (1973a) J Quant Spectrosc Radiat Transf 13:627

Cannon CJ (1973b) ApJ 185:621

Hubený I (1976) Problematika teoretického popisu hvězdných atmosfér. PhD thesis, Astronomický ústav ČSAV Ondřejov

Hubeny I (1988) A computer program for calculating non-LTE model stellar atmospheres. Comput Phys Commun 52:103

Hubeny I (1992) Accelerated lambda iteration (review). In: Heber U, Jeffery CS (eds) The atmospheres of early-type stars. Lecture notes in physics, vol 401. Springer, Berlin, p 377
Hubeny I (2003) Accelerated lambda iteration: an overview. In: Hubeny I, Mihalas D, Werner K (eds) Stellar atmosphere modelling, vol 288. Astronomical Society of the Pacific Conference Series, p 17
Hubeny I, Mihalas D (2014) Theory of stellar atmospheres. Princeton University Press, Princeton and Oxford (in press)
Kubát J (2010) Statistical equilibrium equations for trace elements in stellar atmospheres. In: Monier R, Smalley B, Wahlgren G, Stee P (eds) Non-LTE line formation for trace elements in Stellar atmospheres, vol 43. EDP Sciences, EAS Publications Series, Les Ulis, p 43
Kurucz RL (1993) ATLAS9 stellar atmosphere programs and 2 km/s grid. In: Kurucz RL (ed) Kurucz CD-ROM vol 13. Smithsonian Astrophysical Observatory, Mass, Cambridge
Menzel DH (1937) ApJ 85:330
Mihalas D (1978) Stellar atmospheres, 2nd edn. W. H. Freeman & Co., San Francisco
Mihalas D, Athay RG (1973) Ann Rev A&A 11:187

NLTE Analysis of Spectra: OBA Stars

Jiří Kubát and Brankica Šurlan

Abstract Methods of calculation of NLTE model atmosphere are discussed. The NLTE trace element procedure is compared with the full NLTE model atmosphere calculation. Differences between LTE and NLTE atmosphere modelling are evaluated. The ways of model atom construction are discussed. Finally, modelling of expanding atmospheres of hot stars with winds is briefly reviewed.

Keywords Stars: atmospheres · Stars: winds, outflows · Radiative transfer · Atomic processes · Radiation: dynamics

1 Introduction

As hot stars we usually consider stars of spectral types A, B, and O. These stars are hotter than about 8,500 K (this temperature value depends on who is classifying them); they are also more massive and have several times larger radius than the Sun. Their spectra may be characterized by fewer spectral lines than cool stars, and by the absence of molecular lines, which is given by their higher temperature. Also thanks to temperature the major convection zone caused by hydrogen ionization is absent in their atmospheres. In addition, strong NLTE effects appear in their atmospheres, which influence not only line formation, but the whole atmospheric structure.

However, they also differ depending on their spectral type. The atmospheres of A-type stars are usually very quiet, with almost total absence of atmospheric motions. Consequently, specific phenomena like chemical stratification of their atmospheres

J. Kubát (✉) · B. Šurlan
Astronomický ústav AV ČR, Fričova 298, 251 65 Ondřejov, Czech Republic
e-mail: kubat@sunstel.asu.cas.cz

B. Šurlan
Matematički Institut SANU, Kneza Mihaila 36, 11001 Beograd, Republic of Serbia
e-mail: surlan@sunstel.asu.cas.cz

E. Niemczura et al. (eds.), *Determination of Atmospheric Parameters of B-, A-, F- and G-Type Stars*, GeoPlanet: Earth and Planetary Sciences,
DOI: 10.1007/978-3-319-06956-2_15,

may develop. This is also the reason for strong chemical peculiarities found in many of them. The atmospheres of B-type stars are less quiet, and macroscopic atmospheric motions start to appear there. These stars are very often rapidly rotating, which causes development of circumstellar envelopes and emission lines in their spectra (the case of Be stars). On the other hand, many stars of this type are pulsating (e.g. the β Cep type stars), some even show non-radial pulsations. The O-type stars are typified by strong stellar winds, which cause specific emission lines (with P-Cygni type profiles) in their spectra. For all these spectral types, NLTE effects are essential for both atmospheric structure and line formation.

Consequently, the NLTE approach for analysis of their spectra is inevitable. There are two basic possibilities to calculate stellar atmosphere models with the departures from LTE. The first and consistent one is calculation of full NLTE model atmospheres including all chemical elements. However, this option is still computationally prohibitive, so we usually restrict the number of chemical elements and include only those which are important for the determination of the atmospheric structure. The second option is to solve the NLTE line formation problem for a particular atom or ion (called a trace element) for a given (i.e. fixed) model atmosphere. This model may be calculated assuming either LTE or NLTE. The former option saves significant amount of time necessary for calculations. On the other hand, LTE model atmospheres are physically inconsistent (Mihalas 1978; Hubeny and Mihalas 2014).

2 Trace Elements

Solution of a NLTE line formation problem for trace elements is a two-step solution.

The first step is a calculation of the model atmosphere, which includes only those elements and their transitions which are important for determination of the atmospheric structure, specifically continua of abundant elements and strong atomic lines. Many weaker lines in the optical region may be omitted in this step, since their influence on the atmospheric structure is negligible. This model atmosphere may assume either LTE or NLTE; however, a NLTE model atmosphere should be in principle always preferred in this step.

Having a model atmosphere we solve a NLTE line formation problem, i.e. simultaneous solution of the radiative transfer equation and the equations of statistical equilibrium for a selected element (the *trace element*). Since the model atmosphere (i.e. the full structure) is not solved in this step, the model atom may be very detailed and include many lines and continua important for formation of lines of this elements.

Several conditions have to be fulfilled to allow us to consider a particular element as a trace element. First of all, its influence on the atmospheric structure has to be negligible. Also the opacity of the trace element has to be negligible compared to the opacity of non-trace elements, or NLTE effects on opacities of this element have negligible influence on the atmospheric structure. Trace element also should not be a significant source of free electrons. Simply stating, any detailed trace element calculation *must not* influence the other elements. If this happens, we have to improve

the background model. An example of a trace element may be, e.g. argon in B-type stars (Lanz et al. 2008). These authors used fully blanketed NLTE model atmospheres as background models, which is the best available option. More discussion about NLTE for trace elements can be found in Monier et al. (2010).

3 Full NLTE Model Atmospheres

Calculation of a full NLTE model atmosphere is a task which, from basic global stellar parameters like effective temperature (or luminosity), mass and radius, determines spatial distribution of temperature, density, ionization states, electron density, velocity, etc.

We would like to emphasize that the resulting model atmospheres may differ significantly from the LTE solution, as has already been clearly shown by Auer and Mihalas (1969a).

3.1 Solution of a NLTE Model Atmosphere

Solution of a NLTE model atmosphere means determination of distributions of macroscopic quantities in the stellar atmosphere for given global parameters describing stellar luminosity L_*, mass M_*, and radius R_*. It is achieved via a solution of a system of equations describing physical properties of the atmosphere. We demonstrate these equations for a specific case of the static plane-parallel NLTE model atmosphere. These equations include the equation of radiative transfer, which determines the radiation field described using its specific intensity $I_{\mu\nu}$,

$$\mu \frac{\mathrm{d}I_{\mu\nu}}{\mathrm{d}z} = \eta_\nu - \chi_\nu I_{\mu\nu}, \tag{1}$$

the equations of statistical equilibrium determining atomic level populations n_i,

$$n_i \sum_l \left(R_{il} + C_{il}\right) + \sum_l n_l \left(R_{li} + C_{li}\right) = 0, \tag{2}$$

the equation of hydrostatic equilibrium which determines the density structure ρ,

$$\frac{\mathrm{d}p}{\mathrm{d}m} = g - \frac{4\pi}{c} \int_0^\infty \frac{\chi_\nu}{\rho} H_\nu \, \mathrm{d}\nu, \tag{3}$$

and the equation of radiative equilibrium, which determines the temperature structure T,

$$4\pi \int_0^\infty \left(\chi_\nu J_\nu - \eta_\nu\right) \mathrm{d}\nu = 0. \tag{4}$$

In these equations, $n_i R_{il}$ and $n_i C_{il}$ are the radiative and collisional rates for transitions from level i to level l, respectively, p is the gas pressure, g is the gravitational acceleration, c is the light speed, m is the column mass depth ($\mathrm{d}m = -\rho\,\mathrm{d}z$), ρ is the density, H_ν is the radiative Eddington flux, J_ν is the mean radiation intensity, η_ν and χ_ν are emissivity and opacity, respectively, and $\mu = \cos\theta$ is an angle cosine of a light ray.

This set of equations has to be solved simultaneously. An efficient method was introduced by Auer and Mihalas (1969b) as the complete linearisation method, which is the multidimensional Newton-Raphson method. If this method is combined with the accelerated lambda iteration method, significant saving of computing time may be achieved (e.g. Hubeny and Lanz 1992, 1995; Kubát 1994, 1996, 2003).

3.2 Model Atmosphere Grids

Since the calculation of NLTE model atmospheres is a very time consuming task even for the relatively simple static 1-D case, for practical purposes it is efficient to use pre-calculated grids of model atmospheres and to interpolate between them if a model for required parameters is not available in the grid.

An example of such a grid is the grid of NLTE model line blanketed atmospheres of O and B stars (Lanz and Hubeny 2003, 2007). There is also a grid of LTE line blanketed model atmospheres, which covers almost all reasonable temperatures and gravities, consequently also hot stars (Kurucz 1993).

Using a grid instead of calculation of a model atmosphere we limit ourselves to several fixed values of grid parameters, which can be for example the stellar effective temperature T_{eff}, gravitational acceleration at the stellar surface g, stellar radius $R_\star$, stellar mass $M_\star$, stellar luminosity $L_\star$, and elemental abundances. Since the parameter space can be quite extended, using a grid calculated for a limited range of parameters for model atmosphere analysis may fail, especially if we want to investigate stars with parameters beyond the grid ones. The most efficient possibility is first to use models from a grid to determine rough values of stellar parameters, which may be then refined using detailed model atmosphere calculations. However, if the model grids have sufficiently dense spacing in basic structural parameters, interpolation of the models may work well, as it was shown by Lanz and Hubeny (2003).

4 Comparison of LTE and NLTE Modelling

Since first NLTE model atmospheres were calculated in the late 1960s (Auer and Mihalas 1969a), there has always been a discussion if NLTE model atmospheres are really necessary or if LTE models are sufficient. In any case, the NLTE approximation is more general than the LTE one. The NLTE effects can be quite complicated. Consequently, we can only prove that LTE offers acceptable results *after* we calculate

a NLTE model, which is able to verify necessary conditions for LTE. Assuming LTE means assuming detailed balance in *all* transitions a priori. Even if we succeed to fit a part of the spectrum with the LTE model atmosphere, it can not be a proof that the LTE model describes the atmosphere well.

The basic advantage of LTE models is the fact that they can be calculated very quickly. Using contemporary computers we can obtain an LTE model within one minute or even faster. On the other hand, calculation of a NLTE model atmosphere may last several hours or even more. A question may arise, if we gain anything from these additional hours of computing time. Of course, we get a lot. NLTE model atmosphere calculations give us more accurate level populations, more accurate ionization balance, more accurate opacities, more accurate radiation field, and more accurate temperature and density structure in the resulting models.

Although it is clear that the NLTE model atmospheres are superior to the LTE ones, the latter ones dominated the analysis of hot stars for many years. The reason was the problem of line blanketing, where a huge number of spectral lines in the ultraviolet region caused absorption of radiation, which was re-emitted in the optical region. In LTE, relatively straightforward approximations of opacity distribution function or opacity sampling enabled to handle this effect. On the other hand, in NLTE model atmospheres the influence of the radiation field on level populations had to be taken into account, which was computationally prohibitive until an efficient method enabling treatment of line blanketing in NLTE was developed. This method uses the concept of superlevels and superlines (Anderson 1989). Superlevels are averaged atomic energy levels with similar properties, and superlines are transitions between them. Details about different applications of this method to calculations of NLTE model atmospheres can be found in Dreizler and Werner (1993) and Hubeny and Lanz (1995). Since now the line blanketing in NLTE can be handled in a satisfactory manner and since there are also publicly available computer codes able to solve the problem, e.g. TLUSTY[1] (Hubeny 1988; Hubeny and Lanz 1995) or PRO2[2] (Werner and Dreizler 1999; Werner et al. 2003), LTE line blanketed model atmospheres should be replaced by the NLTE ones.

The basic consequence of switching from LTE to NLTE is that differences in population numbers and also in ionization balance appear. The LTE populations and ionization fractions are systematically in error, especially in the outer parts of the atmosphere, which is the forming region of many spectral lines. The effect of correct treatment of the equations of kinetic equilibrium in NLTE model atmospheres is nicely illustrated in Figs. 5–9 of Lanz and Hubeny (2003). For Rosseland optical depths $\tau_R \lesssim 1$, the error of the ionization balance caused by the assumption of LTE is clearly seen. These errors directly influence the profiles of corresponding lines. In addition, they also influence heating and cooling in the stellar atmosphere and lead to differences in the temperature structure, as illustrated by Fig. 5 in Lanz and Hubeny (2007). At large depths ($\tau_R \gg 1$), the radiation is close to isotropic and the diffusion approximation for radiation transfer can be used, which also means that the

[1] http://nova.astro.umd.edu/index.html

[2] part of TMAP, http://astro.uni-tuebingen.de/~TMAP/

radiation is close to its equilibrium value. If also the particle velocities are close to the equilibrium distribution (as is common in "standard" stellar atmospheres), transition rates are very close to the detailed balance and the microscopic conditions for LTE are fulfilled there.

Since full treatment of NLTE model atmospheres may be computationally very time consuming, simplified method of solving the NLTE problem (radiative transfer + rate equations) for selected trace elements in a *given* model atmosphere is commonly being used. For more details about this approach we refer the reader to the book by Monier et al. (2010). Unfortunately, using the LTE model atmospheres instead of the NLTE ones still dominates this approach. Besides the availability of the LTE models this is probably caused by the fact that the temperature structures of LTE and NLTE models are very similar at large depths. Some authors advocate using the hybrid method (LTE model atmosphere with NLTE radiative transfer for trace elements) to be equivalent to the full NLTE approach. Przybilla et al. (2011) even concluded that " … LTE and NLTE model atmospheres are essentially equivalent for dwarf and giant stars over the range $15{,}000\,\mathrm{K} < T_{eff} < 35{,}000\,\mathrm{K}$, for most practical applications", which can be true if practical applications are dealing only with lines forming at optical depths $\tau_{\mathrm{R}} \gtrsim 1$. For lines forming above $\tau_{\mathrm{R}} \approx 1$, which is the majority of spectral lines, we may expect differences.

Thus, full NLTE modelling (i.e. calculation of NLTE model atmospheres with the solution of the NLTE problem for trace elements) should be always preferred since it uses physically consistent assumptions (see Kubát 2010). In this approach, the influence of radiation on level occupation numbers (hence opacities) is not neglected as in the LTE approach. To be sure that the results are correct, each particular application of the hybrid LTE/NLTE method has to be independently tested. We would like to emphasize that in any case, the hybrid LTE/NLTE approach is significantly superior to pure LTE analysis. To summarize, using LTE model atmospheres is a fast option, while using NLTE model atmospheres is a much more exact option, and should be preferred whenever possible. The best option to save computing time is to calculate NLTE model atmosphere as a background model, and then solve the NLTE problem for trace elements, if the conditions for using trace element approximation are fulfilled.

5 Model Atom Construction

An important part of the NLTE calculation is the construction of a proper model of an atom or ion studied. Some ions are relatively simple, besides hydrogen it is also the neutral helium (e.g. Auer and Mihalas 1972). On the other hand, the total number of levels and corresponding transitions may be enormous for some ions (see Fig. 5 of Hauschildt and Baron 1995, where the number of transitions is too large to plot; they form a continuous black surface and one can hardly find any relevant information from that figure).

To make the NLTE problem tractable, complicated model atoms may be simplified. This is usually done by assuming levels with high quantum number to be in LTE with respect to the ground level of the next ion. This way these levels do not enter the equations of statistical equilibrium. Another possibility is to merge levels, especially for multiplets (e.g. for neutral sodium, Gehren 1975; Boyarchuk et al. 1988). The most sophisticated way to simplify model atoms is by creating superlevels, which can be applied to most complicated ions like iron and nickel. Superlevels are generalized multiplets; the energy levels of all levels from a superlevel are averaged (including proper statistical weights), and similarly the transitions to and from a superlevel members are averaged. Then the NLTE line formation problem is solved for model atom consisting of superlevels. An example how the superlevels can be created can be found in Hubeny and Lanz (1995).

Collecting data for all transitions is not an easy task for most of metallic ions. We have to collect ionization cross sections for all levels included, transition probabilities for all allowed or forbidden radiative transitions, and collisional cross sections for all possible transitions. If data are not available, we have to look for some reasonable approximation. Finally, we have to evaluate values for the merged levels, if they are used.

6 Hot Stars with Winds

Stellar wind is an outflow of matter from the stellar surface and it is a common property of hot massive stars. The strength of the wind depends on a spectral type; generally, higher stellar luminosity and lower stellar gravity support stronger stellar winds. This means that the strongest winds are for O-type supergiants while for dwarf A-type stars the winds are almost absent.

All O-type stars, including O-dwarfs, have stellar wind. Since these stars emit the maximum of their radiation in the UV wavelength region, the fact that they lose mass via stellar winds was discovered by analysis of first ultraviolet spectra of this stellar type (Morton 1967) obtained by the `Aerobee` rocket. The observed spectra showed strong P-Cygni type line profiles, for such lines as of C IV and Si IV. Examples of P-Cygni type line profiles are shown in Fig. 1.

For hot massive stars, the mass-loss rates ($\mathrm{d}M/\mathrm{d}t$), which describe how quickly the star loses its mass, reach values up to $10^{-6}\,\mathrm{M}_\odot\,\mathrm{year}^{-1}$. Terminal wind velocities grow from the photosphere and reach their maximum $v_\infty \sim 3{,}000\,\mathrm{km\,s}^{-1}$ far from the stellar surface. The outflow is driven by radiation, which is absorbed or scattered in continuum (by electrons and by bound-free and free-free transitions) and in spectral lines. The dominant contribution to radiative acceleration in these atmospheres comes from resonance ultraviolet lines of metals, where large flux in the ultraviolet part of spectrum meets large absorption in these lines, which is amplified by the Doppler shift caused by the velocity gradient. On the other hand, the most abundant elements, hydrogen and helium, gain negligible radiative force. The momentum gained by metals is transferred to hydrogen and helium by means of Coulomb

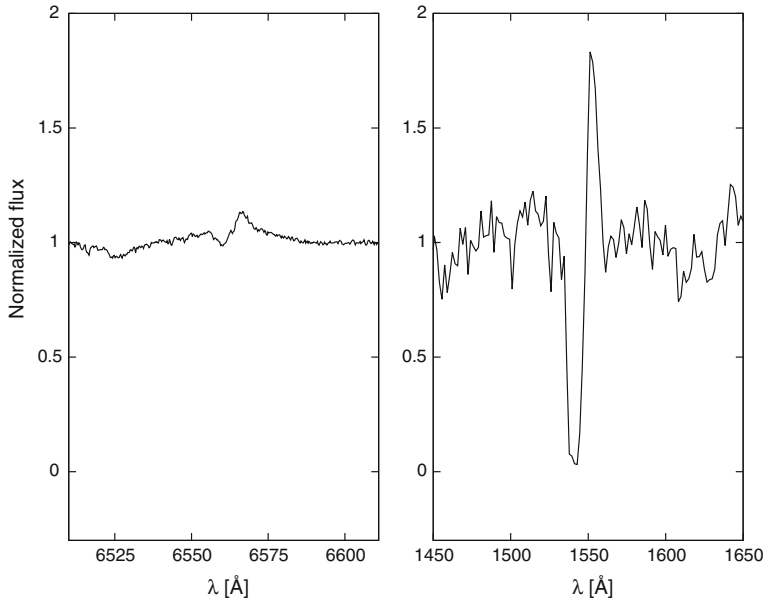

Fig. 1 Illustration of P-Cygni type profiles (normalised to continuum) of the line Hα (*left panel*) and the ultraviolet line of C IV (*right panel*) for the star λ Cep. The ultraviolet spectrum is taken from the IUE archive (http://archive.stsci.edu/iue/), the visual spectrum was observed using the Ondřejov Perek Telescope

collisions between charged ions of metals and hydrogen-helium component. Since winds are present practically in all O-type stars and supergiant B and A-type stars, they have to be taken into account in an analysis of hot stars.

6.1 Modelling of Hot Stars with Winds

The presence of an outflow is quite a complication in calculations of consistent models, which can predict theoretical spectra. To understand how the radiation emerging from the stellar photosphere (static medium) changes passing through their expanding atmosphere, i.e. wind (moving medium), radiative transfer in both media has to be solved. There is a number of methods and computer codes for static media available, but they are not adequate to treat expanding atmospheres of hot stars. The problem of the transfer of radiation in moving media is more complicated, since the wind is expanding, and therefore the Doppler shift of the photon frequencies must be taken into account. Absorption and emission coefficients become angle dependent. Consequently, these coefficients become anisotropic and the aberration of light may become important (the latter effect is usually neglected for stellar winds where $v/c \lesssim 0.01$, see Mihalas et al. 1976).

There are two basic classes of methods (see, e.g. Mihalas and Kunasz 1986) for solving the radiative transfer equation in moving medium, namely the solution in the observer frame and the solution in the co-moving frame. In the observer frame, the computations are straightforward, but the opacity and emissivity become angle dependent. Consequently, the number of frequency and angle points necessary to solve the radiative transfer equation may become enormous, making the task computationally expensive. On the other hand, since the co-moving frame is the local rest frame of the matter, opacity and emissivity are isotropic, but the expressions for solution of the radiative transfer are more complicated.

To simplify treatment of the problem, a *core-halo approximation* is commonly used, which means that photosphere and wind are modelled separately, and that the wind does not influence photosphere, while photospheric flux is a lower boundary condition for wind solution. Usually, the photosphere is assumed to be static and a full NLTE line-blanketed model atmosphere modelling described in Sect. 3.1 is done. Here NLTE modelling is inevitable, since LTE is not valid in the photospheres of O stars. Then the photospheric flux is taken as a lower boundary condition for wind solution, which is usually performed for given velocity, density, and temperature structure, i.e. the NLTE line formation problem, solution of equations of statistical equilibrium together with the radiative transfer equation. Due to the large velocity gradients present in winds of these stars, Sobolev approximation may be used, and the radiative transfer is significantly simplified, since then the system of equations of statistical equilibrium and radiative transfer is local.

With this model, the analysis is done in steps. The lines which are expected not to be influenced by wind are selected (the photospheric lines). These lines serve for $T_{\rm eff}$ determination, similarly to static models. Then the wind line profiles are calculated for given velocity $v(r)$ and density $\rho(r)$ and the mass-loss rate is determined. Illustrative examples of application of such a procedure may be found in Bouret et al. (2012). The most important computer codes for modelling of hot star winds are listed elsewhere in this book (Chap. 18). A more general background of the analysis of hot stars with winds may be found, e.g. in Puls et al. (2008).

7 Summary

For hot stars, the NLTE analysis is necessary. It may be done using either LTE or better NLTE model atmospheres followed by NLTE for trace elements, if required. NLTE model atmospheres should be preferred, since they are more exact. The model atoms have to be carefully constructed. Model grids may save computing time. The systematic influence of stellar wind on emergent radiation has to be taken into account.

Acknowledgments J. K. would like to thank Dr. Ewa Niemczura for inviting him to the Spring School of Spectroscopic Data Analyses in Wrocław. B. Š. thanks the Ministry of Education and Science of Republic of Serbia for supporting this work through the project 176002 "Influence of collisions on astrophysical plasma spectra". The authors are also grateful to all referees (Ivan Hubeny and both anonymous ones) for their invaluable comments. This work was partly supported by the project 13-10589S of the Grant Agency of the Czech Republic (GA ČR).

References

Anderson LS (1989) ApJ 339:558
Auer LH, Mihalas D (1969a) ApJ 156:157
Auer LH, Mihalas D (1969b) ApJ 158:641
Auer LH, Mihalas D (1972) ApJS 24:193
Bouret JC, Hillier DJ, Lanz T, Fullerton AW (2012) A&A 544:A67
Boyarchuk AA, Hubeny I, Kubát J, Lyubimkov LS, Sakhibullin NA (1988) Astrofizika 28:335
Dreizler S, Werner K (1993) A&A 278:199
Gehren T (1975) A&A 38:289
Hauschildt PH, Baron E (1995) JQSRT 54:987
Hubeny I (1988) Comput Phys Commun 52:103
Hubeny I, Lanz T (1992) A&A 262:501
Hubeny I, Lanz T (1995) ApJ 439:875
Hubeny I, Mihalas D (2014) Theory of stellar atmospheres. Princeton University Press, Princeton and Oxford
Kubát J (1994) A&A 287:179
Kubát J (1996) A&A 305:255
Kubát J (2003) In: Piskunov N, Weiss WW, Gray DF (eds) Modelling of stellar atmospheres, IAU Symposium, vol 210, p A8
Kubát J (2010) In: Monier R, Smalley B, Wahlgren G, Stee P (eds) Non-LTE line formation for trace elements in stellar atmospheres. EAS publications series, vol 43, p 43
Kurucz RL (1993) ATLAS9 stellar atmosphere programs and 2 km/s grid, Kurucz CD-ROM, vol 13
Lanz T, Hubeny I (2003) ApJS 146:417
Lanz T, Hubeny I (2007) ApJS 169:83
Lanz T, Cunha K, Holtzman J, Hubeny I (2008) ApJ 678:1342
Mihalas D (1978) Stellar atmospheres, 2nd edn. W. H. Freeman & Co., San Francisco
Mihalas D, Kunasz PB (1986) J Comput Phys 64:1
Mihalas D, Kunasz PB, Hummer DG (1976) ApJ 206:515
Monier R, Smalley B, Wahlgren G, Stee P (Eds) (2010) Non-LTE line formation for trace elements in stellar atmospheres. EAS publications series, vol 43
Morton DC (1967) ApJ 147:1017
Przybilla N, Nieva MF, Butler K (2011) J Phys Conf Ser 328:012015
Puls J, Vink JS, Najarro F (2008) A&A Rev 16:209
Werner K, Dreizler S (1999) J Comput Appl Math 109:65
Werner K, Deetjen JL, Dreizler S, Nagel T, Rauch T, Schuh SL (2003) In: Hubeny I, Mihalas D, Werner K (eds) Stellar atmosphere modelling, Astronomical Society of the Pacific conference series, vol 288, p 31

NLTE Radiative Transfer in Cool Stars

Theory and Applications to the Abundance Analysis for 24 Chemical Elements

Maria Bergemann and Thomas Nordlander

Abstract The interpretation of observed spectra of stars in terms of fundamental stellar properties is a key problem in astrophysics. For FGK-type stars, the radiative transfer models are often computed using the assumption of local thermodynamic equilibrium (LTE). Its validity is often questionable and needs to be supported by detailed studies, which build upon the consistent framework of NLTE. In this review, we outline the theory of NLTE. The processes causing departures from LTE are introduced qualitatively by their physical interpretation, as well as quantitatively by their impact on the models of stellar spectra and element abundances. We also compile and analyse the most recent results from the literature. In particular, we examine the NLTE effects for 24 chemical elements for six well-studied FGK-type stars.

Keywords Line: formation · Radiation mechanisms: general · Radiative transfer · Stars: atmospheres · Stars: late-type

1 Introduction

Local thermodynamic equilibrium (LTE) is a common assumption when solving the radiative transfer problem in stellar atmospheres. The reason for adopting LTE is that it tremendously simplifies the calculation of number densities of atoms and

M. Bergemann (✉)
Institute of Astronomy, University of Cambridge, Madingley Road, Cambridge CB3 0HA, UK
e-mail: mbergema@ast.cam.ac.uk

T. Nordlander
Division of Astronomy and Space Physics, Department of Physics and Astronomy, Uppsala University, Box 516, 75120 Uppsala, Sweden
e-mail: thomas.nordlander@physics.uu.se

E. Niemczura et al. (eds.), *Determination of Atmospheric Parameters of B-, A-, F- and G-Type Stars*, GeoPlanet: Earth and Planetary Sciences,
DOI: 10.1007/978-3-319-06956-2_16,

molecules. However, the trouble is that the assumption essentially implies that stars do not radiate. Quoting Mihalas and Athay (1973), "Departures from LTE occur simply because stars have a boundary through which photons escape into space". In what follows, we will take a short excursion into why this happens and provide a brief overview of the recent developments in the field.

We start with reviewing the theoretical foundations of radiative transfer as it happens in reality, i.e. including its impact on the properties of matter in stellar atmospheres. This approach is known as non-local thermodynamic equilibrium (NLTE). We discuss the NLTE 'mechanics' and summarise the impact on spectral line formation. Finally, we present a list of NLTE abundance corrections for the chemical elements, for which detailed statistical equilibrium calculations are available in the literature.

2 The Framework and Notation

Let us for simplicity take a one-dimensional (1-D) hydrostatic model of a stellar atmosphere, which is some relation of temperature and gas pressure with depth, and consider the transport of radiation outward.

At each depth point, we then assume that matter particles (ions, atoms, electrons, molecules) are in *local thermodynamic equilibrium* with each other. This equilibrium is established by intra-particle collisions, resulting in the Maxwellian velocity distribution and the Saha-Boltzmann distribution of particles over degrees of excitation and ionisation. Thus the fundamental assumption of LTE is that particle collisions establish the energy distribution of matter. The energy distribution of the radiation field may depart from LTE, $J_\nu \neq B_\nu$, but the influence of non-blackbody radiation field[1] on the energy partitioning of matter is ignored. The local rate of energy generation η_ν depends only on the local thermodynamic properties of the gas, i.e. the local kinetic temperature T_e and local pressure. Therefore, the local source function is simply the Planck function B_ν.

However, the physical truth is that photons and matter particles interact in a variety of ways: through photo-excitation and ionisation, radiative recombination, stimulated emission, and other processes. Deep inside the star, typically far below the photosphere, the collision rates are very intense and the photon mean free path l_λ is smaller than the scale over which the physical variables (temperature, pressure) change, so that the radiation field thermalises to the Planck function, $J_\nu \approx B_\nu$. Closer to the stellar surface, l_λ becomes large, larger than the scale height of material. Thus, as photons diffuse outward, their decoupling from matter increases: the radiation field becomes non-local, anisotropic, and strongly non-Planckian. Numerical calculations show that the radiative transition rates driven by the non-local radiation field in the

[1] A non-blackbody spectral energy distribution is in itself NLTE.

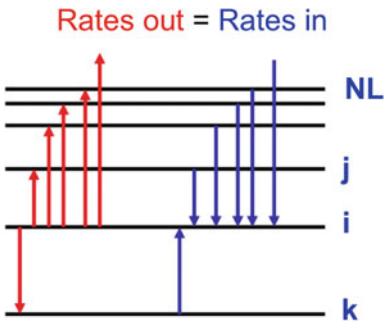

Fig. 1 Illustration of the statistical equilibrium equation for a level i in the model atom; the sum of the rates of all transitions into a level i is balanced by the sum of the rates out

outer atmospheric layers far outweigh collisional transition rates, thus the populations of atomic energy levels differ from the LTE values.

The non-locality arises because of scattering: photons moving through the gas change only their direction in a random way and experience a slight shift in frequency. To account for scattering in the processes of radiative transfer and, correspondingly, establishment of excitation-ionisation equilibrium of an element, the concept of NLTE was introduced. First, the Saha-Boltzmann equations are replaced by the rate equations or their time-independent counterpart, statistical equilibrium (SE) or *kinetic equilibrium* equations. For example, an SE equation for a level i, illustrated in Fig. 1, can be written as:

$$n_i \sum_{j \neq i} P_{ij} = \sum_{j \neq i} n_j P_{ji}. \tag{1}$$

Here, $P_{ij} = C_{ij} + R_{ij}$ is the total of collisional and radiative rates (per particle) which establish the equilibrium number of ions excited to the level i. A subscript ij means that a transition from the level i to the level j occurs. This equation must be written for each level i of every ion c in every unit volume of a stellar photosphere, and it describes the microscopic interaction between atoms, electrons and photons.

To close the system of statistical equilibrium equations, the equation of number conservation can be used for a fixed number density of hydrogen:

$$\sum_{i,c} n_{i,c} = \frac{\alpha_{\rm el}}{\alpha_{\rm H}} \left(\sum_i n_{i,{\rm H}} + n_p \right), \tag{2}$$

where $\alpha_{\rm el}/\alpha_{\rm H}$ is the fraction of all atoms and ions of the element relative to that of hydrogen.

For collisional rates, several theoretical formulae exist, also quantum-mechanical calculations and few experimental data points in the relevant energy regime are available. Collisional rates depend only on the local value of electron temperature and density. For the Maxwellian distribution, the collision-induced transitions from the lower to the upper level are related to the inverse transitions from the upper to

the lower level by the detailed balance principle, i.e. through the Saha-Boltzmann factor $\exp(-E_i/kT)$ and the level statistical weights. The rates of transitions due to inelastic collisions are calculated according to:

$$C_{ij} = n_e \int_{\upsilon_0}^{\infty} \sigma_{ij}(\upsilon)\, \upsilon\, f(\upsilon) d\upsilon, \tag{3}$$

where $\sigma_{ij}(\upsilon)$ is the electron collision cross-section, $f(\upsilon)$ is the Maxwellian velocity distribution, υ_0 is the threshold velocity with $m\upsilon_0^2/2 = h\nu_0$.

The radiation field enters Eq. 1 through the radiative rates R_{ij}:

$$R_{ij} = \int_0^{\infty} \frac{4\pi}{h\nu} \sigma_{ij}(\nu) J_\nu d\nu \quad R_{ji} = \int_0^{\infty} \frac{4\pi}{h\nu} U_{ij} \sigma_{ij}(\nu) \left(\frac{2h\nu^3}{c^2} + J_\nu \right) d\nu \tag{4}$$

where $\sigma_{ij}(\nu)$ is the cross-section of a transition from a state i to a state j, i.e. the monochromatic extinction coefficient per particle in a state i. For bound-bound transitions, $\sigma_{ij}(\nu) = \sigma^{\text{line}}(\nu)$, and for bound-free transitions, $\sigma_{ij}(\nu) = \sigma^{\text{cont}}(\nu)$. The function U_{ij} is expressed as:

$$U_{ij} = \left(\frac{n_i}{n_j} \right)_{\text{LTE}} \exp\left(-\frac{h\nu}{kT} \right), \tag{5}$$

where j is a bound level or a continuum energy state. The mean intensities J_ν at all frequencies relevant to the transition $i \rightarrow j$ are derived from the radiative transfer (RT) equation, which can be written in terms of the optical depth τ:

$$d\tau_\nu(z) = -\kappa_\nu dz, \tag{6}$$

$$\mu \frac{dI_\nu(\tau_\nu, \mu)}{d\tau_\nu} = I_\nu(\tau_\nu, \mu) - S_\nu(\tau_\nu). \tag{7}$$

For the true (thermal) absorption and emission processes, the source function S_ν is defined by the Planck function. In NLTE, a part of the local energy emission at a given point is due to the scattering of photons from the surrounding medium. So, the source function also depends on the radiation field (see Eq. 13), which is at some frequencies non-local. As a result, we have a coupled system of statistical equilibrium and radiative transfer equations which must be solved simultaneously to give the distribution of particles among excitation levels and ionisation stages.

The solution of the coupled SE and RT equations is non-trivial and beyond the scope of this lecture. The most common method is an accelerated lambda iteration (Rybicki and Hummer 1992).

3 NLTE Effects

3.1 Statistical Equilibrium

To quantify the departures from LTE, it is necessary to explore relationships of the kind $n_{\rm NLTE}/n_{\rm LTE}$, i.e. the number density of a given energy level in an atom or a molecule as computed in NLTE compared to LTE. This ratio is termed a departure coefficient, b_i. Although there are several definitions, the one given above (Wijbenga and Zwaan 1972) is the most common. Under LTE, $b_i = 1$ and the level is said to be 'thermalised', i.e. its occupation number is just as that given by the Saha-Boltzmann statistics. Under NLTE, if $b_i < 1$, the level is underpopulated, and if $b_i > 1$, the level is overpopulated relative to its value in LTE.

How do these numbers come about? The algorithm is contained in the statistical equilibrium equations, which determine the relative populations of the energy levels to satisfy the given stellar parameters, the gradients of physical variables in the atmosphere,[2] and the intrinsic atomic properties of an atom or molecule under consideration, i.e. the structure of electronic configurations and the transition probabilities. To understand this better, we can expand the rates in the SE equation for a level i (Mihalas 1978):

$$\begin{aligned}\text{all transitions to a level i: } &\sum_{j>i} n_j \left(\frac{n_i}{n_j}\right)_{\rm LTE} (R_{ji} + C_{ji}) + \sum_{k<i} n_k (R_{ki} + C_{ki}) = \\ \text{all transitions from a level i: } &n_i \sum_{k<i} \left(\frac{n_i}{n_j}\right)_{\rm LTE} (R_{ik} + C_{ik}) + n_i \sum_{j>i} (R_{ij} + C_{ij})\end{aligned} \tag{8}$$

where j may refer to a bound or a free (ion ground-state or continuum) state, and the radiative and collisional rates depend on the mean intensity (Eq. 4). The equations contain both the bound-bound and the bound-free terms, so the mean intensity must be integrated either over the line profile or over a large range of energies from the ionisation edge of a given level.

Neglecting all ionisation processes, Eq. 8 would simplify to:

$$\begin{aligned}&\sum_{j>i} n_j \left(\frac{n_i}{n_j}\right)_{\rm LTE} (A_{ji} + B_{ji}\bar{J} + C_{ji}) + \sum_{k<i} n_k (B_{ki}\bar{J} + C_{ki}) \\ &= n_i \sum_{k<i} \left(\frac{n_i}{n_j}\right)_{\rm LTE} (A_{ik} + B_{ik}\bar{J} + C_{ik}) + n_i \sum_{j>i} (B_{ij}\bar{J} + C_{ij})\end{aligned} \tag{9}$$

where $\bar{J} = \int \psi_\nu J_\nu d\nu$, A_{ji} and B_{ji} the Einstein coefficients for spontaneous and stimulated de-excitation (emission), C_{ji} the rate of collisional de-excitation; the inverse quantities are represented by the coefficients A_{ik}, B_{ik} and C_{ik}.

[2] Assume that the NLTE problem is solved for a fixed model atmosphere structure.

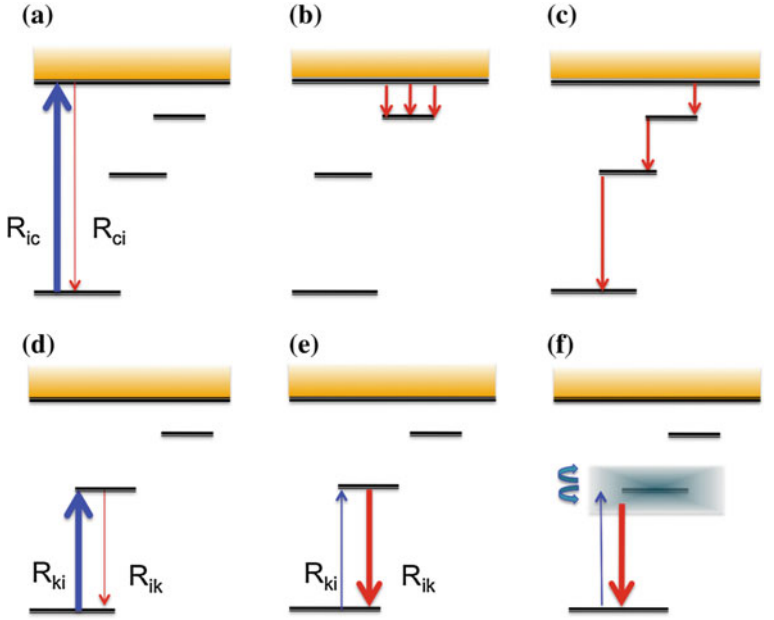

Fig. 2 Illustration of reaction channels for a hypothetical multi-level atom. ν_0 is the central frequency for a spectral line or the frequency of ionisation threshold. See Sect. 3.1. **a** $J_{\nu(\nu \geq \nu 0)} > B_\nu(T)$. **b** $J_{\nu(\nu \geq \nu 0)} > B_\nu(T)$. **c** $J_{\nu 0} > B_{\nu 0}(T)$. **d** $J_\nu > B_\nu(T)$. **e** $J_{\nu 0} > B_{\nu 0}(T)$. **f** $J_{\nu 0} > B_{\nu 0}(T)$

Having solved the equations for all levels in a model atom simultaneously with the RT equation at all relevant frequencies, we end up with the *statistical* (or *excitation-ionisation*) *balance*, which gives us the NLTE values of the atomic number densities n_i.[3] The next step is usually an analysis of the individual rates with the aim to understand how exactly the distribution arises, and in particular to identify the leading channel which drives the departures from LTE under the influence of the radiation field.

Often, there is no need to analyse each individual rate, as most of them are very small, so in practice the statistical equilibrium is established by one or two dominant channels. These channels are, in essence, sequences of processes, which occur under a certain combination of factors, including the optical depth in a line or continuum, the difference between J_ν and the local Planck function, the relative size of cross-sections for different atomic levels.

These channels are schematically illustrated in Fig. 2, and they include:

- **Photoionisation and photon pumping**
  A super-thermal radiation field with mean intensity larger than the Planck function, $J_\nu > B_\nu(T_e)$, leads to over-ionisation (Fig. 2a) and over-excitation (Fig. 2d). The latter process is termed photon pumping.The typical situation is that in a

[3] In the literature, the atomic number densities may also be referred to as population numbers.

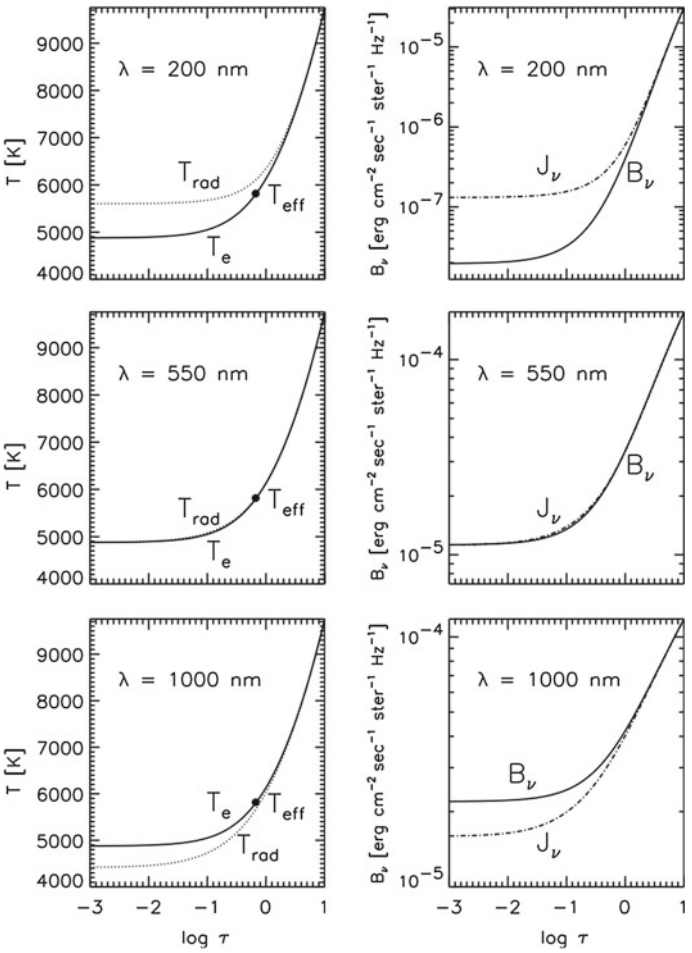

Fig. 3 *Left panels* The comparison of radiation temperatures for different wavelengths with the local kinetic temperature in a stellar atmosphere. *Right panels* The decoupling of the the mean intensity from the Planck function for different wavelengths, as indicated in each sub-plot. Figure courtesy Rob Rutten

stellar atmosphere the mean intensity in the continuum $J_{\nu,c}$ lies significantly above the local Planck function, bluewards of the stellar flux maximum. Thus, over-excitation and over-ionisation affect the neutral atoms (e.g. Mg I, Si I, Fe I), which have ionisation threshold in the blue and UV.

- **Over-recombination**
  If the mean intensity falls below the Planck function, $J_\nu < B_\nu(T_e)$, the shortage of ionisations leads to the net over-recombination to the upper levels (Fig. 2b), as is the case in the infrared (Fig. 3, bottom panel). Over-recombination takes place in the bound-free transitions with the corresponding wavelengths; this is the case for the majority of neutral atoms (Na I, K I, Cr I, Fe I, etc).

- **Photon 'suction'**
  For many elements, the diagram of electronic configurations is very regular, with a sequence of high-probability transitions connecting the lowest and the uppermost (Rydberg) levels. This 'ladder' favours photon suction (Fig. 2c), which represents a successive de-excitation through high-probability transitions to the lower levels. Photon suction is a sequence of spontaneous transitions caused by photon loss, in the atmospheric layers where the line centre optical depth has dropped below unity for every transition involved in the sequence. Such a sequence can include transitions of various frequencies, from UV to IR. Photon suction is balanced by the recombination flow through the bound-free edges in the IR.
- **Photon loss and resonance line scattering**
  If the optical depth falls below unity in a line, $\tau_{\nu 0} < 1$, the photons escape without reconversion to thermal energy. This is termed photon loss. In the framework of statistical equilibrium, radiative excitations are in deficit, and spontaneous de-excitations lead to the over-population of the lower level in a transition out of the upper level (Fig. 2e, f). The effect is particularly important for strong resonance lines (e.g. Na D or Mg b) with very small collisional destruction probability: photon escape in the line itself influences the line source function, causing sub-thermal S_ν.

Of course, in most cases all these processes form a sophisticated bundle, which is very difficult to unfold. The NLTE effects depend upon several factors, including the physical conditions and the atomic structure (ionisation energy, characteristics of the energy levels in the atom, the number of allowed and forbidden transitions, size of cross-sections). However, generally atoms fall into one of the two categories: *photo-ionisation dominated* atoms and *collision-dominated* ions (see Gehren et al. 2001 and references therein):

- **Photo-ionisation-dominated atoms**
  The main NLTE driver is over-ionisation. The typical situation is that low-lying energy levels of over-ionising species have very large photo-ionisation cross-sections, and that their ionisation edges are located in the UV, where $J_\nu > B_\nu(T_e)$. Moreover, the photo-ionisation cross-sections of atoms with complex electronic configurations often have prominent resonances at certain energies which further enhances the radiative rates. For such atoms (e.g., Mg I, Al I, Si I, Ca I, Mn I, Fe I, Co I), the NLTE departure coefficients are generally below unity, i.e. there is a subset of strongly under-populated levels, and this under-population is redistributed over all other levels by collisions or optically thick line transitions. The NLTE effects usually grow with increasing $T_{\rm eff}$, and decreasing [Fe/H] and $\log g$, due to stronger non-local radiation fields in the UV, lesser efficiency of thermalising collisions, and vanishing line blocking at low metallicity.
- **Collision-dominated ions**
  With very small photo-ionisation cross-sections, the statistical equilibrium of collision-dominated ions reflects the interplay between the strong line scattering, over-recombination, and collisional thermalisation. Representative ions with these properties are Na I and K I. We note, however, that this is a general picture in 1-D

hydrostatic model atmospheres, and may not be valid in the statistical equilibrium calculations with 3-D RHD models (see e.g. Lind et al. 2013).

A very detailed discussion of these processes with different thought experiments and toy model atoms, is given in Bruls et al. (1992). We also refer the reader to Mihalas and Athay (1973), who provide an excellent physical basis for the qualitative understanding of the overall picture.

3.2 Spectral Line Formation

Once we know what NLTE effects dominate the statistical equilibrium of an atom, the behaviour of spectral line profiles is easy to understand. The analysis is aided by the diagrams of level departure coefficients for the levels involved in the transition as a function of some reference optical depth, e.g. the optical depth at 500 nm in the continuum. For the strong lines, it is often helpful to explore the depths of formation of various parts of the line profiles,[4] for example the layers where in the core or in the wing $\tau_\nu^l = 1$.

The emergent intensity within a spectral line is given by the radiative transfer equation:

$$I_\nu(\tau_\nu = 0, \mu) = \int_0^\infty S_\nu(\tau_\nu) \mathrm{e}^{-\tau_\nu/\mu} d\tau_\nu/\mu, \tag{10}$$

where $\mu = \cos\theta$, for the photons travelling in the direction specified by the angle θ with respect to the normal. The atomic levels populations are contained in the source function S_ν and in the optical depth τ_ν (Eq. 6). The line extinction coefficient (related to τ_ν via Eq. 6), or opacity, is defined by:

$$\kappa_\nu^l \propto n_i \left(1 - \frac{n_j g_i}{n_i g_j}\right) = b_i \left(1 - \frac{b_j}{b_i} \mathrm{e}^{-\frac{h\nu}{kT}}\right). \tag{11}$$

In the Wien's regime ($h\nu > kT$), the expression reduces to:

$$\kappa_\nu^l \propto b_i. \tag{12}$$

When $b_i < 1$, e.g. as a consequence of NLTE over-ionisation or over-excitation in a transition, the line opacity is decreased and thus the line formation depth increases. As

[4] In the literature, one may often find expressions of the following kind: A spectral line is formed 'at a given optical depth'. The usual interpretation of this depth is the location where $\tau_{\lambda,0} = 1$ (at the wavelength of the line core, λ_0) is achieved. Of course, a spectral line forms over an interval of depths. For some strong lines, this range encompasses the whole stellar atmosphere, i.e. several hundred km.

temperature is higher in the deeper layers, the result is a weakening of the absorption line. The other way around, $b_i > 1$ leads to an increased opacity in the line over an LTE value. The line thus forms in the outer atmospheric layers, where temperatures are lower, which leads to the line strengthening with respect to the continuum.

The line source function can be written as:

$$S^l = \frac{2h\nu^3}{c^2} \frac{1}{\frac{n_i g_j}{n_j g_i} - 1} = \frac{2h\nu^3}{c^2} \frac{1}{\frac{b_i}{b_j}\left(\mathrm{e}^{\frac{h\nu}{kT}} - \frac{b_j}{b_i}\right)}, \tag{13}$$

where we make the assumption of complete redistribution in a line profile, which implies that the frequency and direction of an absorbed and emitted photons are not correlated. When $h\nu > kT$ (in the UV and visual spectral range):

$$\frac{S^l}{B^l_\nu} \approx \frac{b_j}{b_i}. \tag{14}$$

A spectral line is weakened if at the depths of line formation, the departure coefficient of the upper level of a transition, b_j, is larger than that of the lower level, b_i. From the Eq. 14, $b_j > b_i$ implies that the line source function is super-thermal, $S^l > B^l_\nu$. There are more atoms excited to the upper level compared to those on the lower level, than would result under LTE. Hence, there is more emission and less absorption in the line in comparison with the Planck's law. Conversely, the absorption line strengthens when $b_j < b_i$, or $S^l < B^l_\nu$, as there are not enough atoms on the level j to maintain the same emissivity as in LTE.

Weak lines with small opacity relative to the continuum are formed in the deep atmospheric layers. Their intensity profiles simply reflect the profile of κ_ν. Strong lines influence their own radiation field and also the cross-talk between different frequencies within the line is important. The simplest case is that of strong resonance lines, which have a nearly two-level-atom source function. As described above, the surface photon losses cause $J_\nu < B_\nu$ and sub-thermal source function $S^l < B_\nu$, that leads to darker line cores compared to LTE.

In general, there is no simple analytic solution for estimating the effect of b_i inequalities on line profiles. NLTE effects may change the equivalent width of a line, but its profile may also be affected, even if the equivalent width is conserved. Thus, departures from LTE may appear in both curve-of-growth and spectrum synthesis methods, with sometimes subtle differences.

4 The Impact of NLTE on Elemental Abundance Analyses

The effects of NLTE on the abundance determinations in cool stars have been presented in several excellent review articles, perhaps the most up-to-date and comprehensive study being that by Asplund (2005). There is little that can be added to these

Table 1 Stellar parameters for the selected reference stars

Star	$T_{\rm eff}$ [K]	$\log g$	[Fe/H]
Sun	5,777	4.44	0.00
Procyon	6,545	3.99	−0.05
Arcturus	4,247	1.59	−0.52
HD 84937	6,275	4.11	−2.00
HD 140283	5,720	3.67	−2.50
HD 122563	4,578	1.61	−2.74

$T_{\rm eff}$ and $\log g$ have been independently determined by fundamental relations, while [Fe/H] is the typical literature value

papers. We thus restrict the discussion to representative groups of chemical elements with similar NLTE effects, and provide a set of plots, which can be used to gain a qualitative understanding of how the NLTE abundance corrections vary with stellar parameters. These corrections are shown in Fig. 5 for six well-studied stars with parameters listed in Table 1: the Sun, Procyon, Arcturus, HD 84937, HD 122563, and HD 140283. The references to the data are given in Table 2 in the Appendix. Figure 5 also shows the results for the individual chemical elements.

NLTE abundance correction for a given chemical element, $\Delta_{\rm El}$, is defined as: $\Delta_{\rm El} = \log {\rm A(El)}_{\rm NLTE} - \log {\rm A(El)}_{\rm LTE}$, i.e. it is the logarithmic correction, which has to be applied to an LTE abundance determination A of a specific line to obtain the correct value corresponding to the use of NLTE line formation.

Several interesting observations can be made based on these plots. For the lines of the photo-ionisation type ions (B I, Mg I, Al I, Si I, Ca I, Sr I, as well as all neutral Fe-peak atoms: Ti I, Cr I, Mn I, Fe I, Co I, Ni I) the NLTE abundance corrections increase with decreasing metallicity. This tendency simply reflects the fact that the atoms experience a larger degree of over-ionisation and radiative pumping due to stronger $J_\nu - B_\nu$ splits in the low-metallicity atmospheres. The spectral lines are weaker in NLTE compared to LTE, and the NLTE abundances are correspondingly larger.

For the collision-type minority ions, like Na I and K I, the NLTE effects on the line formation are mainly due to photon suction and over-recombination. The spectral lines are typically strengthened, with NLTE abundance corrections in the range from −0.1 to −0.5 dex (Fig. 5). The efficiency of over-recombination, caused by $J_\nu < B_\nu$ in the IR, grows with increasing $T_{\rm eff}$, which is why departures from LTE have the largest effects for warm turn-off stars, like Procyon.

The diagnostic lines of atoms like Li I (671 nm), C I (910, 960 nm), O I (777 nm triplet), Ca II, Sr II, and Ba II, are often stronger in NLTE. However, the effect depends on stellar parameters, elemental abundance, and the atomic data for a transition (see also Johnson et al. 1974). At higher metallicity, or elemental abundance, the strong lines have sub-thermal source functions due to photon loss through the wings. The

Table 2 References to NLTE studies of late-type stars in the literature, which were used to create Figs. 4 and 5

Ion	S_H	References	Spectral lines (nm)
Light elements			
B I	x[a]	Kiselman and Carlsson (1996)	250
Li I	QM[b]	Lind et al. (2009)[c]	670.7
C I	0	Fabbian et al. (2006)	909.5
N I	1/3	Caffau et al. (2009)	12 lines, $744 \leq \lambda \leq 1054$
O I	0	Reetz (1998)	777.1–777.5
O I	1	Sitnova et al. (2013)	615.8, 777.1–777.5, 844.7
Intermediate elements			
Na I	QM[b]	Lind et al. (2011)[c]	568.8, 589.5, 615.4, 819.4
Mg I	x[d]	Zhao et al. (1998)	13 lines, $457 \leq \lambda \leq 892$
Mg I	0.05	Gehren et al. (2006)	7 lines, $457 \leq \lambda \leq 571$
Mg I	0.1	Mashonkina et al. (2008)	6 lines, $457 \leq \lambda \leq 571$
Al I	0.4[e]	Baumueller and Gehren (1997)	396.2, 669.7
Al I	0.002	Gehren et al. (2006), Mashonkina et al. (2008)	396.2
Si I	1	Bergemann et al. (2013)[f], Würl (2012)	9–10 lines, $390 \leq \lambda \leq 723$
S I	1	Takeda et al. (2005)	8 lines, $869 \leq \lambda \leq 1046$
K I	0.001	Takeda et al. (2002)	769.9
Ca I	0.1	Mashonkina et al. (2007, 2008)	422.6, 442.5, 526.1, 534.9, 616.2
Sc I	0.1	Zhang et al. (2008)	567.2
Sc II	0.1	Zhang et al. (2008)	552.6
Ti I	0.05	Bergemann (2011)	453.4, 498.1, 502.2, 843.5
Fe-group elements			
Cr I	0	Bergemann and Cescutti (2010)	425.4, 520.6, 540.9
Mn I	0.05	Bergemann and Gehren (2008)	475.4, 467.1, 601.6, 874.0
Fe I	1	Bergemann et al. (2012b), Lind et al. (2012)[c]	492.0, 499.4, 521.6, 524.2, 606.5, 625.2, 643.0
Co I	0.05	Bergemann et al. (2010)	350.1, 411.0, 412.1
Zn I	1	Takeda et al. (2005)	472.2, 481.1, 636.2
Neutron-capture elements			
Sr I	0	Bergemann et al. (2012a)[c]	460.7
Sr II	0	Bergemann et al. (2012a)[c]	407.7, 421.5, 1,004, 1,033, 1,091
Pb I	0.1	Mashonkina et al. (2012)	405.7
Th II	0.1	Mashonkina et al. (2012)	401.9, 408.6
Eu II	0	Mashonkina et al. (2008, 2012)	413.0
Ba II	0	Mashonkina et al. (1999, 2008)	455.4, 585.3, 649.6

[a] H I collision rates for ionisation from Kunc and Soon (1991); no b-b collisions included in the model atom

[b] Based on quantum mechanical calculations of hydrogen collision rates

[c] Results were extracted using http://www.inspect-stars.net

[d] S_H set as exponentially dependent on upper excitation energy

[e] But $S_H = 0.002$ for levels where $n > 7$, affecting IR lines

[f] Corrections were computed specifically for this work

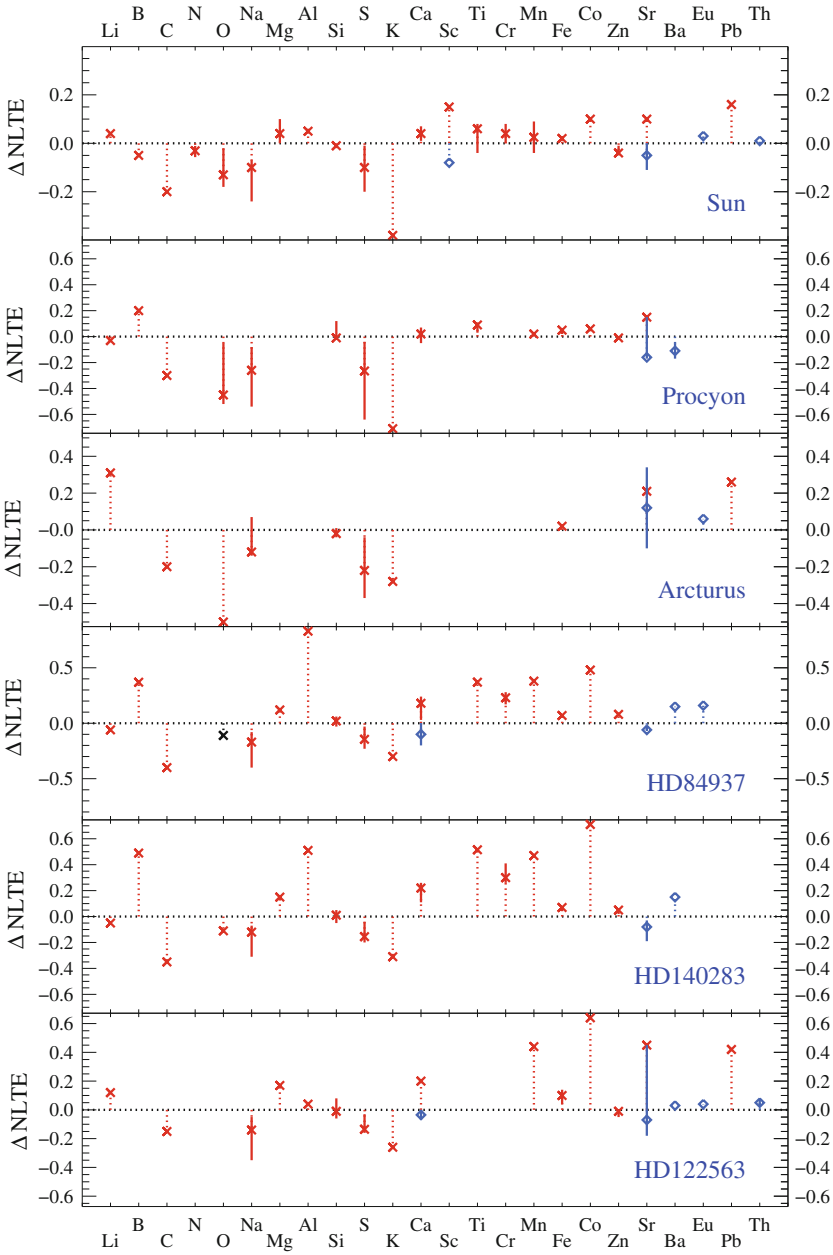

Fig. 4 NLTE effects on 24 elements for six representative, well-studied stars. NLTE effects are given as abundance corrections $\Delta\text{NLTE} = A(X)_{\text{NLTE}} - A(X)_{\text{LTE}}$. *Red crosses* and *blue diamonds* show results obtained from the lines of neutral and ionised atoms, respectively. *Solid*, *vertical lines* indicate min–max ranges of the corrections. The O I NLTE correction for Arcturus is the limiting value taken from Sitnova et al. (2013, Fig. 5). For HD 84937 we adopt the same value as for HD 140283, since Reetz (1998) found the same values for stars with similar parameters

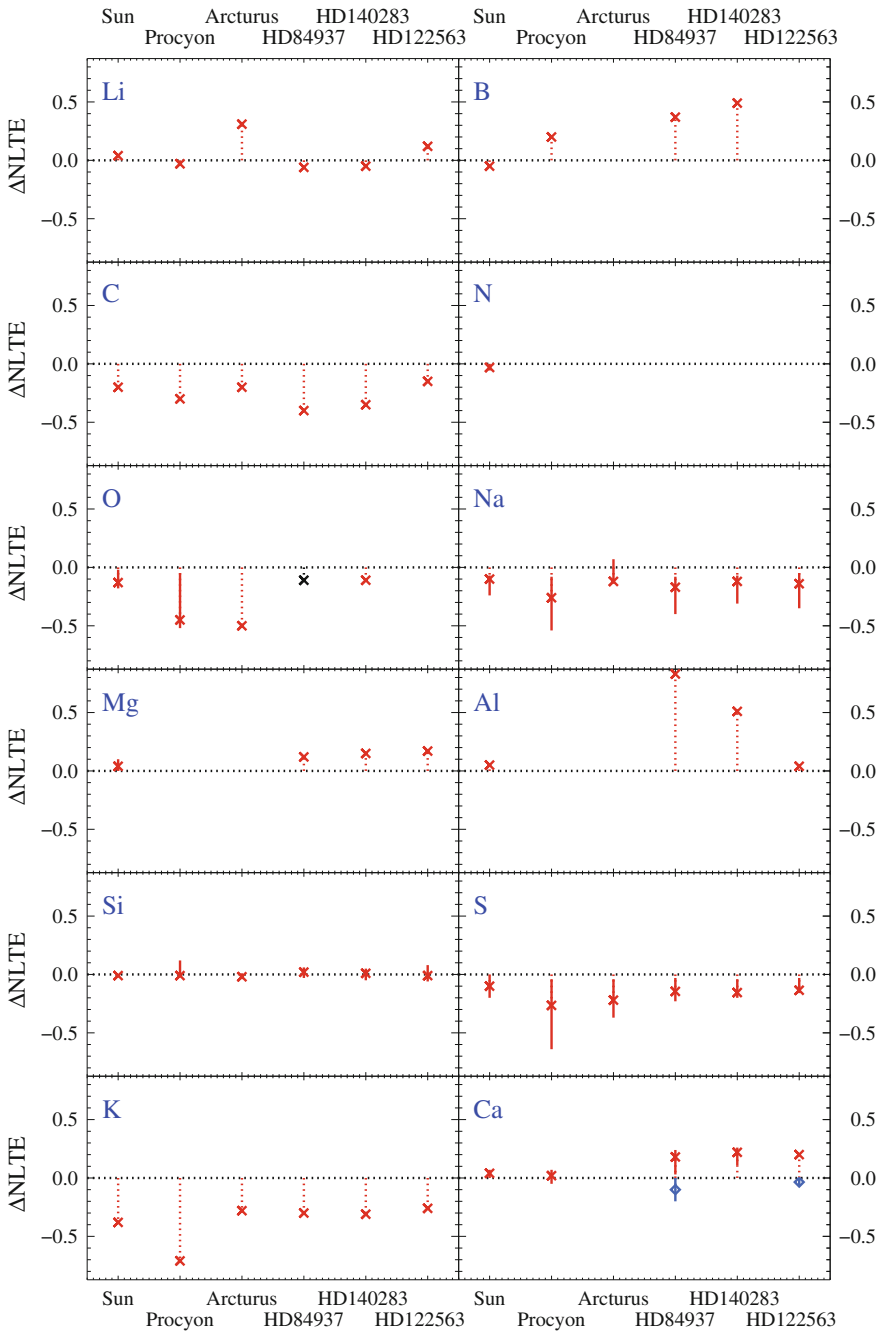

Fig. 5 As Fig. 4, but element-by-element

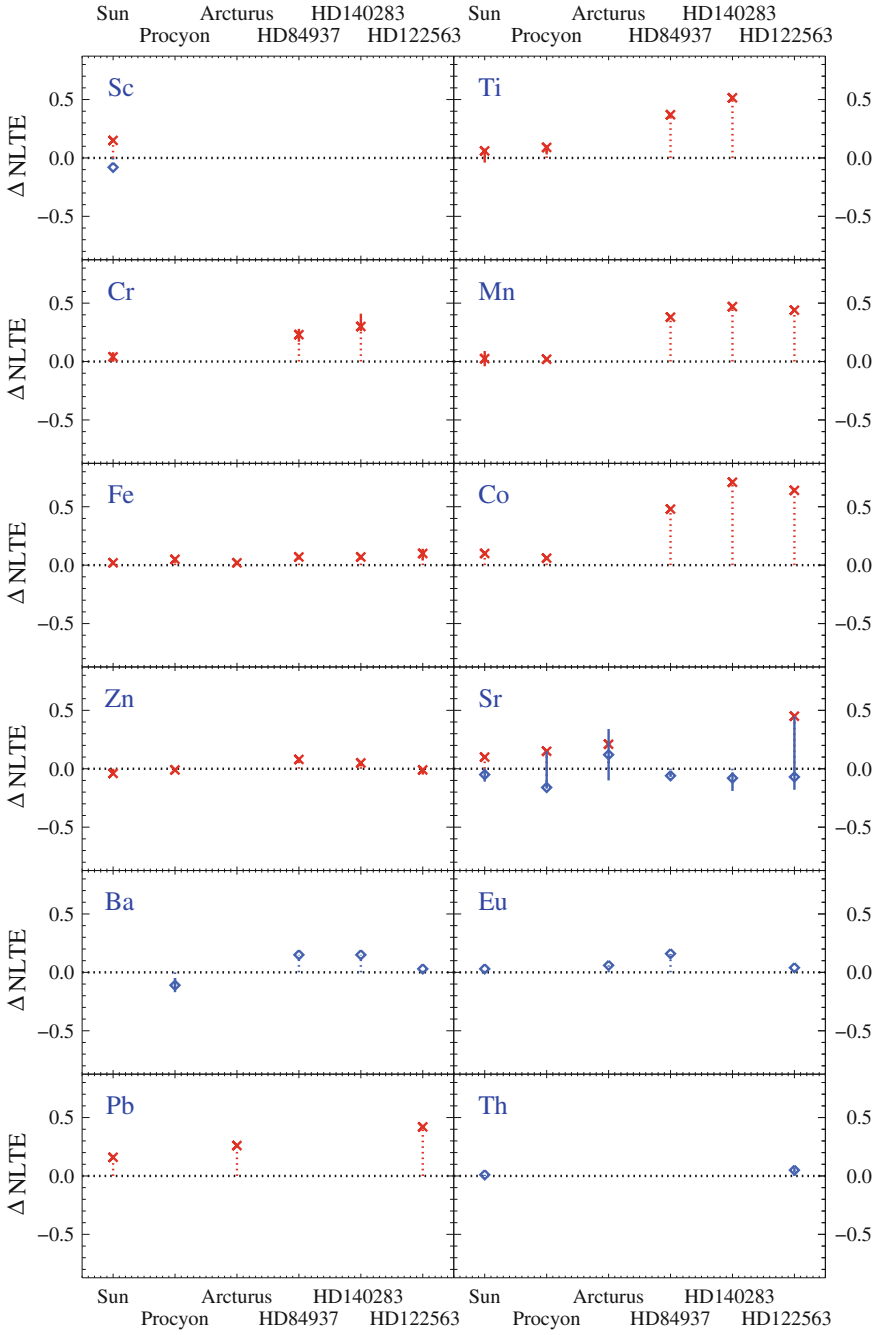

Fig. 5 (continued)

NLTE abundance corrections are negative for C I and O I, as well as for Sr II and Ba II at solar [Fe/H]. However, the NLTE effects for Sr II and Ba II drastically change at low-metallicity ([Fe/H] < -2): the lines tend to be weaker in NLTE and the abundance corrections grow positive. For Eu II, the positive NLTE corrections are caused by radiative pumping which weakens the lines, especially in metal-poor stars.

Note that the lines of atoms affected by hyperfine structure (e.g. Mn II, Ba II) should be treated with HFS components also in the NLTE line formation calculations. This may turn out to be important for higher-metallicity stars.

5 Summary and Conclusions

Non-local thermodynamic equilibrium is a framework, which describes consistently the propagation of radiation in a stellar atmosphere and its coupling to matter. LTE is the boundary case of NLTE, the approximation in the limit of infinitely large collision rates.

In this review lecture, the focus is on NLTE conditions in the atmospheres of cool late-type stars. The impact of NLTE on stellar parameter and abundance determinations can be gained from detailed theoretical and observational analyses, and these are now available for the most important chemical elements observed in the spectra of cool stars. So far, most studies in the literature focused on deviations from LTE in the spectral lines of neutral or singly-ionised atoms.

Generally, the results obtained by independent groups and methods are consistent and they can be summarised as follows. There are several well-defined types of NLTE effects, and consequently several groups of species which behave similarly under the same physical conditions in a stellar atmosphere (i.e. given the same $T_{\rm eff}$, $\log g$, and [Fe/H]). The first group is formed by species sensitive to over-ionisation (e.g. Mg I, Si I, Ca I, Fe I), the second group are collision-dominated species (Na I, K I), and the rest are mixed-type ions (e.g. Li I, O I, Ba II), which may show positive or negative NLTE effects depending upon different factors.

In some cases, the NLTE abundance corrections vary by an order of magnitude between the groups of elements. In other cases, cancellation may occur such that even the LTE analysis may provide the correct abundance *ratios* of two elements. Such pairs are difficult to establish, although, to first approximation, one may form pairs from elements in the same group, taking into account the excitation potential of the line as well as the elemental abundances. We want to stress, however, that a widely-spread 'rule of thumb' that the lines of the same ionisation stage can be safely modelled in LTE is a misconception.

Generally, any element analysed under the assumption of LTE should be regarded with caution (at least) until careful NLTE studies have been conducted. Even then, second-order NLTE effects related to line strengths and excitation potentials may turn out to fundamentally alter the outcome. With these potential pitfalls, we urge the reader to take NLTE corrections into account whenever possible.

Acknowledgments Figure 3 has been kindly provided by Rob Rutten; http://www.staff.science.uu.nl/~rutte101.

References

Asplund M (2005) Ann Rev A&A 43:481
Baumueller D, Gehren T (1997) A&A 325:1088
Bergemann M (2011) MNRAS 413:2184
Bergemann M, Cescutti G (2010) A&A 522:A9
Bergemann M, Gehren T (2008) A&A 492:823
Bergemann M, Pickering JC, Gehren T (2010) MNRAS 401:1334
Bergemann M, Hansen CJ, Bautista M, Ruchti G (2012a) A&A 546:A90
Bergemann M, Lind K, Collet R, Magic Z, Asplund M (2012b) MNRAS 427:27
Bergemann M, Kudritzki RP, Würl M, Plez B, Davies B, Gazak Z (2013) ApJ 764:115
Bruls JHMJ, Rutten RJ, Shchukina NG (1992) A&A 265:237
Caffau E, Maiorca E, Bonifacio P, Faraggiana R, Steffen M, Ludwig HG, Kamp I, Busso M (2009) A&A 498:877
Fabbian D, Asplund M, Carlsson M, Kiselman D (2006) A&A 458:899
Gehren T, Butler K, Mashonkina L, Reetz J, Shi J (2001) A&A 366:981
Gehren T, Shi JR, Zhang HW, Zhao G, Korn AJ (2006) A&A 451:1065
Johnson HR, Milkey RW, Ramsey LW (1974) ApJ 187:147
Kiselman D, Carlsson M (1996) A&A 311:680
Kunc JA, Soon WH (1991) J Chem Phys 95:5738
Lind K, Asplund M, Barklem PS (2009) A&A 503:541
Lind K, Asplund M, Barklem PS, Belyaev AK (2011) A&A 528:A103
Lind K, Bergemann M, Asplund M (2012) MNRAS 427:50
Lind K, Melendez J, Asplund M, Collet R, Magic Z (2013) A&A 554:A96
Mashonkina L, Gehren T, Bikmaev I (1999) A&A 343:519
Mashonkina L, Korn AJ, Przybilla N (2007) A&A 461:261
Mashonkina L, Zhao G, Gehren T, Aoki W, Bergemann M, Noguchi K, Shi JR, Takada-Hidai M, Zhang HW (2008) A&A 478:529
Mashonkina L, Ryabtsev A, Frebel A (2012) A&A 540:A98
Mihalas D (1978) Stellar atmospheres, 2nd edn. W. H. Freeman and Co, San Francisco
Mihalas D, Athay RG (1973) Ann Rev A&A 11:187
Reetz JK (1998) Sauerstoff in kühlen Sternen und die chemische Entwicklung der Galaxis
Rybicki GB, Hummer DG (1992) A&A 262:209
Sitnova TM, Mashonkina LI, Ryabchikova TA (2013) Astron Lett 39:126
Takeda Y, Zhao G, Chen YQ, Qiu HM, Takada-Hidai M (2002) PASJ 54:275
Takeda Y, Hashimoto O, Taguchi H, Yoshioka K, Takada-Hidai M, Saito Y, Honda S (2005) PASJ 57:751
Wijbenga JW, Zwaan C (1972) Solar Phys 23:265
Würl M (2012) NLTE analysis of silicon lines in solar-type stars and red super-giants
Zhang HW, Gehren T, Zhao G (2008) A&A 481:489
Zhao G, Butler K, Gehren T (1998) A&A 333:219

Analysis of Stellar Spectra with 3-D and NLTE Models

Maria Bergemann

Abstract Models of radiation transport in stellar atmospheres are the hinge of modern astrophysics. Our knowledge of stars, stellar populations, and galaxies is only as good as the theoretical models which are used for the interpretation of their observed spectra, photometric magnitudes, and spectral energy distributions. I describe recent advances in the field of stellar atmosphere modelling for late-type stars. Various aspects of radiation transport with 1-D hydrostatic, LTE, NLTE, and 3-D radiative-hydrodynamical models are briefly reviewed.

Keywords Radiative transfer · Hydrodynamics · Methods: observational · Techniques: spectroscopic · Stars: atmospheres

1 Introduction

Models of stellar atmospheres and spectral line formation are a crucial part of observational astrophysics. The models are our ultimate link between observations of stars and their fundamental physical parameters. On the one side, the models allow us to go from observable quantities, i.e stellar fluxes, spectral energy distributions, and photometric magnitudes, to physical parameters of stars, such as effective temperature $T_{\rm eff}$, surface gravity $\log g$, metallicity [Fe/H], abundances, rotation and turbulent velocities. The atmospheric models also allow us to convert theoretical bolometric luminosities from stellar evolution models to their observable quantities, theoretical colours, which are then compared with observations. For example, model versus observed colour-magnitude diagrams are used to determine distances and ages of clusters and field stars. The shapes of stellar energy distributions (SED) serve as a diagnostics of inter-stellar and circumstellar reddening. There are mass- and age-sensitive diagnostics in stellar spectrum, such as the ultra-violet Ca H and K lines,

M. Bergemann (✉)
Institute of Astronomy, University of Cambridge, Madingley Road, Cambridge CB3 0HA, UK
e-mail: mbergema@ast.cam.ac.uk

E. Niemczura et al. (eds.), *Determination of Atmospheric Parameters of B-, A-, F- and G-Type Stars*, GeoPlanet: Earth and Planetary Sciences,
DOI: 10.1007/978-3-319-06956-2_17,

which may help to distinguish a young star from an old star. Detailed chemical abundances are arguably the most important physical quantities, which can be only deciphered from a stellar spectrum. They link stellar properties to nucleosynthesis of elements in the Big Bang, in stars at the end of their life-times, in violent explosions, caused by stellar interactions, and by cosmic ray acceleration in the interstellar medium (ISM). This connection forms the basis of important diagnostic methods to constrain formation and evolution of stars, stellar populations, and galaxies.

In short, all fundamental physical stellar quantities critically depend on the models we use for the analysis of observations. Until recently, we could only use the simplest 1-D hydrostatic models in local thermodynamic equilibrium (LTE) for stellar parameter determinations, for more sophisticated models were far too computationally expensive. Calculation of a 3-D radiative-hydrodynamical (3-D RHD) model required months of CPU time, which was of little use for any practical application in spectroscopic analysis. Moreover, the accurate solution of radiation transport even in the time-independent scheme has been too demanding for quantitative applications. Non-local thermodynamic equilibrium (NLTE) calculations were disfavoured for several reasons. First, inversion of large matrices in the complete linearisation scheme (for solving coupled statistical equilibrium equations in NLTE) was prohibited for atoms with complex atomic structure. Furthermore, the lack of accurate ab initio calculations or experimental atomic data led to the need to introduce simplified treatment of several types of atomic processes in vastly more complex NLTE calculations, which caused a widespread misconception that NLTE calculations are of questionable advantage.

It is crucial to realise that NLTE is not an approximation, in contrast to LTE, which approximates all collision rates by the infinitely large numbers, and fully ignores the influence of radiation field in stellar atmospheres on the energy distribution of matter. However, one may solve time-dependent rate equations, or drop the time dependence, which reduces the problem to solving the equations of statistical equilibrium only (see below).

However, the theory of radiative transfer in stellar atmospheres is one of the most mature field in astrophysics (e.g. the fundamental work by Mihalas (1978)) and the numerical implementation of the theory has seen substantial improvement over the past decade. Moreover, we have enough computational power to simulate stellar convection in 3-D and solve for radiative transfer explicitly taking into account the interaction of gas particles with the radiation field. In this lecture, I summarise the main progress in modelling atmospheres and spectra of cool, F, G, K and M, stars, that has been made during the past decade, and provide a timeline for the developments in the field, which can be expected in the near future. I do not touch upon the problems of radiative transfer in more complex cases, such as expanding supernova shells (Lucy 1999), dusty AGB envelopes (Höfner et al. 2003, and references therein), or chromospheres (e.g. Hansteen et al. 2007).

2 Basic Considerations

The analysis of cool F, G and K stars meets with two main kinds of difficulties. These stars have a sub-surface convection zone and radiation field in their photospheres is highly non-local. As a consequence, neither of the two classical modelling approximations, LTE and 1-D hydrostatic equilibrium, is valid and cannot be justified without detailed ab initio theoretical calculations. An excellent review of NLTE and 3-D simulations from a theoretical perspective is given by Mihalas and Athay (1973) and Spruit et al. (1990); a comprehensive summary of 3-D and NLTE in application to stellar abundance analysis is provided in Asplund (2005).

What is the reason for NLTE? A star is not a perfect black-body and radiation field influences the physical state of matter and vice versa. Therefore, only consistent NLTE radiative transfer will correctly recover the thermodynamic structure of the atmosphere and thus the properties of its radiation field. In NLTE, the particle distribution functions, i.e. the excitation and ionisation states, are influenced by the radiation field that causes them to depart from the LTE values. Why this happens is easy to understand. Stellar atmosphere is the region where radiation escapes into ISM. Deep in the atmospheres, opacity is large and the photon mean free path is very small. Radiation transport occurs over very small length scales, thus connecting gas parcels with very similar thermodynamic properties.

The definition of a *stellar surface* is somewhat vague. Strictly speaking, this is the boundary where material at the most transparent wavelength λ becomes optically thin, $\tau_\lambda < 1$. This wavelength is 1.6 μm, where the H^- opacity in continuum is at its minimum; however, in practice this wavelength is rarely used. It is more common to refer to the $\lambda = 500$ nm, where most of the flux is emitted by a typical solar-like star, or to the Rosseland mean opacity, a Planck-function weighted average over all frequencies.

Photon mean free path is the length scale over which thermalisation takes place.

However, closer to the stellar surface the photon mean free path λ_p becomes large, larger than the scale height of material. Thus, as we move outwards, the decoupling between radiation and matter increases, and radiation becomes non-local, anisotropic, and strongly non-Planckian. Many spectral lines form in NLTE showing shapes which bear no resemblance with the line profiles predicted by classical LTE models. For example, the Mg I line at 12 μm reverts to emission at the solar limb that can be only accounted for by NLTE models. The effect on other spectral features is less obvious, although it may still dramatically impact the line equivalent widths and their detailed profiles, i.e. the total energy absorbed in a line (see next Section).

Another major source of complexity is convection. There are several observable manifestations of stellar convection, the most prominent being stellar surface granulation, which has been in the focus of observational research for more than a

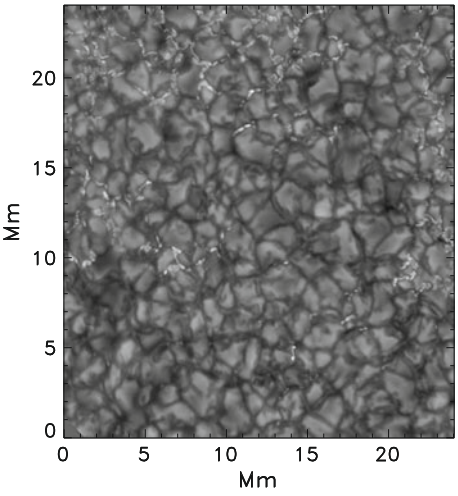

Fig. 1 Solar granulation in the G-continuum (Nordlund et al. 2009). Observations were made by the Swedish 1 m Solar Telescope (Institute of Theoretical Astrophysics, Oslo). Reproduced by permission from the authors and the publisher

decade. Figure 1 shows a patch on the solar surface observed with the Swedish Solar Telescope. The intensity fluctuations correspond to brighter granules and darker inter-granular lanes. The brightness fluctuations are about 20 %, while the actual temperature contrast across the granulation pattern is about 25 %. This mild dependence of surface intensity variation on T is caused by the huge sensitivity of H^- continuum opacity to the temperature. The other key observable are the characteristic C- and inverse C-shaped bisectors of the line profiles that are caused by up- and down-flows (e.g. Gray et al. 2008). The bisectors can be best observed in the very high-quality solar spectrum (Fig. 2).

Indeed, these beautiful observations motivated the development of complex 3-D radiative hydrodynamics (RHD) models (Nordlund et al. 2009) and even larger solar telescopes, such as, e.g. the new German 1.5 m GREGOR telescope. Inhomogeneities, spots, and convective motions were also resolved on the surfaces of red supergiants (Buscher et al. 1990; Wilson et al. 1992; Tuthill et al. 1997; Wilson et al. 1997; Young et al. 2000; Haubois et al. 2009; Ohnaka et al. 2009; Kervella et al. 2009; Ohnaka et al. 2011). More interesting results about atmospheric structure and dynamics of cool stars will soon come to light with new telescopes and missions, such as the Herschel Space Observatory (Teyssier et al. 2012). All these data will need complex theoretical models to understand the physics underlying the observed phenomena.

3 Theory

What we are trying to understand is how the stellar light we detect with our instruments, e.g. in the form of a spectrum, is created in a stellar atmosphere. Thus, the essence of problem is to solve the radiative transfer equation, which describes the temporal and spatial evolution of the radiation field J_ν:

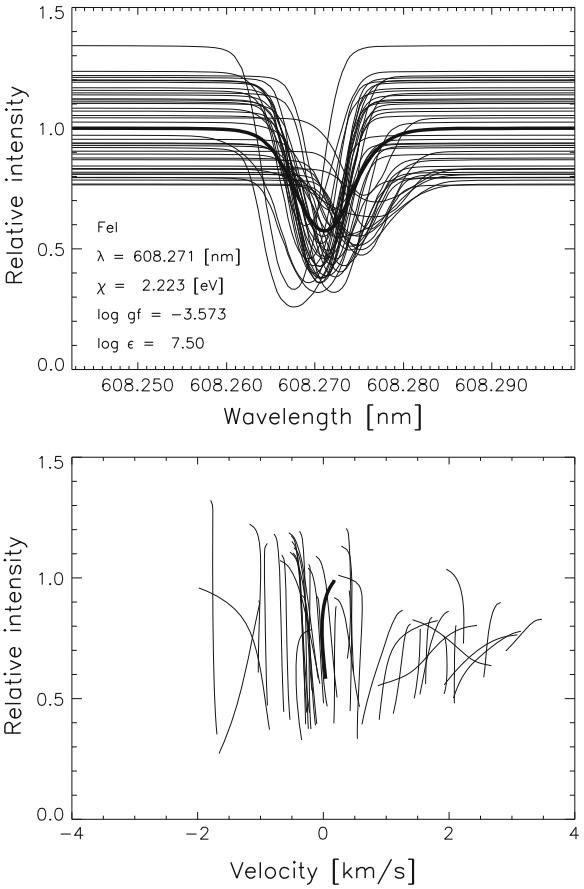

Fig. 2 Line profiles of the Fe I line at 6082 Å in the 3-D RHD simulations of the solar atmosphere (Asplund et al. 2000). *Top panel* spatially-resolved profiles. *Bottom panel* the line bisectors. The *thick lines* on both panels indicate the spatially-averaged profile and the *C-shaped* bisector. The line asymmetries are a consequence of *blue-* and *red-*shifts caused by the influence of the convective velocity fields on the line formation. Reproduced by permission from the authors and the publisher

$$\frac{1}{c}\frac{dI_\nu}{dt} + \frac{dI_\nu}{ds} = \eta_\nu - \alpha_\nu I_\nu, \tag{1}$$

where ds is geometrical path length along the beam, η_ν and α_ν are the monochromatic (linear or volume) emission and extinction coefficients. Clearly, the transport of radiation depends on the medium in which it propagates. Thus, we also need a model that describes the thermodynamic properties in stellar atmospheres, which must include radiation transport.

There are several types of models, vastly different in complexity and computational burden: from the simplest 1-D LTE hydrostatic models to the (presently) most sophisticated 3-D RHD LTE models with scattering. In all cases, the radiative transfer is assumed to be *quasi-static*, i.e. the time derivative is neglected, which is not a bad approximation because the photon propagation time is much shorter than the fluid motion time. The computational timescales range from few seconds of CPU to several months. In the next section, I will summarise the main ingredients of all these model types without going into details of how the equations are solved (see e.g. Mihalas 1978).

3.1 Classical 1-D Static Model Atmospheres

The simplest models are computed using the 1-D hydrostatic LTE approximations. We have to solve several equations:

1. **Equation of radiative transfer** in the static, time-independent, case. For a plane-parallel atmosphere with a geometrical depth z (it is straightforward to generalise this to a spherically-symmetric case):

$$\cos\theta \frac{dI_\nu}{dz} = \alpha_\nu I_\nu - \eta_\nu. \tag{2}$$

   This equation describes a change of specific intensity I_ν, as radiation passes through a slab of a thickness dz. For the plane-parallel approximation, the latter is represented by the projection at angle θ between the direction of the light beam and the z axis. The parameters α_ν and η_ν with dimensions cm^{-1} are the monochromatic linear extinction and emission coefficients; their ratio gives a source function $S_\nu = \dfrac{\eta_\nu}{\alpha_\nu}$. In LTE calculations, the source function is equal to the Planck function $S_\nu = B_\nu$ if only true absorption and emission processes are considered (strict LTE), or approximated by a two-level form, $S_\nu = (\kappa_\nu B_\nu + \sigma_\nu J_\nu)/(\kappa_\nu + \sigma_\nu)$, where κ_ν is the true absorption and σ_ν the scattering coefficient. In 'less strict' LTE, one may include, for example, a coherent isotropic scattering in continuum, e.g. Thomson scattering on electrons e^-.
2. **Equation of flux constancy**, or energy conservation:

$$F = \frac{L}{4\pi R^2} = \sigma {T_{\rm eff}}^4, \tag{3}$$

   where F is the bolometric flux, L the luminosity, R the stellar radius, and $T_{\rm eff}$ the effective temperature. In other words, the divergence of the total energy flux transported to the surface is zero, $\nabla F = 0$ (see the next section on 3-D RHD models), and the total flux is equated to the integral flux from the surface of a black body.

The total flux is usually taken to be the sum of convective and radiative components, $F = F_{\rm conv} + F_{\rm rad}$. The convective flux, $F_{\rm conv}$, is needed because in deeper atmospheric layers, energy is mostly carried by convection. In the standard 'mixing-length' type approximations, $F_{\rm conv} \sim \frac{\alpha_{\rm MLT}}{H_p}$, where H_p is pressure scale height and $\alpha_{\rm MLT}$ the mixing-length parameter. There are attempts to calibrate the mixing length parameter based on 3-D models (see next Section).

3. **Radiative equilibrium equation**[1]:

$$\int_0^\infty \alpha_\nu J_\nu(\tau) d\nu = \int_0^\infty \alpha_\nu S_\nu(\tau) d\nu, \tag{4}$$

where τ is the optical depth, J_ν the mean intensity averaged over all directions, and S_ν the source function. The left-hand side of the equation can be viewed as radiation 'sink' term, and right-hand side as the radiation 'source' term, which in LTE is usually equal to the Planck function (see the next section for how this is treated in 3-D RHD models). In the calculations of energy balance with 1-D hydrostatic models, it is presently possible to evaluate detailed opacity on more than 10^5 wavelength points (e.g. Gustafsson et al. 2008; Grupp 2004). This samples the majority of the atomic and molecular lines, which contribute to the opacity under conditions typical of a late-type star.

4. **Equation of hydrostatic equilibrium**:

$$\nabla P_{\rm tot} = -\rho \frac{G M_r}{r^2}, \tag{5}$$

where ρ is the density, M_r the mass at the radius r, $\nabla P_{\rm tot} = \nabla P_{\rm gas} + \nabla P_{\rm rad}$, i.e the sum of gas and radiative pressures. The latter can be expressed as:

$$\nabla P_{\rm rad} = -1/c \int_0^\infty (\kappa_\nu + \sigma_\nu) F_\nu d\nu. \tag{6}$$

Gas pressure is balanced by the gravitational attraction, which does not change with depth in plane-parallel models. In spherically-symmetric models, $g = g(r)$, so mass (M) and luminosity ($L = 4\pi r^2 F(r)$) are constant throughout the atmosphere. Note that there are some variations, e.g. some models include a turbulent pressure term, $\nabla P_{\rm turb} \sim \rho \upsilon_t^2$, where υ_t is the characteristic velocity, which may be used e.g. in very extended atmospheres (red giant branch or red supergiant stars) to approximate the levitation of the photosphere, the effect of 3-D hydrodynamics. For detailed numerical schemes and practical implementation of the equations, the reader is referred to Kurucz (1993); Grupp (2004); Gustafsson et al. (2008).

[1] Assuming that energy is transported by radiation only.

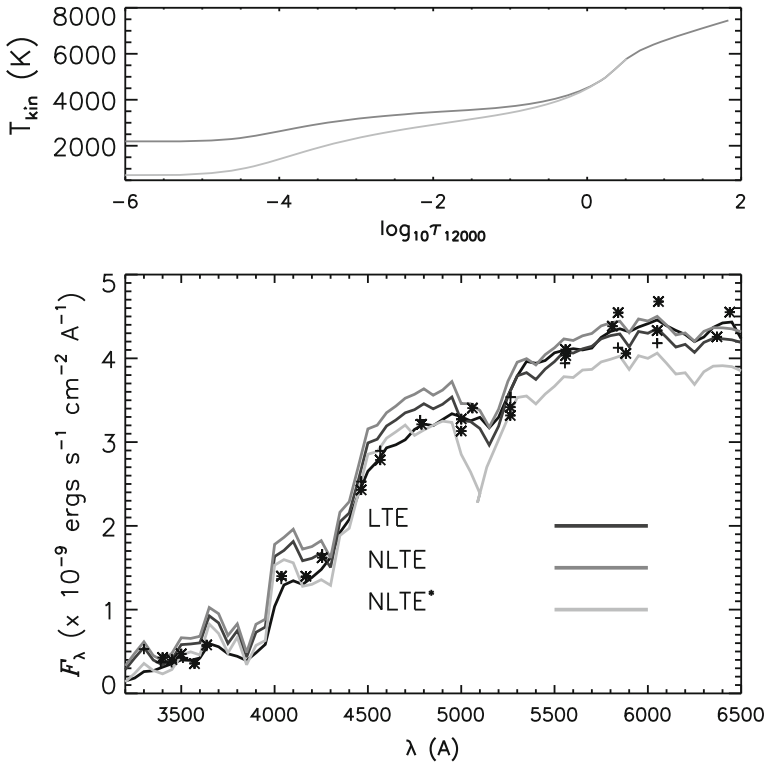

Fig. 3 NLTE model atmospheres (*top*) and synthetic spectra (*bottom*) for Arcturus, a very cool RGB star (*dark* LTE, *light NLTE*). *NLTE** refers to the NLTE calculations with an ad-hoc kinetic temperature structure adjusted to fit the near-UV SED; note, however, that the fit in the optical range has degraded. Reproduced by permission from the authors (Short and Hauschildt 2009) and from the publisher

With the 1-D hydrostatic approximation, it is also possible to compute fully-consistent NLTE models including the feedback on the atmospheric structure. Such models can be computed with the PHOENIX code (Baron and Hauschildt 1998), which is very versatile in its applicability. In NLTE, PHOENIX includes more than 20 elements in the rate equations. NLTE model atmospheres, because of the UV overionization in Fe, lead to *warmer* outer atmospheric layers with respect to LTE for stars with $T_{\rm eff} \gtrsim 5{,}400$ K (Short and Hauschildt 2005, 2009). However, surface cooling by $\sim$150 K is predicted for the cooler stars, like the RGB star Arcturus (Fig. 3, top panel), which is caused by the UV over-ionisation in the bound-free edges of Mg, Si, and Al. This has a major impact on the UV fluxes of cool stars (Fig. 3, bottom panel).

3.2 3-D RHD Model Atmospheres

Full time-dependent, 3-D, RHD simulations of radiative and convective energy transport in stellar atmospheres have existed for more than two decades. The seminal papers in this field are Nordlund (1982), Stein and Nordlund (1998), and Spruit et al. (1990). The 3-D RHD models have substantially gained in complexity since then (e.g. Nordlund et al. 2009; Chiavassa et al. 2011; Collet et al. 2011; Beeck et al. 2012), in particular in the treatment of radiation transport. More details about the state-of-the-art models and their application to modelling stellar spectra will be given in the next section; here I only briefly review the equations of radiative hydrodynamics, needed to compute the models.

The main difference with respect to hydrostatic models (see above) is that one solves time-dependent fluid-hydrodynamics equations for compressible fluid flow. In Eulerian form, the equations are:

1. **The equation of continuity or mass conservation**:

$$\frac{\partial \rho}{\partial t} = -\nabla \cdot (\rho \boldsymbol{v}), \tag{7}$$

where $\boldsymbol{v} = \boldsymbol{v}(x, z, y, t)$ is the velocity vector. The equation essentially means that in the ascending flow, the rapid decrease of density can be balanced by the rapid expansion sideways.

2. **Equation of motion**:

$$\frac{\partial \rho \boldsymbol{v}}{\partial t} = -\nabla \cdot (\rho \boldsymbol{v}\boldsymbol{v}) - \nabla P - \rho \nabla \Phi - \nabla \cdot \tau_{\rm visc}, \tag{8}$$

where P is the gas pressure, Φ the gravitational potential, $\tau_{\rm visc}$ the viscous stress tensor. The first term on the right-hand side is the divergence of the vertical component of Reynold's stress tensor, i.e. the force density on the fluid due to the turbulent fluctuations. Under the assumption of slow and bulky fluid motions, one simply recovers the equation of hydrostatic equilibrium (Eq. 5).
In the 'box-in-a-star' simulations, the gravitational potential is a constant, so $d\Phi/dz = -g$, surface gravity. Box-in-a-star simulations are usually applied to modelling solar-like stars (e.g. Stein and Nordlund 1998).
In contrast, in the 'star-in-a-box' setup, the simulation box includes the whole star (e.g. Freytag et al. 2012). In the 'star-in-a-box' regime, one assumes a spherical potential in the form:

$$\Phi = -\frac{GM}{(r_0^4 + r^4/\sqrt{1} + (r/r_1)^8)^{1/4}}, \tag{9}$$

where r_0 and r_1 are the so-called 'smoothing parameters'. They provide limiting values of gravitational potential for $r \to 0$ and $r \to \infty$. For large 'stars-in-a-box'

models, $r_0 \sim 0.2\, R_{\rm star}$. This setup is applied to model very extended, variable and stochastically pulsating stars, such as cool giants and red supergiants. Note that the size of granules is very different for solar-like and giant stars; it scales with the pressure scale height (Freytag et al. 2002).

3. **Energy conservation**:

$$\frac{\partial E}{\partial t} = -\nabla \cdot (\boldsymbol{v}(E_{\rm int} + P)) - \frac{1}{2}\nabla \cdot \rho v^2 \boldsymbol{v} + Q_{\rm rad} + Q_{\rm visc}, \tag{10}$$

where E is the total energy density, i.e. the sum of internal $\mathrm{E_{int}}$ and kinetic $\mathrm{E_{kin}}$ energies, $Q_{\rm visc}$ is the viscous dissipation term and $Q_{\rm rad}$ is the radiative term, which is expressed as:

$$Q_{\rm rad} = -\nabla \cdot F_{\rm rad} = 4\pi \int_0^\infty \alpha_\nu (I_\nu - S_\nu) d\Omega d\nu. \tag{11}$$

Here the intensity I comes from the solution of radiation transport equation, which is done separately on a system of rays for different outgoing directions. Radiative transfer calculations in 3-D are very expensive, because it is necessary to compute several radiative ray directions for every convective time step in the RHD computation. Therefore, the radiation field is computed using opacity bins, which are constructed by sorting all (line plus continuum) opacities into groups according to their amplitude (Nordlund 1982):

$$Q_{\rm rad} \equiv \sum_{n=1, n_{\rm bins}} (J_{\rm bin} - B_{\rm bin}) w_{\rm bin}, \tag{12}$$

where J and B are the mean intensity and the Planck function, and each quantity in this equation refers to a 'bin' rather than to a wavelength. The $w_{\rm bin}$ term is the weight of each bin, computed as a sum of the weights of individual wavelength points in a bin. Note that in this definition, one assumes that the Planck function does not vary much across a bin. Modern codes (such as Stagger) use up to 12 opacity bins, which sort the opacities according to magnitude and wavelength.

There are several codes available for 3-D RHD modelling: the Copenhagen Stagger code (Nordlund and Galsgaard 1992), MURAM (Vögler et al. 2005), BIFROST (Gudiksen et al. 2011), CO5BOLD (Freytag et al. 2012; Chiavassa et al. 2011), ANTARES (Muthsam et al. 2010). All these codes are capable of simulating stellar convection in the 'box-in-a-star' regime. The CO5BOLD code also supports the 'star-in-a-box' simulations of stellar convection.

In the 'box-in-a-star' regime, the physical domains of the simulations cover a representative portion of the stellar surface. Vertically, they include the whole photosphere as well as the upper part of the convective layers, typically encompassing 12 to 15 pressure scale heights. Horizontally, they extend over an area sufficiently large to host at least about ten granules at the surface. Figure 4 shows a snapshot from a 3-D RHD simulation of the solar surface convection. The granule characterised by warm

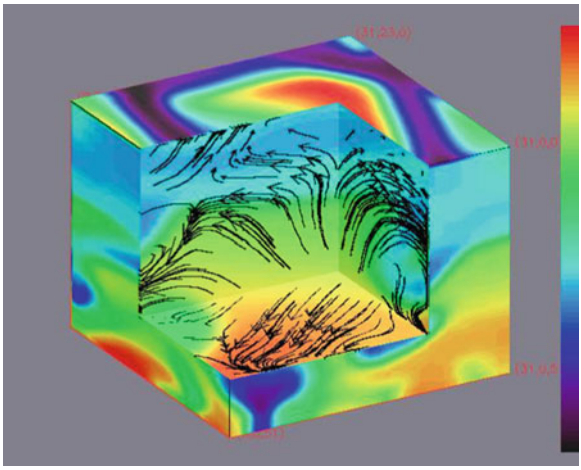

Fig. 4 A granule in the simulation of the solar convection. The colour bar indicates temperature. By permission from the authors (Nordlund et al. 2009) and from the publisher

up flowing material is surrounded by cooler inter-granular lanes, in which material sinks under the influence of gravity. Such models predict a different temperature and pressure structure of a stellar atmosphere, especially for stellar parameters different from the Sun. For example, at low metallicity, 1-D hydrostatic models severely overestimate the average temperatures of the upper atmospheric layers, with profound implications for the spectral line formation (e.g. Collet et al. 2007).

One may also use 3-D RHD models to devise smart calibration relationships, which can be applied in 1-D hydrostatic computations to better approximate the complex physical processes. One of the most interesting applications is the calibration of the *mixing-length parameter*, $\alpha_{\rm MLT}$. Figure 5 shows the behaviour of α with the effective temperature $T_{\rm eff}$ and surface gravity $\log g$. The $T_{\rm eff}$-scale is logarithmic. Evolutionary tracks (Paxton et al. 2011) are also indicated. The α-values are indicated with colours. The solar simulation is indicated with a $\odot$ and the locations of the other simulations are shown with asterisks. In all 1-D hydrostatic models (such as MARCS, ATLAS, MAFAGS), the mixing-length is constant, and, depending on the formulation (e.g. Böhm-Vitense 1958, or Canuto and Mazzitelli 1991), it takes values from 0.5 to 1.5. From Fig. 5, it is obvious that none of these factors are physically sensible across the full HRD. At best, a constant α could be used for the stars very similar to the Sun, but not for any other star.

Grids of 3-D models have been presented in Tanner et al. (2013, 14 models), Trampedach et al. (2013, 37 models), Ludwig et al. (2009, 77 models), Magic et al. (2013, 202 models). Also, spatialf and temporal averages of the full RHD models have been constructed; such models facilitate calculation of large grids of synthetic spectra at a reasonable computation cost, thus allowing to apply them in problems of stellar abundance analysis (e.g. Caffau et al. 2011; Bergemann et al. 2012c; Tremblay et al. 2013).

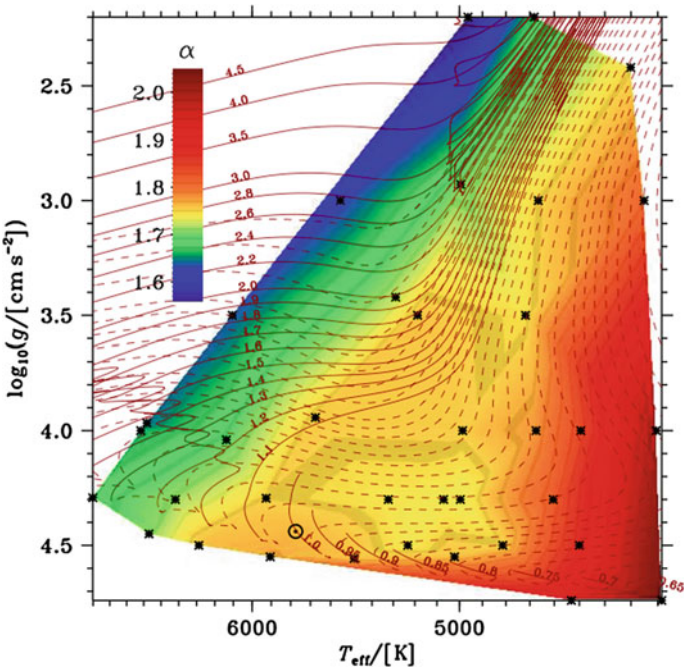

Fig. 5 The behaviour of the calibrated MLT α with $T_{\rm eff}$ and $g_{\rm surf}$ (Figure courtesy of R. Trampedach, see also Trampedach et al. 2013). The $T_{\rm eff}$-scale is logarithmic. We have also plotted evolutionary tracks produced with the MESA-code (Paxton et al. 2011), covering the mass-range 0.65–4.5 $M_{\odot}$, as indicated. The dashed lines correspond to the pre-main-sequence evolution. The α-values were interpolated linearly on Thiessen triangles between the simulations, and indicate the values with colours as shown on the colour bar. The solar simulation is indicated with a $\odot$ and the locations of the other simulations are shown with *asterisks*

`StaggerGrid project` (Collet et al. 2011) is a collaborative project for the construction of a comprehensive grid of time-dependent 3-D RHD model atmospheres of solar- and late-type stars. The project involves several research groups and different RHD codes.

4 Line Formation and Spectrum Synthesis

Once we have a model providing basic thermodynamic quantities of an atmosphere as a function of depth, it is straightforward to calculate the emergent stellar spectra. The model spectra are then directly compared with observations, and stellar parameters can be determined from the best-fit templates (Fig. 6).

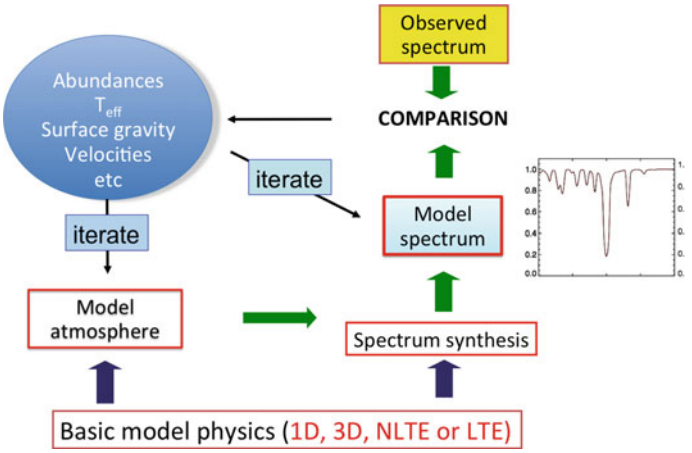

Fig. 6 The basic flow chart of spectroscopic analysis

4.1 LTE Spectrum Synthesis

In LTE, the calculation of model spectra can be easily done in 1-D or 3-D geometry, by computing the formal solution of the radiative transfer equation along a series of rays at different μ angles using the long- or short-characteristics methods (see e.g. Hauschildt and Baron 2006). Long characteristics method is preferred for detailed line profiles, while short characteristics one is used for solving approximate radiation transport in 3-D RHD simulations. If scattering is included, iterative solutions are needed, such as variable Eddington factor (Auer and Mihalas 1970).

In 1-D LTE, very efficient and well-tested codes to compute full synthetic spectra are SIU (Reetz 1999; Schoenrich and Bergemann 2013) and TURBOSPECTRUM (Alvarez and Plez 1998; Plez 2012), SYNTHE (Kurucz 2005). These codes were used to compute full libraries of synthetic spectra (e.g. Murphy and Meiksin 2004; de Laverny et al. 2012) for stellar spectroscopy or population synthesis.

Codes that are able to compute 3-D line formation in LTE include SCATE (Hayek et al. 2011), OPTIM3D (Chiavassa et al. 2009), ASSET (Koesterke et al. 2008), LINFOR3D (Cayrel et al. 2007). These codes can potentially be used to compute full 3-D grids of synthetic spectra. For example, a grid of 3-D synthetic spectra has been recently presented by Allende Prieto et al. (2013).

Figure 7 shows the CN lines computed with a 3-D RHD model of a metal-poor giant, in comparison with the 1-D hydrostatic model (Collet et al. in prep.). In addition to a different temperature structure, temperature and pressure fluctuations in the 3-D models contribute strictly positively to the molecular number density (Uitenbroek and Criscuoli 2011), which is why the abundance derived from molecular lines is lower. In Fig. 7, the CN lines in 3-D provide a -0.4 dex lower abundances compared to the 1-D result.

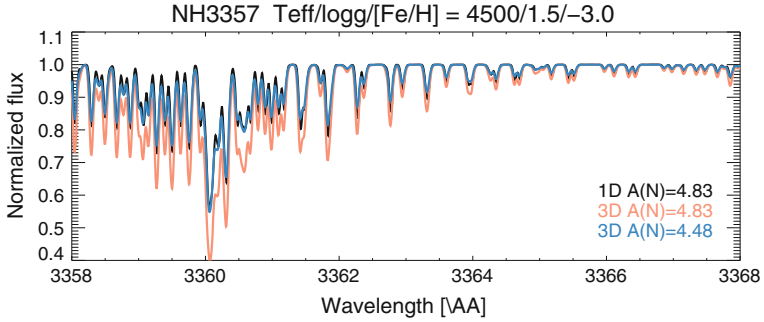

Fig. 7 CN lines computed with a 3-D RHD model of a metal-poor star (Collet et al., in prep)

4.2 NLTE

In NLTE, the problem of radiative transfer and thus modelling a spectrum is much more complex. Radiative transfer shall be solved simultaneously with the rate equations, the latter providing coupling between non-local radiation field and local properties of the gas:

$$\frac{\partial n_i}{\partial t} + \nabla \cdot (n_i \boldsymbol{v}) = \sum_{j \neq i} n_j P_{ji} - n_i \sum_{j \neq i} P_{ij}, \tag{13}$$

where n is the number density of species of a certain type (e.g. atoms on the excitation state i), P the total transition rates (radiative plus collisional) between the states. In the time-independent case, the left-hand term can be neglected and we recover the statistical equilibrium (SE) equations. Even in the 1-D hydrostatic case, the solution of the RT and SE requires very efficient numerical schemes. In 1-D, the most widely-used codes are DETAIL (Butler and Giddings 1985 and the updated version by Bergemann et al. 2012b) and MULTI (Carlsson 1992). The codes are stable and efficient. Presently, they are most useful for the diagnostics and detailed analysis of NLTE effects, especially for complex multi-electron atomic systems, like Fe I, and applications to stellar parameter and abundance analysis of large datasets.

In 3-D, MULTI3D (Botnen and Carlsson 1999; Leenaarts and Carlsson 2009) and MUGA (Auer et al. 1994) are frequently used for the analysis of stellar observations. The codes have been already applied to solve line transfer problems in the Sun and late-type stars. For example, Fig. 8 shows how the Li I line strength varies across the surface of star in a 3-D radiation-hydrodynamic simulation (Lind et al. 2013). Other interesting applications of the fully 3-D NLTE framework include Asplund et al. (2003, Li I), Cayrel et al. (2007, Li I), Asplund et al. (2004, O I), Trujillo Bueno and Shchukina (2007, Sr I), Leenaarts et al. (2009, Ca II), Lind et al. (2013, Ca I, Na I). It is now also possible to perform NLTE line formation with the temporal and spatial averages of 3-D models, such as done by Bergemann et al. (2012c) for Fe I and Bergemann et al. (2013) for Ti I and Si I lines.

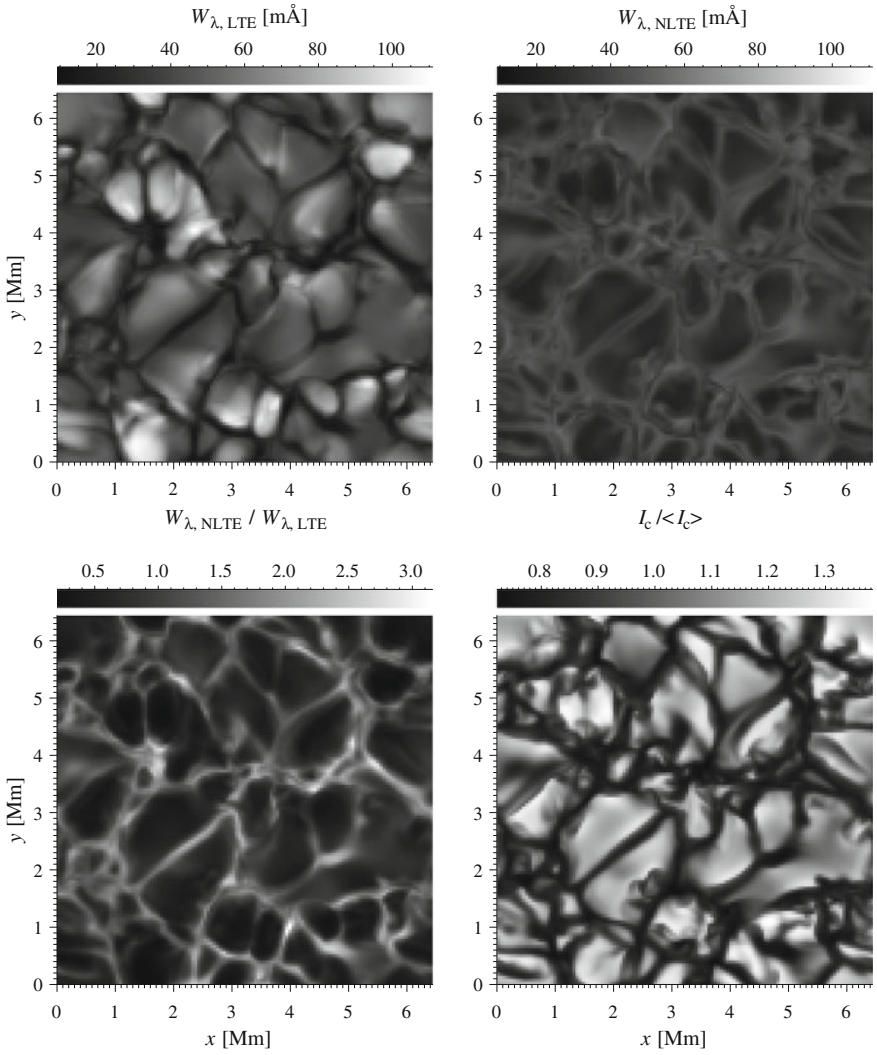

Fig. 8 Variation of the equivalent width for a Li I line at 6707 Å across a surface of a metal-poor star; the NLTE radiative transfer was computed using the 3-D RHD simulation (Lind et al. 2013). Reproduced from permission by the author and the publisher

In general, NLTE effects on spectral line formation are well-understood for most of the chemical elements. The majority of species, whose lines are observed in the spectra of F, G, K and M stars, are affected by NLTE over-ionization. That means, the NLTE lines are weaker, especially if they are on the linear part of the

curve-of-growth. In this case, the NLTE effects on the ionisation balance are typically large for giants and metal-poor stars (e.g. Bergemann et al. 2012c). Resonance line scattering is relevant for strong lines of singly-ionised elements (Bergemann et al. 2012a; Shchukina et al. 2009, Ba II, Sr II:). Atomic lines of neutral species in the IR may show emission line cores (Carlsson and Rutten 1992; Carlsson et al. 1992). A detailed discussion of the NLTE effects in the spectral lines of different elements can be found in (Mashonkina 2013).

While the detailed solution of NLTE radiative transfer in 1-D is straightforward, this is not always simple, especially when it concerns stellar abundance analysis. The most difficult task is usually to assemble a comprehensive model atom using the best atomic data available for a given element. This involves mining large atomic databases, like TOPbase and Kurucz web-servers, NIST, VALD; it is even more difficult to homogenise the atomic information, e.g. electronic configurations and level energies, particularly when the combination of quantum-mechanical and experimental data is needed to ensure the completeness of the model atom. For those workers in the field of observational stellar astrophysics, who are not directly involved in the development of NLTE radiative transfer models, this is a difficult task to undertake.

A simpler approach has been developed, which allows to bypass difficult statistical equilibrium calculations. The idea is to use *NLTE abundance corrections*, which can be pre-computed for a large grid of model atmospheres and element abundances. The NLTE abundance correction is then applied to a best-fit LTE abundance. Numerous tests showed that the accuracy of NLTE element abundances obtained by this method is very good.

NLTE abundance correction for a given chemical element, $\Delta_{\rm El}$, is defined as:

$$\Delta_{\rm El} = \log {\rm A(El)}_{\rm NLTE} - \log {\rm A(El)}_{\rm LTE} \tag{14}$$

i.e., it is the the logarithmic correction, which has to be applied to an LTE abundance determination A of a specific line to obtain the correct value corresponding to the use of NLTE line formation.

INSPECT[2] is the first project which allows one to compute NLTE corrections on-line; one may also request LTE or NLTE abundance for a measured equivalent width of a spectral line, provided stellar parameters are known. The following species are available: Li I, Na I, Ti I, Fe I/II, Sr II. Smaller databases of NLTE corrections are also provided in the literature (e.g., Bergemann and Gehren 2008: Mn I, Merle et al. 2011: Mg I, Ca I).

[2] http://www.inspect-stars.net.

5 Conclusions

We are now entering the new era of observational stellar astrophysics, moving away from 1-D hydrostatic models with LTE—which is known as 'classical' approach—to 3-D radiative hydrodynamics with NLTE. The transition is slow, mostly because of the associated computational challenges. However, the need for more realistic models, which provide more accurate and un-biased results, i.e. fundamental stellar parameters and element abundances, is now as urgent as never before. Large-scale stellar surveys (like Gaia-ESO and APOGEE) provide observed spectra of unprecedented quality and pave the way to massive applications of the new models. From the recent developments in theory, it seems that most promising approach is to compute NLTE line formation with the averages of full 3-D RHD models.

Acknowledgments Figure 1 reproduced by permission of the authors; the image was observed with the Swedish 1-m Solar Telescope. The SST is operated on the island of La Palma by the Institute for Solar Physics in the Spanish Observatorio del Roque de los Muchachos of the Instituto de Astrofisica de Canarias. The Institute for Solar Physics is a national research infrastructure under the Swedish Research Council. It is managed as an independent institute associated with Stockholm University through its Department of Astronomy. Figure 2: Asplund et al. A&A, 359, 729, 2000, reproduced with permission (c) ESO. Figures 3, 4 reproduced by permission of the AAS. Figure 8: Lind et al. A&A, 554, A96, 2013, reproduced with permission (c) ESO.

References

Allende Prieto, C., Koesterke, L., Ludwig H. G., Freytag, B., Caffau, E., A&A, 550, A103 (2013).
Alvarez R, Plez B (1998) A&A 330:1109
Asplund M (2005) Ann. Rev. A&A 43:481
Asplund, M., Nordlund, Å, Trampedach, R., Allende Prieto, C., Stein, R. F., A&A, 359, 729 (2000).
Asplund M, Carlsson M, Botnen AV (2003) A&A 399:L31
Asplund, M., Grevesse, N., Sauval, A. J., Allende Prieto, C., Kiselman, D., A&A, 417, 751 (2004).
Auer, L., Bendicho, P. F., Trujillo Bueno, J., A&A, 292, 599 (1994).
Auer LH, Mihalas D (1970) MNRAS 149:65
Baron E, Hauschildt PH (1998) ApJ 495:370
Beeck B, Collet R, Steffen M et al (2012) A&A 539:A121
Bergemann M, Gehren T (2008) A&A 492:823
Bergemann M, Hansen CJ, Bautista M, Ruchti G (2012a) A&A 546:A90
Bergemann M, Kudritzki RP, Plez B, Davies B, Lind K, Gazak Z (2012b) ApJ 751:156
Bergemann M, Lind K, Collet R, Magic Z, Asplund M (2012c) MNRAS 427:27
Bergemann, M., Kudritzki, R. P., Davies, B., Plez, B., Gazak, Z., Chiavassa, A. In: Kervella, P., Le Bertre, T., Perrin, G. (eds), EAS Publications Series, Vol. 60, p. 103 (2013).
Böhm-Vitense E (1958) Zeitschrift fur Astrophysik 46:108
Botnen, A., Carlsson, M. In: Miyama, S. M., Tomisaka, K., Hanawa, T. (eds) Numerical Astrophysics, Astrophysics and Space Science Library, Vol. 240, p. 379 (1999).
Buscher DF, Baldwin JE, Warner PJ, Haniff CA (1990) MNRAS 245:7P
Butler, K., Giddings, J., Newsletter on Analysis of Astronomical Spectra, University of London, 9 (1985).
Caffau E, Ludwig HG, Steffen M, Freytag B, Bonifacio P (2011) Solar Physics 268:255
Canuto VM, Mazzitelli I (1991) ApJ 370:295

Carlsson, M., In: Giampapa, M. S., Bookbinder, J. A. (eds) Cool Stars, Stellar Systems, and the Sun, Astronomical Society of the Pacific Conference Series, Vol. 26, p. 499.
Carlsson M, Rutten RJ (1992) A&A 259:L53
Carlsson M, Rutten RJ, Shchukina NG (1992) A&A 253:567
Cayrel R, Steffen M, Chand H et al (2007) A&A 473:L37
Chiavassa A, Plez B, Josselin E, Freytag B (2009) A&A 506:1351
Chiavassa A, Freytag B, Masseron T, Plez B (2011) A&A 535:A22
Collet R, Asplund M, Trampedach R (2007) A&A 469:687
Collet R, Magic Z, Asplund M (2011) Journal of Physics: Conference Series 328:012003
de Laverny P, Recio-Blanco A, Worley CC, Plez B (2012) A&A 544:A126
Freytag B, Steffen M, Dorch B (2002) Astronomische Nachrichten 323:213
Freytag B, Steffen M, Ludwig HG, Wedemeyer-Böhm S, Schaffenberger W, Steiner O (2012) Journal of Computational Physics 231:919
Gray DF, Carney BW, Yong D (2008) AJ 135:2033
Grupp F (2004) A&A 426:309
Gudiksen BV, Carlsson M, Hansteen VH, Hayek W, Leenaarts J, Martínez-Sykora J (2011) A&A 531:A154
Gustafsson B, Edvardsson B, Eriksson K, Jorgensen UG, Nordlund Å, Plez B (2008) A&A 486:951
Hansteen VH, Carlsson M, Gudiksen B (2007) The Physics of Chromospheric Plasmas 368:107
Haubois X, Perrin G, Lacour S et al (2009) A&A 508:923
Hauschildt PH, Baron E (2006) A&A 451:273
Hayek W, Asplund M, Collet R, Nordlund Å (2011) A&A 529:A158
Höfner S, Gautschy-Loidl R, Aringer B, Andersen A, Jorgensen UG (2003) Astronomische Nachrichten Supplement 324:19
Kervella P, Verhoelst T, Ridgway ST, Perrin G, Lacour S, Cami J, Haubois X (2009) A&A 504:115
Koesterke, L., Allende Prieto, C., Lambert, D. L., ApJ, 680, 764 (2008).
Kurucz RL (1993) The Physics of Chromospheric Plasmas 44:87
Kurucz RL (2005) Mem. del. Soc. Astron. Italiana 8:14
Leenaarts, J., Carlsson, M. In: Lites, B., Cheung, M., Magara, T., Mariska, J., Reeves, K. (eds) The Second Hinode Science Meeting: Beyond Discovery-Toward Understanding, Astronomical Society of the Pacific Conference Series, Vol. 415, p. 87 (2009).
Leenaarts, J., Carlsson, M., Hansteen, V., Rouppe van der Voort, L., ApJ, 694, L128 (2009).
Lind K, Melendez J, Asplund M, Collet R, Magic Z (2013) A&A 554:A96
Lucy LB (1999) A&A 344:282
Ludwig HG, Caffau E, Steffen M, Freytag B, Bonifacio P, Kučinskas A (2009) Mem. del. Soc. Astron. Italiana 80:711
Magic Z, Collet R, Asplund M, Trampedach R, Hayek W, Chiavassa A, Stein RF, Nordlund Å (2013) A&A 557:A26
Mashonkina, L., arXiv:1306.6426 (2013).
Merle T, Thévenin F, Pichon B, Bigot L (2011) MNRAS 418:863
Mihalas D (1978) Stellar atmospheres, 2nd edition, San Francisco. W. H, Freeman and Co
Mihalas D, Athay RG (1973) Ann. Rev. A&A 11:187
Murphy T, Meiksin A (2004) MNRAS 351:1430
Muthsam HJ, Kupka F, Löw-Baselli B, Obertscheider C, Langer M, Lenz P (2010) New Astronomy 15:460
Nordlund Å (1982) A&A 107:1
Nordlund, Å., Galsgaard, K. In: Electromechanical Coupling of the Solar Atmosphere, AIP, p. 13 (1992).
Nordlund Å, Stein RF, Asplund M (2009) Living Reviews in Solar Physics 6:2
Ohnaka K, Hofmann KH, Benisty M et al (2009) A&A 503:183
Ohnaka K, Weigelt G, Millour F et al (2011) A&A 529:A163
Paxton B, Bildsten L, Dotter A, Herwig F, Lesaffre P, Timmes F (2011) ApJS 192:1
Plez, B., Astrophysics Source Code, Library, arXiv:1205.004 (2012).

Reetz J (1999) Ap&SS 265:171
Schoenrich, R., Bergemann, M., arXiv:1311.5558 (2013).
Shchukina NG, Olshevsky VL, Khomenko EV (2009) A&A 506:1393
Short CI, Hauschildt PH (2005) ApJ 618:926
Short CI, Hauschildt PH (2009) ApJ 691:1634
Spruit HC, Nordlund Å, Title AM (1990) A&A 28:263
Stein RF, Nordlund Å (1998) ApJ 499:914
Tanner JD, Basu S, Demarque P (2013) ApJ 767:78
Teyssier D, Quintana-Lacaci G, Marston AP et al (2012) A&A 545:A99
Trampedach R, Asplund M, Collet R, Nordlund Å, Stein RF (2013) ApJ 769:18
Tremblay PE, Ludwig HG, Freytag B, Steffen M, Caffau E (2013) A&A 557:A7
Trujillo Bueno, J., Shchukina, N., ApJ, 664, L135 (2007).
Tuthill PG, Haniff CA, Baldwin JE (1997) MNRAS 285:529
Uitenbroek H, Criscuoli S (2011) ApJ 736:69
Vögler A, Shelyag S, Schüssler M, Cattaneo F, Emonet T, Linde T (2005) A&A 429:335
Wilson RW, Baldwin JE, Buscher DF, Warner PJ (1992) MNRAS 257:369
Wilson RW, Dhillon VS, Haniff CA (1997) MNRAS 291:819
Young JS, Baldwin JE, Boysen RC et al (2000) MNRAS 315:635

Current Status of NLTE Analysis of Stellar Atmospheres

Jiří Kubát

Abstract Various available codes for NLTE modelling and analysis of hot star spectra are reviewed. Generalizations of standard equations of kinetic equilibrium and their consequences are discussed.

Keywords Radiation mechanisms: general · Radiation mechanisms: non-thermal · Radiation: dynamics · Stars: atmospheres · Radiative transfer · Atomic processes

1 Importance of Radiation

Radiation is not only an information source about stellar atmospheres; it has also the ability to interact with the matter in the atmosphere and to alter its state.

Each photon has a momentum $h\nu/c$. Consequently, when it is absorbed, the absorbing ion receives this amount of momentum. If it is scattered, the atom may receive from no momentum (if radiation is scattered in the forward direction) to $2h\nu/c$, if radiation is scattered backwards. This momentum gain is redistributed to other particles by elastic collisions and, as a consequence, acceleration of matter by radiation occurs.

The energy of a photon ($h\nu$) can also be transferred to matter. In the case of ionization, part of this energy is used to ionize the atom and the rest goes to kinetic energy of electrons, $h\nu \rightarrow h\nu_{\rm ion} + \frac{1}{2} m_{\rm e} v_{\rm e}^2$. In the case of excitation, all photon energy is used for this process, $h\nu \rightarrow h\nu_{\rm exc}$. In the case of the free-free absorption the photon energy causes an increase of the electron kinetic energy, $h\nu \rightarrow \frac{1}{2} m_{\rm e} \Delta v_{\rm e}^2$. Reverse processes (recombination, de-excitation, and free-free emission) cause release of a photon and lowering the atomic internal or electron kinetic energy (or both). In the above-mentioned cases of bound-free and free-free transitions there is an energy exchange

J. Kubát(✉)
Astronomický ústav AV ČR, Fričova 298, 251 65 Ondřejov, Czech Republic
e-mail: kubat@sunstel.asu.cas.cz

E. Niemczura et al. (eds.), *Determination of Atmospheric Parameters of B-, A-, F- and G-Type Stars*, GeoPlanet: Earth and Planetary Sciences,
DOI: 10.1007/978-3-319-06956-2_18,

with electron kinetic energy. In this case, subsequent elastic collisions re-establish the equilibrium velocity distribution with a slightly different temperature. Consequently, the thermal energy increases or decreases and we talk about radiative heating or cooling. If the energy exchange is with atomic internal energy, a change of excitation or ionization balance occurs. If the radiation changes in the excitation and ionization states dominate, then we have to take into account these effects explicitly and we have to use the NLTE approximation and solve the kinetic equilibrium equations.

2 NLTE Model Atmosphere Codes

The solution of the kinetic equilibrium equations[1] (see Hubeny and Mihalas 2014) for given radiative and collisional rates is a relatively simple task; it is just a solution of set of linear equations. The task of NLTE modelling is more difficult. It is the *simultaneous* solution of the equations of kinetic equilibrium with other equations describing the stellar atmosphere. These equations form a set of non-linear integro-differential equations.

The basic task is to solve the equations of kinetic equilibrium together with the radiative transfer equation to determine simultaneously the level population numbers n_i and the radiation field. In this case, temperature $T(r)$, density $\rho(r)$, and velocity $v(r)$ are fixed. This is the standard NLTE task, which may be applied also to trace element NLTE calculations.

The task of calculation of a static NLTE model atmosphere is more complicated. It means adding two equations to the set of simultaneously solved equations, namely the equation of hydrostatic equilibrium and the equation of radiative equilibrium. Consequently, temperature $T(r)$ and density $\rho(r)$ are not fixed, but they are consistently calculated. Then the results of solution of this set of non-linear equations are the NLTE level populations, radiation field, temperature, total density, and electron density. Adding the two structural equations causes significant slowing down of the convergence.

If we replace the hydrostatic equilibrium equation by the equation of motion and add the continuity equation, we may solve hydrodynamic NLTE model atmospheres and determine also the velocity field $v(r)$. However, this full task is too complicated even for the case of 1-D atmospheres, so restricted problems are usually being solved.

Different codes solve different sets of equations using different numerical approaches. Below we list some representative examples of such codes.

Development of any NLTE model atmosphere code is a complicated and time consuming task, which usually takes several years or even decades. The description of such code is then usually spread over many publications, if they exist at all. In other cases, the most relevant information can appear only on a web page, which may be even variable over time. Therefore, it is sometimes very difficult to pick up only a single clear reference to a particular code, where everything important about

[1] These equations are often referred to as the equations of statistical equilibrium. Here we use the term kinetic equilibrium equations as in the textbook by Hubeny and Mihalas (2014).

the code is described. References in this chapter were found with a belief that they give the most appropriate reference to particular codes. The author apologizes if he omitted references which describe the code better. The web page address was added in the footnote for all cases when it was known to the author.

A list of model atmosphere, NLTE, and radiative transfer codes was compiled also by Hummer and Hubeny (1991) and Sakhibullin (1996); we refer the interested reader there.

2.1 NLTE Problem for a Given Structure

There are many codes which solve the NLTE problem for a given (i.e. fixed) atmospheric structure. Here we list several of them, each of which represents possible method for the solution of the problem.

One of the first codes which was able to solve the NLTE problem started to be developed in mid-1960s. It was the code PANDORA[2] (see Avrett and Loeser 2003). This code is based on the equivalent two-level atom approach and uses 1-D radiative transfer. The code LINEAR (Auer et al. 1972) uses the complete linearization method for solution of the multi-level line formation. The code MULTI[3] (Carlsson 1986) uses the accelerated lambda iteration method for solution of 1-D NLTE multi-level problems both in static and moving atmospheres in plane-parallel approximation. Rybicki and Hummer (1991, 1992, 1994) developed a method and a computer code MALI for multi-level radiative transfer using accelerated lambda iteration method. The code described by Auer et al. (1994) and Fabiani Bendicho et al. (1997) solves 2-D multi-level NLTE radiative transfer problem, using again the accelerated lambda iteration method.

Various aspects of the solution of the NLTE problem for trace elements together with a couple of codes were discussed in detail at the summer school "NLTE Line Formation for Trace Elements in Stellar Atmospheres" (Monier et al. 2010).

2.2 Static NLTE Model Atmospheres

The pioneering work on the complete linearization method by Auer and Mihalas (1969) led to a development of a computer code for calculations of static plane-parallel NLTE model atmospheres, which was later described in Mihalas et al. (1975). An independent code using the same method was developed by Kudritzki (1976). The most sophisticated NLTE static plane-parallel model atmosphere code is the code TLUSTY,[4] which was initially developed using the complete linearization method (Hubeny 1975, 1988). Now it combines the latter method with the accelerated lambda

[2] http://www.cfa.harvard.edu/~avrett/pandora.html

[3] http://folk.uio.no/matsc/mul22/

[4] http://nova.astro.umd.edu/index.html

iteration method (Hubeny and Lanz 1995) and enables treatment of NLTE line-blanketing using the method of superlevels and superlines. This code is accompanied with the code SYNSPEC,[5] which solves the radiative transfer equation including pre-calculated NLTE populations for the given model atmosphere in detail.

Another code calculating NLTE line-blanketed model atmospheres is PRO2 belonging to the Tübingen NLTE Model Atmosphere Package (TMAP,[6] Werner and Dreizler 1999; Werner et al. 2003), which focuses on modelling the atmospheres of high gravity stars (e.g. white dwarfs) in NLTE. We should also mention a multi-purpose model atmosphere code PHOENIX,[7,8] which started as a combination of two original codes, for cool stars (Allard 1990), and for novae atmospheres (Hauschildt 1991).

Static spherically-symmetric model atmospheres were first calculated using a complete linearization method by Mihalas and Hummer (1974). An independent code using the same method was developed by Gruschinske (1978). Another independent computer code ATA[9] uses the accelerated lambda iteration method and combines it with the linearization method to calculate static NLTE model atmospheres of spherically-symmetric stellar atmospheres (Kubát 1994, 1996, 1997, 2001, 2003).

2.3 NLTE Wind Model Codes

There exist several codes, which solve the NLTE model of the wind assuming a given density and velocity structure. These codes solve simultaneously the equations of kinetic equilibrium and the radiative transfer equation, which is mostly treated using the Sobolev approximation. In some codes the more exact co-moving frame solution of the radiative transfer in spectral lines is used. The continuum radiative transfer may be treated as in the static case due to weak dependence of the opacity on frequency for continuum transitions.

The code CMFGEN[10] (Hillier 1987, 1990; Hillier and Miller 1998; Busche and Hillier 2005) solves the equations of kinetic equilibrium and radiative transfer equation in the co-moving frame. The velocity field is assumed to follow the β-law. In addition, temperature structure of the models can be iteratively determined. This code may be considered as one of the top codes for solution of this task.

The code PoWR[11] (Hamann 1985; Hamann and Gräfener 2004) solves also the equations of kinetic equilibrium and radiative transfer equation in the co-moving frame. The code was primarily designed for Wolf-Rayet stars atmosphere modelling;

[5] http://nova.astro.umd.edu/Synspec49/synspec.html

[6] http://astro.uni-tuebingen.de/~TMAP/

[7] http://www.hs.uni-hamburg.de/EN/For/ThA/phoenix/

[8] http://perso.ens-lyon.fr/france.allard/

[9] http://www.asu.cas.cz/~kubat/ATA/

[10] http://kookaburra.phyast.pitt.edu/hillier/web/CMFGEN.htm

[11] http://www.astro.physik.uni-potsdam.de/~wrh/PoWR/

however, nowadays it is also being applied to other types of stars with expanding atmospheres (e.g. Šurlan et al. 2013).

Similarly, the code FASTWIND (Santolaya-Rey et al. 1997; Puls et al. 2005) solves the NLTE model for a given velocity and density structure and has been applied to many studies. On the other hand, the code WM- BASIC[12] (e.g. Pauldrach 1987; Pauldrach et al. 1986, 2012) solves line blocked and blanketed NLTE model of stellar winds and also their stationary hydrodynamic stratification.

The ISA- WIND code (de Koter et al. 1993) solves the equations of statistical equilibrium and the radiative transfer equation in Sobolev approximation for given velocity, density, and temperature structure.

There are also several codes focused on modelling supernovae, like the code HYDRA (Höflich 2003), which combines radiative hydrodynamics and NLTE radiative transfer. NLTE radiative transfer in supernovae is solved using the Monte Carlo method by Kromer and Sim (2009). The Monte Carlo method was used for NLTE calculations in circumstellar disks in the code HDUST by Carciofi and Bjorkman (2006, 2008).

2.4 Hydrodynamic Models with NLTE

The most important task in stellar wind modelling is consistent determination of the radiative force which drives the wind. Usually the so-called CAK approximation is being used, where the radiative force is expressed with the help of three parameters: k, α, and δ (Castor et al. 1975; Abbott 1982). However, this approach is far from being consistent even if the parameter k is replaced by the more appropriate parameter Q introduced by Gayley (1995). There have been several attempts to improve calculation of the radiative force using detailed lists of lines. The first such calculations were done by Abbott (1982). Consistent calculation of the radiative force is enabled by the code WM- BASIC (see Pauldrach et al. 2012, and references therein). Monte Carlo calculations of the radiative force using NLTE radiative transfer with the ISA- WIND code were done by Vink et al. (1999). Recently, Krtička and Kubát (2004, 2010) developed a code for the consistent solution of wind hydrodynamic equations including equations of kinetic equilibrium.

3 Generalized Kinetic Equilibrium

Currently the most frequently applied mode of NLTE calculations is the simultaneous solution of *static* (i.e. for macroscopic velocity $v = 0$) and stationary ($\partial/\partial t = 0$) equations of kinetic equilibrium and the radiative transfer equation. This basic set of equations may be extended by other constraint equations for the determination of temperature, density, and velocity. However, there are many possible generalizations

[12] http://www.usm.uni-muenchen.de/people/adi/adi.html

which go beyond this "standard" task. More processes than simple one-electron excitation and ionization may be included, and the assumption of static stationary medium in equilibrium may be relaxed.

3.1 Additional Processes in the Equations of Kinetic Equilibrium

A standard model atom consists of a number of energy levels, among which collisional and radiative (both allowed and forbidden) transitions occur. Usually, only transitions between levels of a particular ion and ionization transitions from these levels to the ground level of the next higher ion are considered. This set of atomic levels and transitions is usually sufficient for calculations of NLTE model atmospheres of hot stars.

However, there exist more processes which may change the state of the atoms. As an example, we may consider Auger ionization, which occurs as a consequence of a strong X-ray radiation.

Strong X-rays (or collisions) may expel an inner-shell electron. This is followed by fluorescence or by another ionization. The equations of kinetic equilibrium gains an additional term $n_i \sum_{j>i} R_{ij}^{\rm Auger}$, which describes this process,

$$- n_i \sum_{j\neq i} \left(R_{ij} + C_{ij}\right) - n_i \sum_{j>i} R_{ij}^{\rm Auger} + \sum_{j\neq i} n_j \left(R_{ji} + C_{ji}\right) = 0. \qquad (1)$$

The Auger ionization is considered as a two-electron ionization process. States with inner-shell vacancy are not explicitly included in the equations of kinetic equilibrium. This form of the kinetic equilibrium equations was included to wind ionization calculations by Krtička and Kubát (2009).

3.2 Full Kinetic Equilibrium Equations

The full form of the equations of kinetic equilibrium (in the classical limit) reads (Mihalas 1978, Eq. 5–48),

$$\frac{\partial n_i}{\partial t} + \nabla \cdot (n_i \mathbf{v}) = \sum_{j\neq i} \left(n_j P_{ji} - n_i P_{ij}\right). \qquad (2)$$

As discussed in Chap. 14, the left hand side is usually neglected. However, it may become important for dynamical atmospheres. Non-equilibrium hydrogen ionization using the left hand side of the equations of kinetic equilibrium was solved by Leenaarts et al. (2007). The time derivative is important if the relaxation timescale is longer than the dynamic timescales. Examples are the dynamic ionization of the

solar chromosphere (Carlsson and Stein 2002) or rapidly expanding atmospheres of supernovae (Utrobin and Chugai 2005). This list of examples is far from complete and has to serve as an indication of the importance of the full treatment of the equations of kinetic equilibrium.

3.3 Non-Maxwellian Velocity Distribution

The presence of non-thermal electrons, which may happen, for example, as a consequence of solar flares, is a reason why collisional transitions do not support the system to evolve towards the equilibrium distribution of excitation and ionization states. They rather cause that the populations differ from their equilibrium values. In this case, we may rewrite the equations of kinetic equilibrium as

$$-n_i \sum_{j \neq i} \left(R_{ij} + C_{ij} + C_{ij}^{\mathrm{nt}} \right) + \sum_{j \neq i} n_j \left(R_{ji} + C_{ji} \right) = 0, \tag{3}$$

where the term $n_i C_{ij}^{\mathrm{nt}}$ describes the non-thermal collisional excitation. This type of equations was used for inclusion of electron beams in solar flares (Kašparová and Heinzel 2002). To include the non-thermal collisional rates consistently, we have to solve the kinetic equation for electrons instead of the assumption of equilibrium distribution of their velocities.

3.4 Polarization

A significantly more general case is the case when we include polarized radiation and polarization of atomic levels. Then the radiation is described using the Stokes vector for intensities

$$I = (I, Q, U, V)^{\mathrm{T}} . \tag{4}$$

The radiative transfer equation becomes

$$\frac{\mathrm{d}I}{\mathrm{d}s} = \eta - \kappa I, \tag{5}$$

where the emission coefficient η is a vector quantity and the opacity κ is a tensor quantity.

Instead of the equations of kinetic equilibrium we have to solve the more general density matrix evolution equation,

$$\frac{\mathrm{d}\rho^K}{\mathrm{d}t} = 0, \tag{6}$$

which, in addition to classical occupation numbers, solves also for coherences between them. For more details see Štěpán and Trujillo Bueno (2013, and references therein).

4 Summary

The necessity to consider the equations of kinetic equilibrium (the NLTE approach) is a consequence of radiation-matter interaction. There exist many codes which can handle this relatively complicated task. Not all codes which claim "NLTE" solve the same task, one has always to distinguish between codes for model atmosphere calculations and codes for solution of the restricted NLTE problem (radiative transfer + kinetic equilibrium). The codes which calculate synthetic spectrum are much simpler. They may enable input of NLTE population numbers, but their task is just the formal solution of the radiative transfer equation (solution for given opacity and emissivity). There is also a number of codes which handle results of the previously mentioned codes in a user-friendly manner.

Although NLTE model atmospheres and NLTE line formation problems offer results which are much closer to reality than those using the pure LTE approach, they are not the final step in generalization. Much more has still to be done to include radiation-matter interactions properly.

Acknowledgments The author would like to thank Dr. Ewa Niemczura for inviting him to the Spring School of Spectroscopic Data Analyses in Wrocław. He is also grateful to both referees for their invaluable comments. This work was partly supported by the project 13-10589S of the Grant Agency of the Czech Republic (GA ČR).

References

Abbott DC (1982) ApJ 259:282
Allard F (1990) Model atmospheres for M dwarfs. Ph.D. thesis, Centre de Recherche Astrophysique de Lyon
Auer L, Fabiani Bendicho P, Trujillo Bueno J (1994) A&A 292:599
Auer LH, Mihalas D (1969) ApJ 158:641
Auer LH, Heasley JN, Milkey RW (1972) A computational program for the solution of non-LTE transfer problems by the complete linearization method. Contributions from the Kitt Peak National Observatory 555
Avrett EH, Loeser R (2003) Solar and stellar atmospheric modelling using the Pandora computer program. In: Piskunov N, Weiss WW, Gray DF (eds) Modelling of Stellar atmospheres, IAU symposium, vol 210. ASP, San Francisco, p 21
Busche JR, Hillier DJ (2005) AJ 129:454
Carciofi AC, Bjorkman JE (2006) ApJ 639:1081
Carciofi AC, Bjorkman JE (2008) ApJ 684:1374
Carlsson M (1986) Computer program for solving multi-level non-LTE radiative transfer problems in moving or static atmospheres. Uppsala Astronomical Observatory Reports 33

Carlsson M, Stein RF (2002) ApJ 572:626
Castor JI, Abbott DC, Klein RI (1975) ApJ 195:157
Fabiani Bendicho P, Trujillo Bueno J, Auer L (1997) A&A 324:161
Gayley KG (1995) ApJ 454:410
Gruschinske J (1978) Ausgedehnte statische Modell-Photosphaeren heisser Sterne. Ph.D. thesis, Universität Kiel
Hamann WR (1985) A&A 145:443
Hamann WR, Gräfener G (2004) A&A 427:697
Hauschildt P (1991) Non-LTE Modellatmosphären für Novae und Supernovae. Ph.D. thesis, Universität Heidelberg
Hillier DJ (1987) ApJS 63:947
Hillier DJ (1990) A&A 231:116
Hillier DJ, Miller DL (1998) ApJ 496:407
Höflich P (2003) ALI in rapidly expanding envelopes. In: Hubeny I, Mihalas D, Werner K (eds) Stellar atmosphere modelling, Astronomical society of the Pacific conference series, vol 288. ASP, San Francisco, p 185
Hubeny I (1975) Improved complete-linearization method for the solution of the non-LTE line transfer problem. Bull Astron Inst Czechoslov 26:38
Hubeny I (1988) A computer program for calculating non-LTE model stellar atmospheres. Comput Phys Commun 52:103
Hubeny I, Lanz T (1995) ApJ 439:875
Hubeny I, Mihalas D (2014) Theory of Stellar atmospheres. Princeton University Press, Princeton (in press)
Hummer DG, Hubeny I (1991) Computer codes for stellar atmospheric modelling. In: Crivellari L, Hubeny I, Hummer DG (eds) Stellar atmospheres—beyond classical models, vol 341. Kluwer Academic Publication, Dordrecht, NATO ASI C, p 119
Kašparová J, Heinzel P (2002) A&A 382:688
de Koter A, Schmutz W, Lamers HJGLM (1993) A&A 277:561
Kromer M, Sim SA (2009) MNRAS 398:1809
Krtička J, Kubát J (2004) A&A 417:1003
Krtička J, Kubát J (2009) MNRAS 394:2065
Krtička J, Kubát J (2010) A&A 519:A50
Kubát J (1994) A&A 287:179
Kubát J (1996) A&A 305:255
Kubát J (1997) A&A 326:277
Kubát J (2001) A&A 366:210
Kubát J (2003) Calculation of spherically symmetric NLTE model atmospheres using ALI and a thermal balance method. In: Piskunov N, Weiss WW, Gray DF (eds) Modelling of Stellar atmospheres, IAU symposium, vol 210. ASP, San Francisco, A8
Kudritzki RP (1976) A&A 52:11
Leenaarts J, Carlsson M, Hansteen V, Rutten RJ (2007) A&A 473:625
Mihalas D (1978) Stellar atmospheres, 2nd edn. W. H. Freeman & Co., San Francisco
Mihalas D, Hummer DG (1974) ApJS 28:343
Mihalas D, Heasley JN, Auer LH (1975) A non-lte model stellar atmosphere computer program. NASA STI/Recon Technical Report no 76, p 30128
Monier R, Smalley B, Wahlgren G, Stee P (eds) (2010) Non-LTE line formation for trace elements in Stellar atmospheres, vol 43. EAS Publications Series, EDP Sciences, Les Ulis
Pauldrach A (1987) A&A 183:295
Pauldrach A, Puls J, Kudritzki RP (1986) A&A 164:86
Pauldrach AWA, Vanbeveren D, Hoffmann TL (2012) A&A 538:A75
Puls J, Urbaneja MA, Venero R, Repolust T, Springmann U, Jokuthy A, Mokiem MR (2005) A&A 435:669
Rybicki GB, Hummer DG (1991) A&A 245:171

Rybicki GB, Hummer DG (1992) A&A 262:209
Rybicki GB, Hummer DG (1994) A&A 290:553
Sakhibullin NA (1996) Computer codes for stellar atmospheres analysis used in the CIS. In: Adelman SJ, Kupka F, Weiss WW (eds) Model atmospheres and spectrum synthesis, astronomical society of the Pacific conference series, vol 108. ASP, San Francisco, p 207
Santolaya-Rey AE, Puls J, Herrero A (1997) A&A 323:488
Štěpán J, Trujillo Bueno J (2013) A&A 557:A143
Šurlan B, Hamann WR, Aret A, Kubát J, Oskinova LM, Torres AF (2013) A&A 559:A130
Utrobin VP, Chugai NN (2005) A&A 441:271
Vink JS, de Koter A, Lamers HJGLM (1999) A&A 350:181
Werner K, Dreizler S (1999) The classical stellar atmosphere problem. J Comput Appl Math 109:65
Werner K, Deetjen JL, Dreizler S, Nagel T, Rauch T, Schuh SL (2003) Model photospheres with accelerated lambda iteration. In: Hubeny I, Mihalas D, Werner K (eds) Stellar atmosphere modelling, astronomical society of the Pacific conference series, vol 288. ASP, San Francisco, p 13

Spectroscopic Analysis of Cool Giants and Supergiants

Maria Bergemann, Rolf-Peter Kudritzki and Ben Davies

Abstract Cool red giants and supergiants are among the most complex and fascinating stars in the Universe. They are bright and large, and thus can be observed to enormous distances allowing us to study the properties of their host galaxies, such as dynamics and chemical abundances. This review lecture addresses various problems related to observations and modelling spectra of red giants and supergiants.

Keywords Stars: late-type · Stars: massive · Supergiants · Stars: atmospheres · Techniques: spectroscopic

1 Introduction

Cool evolved stars are perhaps the most enigmatic cosmic objects with luminosities spanning several orders of magnitude. The stars are at the end stages of stellar evolution (Fig. 1) occupying the coolest vertical strip on the Herzsprung-Russell diagram, the Hayashi limit for fully convective stars.

M. Bergemann (✉)
Institute of Astronomy, University of Cambridge, Cambridge, UK
e-mail: mbergema@ast.cam.ac.uk

R.-P. Kudritzki
Institute for Astronomy, University of Hawaii, 2680 Woodlawn Drive, Honolulu, HI 96822, USA
e-mail: kud@ifa.hawaii.edu

R.-P. Kudritzki
Max-Planck-Institute for Astrophysics, Karl-Schwarzschild-Str. 1, 85741 Garching, Germany

B. Davies
Astrophysics Research Institute, Liverpool John Moores University, IC2,
Liverpool Science Park, 146 Brownlow Hill, Liverpool L3 5RF, UK
e-mail: B.Davies@ljmu.ac.uk

E. Niemczura et al. (eds.), *Determination of Atmospheric Parameters of B-, A-, F- and G-Type Stars*, GeoPlanet: Earth and Planetary Sciences,
DOI: 10.1007/978-3-319-06956-2_19,

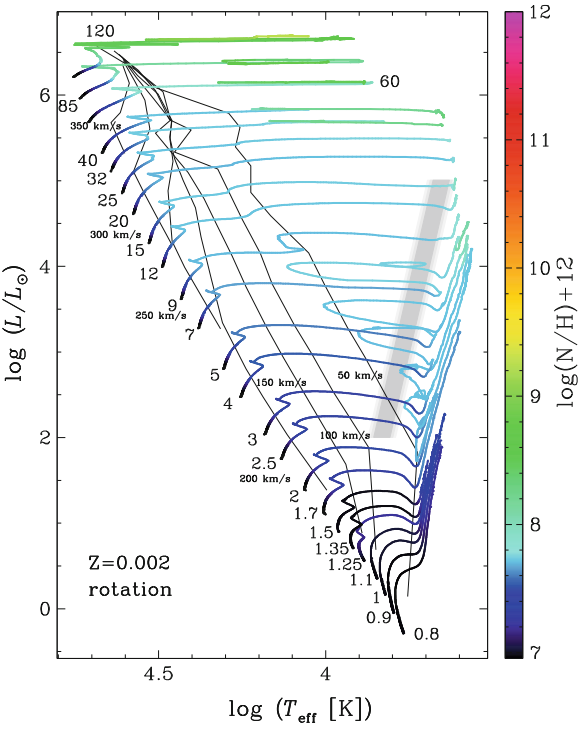

Fig. 1 Stellar tracks including the effect of rotation for stellar models with initial mass of 0.8–120 $M_{\odot}$ (Georgy et al. 2013). Cool giants and red supergiants occupy the stripe extending vertically from $1 < \log(L/L_{\odot}) < 6$

Low- and intermediate-mass stars evolve to the red giant branch (RGB) and asymptotic giant branch (AGB) after having spent most of their lifetime on the main-sequence. These stars are cool and luminous, with effective temperatures, $T_{\rm eff}$, between 2,000 and 5,500 K and luminosities, L, between 10 and 10^4 $L_{\odot}$. The stars have a wide range of ages, from 1 to >10 Gyr, and thus trace chemical composition of interstellar matter in galaxies now and in the past.

High-mass stars are those with masses from 10 to 60 $M_{\odot}$; they evolve and explode quickly. Red supergiants (RSG) are young, typically <50 Myr, yet extremely bright with L from 10^4 to 10^6 $L_{\odot}$.

Nucleosynthesis taking place in the interior of a star has as a consequence that, as evolution proceeds, the stellar atmosphere acquires abundance patterns that strongly differ from the chemical composition of the natal cloud in which the star was born. This is referred to as self-pollution: dredge-up episodes bring material from the interior to the surface. Thus the stellar atmosphere becomes enriched or depleted in different chemical elements, e.g., He, C and N, and *s*-process elements (e.g. Lambert 1992; Vassiliadis and Wood 1993; Herwig 2005). These abundance peculiarities are extreme on the AGB phase. The newly synthesised elements are returned into the

ISM, as stars lose mass through winds. Giant stars are thus the primary producers of chemical elements, and much can be learnt about stellar evolution from the analysis of abundance ratios as a function of the evolutionary stage of a star.

Giant stars serve as a primary gauge of cosmic abundances. They are the key targets in studies of Galactic chemical evolution and stellar archaeology. Ongoing observational programmes search for very- and ultra-metal poor (UMP) stars in the Galactic halo and in the bulge (Beers and Christlieb 2005); many of such objects are old red giants. Some large-scale stellar surveys, such as Apache Point Galactic Experiment from Sloan Digital Sky Survey (APOGEE) focus entirely on RGB stars, for their intrinsic brightness allows to probe a very large range of distances in the Galaxy. Individual giant stars can be observed with modern telescopes in the nearby galaxies of the Local Group (e.g. Guhathakurta et al. 2006; Kirby et al. 2010). Moreover, RGB and AGB stars dominate the integrated light of spatially unresolved systems, such as extra-Galactic globular clusters, dwarf spheroidal galaxies (dSph), and elliptical galaxies, thus allowing us to determine chemical composition of stellar populations from their composite spectra.

The atmospheres of giant stars are not fully in hydrostatic and thermodynamic equilibrium. Theory can explain observations only if very complex physical phenomena are included in the models: outflows, shocks, winds, pulsations, indicating that we are dealing with stars far more complex than the Sun. Violent convective motions penetrate their atmospheres and influence the physical state of matter. The extremely low densities of giant photospheres are to be blamed for the fact that matter and radiation are not in equilibrium.

All these phenomena will be briefly reviewed below (for a status update see also the review by Ryde 2010). First, we recap the most recent results from imaging and spectroscopy of cool stars (Sect. 2), which convincingly show that the stars are more sophisticated compared to their evolutionary predecessors, unevolved main-sequence stars, and give a glimpse to their complex physics. Section 3 describes the methods used for stellar parameter analysis. In Sect. 4, we review the key results of state-of-the-art modelling of cool giant spectra.

2 Observations

With the recent developments in astronomical instrumentation, in particular adaptive optics, it has become possible to obtain unique observations of giants in their native spectral range, infra-red (IR).[1]

Diffraction-limited imaging observations of giants and supergiants can be done with ground-based interferometric telescopes, such as VLT/NACO (Kervella et al. 2009). Surface inhomogeneities on RSGs were detected in the JHK bands. Betelgeuse, our closest red supergiant with a radius $R \sim 800\,R_{\odot}$, appears to have a complex circumstellar envelope with an outflow, or plume, extending to enormous

[1] Very cool stars, such as RGB and RSG, emit the most light in the IR.

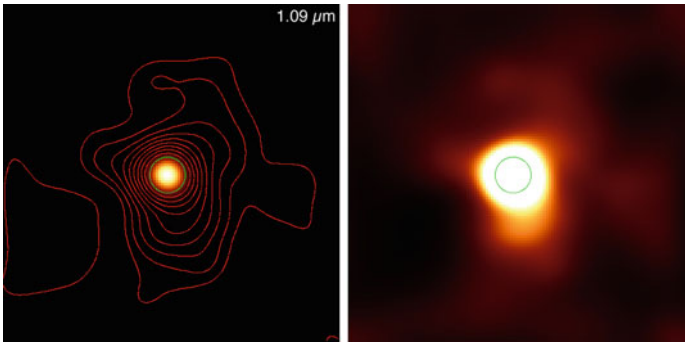

Fig. 2 Interferometric observations of Betelgeuse taken with VLT/NACO at 1.09 μm (Kervella et al. 2009). The *left image* has a linear colour scale; the contours indicate different flux levels in increasing powers of 2. The *right plot* corresponds to a square-root colour scale and it also shows the photospheric radius of the star at 43.7 mas (*green circle*)

distances of several stellar radii (Fig. 2). A combined analysis of different photometric bands suggests the presence of a very cool layer on top of Betelgeuse's photosphere, perhaps made of CN or water molecules (Kervella et al. 2009), and dusty envelopes, which produce flux excess in the far-IR stellar spectral energy distributions (Tsuji 2000). Interferometric long-baseline observations in optical filters (Quirrenbach et al. 1993), discovered another interesting effect: the star imaged in different filters, e.g. TiO 712 nm versus continuum at 754 nm, has a different size! The difference in diameter for the coolest M-type giants and supergiants is nearly 10 %, which suggests huge extension of their atmospheres.

Other interesting results about atmospheric structure and dynamics of cool stars were delivered by space missions, such as the Herschel Space Observatory (HSO, e.g. Teyssier et al. 2012). Figure 3 shows the image of Betelgeuse made by superposition of images taken at 70–160 μm (Decin et al. 2012). The image reveals a dusty envelope and multiple arc-like structures caused by the interaction of stellar wind and interstellar matter, so-called bow shocks. The morphology of these structures can be explained by sophisticated 3-D time-dependent hydrodynamical simulations of the stellar envelopes.

Spectroscopic observations reveal complexities of a different type. Red giants and supergiants are very cool stars, with effective temperatures from ∼3,000 to 5,000 K. In these conditions, various molecules very efficiently absorb radiation. Thus, the spectra are severely distorted by molecular bands, such as CN, NH, H_2O, and particularly TiO (Allard et al. 2000), which absorbs most of the radiation in the optical window (Fig. 4 top panel). Although molecules are ubiquitous and are sensitive probes of atmospheric physics, their modelling is very difficult (Sect. 4) and complex 3-D radiative hydrodynamics calculations are needed (Uitenbroek and Criscuoli 2011).

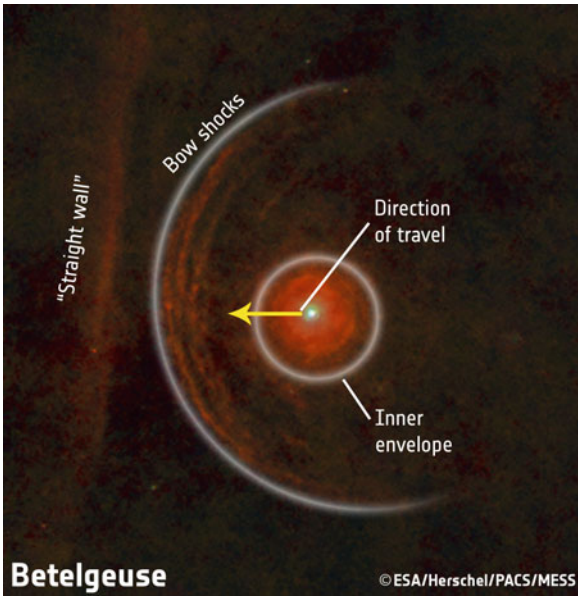

Fig. 3 Herschel image of Betelgeuse (Decin et al. 2012). The image shows the morphology of the stellar environment (see text)

Very high-resolution observations of cool giants (e.g. Dravins 1990; Gray et al. 2008; Ramírez et al. 2010; Gray 2012) show that the spectral lines are not symmetric. The reversed-*C* shapes of the line profiles indicate large convection cells at the surface of stars.

The IR part of giant spectra is much less contaminated by molecular absorption that significantly simplifies the problem of spectral analysis. Targeting the near-IR region also has the benefit that the stellar flux is less extinguished by interstellar absorption, allowing studies deep into the galaxy. For example, cool giants and supergiants have been used to study the abundances in the Galactic Centre (Carr et al. 2000; Cunha et al. 2007; Davies et al. 2009b), the Scutum Arm tangent and the end of the Galactic Bar (Davies et al. 2009a), and the Galactic Bulge (Rich et al. 2007).

Thus in terms of science, spectroscopy of RGB, AGB, and RSG stars has a great potential in the IR.

3 Stellar Parameters

The basic parameters of cool stars can be estimated by different methods. Here, we focus on the spectroscopic techniques that have been developed to determine effective temperature $T_{\rm eff}$, surface gravity $\log g$, and metallicity [Fe/H] of a star.

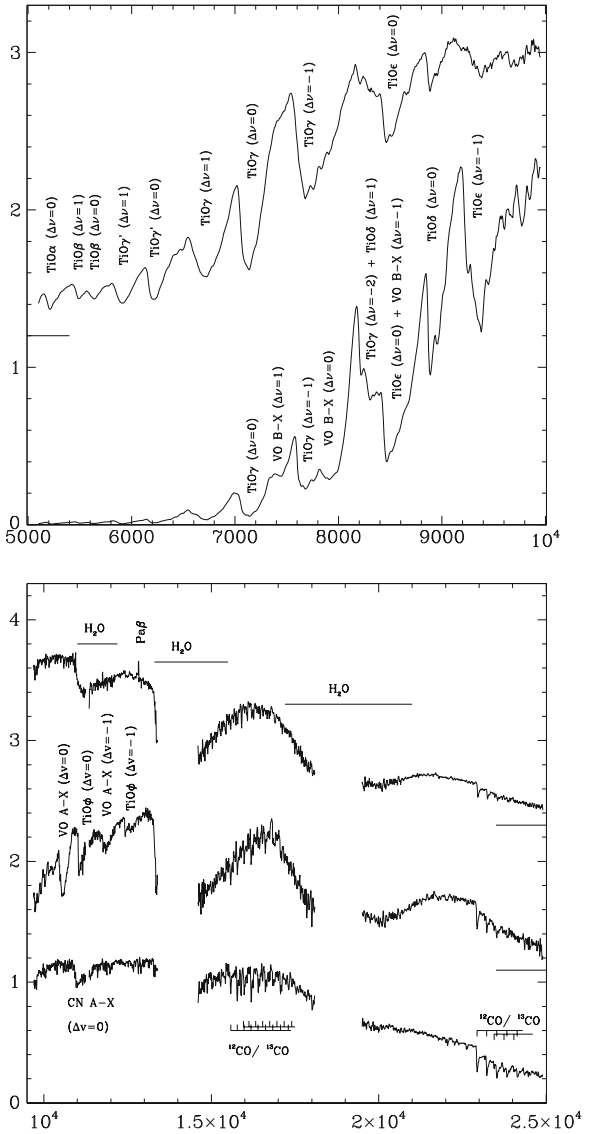

Fig. 4 Spectra of cool stars (Lançon and Wood 2000). *Top* a spectrum of a warm Mira star in the optical window below 1 μm; the TiO bands are prominent. *Bottom* the IR spectra of a warm Mira star, cool Mira star, and the red supergiant (*top–bottom*)

The perhaps most stable and simple method to estimate stellar parameters is the method of excitation-ionization balance for a pair of chemical species, such as Fe I and Fe II. The simplicity comes mainly from the application of the curve-of-growth technique (Gray 2008). First, one computes the abundance from the measured line

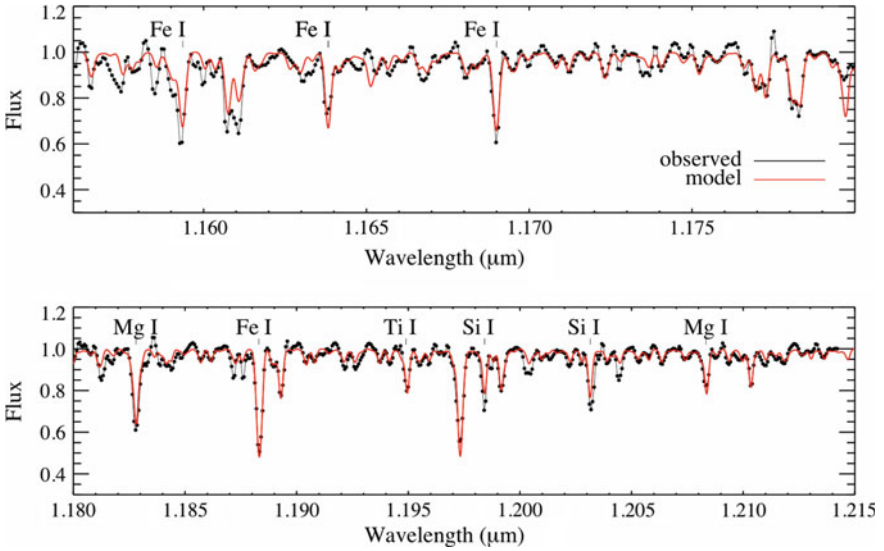

Fig. 5 Comparison of the observed (*black*) and theoretical NLTE (*red*) spectra for Betelgeuse

equivalent width. The $T_{\rm eff}$ is then set by minimising the magnitude of the slope of the relationship between the abundance of iron from Fe I lines and the excitation potential of each line. The surface gravity is then estimated by minimising the difference between the abundance of iron measured from Fe I and Fe II lines. Iterations are needed to have the above criteria satisfied. The method offers several advantages: efficiency, fast convergence and easy implementation. The downside is the need for a statistically significant sample of clean unblended lines; moreover, the method is very sensitive to the physics of the models. Recent studies showed that standard 1-D hydrostatic model atmospheres and LTE line formation fail for giant stars, producing unphysically low estimates of temperature, surface gravity, and metallicity (e.g. Bergemann et al. 2012b; Ruchti et al. 2013).

For cooler stars, such as RSG, the excitation-ionization balance method is not useful. First, their optical spectra are too blended to allow a meaningful estimate of a line equivalent width. Adjacent spectral lines blend with one another, and it is not possible to separate their individual profiles. Second, most of the lines from singly-ionized elements vanish, and there is no constraint on the ionization balance. The method of global spectrum synthesis (Fig. 5), which relies on all spectral lines present in the observed spectrum, is much more suitable for the analysis of RSGs. Each parameter affects the relative strengths of the lines in subtly different ways, meaning that the parameters may be determined via a χ^2 minimisation search within a precomputed grid of model spectra (see Gazak et al. 2014, submitted).

The principal diagnostics of effective temperatures for RSGs have been the strengths of the optical TiO bands which define the spectral classification sequence. These features were modelled by Levesque et al. (2005, 2006) using the MARCS

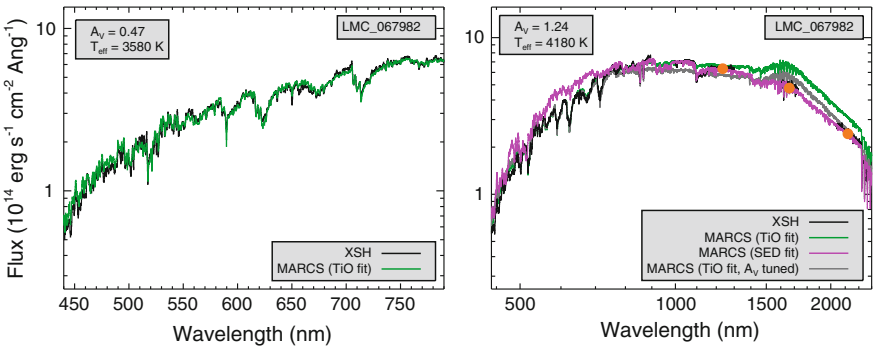

Fig. 6 A theoretical fit to the optical spectrum (*left*) and to the complete SED for a red supergiant in LMC (Davies et al. 2013). The observed spectrum from the X-Shooter instrument at VLT is shown with a *black line*. On the *right plot*, the *magenta* and *green lines* correspond to the MARCS 1-D LTE theoretical spectra computed with different $T_{\rm eff}$. The *orange symbols* indicate spectro-photometric measurements for the star

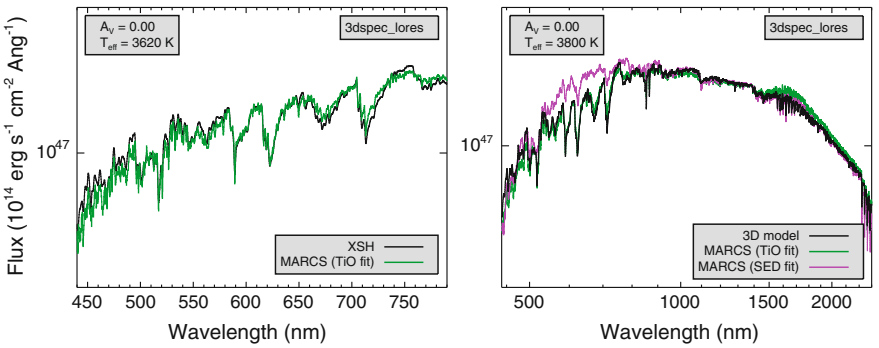

Fig. 7 A theoretical fit to the optical spectrum (*left*) and to the complete SED (*right*) for a red supergiant. 3-D model atmospheres (*black line*) improve the consistency between the TiO bands and the IR 1.6 μ diagnostics (Davies et al. 2013)

model atmospheres in order to determine the temperature scale for such stars. However, it has since been shown that, as a consequence of deviations from hydrostatic equilibrium in RSG atmospheres, the 1-D hydrostatic models underpredict the strengths of the TiO bands (Fig. 6). This leads to effective temperatures which are too low (Davies et al. 2013). Spectra computed with 3-D hydrodynamical models (Fig. 7, see also Sect. 4.1) tend to have deeper TiO absorption bands and brighter fluxes at the minimum of opacity, 1.6 μm, compared to 1-D hydrostatic models thus alleviating the problem, at least in part.

Red giants and supergiants are very useful as metallicity indicators. Their spectra are rich in metallic lines, allowing for abundances to be determined for a range of elements. Such work typically targets the near-IR, which coincides with the flux peak of the stars, and which avoids the regions of the spectrum dominated by problematic

TiO bands. More recently, this work is being adapted so that metallicities may be retrieved at lower spectral resolutions. This is done by isolating a region in the J-band (Fig. 5) which is relatively free of the molecular lines that plague the spectra of these stars, alleviating the problem of line-blending. This means that RSGs may be studied at distances of several Mpc, making them excellent probes of their host galaxies' abundances (Davies et al. 2010). The atomic lines of Fe, Ti, Si and Mg present in this region provide sufficient information to solve for the primary free parameters in model atmospheres, i.e. effective temperature, gravity, microturbulence and metallicity.

4 Physics of Giant Atmospheres

Here we review those aspects of the physics of giants and RGSs, which can be presently addressed with theoretical models of atmospheres and spectral line formation. These aspects include:

- Molecular line opacities;
- Deviations from hydrostatic equilibrium;
- Deviations from local thermodynamic equilibrium;
- Chromospheres, MOLspheres, winds, mass loss.

For some of these aspects, such as MOLspheres[2] and chromospheres (see below), the models are semi-empirical, in a sense that they are tuned to reproduce observations.

NLTE and 3-D hydrodynamical calculations can be performed based on ab initio physical considerations.

4.1 Molecular Line Opacities

Until recently, one of the main limitations of spectroscopic models for giants was the absence of accurate data for molecular line transitions. Complete TiO line lists, which include tens of millions of transitions, have been published only recently (Plez 1998). However, other diatomic molecules have a significant contribution in giant spectra, including CN, CO, MgH, VO (de Laverny et al. 2012). The major challenge is to include all these atomic data in spectral synthesis codes and stellar atmosphere models to correctly recover their temperature and pressure structures and predict the emergent spectra. So far, only simplified 1-D LTE hydrostatic models, like MARCS (Gustafsson et al. 2008) or PHOENIX (Hauschildt et al. 1997), which include accurate opacity sampling (OS) schemes, have been able to cope with the bulky line lists. Such models are used to model RSG and RGB spectra at present.

[2] MOLsphere is a term used for a warm optically-thick water envelope around cool stars, which has been proposed in some studies to explain the IR observations (Tsuji 2001).

4.2 3-D Hydrodynamics and Giant Convective Cells

Recently, it became possible to compute 2-D and 3-D radiative hydrodynamics (3-D RHD) models of stellar convection (e.g. Stein and Nordlund 1998; Freytag et al. 2002; Chiavassa et al. 2011). Depending on the properties of a star, e.g. a smaller giant or a larger supergiant, the codes may work in two diametrically different modes. The first local setup is known as *box-in-a-star* and it is usually applied to modelling solar-like stars (e.g. Freytag et al. 2002). The second, global *star-in-a-box* setup is applied to model very extended, variable and stochastically pulsating stars. These are characteristics of red supergiants. The difference is essentially that in the local setup, the equations of compressible hydrodynamics and non-local radiation transport are solved only in a small box on a surface of a star. In contrast, in the *star-in-a-box* regime, the simulation box includes the whole star.

The 3-D RHD models are much more successful than classical 1-D hydrostatic models in reproducing a wealth of observational information, including the line shapes and bisectors, centre-to-limb variation and brightness contrast (Asplund 2005). However, such models are exceptionally sophisticated and cannot be computed for a large range of stellar parameters due to prohibitively long computation times. At present, the use of 3-D RHD models is restricted to the analysis of individual stars, such as the bright metal-poor giant HD 122563 (Collet et al. 2009) and the red supergiant Betelgeuse (Chiavassa et al. 2010). The 3-D RHD models are also used to explore the validity range of simpler 1-D hydrostatic model atmospheres (e.g. Collet et al. 2007).

Figure 8 shows a snapshot from a star-in-a-box simulation of convection on Betelgeuse, as computed with the CO5BOLD code (Chiavassa et al. 2011). The emergent intensity is shown at the wavelength of 500 nm. Huge giant convection cells predicted by the model are consistent with imaging observations of the star from space, e.g from the Hubble Space Telescope (Gilliland and Dupree 1996).

4.3 NLTE

Another major complication in the analysis of spectra of cool giants is to include departures from Local Thermodynamic Equilibrium (LTE). As a consequence of very low surface densities, $-0.5 < \log g < 3$, collisions between particles are too weak to establish local equilibrium in a stellar atmosphere. Each parcel of the gas is influenced by photons originating elsewhere. This is what we call *non-local radiation field*, and thus non-local thermodynamic equilibrium. Research in NLTE physics of cool giant and supergiant atmospheres is still at its infancy. However, it is clear already now, that spectral lines of different atoms and molecules do not form under LTE conditions.

Bergemann et al. (2012a, b, 2013) proved from ab initio statistical equilibrium calculations, that ions such as Fe I, Ti I, Si I, Cr I, Ti I, are very sensitive to strong

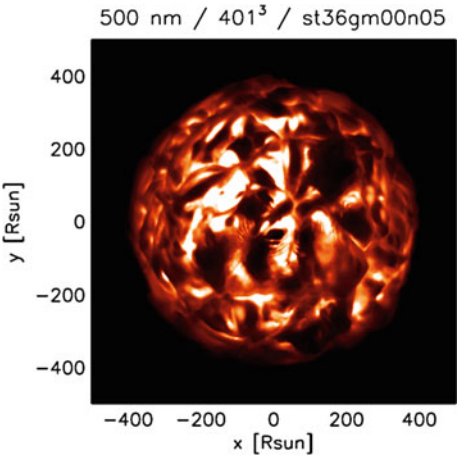

Fig. 8 Emergent intensity at 500 nm from a 3-D RHD simulation of convection for a red supergiant Betelgeuse. The model is characterised by $T_{\rm eff} = 3{,}710$ K, $\log g = 0.047$, and the solar metallicity. The cubic grid contains 401^3 nodes (Chiavassa et al. 2011)

photo-ionising radiation fields. In this case, the effect of NLTE is to reduce the number densities of atoms in a minority ionisation stage, thus for a given abundance the line equivalent width is smaller than that given by LTE. This effect is larger in metal-poor stars. At solar metallicity, the opposite behaviour is encountered sometimes. For example, the IR transitions of Si I and Ti I show *negative* NLTE effects such that the LTE abundance is higher than the NLTE one (Fig. 9). According to recent studies, the LTE and NLTE abundances may differ by an order of magnitude, from -0.5 to $+1.0$ dex, depending on the element and ionisation stage, intrinsic line parameters (wavelength, level excitation potential), and stellar parameters.

The NLTE analysis of molecular spectral lines is an unexplored territory. New studies show the effect of NLTE is to cause stronger molecular absorption bands that leads to extra cooling in the outer atmospheric layers (Lambert et al. 2013).

Detailed theoretical and observational studies are necessary to understand how NLTE influences the estimates of stellar parameters and abundances from giant spectra.

4.4 Chromospheres, MOLspheres, Winds, and Mass Loss

Figure 10 shows the late-type stars in the H-R diagram (Ayres 2010). The illustration is similar to the Linsky and Haisch (1979) diagram of *solar* and *non-solar* type stars; the former with chromospheres, transition regions, and coronae, and the latter with chromospheres only. It is thought that the absence of a corona is a consequence of strong winds (see also Dehaes et al. 2011).

Chromospheres are easy to detect through observations. For instance, high-quality spectroscopic observations of RGB tip stars in globular clusters produced compelling evidence for chromospheric activity, based on the emission wings of Hα

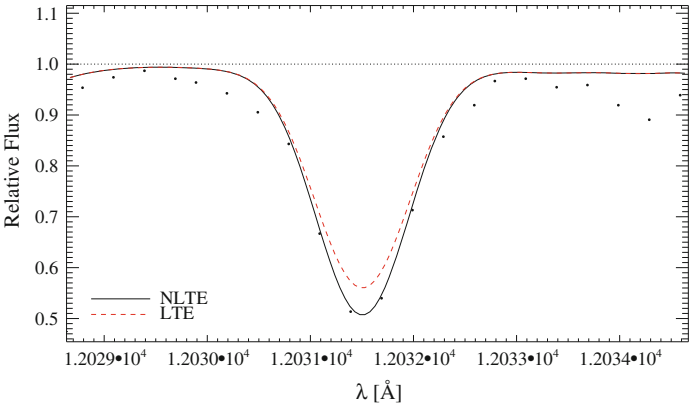

Fig. 9 Subaru/IRCS high resolution observations (*black dots*) J-band observations of Si I lines in the spectrum of the Per OB1 RSG HD 14270 (12,031 Å) compared with a LTE (*red dashed*) and a NLTE (*black solid*) fit. The fit profiles have been calculated with $T_{\rm eff} = 3{,}800$ K, $\log g = 1.0$, $[Z] = 0.0$, and microturbulence $\xi_{\rm t} = 5\,{\rm km\,s^{-1}}$ (Bergemann et al. 2013)

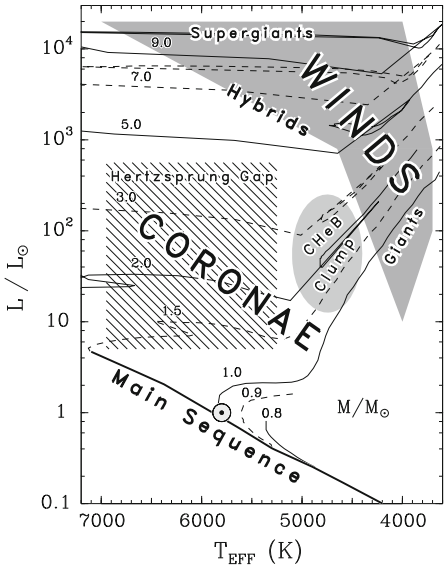

Fig. 10 An H-R diagram of late-type stars (Ayres 2010). Stellar winds and chromospheres are typical for cool giants and supergiants

line at 656.3 nm (Meszaros et al. 2008). According to models, the wings form in the chromosphere,[3] although they are also affected by stellar pulsations. Other diagnostic features sensitive to activity are the UV Ca H and K lines at 395 nm and the Mg II resonance lines at 280 nm (e.g. Leenaarts et al. 2013). These strong lines develop chromospheric emission in the innermost cores. Since stellar rotation, and

[3] Interestingly, only stars with $\log(L/L_{\odot}) \geq 2.4$ show emission wings.

thus chromospheric activity, declines with the age of a star, the strength of the line core emission is a useful measure of stellar ages (Soderblom et al. 1991). Strong correlation was also discovered between the strengths of Mg II resonance lines and TiO molecular bands (Steiman-Cameron et al. 1985).

The inability to fit some features in the IR spectra of cool giants with 1-D hydrostatic LTE models gave rise to extensions of the classical models. Such extended models, for example, include MOLsphere, a very cool molecular layer above the photosphere (Tsuji 2001, 2008). The models assume a very low temperature of 1,000–2,000 K and the column density of molecules is adjusted to fit the observed spectra. It is unclear whether the appeal to such ad-hoc extensions is justified given the major uncertainties in the analysis of molecular spectral lines caused by the limitations of 1-D hydrostatic models with LTE.

Red giants and supergiants lose mass through low-speed winds of few tens of $\mathrm{km\,s^{-1}}$. The rate of mass loss can be very high, for AGB stars up to $10^{-5} M_{\odot}$/year and for RSGs up to $10^{-4} M_{\odot}$/year (De Beck et al. 2010). In- and out-flow motions are 'seen' in the high-resolution spectra of giants: the most pronounced features are shifts and asymmetries of strong line cores, like Hα. Mass outflows are responsible for the circumstellar shells that cause IR emission in the stellar spectra. Some insight into the mass loss phenomenon can also be gained from interferometry. It has been suggested that RSG winds contribute to larger radii at 712 nm as measured by interferometric techniques.

Models of oxygen-rich stars with effective temperatures below 3,000 K must include dust formation (Ferguson et al. 2001). The effect of the latter is two-fold: dust condensation warms up the atmosphere and decreases the abundance of elements locked up in the gas phase. Different elements, such as Ti, Zr, and Al, condense into dust grains. For an observer, the most relevant is the change in the number density of TiO, which can be detected in the spectra. The impact of more sophisticated models on the abundance analysis and stellar parameter determinations remains to be quantified.

5 Conclusions

To conclude, modelling spectra of cool giants and supergiants is, doubtlessly, a very challenging problem. Different physical phenomena must be included in the atmosphere and line formation models to allow for an accurate determination of surface parameters: molecular line opacities, deviations from 1-D hydrostatic equilibrium and from local thermodynamic equilibrium, chromospheres, winds, and mass loss. We have attained the necessary minimum level of complexity to address the simpler problems, like the determination of metallicity and bolometric flux. However, more detailed investigations, like the analysis of TiO or CO molecular bands and the interpretation of strong lines like Hα, Ca H and K, Mg II, which contain the essential physics, shall await for more complex models including the above-mentioned

effects. In the view of the enormous perspectives offered by observing giants and RSGs throughout the Milky Way and in other galaxies, the need for more physically-realistic models is well-justified.

Acknowledgments Figures from the following papers have been reproduced with permission from the authors and from the publishers (c) ESO: Chiavassa et al. A&A, 535, A22, 2011; Decin et al. A&A, 548, A113, 2012; Georgy et al. A&A, 558, A103, 2013; Lancon and Wood A&AS, 146, 217, 2000; Kervella et al. A&A, 504, 115, 2009. Figures from the following papers have been reproduced by permission of the AAS: Davies et al. ApJ, 767:3, 2013. This work was partly supported by the European Union FP7 programme through ERC grant number 320360.

References

Allard F, Hauschildt PH, Schwenke D (2000) ApJ 540:1005
Asplund M (2005) Ann Rev A&A 43:481
Ayres T (2010) Mem del Soc Astron Italiana 81:553
Beers TC, Christlieb N (2005) Ann Rev A&A 43:531
Bergemann M, Kudritzki R-P, Plez B et al (2012) ApJ 751:156
Bergemann M, Lind K, Collet R, Magic Z, Asplund M (2012) MNRAS 427:27
Bergemann M, Kudritzki R-P, Würl M et al (2013) ApJ 764:115
Carr JS, Sellgren K, Balachandran SC (2000) ApJ 530:307
Chiavassa A, Freytag B, Masseron T, Plez B (2011) A&A 535:A22
Chiavassa A, Haubois X, Young JS et al (2010) A&A 515:A12
Collet R, Asplund M, Trampedach R (2007) A&A 469:687
Collet R, Nordlund Å, Asplund M, Hayek W, Trampedach R (2009) Mem del Soc Astron Italiana 80:719
Cunha K, Sellgren K, Smith VV et al (2007) ApJ 669:1011
Davies B, Kudritzki R-P, Figer DF (2010) MNRAS 407:1203
Davies B, Kudritzki R-P, Plez B et al (2013) ApJ 767:3
Davies B, Origlia L, Kudritzki R-P et al (2009) ApJ 694:46
Davies B, Origlia L, Kudritzki R-P et al (2009) ApJ 696:2014
De Beck E, Decin L, de Koter A et al (2010) A&A 523:A18
de Laverny P, Recio-Blanco A, Worley CC, Plez B (2012) A&A 544:A126
Decin L, Cox NLJ, Royer P et al (2012) A&A 548:A113
Dehaes S, Bauwens E, Decin L et al (2011) A&A 533:A107
Dravins D (1990) A&A 228:218
Ferguson JW, Alexander DR, Allard F, Hauschildt PH (2001) ApJ 557:798
Freytag B, Steffen M, Dorch B (2002) Astron Nachr 323:213
Georgy C, Ekström S, Eggenberger P et al (2013) A&A 558:A103
Gilliland RL, Dupree AK (1996) ApJL 463:L29
Gray DF (2008) The observation and analysis of stellar photospheres. Cambridge University Press, Cambridge
Gray DF (2012) AJ 143:112
Gray DF, Carney BW, Yong D (2008) ApJ 135:2033
Guhathakurta P, Rich RM, Reitzel DB et al (2006) AJ 131:2497
Gustafsson B, Edvardsson B, Eriksson K et al (2008) A&A 486:951
Hauschildt PH, Baron E, Allard F (1997) ApJ 483:390
Herwig F (2005) Ann Rev A&A 43:435
Kervella P, Verhoelst T, Ridgway ST et al (2009) A&A 504:115
Kirby EN, Guhathakurta P, Simon JD et al (2010) ApJS 191:352

Lambert DL (1992) In: Edmunds MG, Terlevich R (eds) Elements and the cosmos. Cambridge University Press, New York, p 92
Lambert J, Josselin E, Ryde N, Faure A (2013) EAS Publ Ser 60:111
Lançon A, Wood PR (2000) A&AS 146:217
Leenaarts J, Pereira TMD, Carlsson M, Uitenbroek H, De Pontieu B (2013) ApJ 772:90
Levesque EM, Massey P, Olsen KAG et al (2005) ApJ 628:973
Levesque EM, Massey P, Olsen KAG et al (2006) ApJ 645:1102
Linsky JL, Haisch BM (1979) ApJ 229:L27
Meszaros S, Dupree AK, Szentgyorgyi A (2008) AJ 135:1117
Plez B (1998) A&A 337:495
Quirrenbach A, Hummel CA, Buscher DF et al (1993) ApJ 416:L25
Ramírez I, Collet R, Lambert DL, Allende Prieto C, Asplund M (2010) ApJ 725:L223
Rich RM, Origlia L, Valenti E (2007) ApJ 665:L119
Ruchti GR, Bergemann M, Serenelli A, Casagrande L, Lind K (2013) MNRAS 429:126
Ryde N (2010) Astron Nachr 331:433
Soderblom DR, Duncan DK, Johnson DRH (1991) ApJ 375:722
Steiman-Cameron TY, Johnson HR, Honeycutt RK (1985) ApJ 291:L51
Stein RF, Nordlund A (1998) ApJ 499:914
Teyssier D, Quintana-Lacaci G, Marston AP et al (2012) A&A 545:A99
Tsuji T (2000) ApJ 538:801
Tsuji T (2001) A&A 376:L1
Tsuji T (2008) A&A 489:1271
Uitenbroek H, Criscuoli S (2011) ApJ 736:69
Vassiliadis E, Wood PR (1993) ApJ 413:641

What Influences the Results?

Barry Smalley

Abstract There are many factors which can influence the results from spectroscopic analyses, some more subtle than others. A small selection of them are presented here. Fixing $\log g$ using external constraints such as from planetary transits or asteroseismology is discussed. An investigation on how astrophysical gf values might be affected by uncertainties in collisional damping and choice of microturbulence is given. The influence of star spots on line profiles is explored. Finally, some examples from the literature are discussed.

Keywords Line: profiles · Stars: atmospheres · Stars: fundamental parameters · Stars: solar-type

1 Introduction

What influences the results? The answer is that rather a lot of factors can affect the results that we obtain from spectroscopic analyses. Here is a quick incomplete list:

Atomic data: $\log gf$, damping constants, missing/bad lines, hyperfine structure, isotopes
Model Atmosphere Physics: NLTE, convection, turbulence, star spots, abundance clouds
Code internals: partition functions, continuous opacities, numerical precision
Analysis Method: equivalent widths, line-profile fitting, choice of spectral lines and wavelength regions
Data Quality: signal-to-noise, spectral resolution, scattered light, continuum normalisation, telluric/interstellar lines

B. Smalley (✉)
Astrophysics Group, Keele University, Staffordshire ST5 5BG, UK
e-mail: b.smalley@keele.ac.uk

E. Niemczura et al. (eds.), *Determination of Atmospheric Parameters of B-, A-, F- and G-Type Stars*, GeoPlanet: Earth and Planetary Sciences,
DOI: 10.1007/978-3-319-06956-2_20,

Stellar properties: binarity, variability
Something else!
Even this list is rather long, so only a few topics will be discussed here.

2 Need a Reality Check

In order to be able to investigate what might be influencing the results, we need some benchmark stars with known properties. Unfortunately, the number of fundamental stars with accurate values of effective temperature ($T_{\rm eff}$) and surface gravity ($\log g$) is rather limited and, except for the Sun, their values are good to no better than 1 or 2 %. However, the situation continues to improve with an ever increasing number of double-lined eclipsing binaries with high-precision masses and radii (Torres et al. 2010), as well as the advent of high-precision asteroseismic $\log g$ values and the increasing number of stars with directly measured angular diameters from interferometry (e.g. Creevey et al. 2013).

Even worse is the fact that atmospheric composition is not a directly measurable quantity, even for the Sun. The closest we get to a direct measurement is via solar system material. For example, the photosphere iron abundance from state-of-art modelling is $\log A({\rm Fe}) = 7.50 \pm 0.04$, which is noticeably different from that obtained from the analysis of meteorites $\log A({\rm Fe}) = 7.45 \pm 0.01$ (Asplund et al. 2009, see). The question is which is the 'true' solar atmosphere composition?

3 Fixing $\log g$ in Spectral Analyses

Stellar surface gravity is quite poorly constrained by spectroscopic methods. The density of a star can be obtained from the analysis of planetary transits (Winn 2010; Seager 2011) or from asteroseismology (Aerts et al. 2010), which can yield much more precise values for $\log g$. Hence, fixing $\log g$ is often used in spectral analyses in these contexts. But, could this result in misleading or biased results?

Consider the following scenario using the Solar Na D lines. In Fig. 1 the profile calculated using an ATLAS9 model and the Kurucz `gfall` line list for the actual parameters of the Sun does not agree with the observed profile. This is due to some deficiency in the model atmosphere and/or atomic data used for the line profile calculation. Hence, in this example, the line is not suitable for fixing parameters. In reality, of course, this line could be used if you use the correct atomic data. Nevertheless, we assume that we can use this line to fix parameters.

Now imagine that we do not know the parameters of the Sun, but are able to fix $\log g = 4.44$ from some other method (e.g. from planetary transit or asteroseismology). We fit the profile to determine $T_{\rm eff}$ and get 5,700 K. A difference approaching 100 K. If we did not know the actual $T_{\rm eff}$ of the Sun, how would we know that this is incorrect? Similarly, if we were to fix $T_{\rm eff}$ to the known Solar value, this would lead

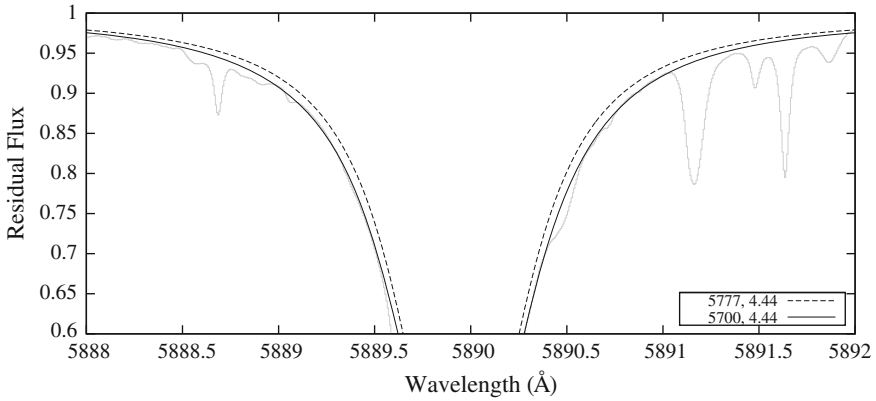

Fig. 1 The effect of fixing $\log g = 4.44$ on the $T_{\rm eff}$ obtained from the Solar Na D lines. The profile for the actual parameters for the Sun (*dashed line*) is clearly discrepant, while a $T_{\rm eff}$ of 5,700 K fits the profile (*solid line*)

to an incorrect value of $\log g$ obtained from the Na D lines. Hence, fixing one stellar parameter could lead to incorrect other parameters!

Of course, other lines and methods discussed elsewhere in this volume will behave differently and lead to other systematics. This is why using as many methods and diagnostics as possible is recommended, including comparison with standard stars.

Therefore, fixing $\log g$ and/or $T_{\rm eff}$ can be a good idea, but the behaviour of the diagnostics used should be carefully evaluated using fundamental stars to ensure that this does not result in any unintended systematics. In some cases, it might be better to leave the parameters unconstrained and compare the results, in order to evaluate the differences.

4 Astrophysical *gf* Values

Given that the Solar parameters are well known, analyses are often performed relative the Sun. This negates a lot of the problems due to uncertain model physics and missing or poor atomic data. Differential results avoid the uncertainties in Solar abundances and leads to improved precision. This is widely-used and can give good results for stars with parameters not too dissimilar to the Sun.

However, the method usually assumes that the differences are due to the $\log gf$ values alone. Other factors could have given rise to some of the discrepancies in line strengths, such as damping constants and microturbulence. Let us examine the effect that these two might have.

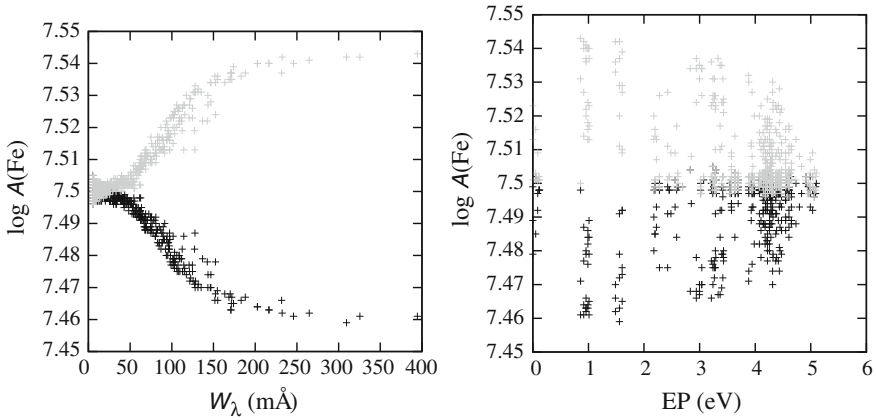

Fig. 2 The effect of changing van der Waals damping constants by ±10 %. The left-hand panel shows the changes with equivalent width, mimicking the effect of an incorrect microturbulence. The *right-hand* panel shows the changes with excitation potential, mimicking the effect of an incorrect $T_{\rm eff}$

4.1 Collisional Broadening

In a study of the effect of collisional broadening, (Ryan 1998) found that even relatively weak spectral lines can be affected by the choice of damping and that errors can depend on excitation potential. These can lead to errors in the determination of $T_{\rm eff}$ and microturbulence ($\xi_{\rm t}$).

A set of simulated 'observed' equivalent widths (W_0/λ) were generated using an ATLAS9 model with $T_{\rm eff} = 6{,}000$ K, $\log g = 4.5$ and $\log A({\rm Fe}) = 7.50$. The Fe I lines were taken from the Kurucz `gfall` line list in the wavelength range 5,000–6,000 Å. Only lines with calculated equivalent widths in the range 5–100 mÅ were retained. Figure 2 shows the effect of uncertainties in van der Waals broadening. Even relatively small uncertainties or systematics can induce a noticeable trend in $\log A({\rm Fe})$ with equivalent width and excitation potential, mimicking a change in microturbulence and effective temperature, respectively.

In order to investigate the effect of systematics errors in damping constants, astrophysical gf values were created at $T_{\rm eff} = 6{,}000$ K using the same line list but with the van der Waals damping constants increased by +20 %. Figure 3 shows the difference in $\log A({\rm Fe})$ obtained for a model with $T_{\rm eff} = 6{,}500$ K. There are small, but non-negligible, trends with both equivalent width and excitation potential, which could lead to systematic errors in the determination of $T_{\rm eff}$ and $\xi_{\rm t}$.

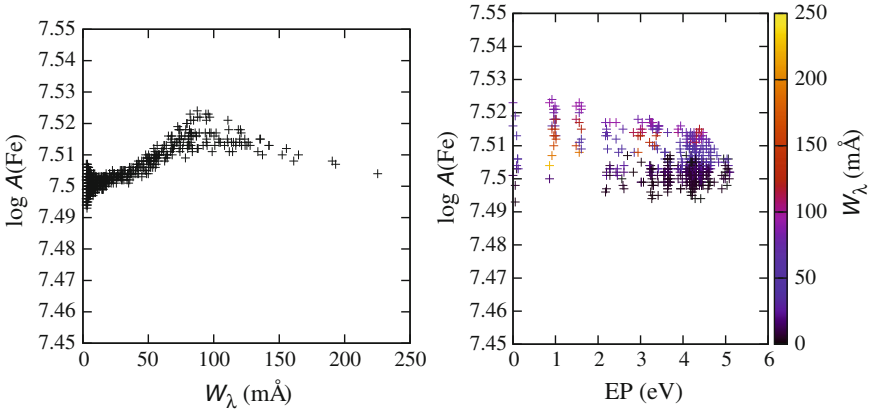

Fig. 3 The effect of systematic errors in van der Waals damping on abundance determination using astrophysical gf values. The plot shows how the differences in log A(Fe) at $T_{\rm eff} = 6{,}500$ K vary with equivalent width (*left*) and excitation potential (*right*). Note that relatively weak lines ($\sim$50 mÅ) show trends in both, potentially leading to systematic errors in $T_{\rm eff}$ and $\xi_{\rm t}$

Table 1 A selection of solar microturbulence values

Reference	Value (km s^{-1})
Blackwell et al. (1984)	0.85
Edvardsson et al. (1993)	1.15
Santos et al. (2004)	1.00
Valenti and Fischer (2005)	0.85
Bruntt et al. (2010)	0.95

4.2 The Solar Microturbulence Value

Table 1 gives a selection of values of microturbulence obtained for the Sun. There is a spread of 0.3 km s^{-1}. Hence, which value to use in an astrophysical gf determination and what might the effect be of an incorrect choice?

Now let us examine what might happen if we adopted the wrong value of microturbulence when generating our astrophysical gf values. As previously, our astrophysical gf values were created for a model with $T_{\rm eff} = 6{,}000$ K but with microturbulence of 0.9 km s^{-1} instead of correct value in the model of 1.0 km s^{-1}. Figure 4 shows the differences in log A(Fe) obtained at $T_{\rm eff} = 6{,}500$ K. The 'true' value of microturbulence in the simulated observations was 1.0 km s^{-1}. If in our analysis we assume this value of microturbulence, there is clear downward trend with equivalent width, including that we appear to have over-estimated the value. Alternatively, looking at how log A(Fe) varies with excitation potential, might lead us to conclude that we need a higher $T_{\rm eff}$. Either way, one or more of the stellar parameters would be incorrectly determined. If we reduce microturbulence to the incorrect 0.9 km s^{-1} we get

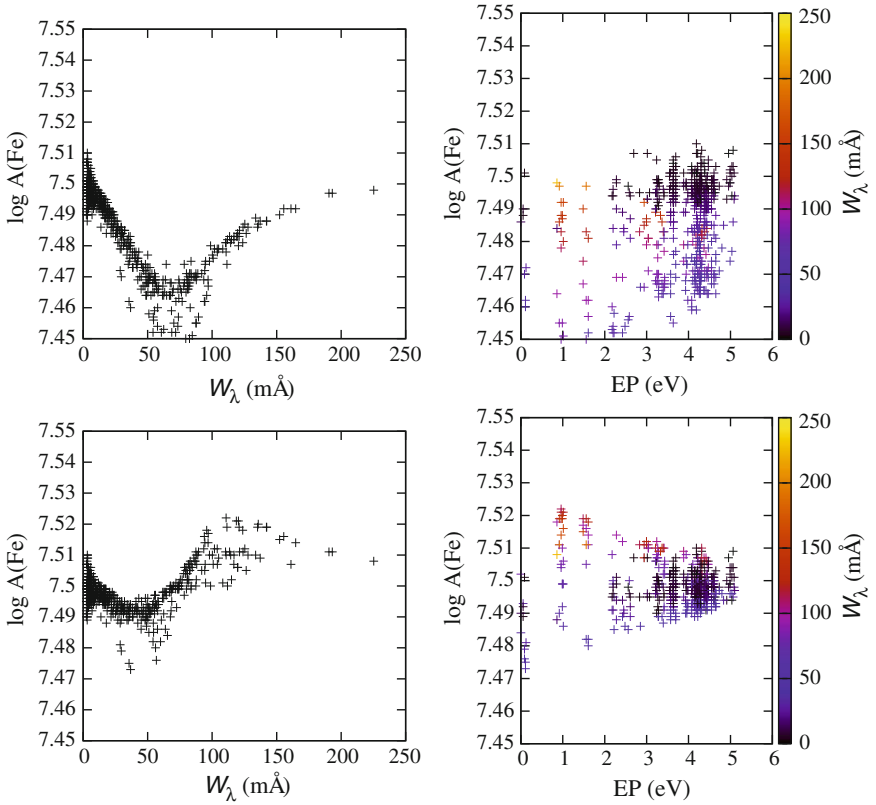

Fig. 4 The effect of systematic errors in microturbulence on abundance determination using astrophysical gf values. The *upper panel* show differences at $T_{\rm eff}$ = 6,500 K for $\xi_{\rm t}$ = 1.0. The *lower panel* shows the differences when a value of $\xi_{\rm t}$ = 0.9 is used. In both cases there are trends that could lead to incorrect parameter determination

significantly less trends with equivalent width and excitation potential. Hence, our assumed microturbulence when generating our astrophysical gf values has lead to systematic errors in our parameter determination.

5 Hyperfine Structure

The splitting of energy levels due to hyperfine structure (hfs) causes spectral lines of certain elements to be composed of multiple components (e.g. Wahlgren 2005). Figure 5 demonstrates the importance of including hfs in spectrum syntheses. In addition, the splitting due to different isotopes can also be important in certain circumstances, especially in chemically peculiar stars (e.g. Cowley et al. 2008).

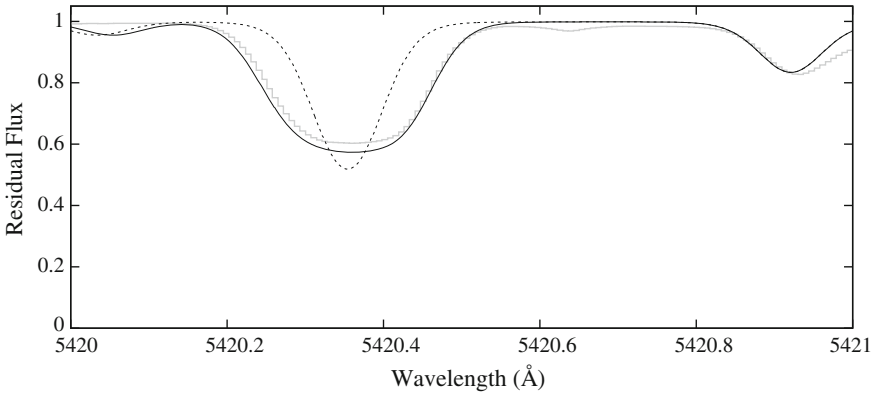

Fig. 5 The Solar Mn I line at 5,420 Å. The *solid line* is a synthesis using the Kurucz `gfhyperall` line list which agrees well with the observed line profile from the KPNO Solar Atlas (*grey line*). A synthesis using the `gfall` line list without hyperfine splitting is clearly discrepant (*dotted line*)

6 Observational Systematics

Observational data needs careful reduction and analysis in order to avoid introducing systematics. For example, scattered light might be present in spectrographs which weakens spectral lines, leading to incorrect abundances if due allowance is not made in the analysis. In addition, noise affects continuum determination, by hiding weak lines leading to systematic over or under estimation of the continuum. These uncertainties affect both equivalent width measurements and line profile fitting.

Telluric lines affect region around the Na D lines and Hα, as well as the obvious bands longward of 6,800 Å. Less apparent are weaker H_2O lines toward the blue end of the spectrum (Fig. 6).

7 Stellar Physics

The physical processes occurring within a stellar atmosphere are complex, including convection and turbulence, rotational mixing, oblateness and gravity darkening, NLTE, surface homogeneity ("spots"), element stratification ("clouds") and pulsations. Our models either neglect some of them or use simplified approximations. Homogeneous, single $T_{\rm eff}$ models are clearly not appropriate in certain circumstance. For example, Altair's surface temperature varies from 8,740 K at the pole to 6,890 K at equator (Peterson et al. 2006).

As a simple heuristic, consider a simulation of a spotted star with 5 % spot coverage, by taking two models with $T_{\rm eff} = 6{,}000$ K for the photosphere and $T_{\rm eff} = 5{,}000$ K for the spot. Both models have $\log g = 4.5$. Synthetic spectra for these models were combined in the ratio 95 and 5 %. Fitting with single $T_{\rm eff}$ model to the

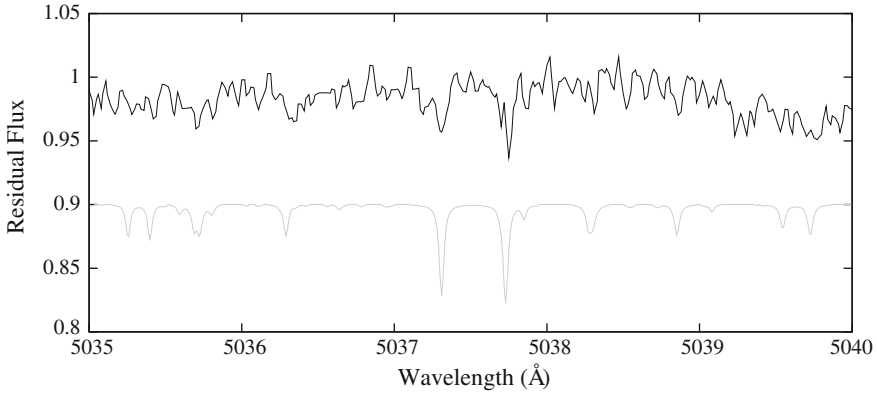

Fig. 6 Part of the HERMES (Raskin et al. 2011) spectrum of the rapidly rotating star KIC 08382172. The spectral lines are washed out, but the sharp telluric lines are clearly present, as indicated by the lower telluric line synthesis

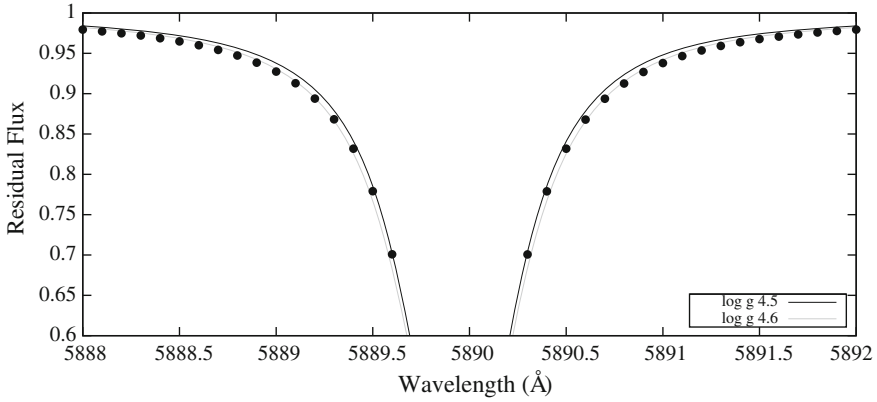

Fig. 7 Effect of 'Spots' on a Na D line. Fitting to the *spotted star* with a single $T_{\rm eff}$ model yields a profile that is too narrow for the 'correct' $\log g = 4.5$ (*dark line*). A model with $\log g = 4.6$ gives a slightly better fit (*grey line*)

Hα profile gives 5,950 K. This agrees with that obtained using Stefan's Law:

$$T_{\rm eff} = \left(0.95 \times 6000^4 + 0.05 \times 5000^4\right)^{0.25} = 5953\,{\rm K}.$$

But, what $\log g$ does the Na D lines give? Figure 7 shows that a model with $\log g = 4.6$ gives a slightly better fit than one with the 'true' value of $\log g = 4.5$. Hence, this scenario suggests that spectroscopic $\log g$ might be overestimated in spotted stars. The differences in the line profiles are, however, quite subtle and might be hidden within the noise of real observations (see Sect. 6).

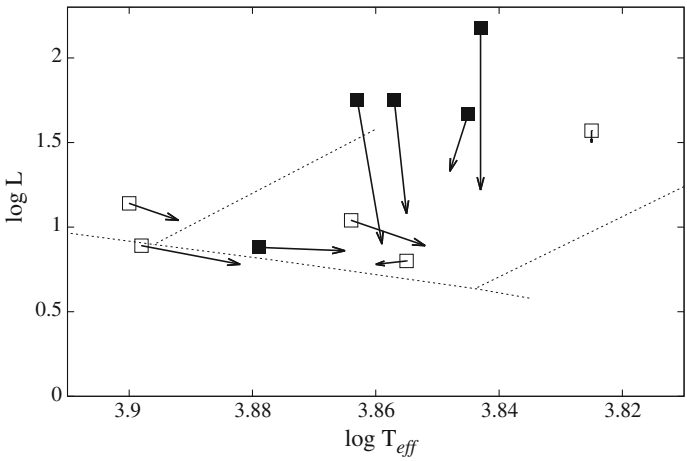

Fig. 8 Position of pulsating Am stars from (Balona et al. 2011) obtained from spectroscopic analyses (*solid squares*) and photometry (*open squares*), compared to their position obtained from using $T_{\rm eff}$ from *uv* by photometry and log *L* using HIPPARCOS parallaxes. Several of the stars which previously were outside the instability strip (*dotted lines*) are now contained within it

Recall what happened when we fixed log *g* earlier. Hence, one must be careful when applying external constraints, just in case some other missing physics affects the results.

8 A Few Examples from the Literature

8.1 Surface Gravities of Am Stars

The determination of log *g* for A-type stars is notoriously difficult. For example, consider the pulsating Am stars presented in Balona et al (2011) with literature values stellar parameters, either obtained from spectroscopy or photometry. Using *uvby* photometry to determine $T_{\rm eff}$ and log *L* using HIPPARCOS parallaxes, the positions of the stars with spectroscopic parameters appear to radically change (Fig. 8). Hence, errors in log *g* can cause a large changes in the position of stars in the H-R Diagram.

8.2 WASP-13

Gómez Maqueo Chew et al. (2013) presented a comparison of several methods used to determine the stellar parameters for the transiting planet hosting star WASP-13: Spectrum synthesis fitting using SME based on a modified version of the procedure

given in Valenti and Fischer (2005); an equivalent width method with UCLSYN (Doyle et al. 2013); the ARES/MOOG equivalent width method of (Sousa et al. 2008) using two different line lists. They found mean values of $T_{\rm eff} = 5{,}989 \pm 51$ K, $\log g = 4.16 \pm 0.08$ and $\log A({\rm Fe}) = 7.56 \pm 0.04$. These are in agreement with that found from Hα (5950 ± 70 K) and $\log g = 4.10 \pm 0.04$ obtained from analysis of the planetary transit. In addition the InfraRed Flux Method (IRFM) (Blackwell and Lynas-Gray 1998) gives $T_{\rm eff} = 5935 \pm 183$ K and an independent Stellar Parameter Classification (SPC) analysis gave $T_{\rm eff} = 5982 \pm 50$ K (Torres et al. 2012). Everything is therefore consistent to within the errors, but there is nonetheless a spread in values of 106 K in $T_{\rm eff}$, 0.17 dex in $\log g$ and 0.06 dex in $\log A({\rm Fe})$. Hence, investigation of the origins and reducing the spread in results is highly desirable.

8.3 θ *Cygni*

The 4th-magnitude θ Cyg is the brightest star in *Kepler* Field. It has a low-mass close companion (Desort et al. 2009) and a common proper motion M-type wide companion (Bidelman 1980). The literature suggests it is a normal slowly-rotating solar-composition F5 IV-type star with $T_{\rm eff} \sim 6700 \pm 100$ K and $\log g \sim 4.3 \pm 0.1$ dex (shown as the central box in Fig. 9).

As part of an asteroseismic study of this star (Guzik et al. in prep.), six independent spectroscopic analyses were performed using the equivalent width based methods of Bruntt (2010), Doyle (2013) and Sousa (2008), while Frasca (2006), Lehmann (2011) and Latham (2012) used spectral fitting techniques. Somewhat alarmingly, there is a relatively large spread in the values of $T_{\rm eff}$ and $\log g$ obtained from these spectral analyses. Examination of their locations in the $T_{\rm eff} - \log g$ diagram, shows that there appears to be a correlation between these two parameters (Fig. 9). This corresponds to the approximate location of Fe I and Fe II ionization balance. This coupling between the two parameters is a known and common problem with spectral analyses, with some methods more susceptible than others. For example, the Sousa method is differential to the Sun, with a line list specifically prepared for precise analysis of Solar-type stars and, therefore, θ Cyg is rather too hot for this differential analysis. Also, in tests of SPC used by Latham it has been noticed that the $\log g$ values can disagree systematically with cases that have independent dynamical determinations of the gravity for effective temperatures near 6,500 K and above (e.g. for Procyon and Sirius).

The spectral analyses were, therefore, repeated using a fixed $\log g = 4.23 \pm 0.03$ obtained from the asteroseismic analysis, obtaining an average $T_{\rm eff} = 6697 \pm 78$ K. The result agrees well with 6672 ± 47 K from the IRFM and 6767 ± 87 K from interferometry (Ligi et al. 2012). It is worth noting that an earlier angular diameter measurement by Boyajian et al. (2012) gave a discrepant $T_{\rm eff} = 6381 \pm 65$ K and that the $\log g$ values obtained from *uvby* and Geneva photometry were both too high.

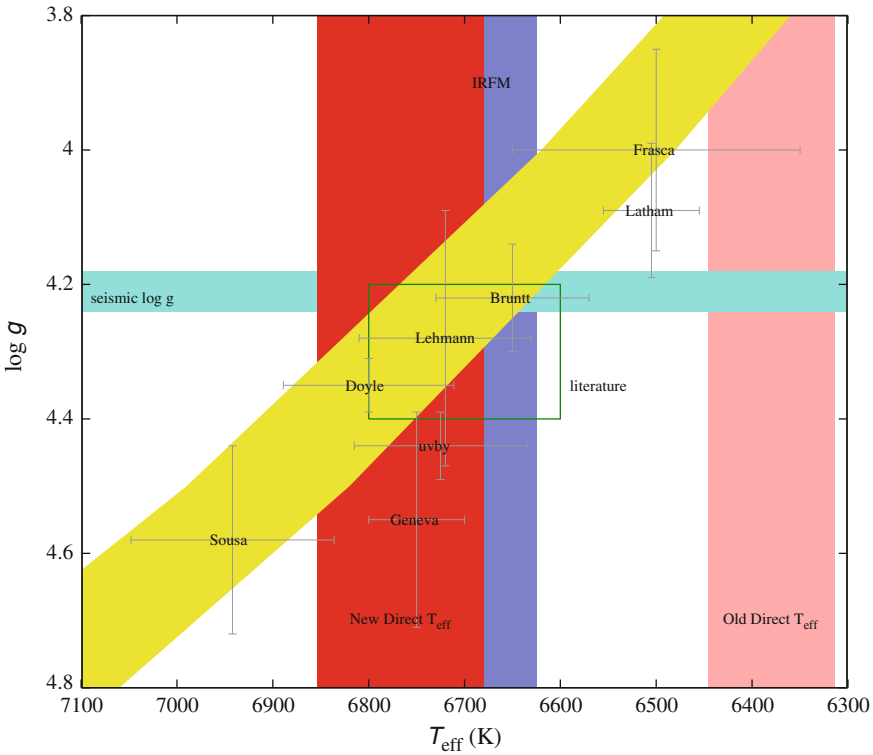

Fig. 9 Comparison of various parameter determinations for θ Cygni. See text for details

This study demonstrates the important point that the direct determinations of stellar parameters are not always totally reliable and that as many methods as possible should be used to determine stellar parameters.

9 Summary

There are *too* many factors which can influence the results from spectroscopic analyses and could lead to systematic errors in parameters and abundances obtained. It is, therefore, important to use as many diagnostics as possible, both spectroscopic and photometric, in order to evaluate the overall uncertainties in the results.

High-precision fitting to high signal-to-noise data is certainly possible, but the overall accuracy of the resultant stellar properties is less certain. Realistically the typical errors are $T_{\rm eff} \pm 50 \sim 100$ K, $\log g \ \pm 0.1 \sim 0.2$ dex and $\pm 0.05 \sim 0.10$ dex for abundances.

References

Aerts C, Christensen-Dalsgaard J, Kurtz DW (2010) Asteroseismology. Springer, Berlin
Asplund M, Grevesse N, Sauval AJ, Scott P (2009) Ann Rev A&A 47:481
Balona LA, Ripepi V, Catanzaro G et al (2011) MNRAS 414:792
Bidelman WP (1980) PASP 92:345
Blackwell DE, Booth AJ, Petford AD (1984) A&A 132:236
Blackwell DE, Lynas-Gray AE (1998) A&AS 129:505
Boyajian TS, McAlister HA, van Belle G et al (2012) ApJ 746:101
Bruntt H, Bedding TR, Quirion P-O et al (2010) MNRAS 405:1907
Bruntt H, Deleuil M, Fridlund M et al (2010) A&A 519:A51
Buchhave LA, Latham DW, Johansen A et al (2012) Nature 486:375
Cowley CR, Hubrig S, Castelli F (2008) Contributions of the astronomical observatory Skalnate Pleso 38:291
Creevey OL, Thévenin F, Basu S et al (2013) MNRAS 431:2419
Desort M, Lagrange A-M, Galland F et al (2009) A&A 506:1469
Doyle AP, Smalley B, Maxted PFL et al (2013) MNRAS 428:3164
Edvardsson B, Andersen J, Gustafsson B et al (1993) A&A 275:101
Frasca A, Guillout P, Marilli E et al (2006) A&A 454:301
Gómez Maqueo Chew Y, Faedi F, Cargile P et al (2013) ApJ 768:79
Lehmann H, Tkachenko A, Semaan T et al (2011) A&A 526:A124
Ligi R, Mourard D, Lagrange AM et al (2012) A&A 545:A5
Peterson DM, Hummel CA, Pauls TA et al (2006) ApJ 636:1087
Raskin G, van Winckel H, Hensberge H et al (2011) A&A 526:A69
Ryan SG (1998) A&A 331:1051
Santos NC, Israelian G, Mayor M (2004) A&A 415:1153
Seager S (2011) Exoplanets. University of Arizona Press, Tucson
Sousa SG, Santos NC, Mayor M et al (2008) A&A 487:373
Torres G, Andersen J, Giménez A (2010) A&A Rev 18:67
Torres G, Fischer DA, Sozzetti A et al (2012) ApJ 757:161
Valenti JA, Fischer DA (2005) ApJS 159:141
Wahlgren GM (2005) Mem Soc Astron Ital Suppl 8:108
Winn JN (2010), In: Seager S (ed) Exoplanets. University of Arizona Press, Tucson

Solar Abundance Problem

Maria Bergemann and Aldo Serenelli

Abstract The chemical composition of the Sun is among the most important quantities in astrophysics. Solar abundances are needed for modelling stellar atmospheres, stellar structure and evolution, population synthesis, and galaxies as a whole. The solar abundance problem refers to the conflict of observed data from helioseismology and the predictions made by stellar interior models for the Sun, if these models use the newest solar chemical composition obtained with 3-D and NLTE models of radiative transfer. Here we take a close look at the problem from observational and theoretical perspective. We also provide a list of possible solutions, which have yet to be tested.

Keywords Sun: abundances · Sun: photosphere · Sun: helioseismology · Sun: evolution

1 Introduction

Until recently, we thought we understand the Sun very well: its surface temperature, surface pressure, age and mass, interior physical properties, abundances of different chemical elements. After all, most of these parameters can be determined by very precise direct methods: solar effective temperature is known to an astonishing accuracy of 0.01 %, as measured from the radiant bolometric flux; neutrino fluxes provide the temperature in the solar core; solar age is obtained from isotopic ratios in meteorites; helioseismology—the analysis of propagation of acoustic waves in the

M. Bergemann (✉)
Institute of Astronomy, University of Cambridge, Madingley Road, Cambridge CB3 0HA , UK
e-mail: mbergema@ast.cam.ac.uk

A. Serenelli
Institut de Ciències de l'Espai, Facultat de Ciències, Campus UAB, 08193 Bellaterra, Spain
e-mail: aldos@ice.csic.es

E. Niemczura et al. (eds.), *Determination of Atmospheric Parameters of B-, A-, F- and G-Type Stars*, GeoPlanet: Earth and Planetary Sciences,
DOI: 10.1007/978-3-319-06956-2_21,

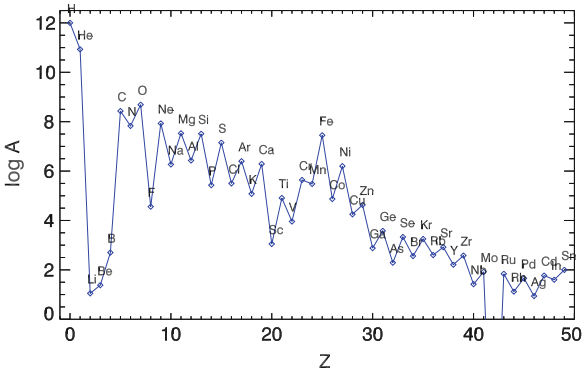

Fig. 1 Present-day solar abundances, taken from AGSS09, as a function of atomic number

solar interior—gives accurately the depth of the convective zone and surface helium abundance. It turned out, however, that what is still not known exactly is the solar chemical composition. The main reasons for this gap in our knowledge of the Sun will be discussed in this lecture.

The first paper giving a reference set of the solar abundances for many chemical elements—standard solar composition (SSC), appeared about a century ago (Russell 1929). However, only a few decades later, when computer power increased enough to run complex numerical algorithms, this dataset acquired its main value. The abundances were rightly plugged into a variety of astrophysical models. The first major application of SSC was found in the standard solar models (SSM), which predict evolution of the Sun from its formation till present. The SSC went into models of stellar evolution, stellar populations, and galaxies, becoming a ruler for measuring how dissimilar from *the Sun* are other cosmic objects. Highly accurate solar abundance distribution is nowadays needed for research into the physics of Galactic formation and evolution (e.g. Gehren et al. 2006; Feltzing and Chiba 2013), to search for solar twins, i.e. stars very similar to the Sun and thus potentially hosting earth-like planets (Meléndez et al. 2012). The Sun has also traditionally been used as a laboratory for particle physics, particularly for setting constraints on the properties of dark matter candidates such as axions, using the sensitivity of helioseismic probes of the solar structure (Schlattl et al. 1999). Also in this case, highly accurate chemical composition of the Sun is needed: abundances in the solar interior determine the radiative opacities and affect the interaction between dark matter and baryons. For example, for certain dark matter candidate particles, interaction with baryons depends strongly on the properties of nuclei—charge, spin—and a detailed knowledge of the chemical composition and profiles in the solar interior is necessary. Another example is that of non-annihilating dark matter particles, which can strongly modify the energy transport in the solar interior.

Very recently, a revision of the SSC was proposed by Asplund et al. (2009, hereafter AGSS09). The new dataset (Fig. 1) immediately became a new standard in

astronomy. But more than that, it led to a conflict with the theory of stellar evolution, thus motivating a rapid increase of research efforts in the field. The predictions of standard solar models are now in conflict with the internal structure of the Sun, as measured by the helioseismology. This is known as *the solar abundance problem* (Serenelli et al. 2009). The problem has not been solved yet. Here we only review the methods, recent progress in the field, and provide our opinion on the problem.

2 Nomenclature

There are two commonly-used abundance scales: astronomical and cosmo-chemical. The astronomical scale sets the 'zero' point at $\log \varepsilon(\mathrm{H}) = 12$, so then the abundance of each other element is given by:

$$A(\mathrm{El}) = \log \varepsilon(\mathrm{El}) = \log(n_{\mathrm{El}}/n_{\mathrm{H}}) + 12,$$

where n_{El} is the number density of element atomic. The distribution of abundances on the astronomical scale, also known as *log* scale, is shown in Fig. 1. The cosmo-chemical scale normalises all abundances to the number of Si atoms, $N_{\mathrm{Si}} = 10^6$. The latter can be coupled to the astronomical scale through a reference element, usually Si, because it can be easily measured in the solar spectrum and in meteorites.

Furthermore, to compare with the models of stellar structure and evolution, it is necessary to introduce the notations of mass fractions:

$$X + Y + Z = 1,$$

where X, Y, Z are the mass fractions of H, He, and all other heavier elements, Z being the so-called metallicity.[1]

3 Methods

Different methods have been developed to determine solar abundances. They include empirical, semi-empirical, and theoretical methods. The former two subclasses refer to an analysis of the observed solar spectrum, from the IR and optical (photospheric spectrum) to X-ray (corona), sunspots, measurements of the solar wind, flares, and energetic particles. Another rich source of information is provided by the most primitive CI chondritic meteorites that have avoided chemical fractionation and are thus

[1] Note, however, another very common definition of *metallicity* in stellar astrophysics, which is the relative abundance of iron in a star relative to the Sun, $[\mathrm{Fe/H}] = \log(n_{\mathrm{Fe}}/n_{\mathrm{H}})_{\mathrm{star}} - \log(n_{\mathrm{Fe}}/n_{\mathrm{H}})_{\mathrm{Sun}}$. Both definitions are used interchangeably, and there are transformation relations between Z and [Fe/H].

believed to preserve the solar system pristine relative abundances of refractory metals (Lodders et al. 2009). Theoretical methods include inversions of helioseismic data (e.g. Basu and Antia 2004) and nucleosynthesis models for heavy noble gases (e.g. Asplund et al. 2009).

The notation of photospheric abundances strictly applies only to the abundances determined from the spectral lines, which are formed in the solar 'photosphere', i.e. where the dominant part of the solar radiation flux is emitted. However, the region is poorly defined. Usually, lines formed at optical depths $-5 < \log \tau_{500} < 0$ are tagged as photospheric, even though the T minimum occurs at $\log \tau \sim -3$ and above this point chromosphere has a non-negligible influence on the line formation. The entire UV quasi-continuum at $\lambda < 250\,\mathrm{nm}$ has a chromospheric origin. But also IR lines, as well as some strong lines in the UV and optical (e.g., Ca triplet at 850 nm and Hα), may show signatures of chromospheric emission in the cores.

Unfortunately, each method is prone to its own limitations and thus provides only a subset of data points on the element abundance diagram. So, volatile elements: H, He, C, N, O and noble gases are absent or heavily depleted in meteorites; the solar photospheric spectrum does not contain lines of elements with very high ionisation potential, such as He and other noble gases; some elements have spectral lines in the wavelength regions inaccessible from the ground, such as the B line in the far-UV. Furthermore, to convert the abundances derived by different methods to the same scale, a reference element is needed. For homogenising meteoritic and photospheric scales, Si is often used as the anchor point between the two scales. Abundances from solar wind, corona, flares, or sunspots are converted to the photospheric scale using Ne/Mg or Ne/O ratios. This involves modelling the complex dynamical behaviour of elements with different ionisation potentials in the outermost layers of the Sun, and the robustness of such methods is questionable.

In short, the following methods are used for the analysis of different element groups:

- Inert He has a very high ionisation potential (24.6 eV), and the important lines are located in the far UV. Its abundance can be inferred from the solar wind and corona, but the value is poorly-constrained and highly variable. Theoretical models of stellar evolution and the data from helioseismology (Basu and Antia 2004) provide a more accurate estimate, consistent with each other to 10 % (see below).
- Light elements Li, Be, and B are determined from the solar spectrum. The important lines are, however, model dependent: because of very low abundances and very simple electronic configurations, the atoms give rise to one or few spectral lines only (Li I) or they are located in a very problematic part of a spectrum (Be II, B I). Lithium is depleted in the Sun by a factor of $\sim$150 compared to meteorites, but Be and B are consistent.

- Volatile elements C, N, O can be determined from the solar coronal and photospheric spectrum, where they are present in the form of atomic and molecular (e.g. CO, C_2, CH, OH, NH, CN) lines. Despite the wealth of spectral lines, the abundances of C, N, and O have always been a matter of debate.
- The abundances of refractory elements[2] can be determined from meteorites and from the solar photospheric spectrum. The two techniques give generally consistent values, apart from selected elements like Co, W, Au, Pb, Pd (Asplund et al. 2009). Meteoritic abundances can be directly measured in a laboratory through chemical analysis. However, some degree of aqueous alteration might be present and samples have to be selected carefully (Lodders et al. 2009). In contrast, photospheric abundances are model-dependent, because they require a model of radiation transport in the solar atmosphere. Moreover, there are non-negligible differences in the results caused by different spectroscopic techniques, which are partly subjective (more below). Re-determinations of meteoritic abundances of refractory elements have been very robust over the years, therefore they can be taken as a reference.
- Kr and Xe are determined from nucleosynthesis models of slow-neutron capture process. The neutron-capture cross-section is accurately known from experimental measurements (Lodders et al. 2009).

4 Solar Abundance Problem

The solar abundance problem refers to the conflict of observed data from helioseismology and the predictions made by stellar interior models for the Sun. The 'problem' emerged only recently, when a new set of solar abundances computed with the 3-D and NLTE spectroscopic methods became available. When used as a basis for calibrating the solar models, the new abundances lead to the solar interior properties, which cannot describe the present-day Sun.

To understand the roots of this problem, we first need to delve into some aspects of spectroscopic analysis that is the subject of the next section.

4.1 Solar Abundances and Metallicity

Traditionally, solar abundance has been derived from the analysis of the solar spectrum based on one-dimensional (1-D) hydrostatic model atmospheres. Moreover, local thermodynamic equilibrium (LTE) has been generally adopted. Both approximations were necessary in the past because of computational limitations (see Chap. 17). An example of an SSC based on these assumptions is that of

[2] We follow the definition of refractory versus volatile elements used in planetary sciences (not in industry), as e.g. in Taylor (2001). In this definition, a material which has relatively high condensation temperature is refractory.

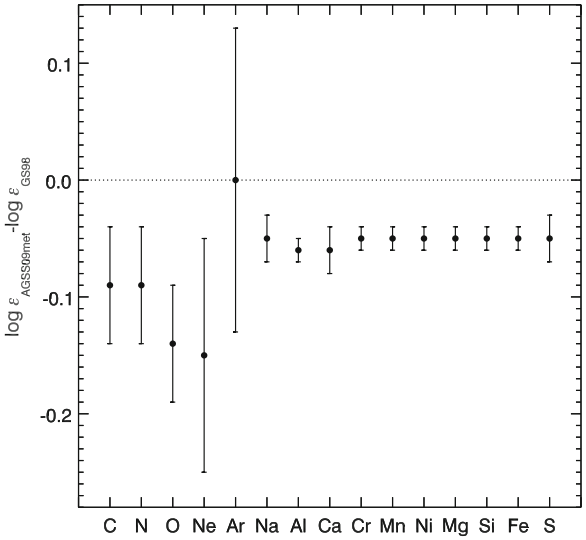

Fig. 2 Difference between AGSS09 and GS98 solar abundances. Elements shownhere are the most relevant for solar model calculations. We use photospheric abundances for the volatile elements and meteoritic abundances for all other elements in both sets of abundances

Grevesse and Sauval (1998, hereafter, GS98), which is in fact one of the most famous datasets in astronomy.

Recently, stellar spectroscopy has evidenced two major developments. First it has become possible to perform three-dimensional (3-D) radiation hydrodynamics (RHD) simulations (Nordlund et al. 2009, see for an extensive review on the topic). Another major improvement is the development of accurate NLTE radiation transport models. The 3-D RHD and NLTE models are very successful in describing a great variety of observational data, such as centre-to-limb variation of the solar radiation field, shapes and asymmetries of spectral lines, brightness intensity contrast, and they predict consistent abundances for various diagnostic lines of a given chemical element. Up to date, the most complete and consistent SSC set is that by Asplund et al. (2009).

For the reasons given in Sect. 3, meteoritic abundances of refractory elements and photospheric abundances for the volatile elements have been traditionally used in solar interior models. In what follows, we adopt this combination as our reference solar abundances, both for AGSS09 and GS98. Figure 2 shows the difference between GS98 and AGSS09 results for the elements most relevant to the solar abundance problem (C, N, O, Ne, Ar, Na, Al, Ca, Cr, Mn, Ni, Mg, Si, Fe, S). The error bars correspond to those from AGSS09.

AGSS09 abundances are systematically lower than the older GS98 values, that can be explained by several reasons [see a detailed discussion in AGSS09 and in

Grevesse et al. (2011)]. First, 3-D RHD models produce temperature fluctuations in the solar atmosphere, which are absent by construction in 1-D models, that results in lower molecular abundances. Secondly, it was recognised that the important forbidden [O I] line at 630 nm is blended by a Ni I line, a fact that was overlooked in previous studies and led to an overestimation of the O abundance. Finally, the NLTE abundance obtained from the O I 777 nm triplet is lower compared to LTE. According to AGSS09, CNO atomic and molecular indicators are now in a good agreement. Another important element, Ne, is lower in AGSS09 because its abundance is determined from the measured Ne/O ratio in the solar corona and the photospheric O abundance. Finally, for the refractory elements, the difference is caused by the lower abundance of the photospheric determination of Si, the anchor element between the photospheric and meteoritic scales. The AGSS09 Si abundance is 0.05 dex lower compared to GS98, and this brings down all refractory abundances by the same amount.

Note that another set of CNO solar abundances has been recently provided by the CO5BOLD collaboration (Caffau et al. 2011). These abundances are also based on a 3-D RHD model of the solar atmosphere, but using a different approach to abundance determinations. CO5BOLD abundances of CNO elements lie in between GS98 and AGSS09 and the quoted uncertainties are larger than those given in AGSS09. The differences between AGSS09 and CO5BOLD have been attributed to the differences in the spectrum normalisation and the choice of diagnostic lines (Grevesse et al. 2011, 2012), which are both partly subjective aspects of a spectroscopic analysis.

In summary, the differences between GS98 and AGSS09 abundances amount to 20–40 % for CNO, Ne and 12 % for refractories. Since spectroscopy provides only the relative abundances of metals to hydrogen, it is very convenient to combine all these numbers into the metal-to-hydrogen mass ratio $(\mathrm{Z/X})_\odot$. For the three sets of SSC discussed above, the values[3] are:

$$(\mathrm{Z/X})_{\mathrm{GS98}} = 0.0229; \quad (\mathrm{Z/X})_{\mathrm{CO5BOLD}} = 0.0209; \quad (\mathrm{Z/X})_{\mathrm{AGSS09}} = 0.0178.$$

The Z/X ratio is one of the three fundamental constraints that have to be satisfied by SSMs. The value of Z/X provided by CO5BOLD is obtained by complementing their photospheric measurements with abundances from Lodders et al. (2009) for refractories and noble gases.

[3] Note that the given (Z/X) were computed using photospheric abundances for the volatile elements and meteoritic abundances for all other elements. Therefore, it is slightly different from the present-day photospheric value, as e.g. given by Asplund et al. (2009, Table 4), $(Z/X) = 0.0181$.

SSMs are one-dimensional evolutionary models of a $1\,M_\odot$ star, starting from a homogeneous model in the pre-main sequence up to the present-day age of the solar system, $\tau_\odot = 4.57\,\mathrm{Gyr}$. At this age, the model has to satisfy three observational constraints: the present-day luminosity and radius ($L_\odot = 3.8418 \times 10^{33}\,\mathrm{erg\,s^{-1}}$ and $R_\odot = 6.9598 \times 10^{10}\,\mathrm{cm}$) and the $(Z/X)_\odot$. Three free parameters are calibrated to fulfil these conditions: the mixing length parameter α_{MLT} that controls the efficiency of convection in the Mixing Length Theory, Y_{ini} and Z_{ini}. The relative abundances of individual metals are assumed to be the same for a given $(Z/X)_\odot$. The initial hydrogen abundance is determined from the normalisation $X + Y + Z = 1$.

4.2 Helioseismology and the Standard Solar Models

From the discussion above, it is clear that solar abundances are critical for the calibration of SSM. Here, we focus our discussion on the GS98 and AGSS09 abundances, and label the solar models accordingly, i.e. GS98 SSM and AGSS09 SSM.

The internal structure of the Sun can be accurately determined by helioseismology. The observed oscillation spectrum can be derived from the measured light curves or from the Doppler shifts of photospheric absorption lines. The quantities we are interested in are the trapped 'eigenmodes', i.e. standing waves. The resonant cavity of these modes has its outer boundary in the solar atmosphere but the location of the inner boundary depends on the characteristics of each individual mode: its frequency and angular degree. As a result, different modes map the Sun to different depths and that allows to determine the physical properties of the interior structure as a function of depth, all the way down to the core [see Christensen-Dalsgaard (2002) for a comprehensive review on helioseismology]. Several very important physical characteristics of the Sun can be derived: the radial profile of the sound speed and the density in the interior, the location of the base of the convective envelope R_{CZ}, and the helium abundance of the envelope Y_{S}.

The main results for the SSMs and the results from helioseismology are presented in Table 1. SSMs results are taken from Serenelli et al. (2011) but, with small differences, they are common to SSM calculations from other authors (Montalbán et al. 2004; Delahaye and Pinsonneault 2006; Guzik and Mussack 2010). The $\langle \delta c/c \rangle$ and $\langle \delta \rho/\rho \rangle$ ratios are the average root-mean-square deviations of the relative difference between the model (SSM) and the solar (helioseismic) quantities. Note that the errors for the helioseismic R_{CZ} and Y_{S} are extremely small. Figure 3 also shows the relative differences of the sound speed profile and of the mean density profile for both models.

First of all, the GS98 SSM shows a very good agreement with the helioseismic inferences for Y_{S} and R_{CZ} (Table 1). The results obtained with the AGSS09

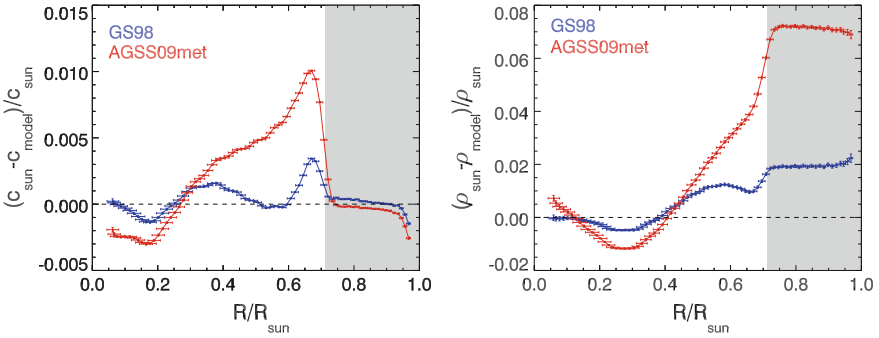

Fig. 3 Profiles of the relative difference in sound speed (*left panel*) and density (*right panel*) between the Sun and two SSMs. Models are labelled according to the SSC that was adopted in the calibration of the SSM. The grey area denotes the solar convective envelope. The error bars reflect the uncertainties from the helioseismic data. Figure reproduced by permission of the AAS: Serenelli et al. (2011)

Table 1 Main characteristics of the standard solar models and comparison to the solar (helioseismic) results

	$(Z/X)_\odot$	$Z_\odot$	Y_S	$R_{CZ}/R_\odot$	$\langle \delta c/c \rangle$	$\langle \delta\rho/\rho \rangle$	Z_{ini}	Y_{ini}
GS98	0.0229	0.0170	0.243	0.712	0.0009	0.011	0.0187	0.272
AGSS09	0.0178	0.0134	0.232	0.723	0.0037	0.040	0.0149	0.262
Solar	0.0229/0.0178[a]	0.0168/0.0131[a]	0.2485[b] $\pm$0.0035	0.713[b] $\pm$0.001	0 (def)	0 (def)	–	–

[a] Refers to GS98 and AGSS09 SSCs, respectively
[b] Basu and Antia (2004)

composition are in stark contrast with the latter. Furthermore, the choice of $(Z/X)_\odot$ has a direct impact on the calibration of solar models, as seen from the differences in the initial mass fractions of helium and of metals, Y_{ini} and Z_{ini}. The changes in Z_{ini} almost directly reflect the differences in $(Z/X)_\odot$. Metals are the dominant contributors to the radiative opacity κ in the solar interior, which in turn determines the temperature gradient in the radiative region (white area, Fig. 3). A lower metallicity leads to a smaller temperature gradient in this region and, by virtue of the Schwarzschild convection criterion, a shallower depth of the convective envelope R_{CZ} (Table 1). In the convective envelope (shaded area, Fig. 3), where the temperature gradient does not depend on κ, but only on the equation of state, both the GS98 and AGSS09 models agree well with the seismic data, $\delta c/c \sim 0$. However, in the radiative zone, where κ affects the solar structure, differences in the sound speed profiles show up.

The density values at different solar radii are strongly correlated because the density profile is constrained by the total mass of the Sun. The large differences seen in the convective envelope are anti-correlated with changes in the deeper interior where density is larger (region between 0.15 and $0.4\,R_\odot$). A smaller difference between the Sun and the model in a deep region leads to a large, compensating difference in

outer layers. Finally, the surface He abundance Y_S is also affected by the metallicity of the models. The reason is that SSMs are constrained by $L_\odot$. The AGSS09 SSM, with its shallower temperature gradient, has a lower core temperature, leading to a slower rate of nuclear energy generation. But, because nuclear reactions are the only relevant energy source in the Sun, the decrease in temperature has to be compensated by another means so that the fusion of hydrogen still produces energy at the same rate. This is achieved in the AGSS09 SSM by the increase of hydrogen abundance or, equivalently, by the decrease of helium abundance. The lower Y_S in the AGSS09 SSM also conflicts with helioseismology.

In summary, all manifestations of the solar abundance problem can be traced back to the lower radiative opacity in the interior that is a consequence of lower metal abundances in the AGSS09 dataset. Oxygen, neon, and iron are very important in this respect, as they contribute to κ in the region around R_{CZ}, where their fractional contribution to κ is about 25, 15, and 10 % respectively (Basu and Antia 2008, Fig. 12; Villante et al. 2013, Fig. 10) Other abundant refractories like magnesium and silicon are less relevant (opacity contribution of <4 %).

5 Possible Solutions

The implications of the solar abundance problem in the astrophysical context are, in fact, very large. The problem is that stellar evolution models, when applied to the Sun, produce results which are incompatible with observations (helioseismology), if these models adopt the solar chemical composition obtained by the state-of-the-art spectroscopic models. However, both stellar evolution and stellar atmosphere theory are general. All models based on these theories are calibrated on the Sun and they are routinely used to interpret any other star or stellar population. Therefore, our understanding of stars and galaxies in general is nowhere better than our current knowledge of the Sun.

What are the possible ways to reconcile the spectroscopic measurements with the solar interior models? Here we review the key possibilities that can be or have already been considered.

- Model atmospheres. It is difficult to assess and quantify uncertainties in stellar atmosphere models. Possible sources of uncertainties are: numerics (e.g., numerical methods, resolution of simulations), accuracy of the input physics (e.g., the equation of state), approximate treatment of physical processes (e.g. simplified radiative transfer). The models can be tested by comparison with observations and by comparing models from different groups. For example, Beeck et al. (2012) showed that the average stratifications of different 3-D hydrodynamical model atmospheres agree well with each other. The 3-D hydro models are also much more successful than classical 1-D static models in reproducing a wealth of observational information, including the line shapes, centre-to-limb variation, brightness

contrast (Asplund et al. 2009). However, there are implicit assumptions, which remain to be tested.
- The spectroscopic analysis. This is also a highly non-trivial problem: the uncertainties in the atomic data, line broadening, the continuum placement, selection of lines, directly impact the calculated abundances.

The NLTE radiative transfer and 3-D hydrodynamical model atmospheres are clearly setting a new basis for spectroscopy; however, it is still very difficult to combine them in one framework. The 3-D NLTE calculations can be performed on realistic timescales only for the simplest atoms, such as Li and O. More complex atoms can be only treated in a very approximated form (see Chap. 17). Future developments related to 3-D and NLTE may eventually lead to a revisions of abundances. However, it is unclear whether the abundances will increase back to the level needed for the solar abundance problem to disappear.

From the perspective of solar models, a number of possibilities to solve the solar abundance crisis have also been considered.

- The accuracy of radiative opacities for stellar interior models could be questioned. Recently, Villante et al. (2013) have shown that current helioseismic and solar neutrino data constrain well the opacity profile of the Sun, independently of the reference solar models and abundances. But in models, the opacity profile results from a combination of atomic opacity calculations and a given solar abundance. The effects of a decreasing metallicity can be mimicked by an increase in opacity. In fact, it has been shown that an increase in the radiative opacities in the range of 15–20 % at the base of the convective zone, smoothly decreasing to 3–4 % in the solar core, would suffice to reconcile AGSS09 composition with the helioseismic results (Basu and Antia 2004; Christensen-Dalsgaard et al. 2009; Villante 2010). This solution is very attractive, because radiative opacities are the result of very sophisticated (and, unfortunately, incomplete) theoretical calculations of interaction of atoms and radiation in extremely dense physical environments. There is basically no experimental data to support these calculations. In contrast to the atmosphere models, presently the best that can be done to gain confidence in such calculations is to compare the results from different groups. Three opacity sets have been compared by Blancard et al. (2012), who found much more modest differences amounting to just 3 % at the base of the convective zone, much smaller than needed. A possible way out of problem imposed by the degeneracy between opacity and composition might be offered by solar neutrino measurements. In particular, the neutrino fluxes originating in the CN-cycle depend linearly with the C and N abundance in the solar core. But C and N do not affect the solar opacity, so if the CN neutrino fluxes are measured (e.g. by the Borexino Experiment or SNO+) the solar core C and N abundance can be determined independently of the solar opacity (Serenelli et al. 2013).
- Enhanced gravitational settling in the Sun. In the conditions of the solar interior, chemical elements suffer a slow segregation process due to the combined effect of the gravitational and electric field. This process, generally known as gravitational settling, affects differently elements (actually, isotopes) based on their nuclear

charge to mass ratio Z_{nuc}/A_{nuc}. However, in the Sun, settling rates are quite similar for all metals and helium (Turcotte et al. 1998). SSM calculations show that the gravitational settling has led to the ∼10–12 % decrease of the solar surface metallicity and helium abundance with respect to the primordial values (compare the initial and surface values in Table 1). Increasing the efficiency of settling, one could construct a solar model with the initial composition comparable to GS98 and a low metallicity in the convective envelope, compatible with AGSS09. However, such a model would predict a too low Y_S, worsening the agreement with helioseismology, as discussed, for example, in Guzik and Mussack (2010). They do not offer a satisfactory solution. In order to improve the agreement with helioseismology, an ad-hoc modification of settling rates should be applied such that metals sink faster, but helium slower. Such an ad-hoc solution is not sufficiently justified and should be avoided.

- Solar models with the accretion of metal-poor material. Young stars interact and accrete material from their proto-planetary disk [see Williams and Cieza (2011) for a comprehensive review]. In the inner solar system, planets are clearly metal-rich compared to the Sun. This is true for Jupiter as well. The process of planet formation is likely to alter the average composition of the proto-planetary disk. If a part of the disk, partially depleted in metals, is accreted onto the young Sun, the solar interior will have a higher metal content than the envelope. Such models have been considered by Castro et al. (2007), Guzik and Mussack (2010) and in more detail by Serenelli et al. (2011). Unfortunately, only partial solutions to the problem have been found. One can fine-tune the mass and chemical composition of the accreted material so that R_{CZ} is close to the seismic value, but at the expense of Y_S. Under some conditions, Y_S agreement can be improved, but at the expense of degrading R_{CZ}.
- Enhanced solar neon abundance. As discussed before, the determination of the solar neon abundance is indirect. The coronal Ne/O ratio can be measured and, by assuming that the same ratio is present in the solar photosphere, the photospheric neon abundance can be determined. Keep in mind that this is a strong assumption. How different elements are transported from stellar photospheres to corona is far from being well understood, and this also depends strongly on other issues such as the stellar activity (Robrade et al. 2008). As a consequence, the Ne/O coronal ratio is not constant in time (neither for the Sun nor for other stars).

  Neon is an interesting element for SSMs because it contributes to the radiative opacity at the base of the convective envelope. Bahcall et al. (2005) and Antia and Basu (2005) constructed solar models with arbitrarily enhanced neon abundance and found that an increase of a factor of about 2 would be necessary to solve the solar abundance problem. Drake and Testa (2005) found, based on X-ray spectroscopy of nearby active stars, that neon abundances were a factor of 2.5 larger with respect to oxygen in those stars with respect to the measured solar value and concluded that the solar value was underestimated. However, it is now thought that the large Ne/O values observed in the coronae of very active stars are linked to the high activity levels and do not reflect the photospheric Ne/O ratio

(Robrade et al. 2008). Thus it does not seem likely that the solar Ne/O could be large enough to solve the solar abundance problem.

- Non-standard solar models (non-SSM). Undoubtedly the SSM, with all its intricacies, is a simplified picture of the actual Sun and its evolution. Physical processes such as rotation or internal magnetic fields are not accounted for in the SSM, and effects such as the transport of angular momentum in the solar interior might have measurable consequences in the solar structure. Modelling these processes is an inherently multi-dimensional problem and such models (to study not just the present-day structure, but the evolution of the course of 4.57 Gyr) have not yet been constructed. The models are also not feasible with present-day computational capabilities. Simplified prescriptions have been implemented into 1-D solar models. These parametrized models present a number of problems: first they contain new free parameters that have to be tuned to reproduce various observables (e.g. the internal rotation profile of the Sun), losing their predictive power. Second, such models based on the GS98 composition give an overall description of the solar structure that is worse than SSM results using AGSS09 [see e.g. Turck-Chièze et al. (2010)]. So, for non-SSM, the problem lies at a much deeper level: it is not yet possible to include realistic description of dynamical processes in the solar interior.

6 Epilogue

The solar abundance problem is that stellar evolution models, when applied to the Sun, produce results which are incompatible with observations (helioseismology), if these models adopt the solar chemical composition obtained by the state-of-the-art spectroscopic models. This should be taken as a manifestation of our incomplete understanding of the theories of stellar atmospheres and/or of stellar structure and evolution.

As discussed in these notes, at present there is no clear solution to the problem. A plausible solution is that radiative opacity calculations for stellar interiors are off by 3–20 % or so. While only 3 % is the maximum discrepancy that has been found among different opacity calculations, changes of up to 20 % might not be unreasonable. For example, the OPAL opacities (Rogers and Iglesias 1992), that first saw the light back in 1992, implied changes of up to a factor of 3 with respect to previously available calculations.

Continuous progress in different subfields might lead to a revision of the solar abundances and to changes in the solar interior models. Various options remain to be studied in greater detail and with more powerful computers, including radiative transfer models in the solar atmosphere, opacity calculations and laboratory experiments, inclusion of more realistic physics in the stellar interior modelling. It is up to you, new generation of scientists, to find the ultimate solution to the problem.

Acknowledgments AMS is supported by the MICINN grant AYA2011-24704. This work was partly supported by the European Union FP7 programme through ERC grant number 320360. Figure 3 reproduced by permission of the AAS: Serenelli et al. (2011).

References

Antia HM, Basu S (2005) Astrophys J Lett 620:L129
Asplund M, Grevesse N, Sauval AJ, Scott P (2009) Ann Rev A&A 47:481
Bahcall JN, Basu S, Serenelli AM (2005) Astrophys J 631:1281
Bahcall JN, Serenelli AM, Pinsonneault M (2004) Astrophys J 614:464
Basu S, Antia HM (2004) Astrophys J 606:L85
Basu S, Antia HM (2008) Phys Rep 457:217
Beeck B, Collet R, Steffen M et al (2012) A&A 539:A121
Blancard C, Cossé P, Faussurier G (2012) Astrophys J 745:10
Caffau E, Ludwig H-G, Steffen M, Freytag B, Bonifacio P (2011) Solar Phys 268:255
Castro M, Vauclair S, Richard O (2007) A&A 463:755
Christensen-Dalsgaard J (2002) Rev Mod Phys 74:1073
Christensen-Dalsgaard J, di Mauro MP, Houdek G, Pijpers F (2009) A&A 494:205
Delahaye F, Pinsonneault MH (2006) Astrophys J 649:529
Drake JJ, Testa P (2005) Nature 436:525
Feltzing S, Chiba M (2013) New Astron Rev 57:80
Gehren T, Shi JR, Zhang HW, Zhao G, Korn AJ (2006) A&A 451:1065
Grevesse N, Asplund M, Sauval AJ, Scott P (2011) Can J Phys 89:327
Grevesse N, Asplund M, Sauval AJ, Scott P (2012) In: Progress in solar/stellar physics with helio- and asteroseismology. ASP conference series, vol 462, p41
Grevesse N, Sauval AJ (1998) Solar composition and its evolution—from core to corona, p 161
Guzik JA, Mussack K (2010) Astrophys J 713:1108
Lodders K, Palme H, Gail H-P (2009) Landolt Börnstein, p 44
Meléndez J, Bergemann M, Cohen JG et al (2012) A&A 543:A29
Montalbán J, Miglio A, Noels A, Grevesse N, di Mauro MP (2004) In: SOHO 14 helio- and asteroseismology: towards a golden future, danesy D (ed) ESA special publication, vol 559, p 574
Nordlund Å, Stein RF, Asplund M (2009) Living Rev Sol Phys 6:2
Robrade J, Schmitt JHMM, Favata F (2008) A&A 486:995
Rogers FJ, Iglesias CA (1992) Astrophys J 401:361
Russell HN (1929) Astrophys J 70:11
Schlattl H, Weiss A, Raffelt G (1999) Astropart Phys 10:353
Serenelli AM, Basu S, Ferguson JW, Asplund M (2009) Astrophys J 705:L123
Serenelli AM, Haxton WC, Peña-Garay C (2011) Astrophys J 743:24
Serenelli A, Peña-Garay C, Haxton WC (2013) Phys Rev D 87:043001
Taylor SR, Solar system evolution: a new perspective. Cambridge University Press, Cambridge (2001)
Turck-Chièze S, Palacios A, Marques JP, Nghiem PAP (2010) Astrophys J 715:1539
Turcotte S, Richer J, Michaud G, Iglesias CA, Rogers FJ (1998) Astrophys J 504:539
Villante FL (2010) Astrophys J 724:98
Villante FL, Serenelli AM, Delahaye F, Pinsonneault MH (2013) arXiv:1312.3885
Williams JP, Cieza LA (2011) Ann Rev A&A 49:67

Magnetic Chemically Peculiar Stars

Markus Schöller and Swetlana Hubrig

Abstract Chemical peculiar (CP) stars are main-sequence A and B stars with abnormally strong or weak lines for certain elements. They generally have magnetic fields and all observables tend to vary with the same period. Chemically peculiar stars provide a wealth of information; they are natural atomic and magnetic laboratories. After a brief historical overview, we discuss the general properties of the magnetic fields in CP stars, describe the oblique rotator model, explain the dependence of the magnetic field strength on the rotation, and concentrate at the end on HgMn stars.

Keywords Stars: abundances · Stars: chemically peculiar · Stars: magnetic field · Stars: atmospheres

1 Introduction

Ap and Bp stars are main-sequence A and B stars, in the spectra of which lines of some elements are abnormally strong or weak (e.g. Si, Sr, Cr, Eu, He, …). They generally have magnetic fields that can be detected through observations of circular polarisation in spectral lines. Observables, such as the magnitudes in various photometric bands, the spectral line equivalent widths, and the magnetic field, vary with the same period, which can range from half a day to several decades. Abnormal line strengths correspond to element overabundances (by up to 5–6 dex with respect to the Sun) and are confined to the stellar outer layers. The class of chemically peculiar (CP) stars is roughly represented by three subclasses: the magnetic Ap and Bp stars,

M. Schöller (✉)
European Southern Observatory, Karl-Schwarzschild-Str. 2, 85748 Garching, Germany
e-mail: mschoell@eso.org

S. Hubrig
Leibniz-Institut für Astrophysik Potsdam, An der Sternwarte 16, 14482 Potsdam, Germany
e-mail: shubrig@aip.de

E. Niemczura et al. (eds.), *Determination of Atmospheric Parameters of B-, A-, F- and G-Type Stars*, GeoPlanet: Earth and Planetary Sciences,
DOI: 10.1007/978-3-319-06956-2_22,

Table 1 Different groups of chemically peculiar stars

Peculiarity type	Spectral type	$T_{\rm eff}$ [K] range	Magnetic	Spots
He-strong	B1–B4	17,000–21,000	Yes	Yes
He-weak	B4–B8	13,000–17,000	Yes	Yes
Si	B7–A0	9,000–14,000	Yes	Yes
HgMn	B8–A0	10,000–14,000	Yes?	Yes!
SrCrEu	A0–F0	7,000–10,000	Yes	Yes
Am	A0–F0	7,000–10,000	Yes?	No

the metallic-line Am stars, and the HgMn stars. An overview of the different groups of CP stars can be found in Table 1.

Chemically peculiar stars provide a wealth of information. For example, Castelli and Hubrig (2004) analysed a spectrum of the HgMn star HD 175640, observed with UVES at a spectral resolution of $R \sim 90{,}000$–$100{,}000$ and a spectral coverage of 3,040–10,000 Å). They used an ATLAS12 model atmosphere (Kurucz 1997) with the SYNTHE code (Kurucz 1993) to model this spectrum. They were able to obtain abundances for 49 ions, using 200 lines for abundances of light elements, 230 lines for abundances of iron group elements, and 130 lines for abundances of elements with $Z \geq 31$. They identified 80 Ti II emission lines, 40 Cr II emission lines, and used 100 components to study the Mn II hyperfine structure, 140 components for the Ga II isotopic structure, 15 components for the Ba II hyperfine structure, and 30 components for Hg II isotopic and hyperfine structure. Still, there remained 170 unidentified absorption lines and 30 unidentified emission lines.

The difference between a non-peculiar star and a CP star can be striking. Looking at the spectrum of Vega, in the region between 5,000 and 6,000 Å there are only a few lines of Na I, Mg I, Si II, and Fe II. On the other hand, CP stars can have a dozen lines within a spectral range of 10 Å, which can be seen in Fig. 1. The overabundances seen in CP stars are the result of selective diffusion of the different elements (Michaud 1970). See also Chap. "Diffusion and its Manifestation in Stellar Atmospheres".

2 A Brief Historical Overview

The first detection of a magnetic field in a star other than the Sun was achieved in CS Vir by Babcock (1947). He essentially determined the longitudinal magnetic field in this star. Today, mean longitudinal magnetic field measurements throughout the variation period have been obtained for less than 100 stars. The resolution of magnetically split lines requires a strong enough magnetic field and sufficiently slow rotation. Resolved magnetically split lines were first discovered in Babcock's star, HD 215441 (Babcock 1960), for which he measured a mean magnetic field modulus of $\langle B \rangle \sim 34$ kG, and which is the strongest magnetic field modulus measured in an Ap star to date. In 1987, twelve stars with magnetically resolved lines were known,

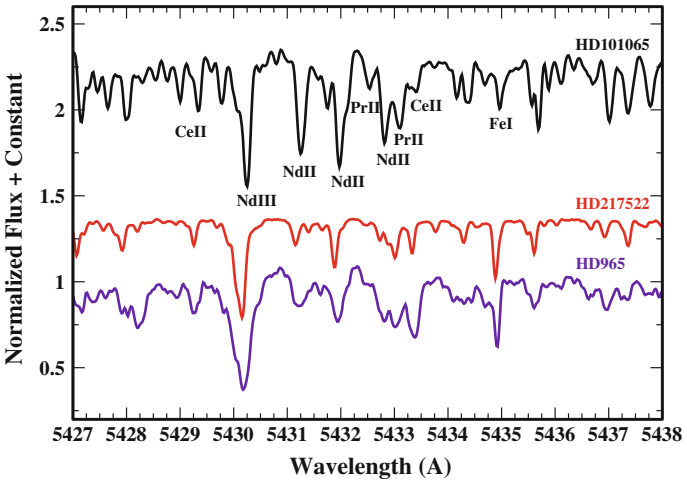

Fig. 1 UVES observations of HD 101065, HD 217522, and HD 965. The magnetically insensitive Fe I line at λ 5,434 Å is sharp and has a similar width in all three spectra. *Credit* Hubrig et al. (2002)

only four of which were studied throughout their variation period. In 2001, 44 stars with magnetically resolved lines were known, 24 of which were studied throughout their variation period (Mathys et al. 1997; Mathys et al. (in preparation)). First systematic determinations of the crossover effect and the mean quadratic magnetic field were published by Mathys (1995a, b). A full phase coverage was achieved for about two dozen stars. The bulk of the published material on broad-band linear polarisation (BBLP) was gathered by Leroy between 1990 and 1995 (Leroy 1995, and references therein). Variations in BBLP were well studied for about 15 stars. See Chap. "Magnetic Fields" on a detailed discussion of stellar magnetic fields.

3 General Properties of Magnetic Fields in Ap Stars

The strongest magnetic fields tend to be found in more massive stars. They are also found only in fast-rotating stars (Hubrig et al. 2001). All stars with rotation periods exceeding 1,000 days have magnetic fields below 6.5 kG. From the finding that the longitudinal magnetic field averaged over the stellar disk is not zero, one can directly conclude that the magnetic field needs to be organised on a larger scale, i.e. it is a dipole or a superposition of a dipole and a quadrupole. The circular polarisation from tangled, solar-like magnetic fields mostly cancels out in a disk integration. The magnetic field of Ap stars thus has a significant dipole-like component. For a dipole, the ratio between the longitudinal magnetic field and the magnetic field modulus $\langle B_z \rangle / \langle B \rangle$ is 0.3, for a quadrupole it is 0.05. If toroidal or higher-order multipolar components were sufficient to account for the observed longitudinal magnetic field,

these would induce strong distortions of the spectral line profiles in Stokes I, i.e. in integral light, which we do not see.

The magnetic field covers the whole stellar surface homogeneously, i.e. the distribution of the field strength over the star is fairly narrow. Evidence for this comes from the fact that the magnetic field is observed at all phases, the continuum is reached between the split components of resolved lines, and that the resolved magnetically split components are rather narrow (Mathys et al. 1997).

Magnetic fields have severe effects on the structure of stellar outer layers. They are responsible for magnetically controlled winds and elemental abundance stratification. Evidence for abnormal atmospheric structure comes from the fact that profiles of hydrogen Balmer lines in cool Ap stars can not be fitted by conventional models (Ryabchikova et al. 2002). This has also a potential impact on the longitudinal magnetic field determination by Balmer line polarimetry. The core-wing anomaly (Cowley et al. 2001) of the hydrogen Balmer lines leads to the impossibility of fitting the Balmer lines with one effective temperature. For example, to fit the Hβ line in HD 965, one needs to assume $T_{\rm eff} = 5{,}500$ K for the core and $T_{\rm eff} = 7{,}000$ K for the wings.

4 The Oblique Rotator and the Geometric Structure of the Magnetic Field

The magnetic field is not symmetric with respect to the stellar rotation axis. Other surface features, e.g. the abundance distribution, are determined by the magnetic field. Observed variations result from changing aspects of the visible hemisphere as the star rotates. Thus, the variation period is the rotation period of the star. No intrinsic variations of the magnetic field have been observed in Ap stars over timescales of decades.

In early models of the magnetic field, a quasi-sinusoidal variation of the longitudinal magnetic field was assumed. In the simplest model, a dipole centred at the star's centre and with an axis inclined with respect to the stellar rotation axis, was employed. From stars with magnetically resolved lines, it can be seen that the mean magnetic field modulus generally has one maximum and one minimum per rotation period, even for stars with a reversing longitudinal magnetic field (Mathys et al. 1997). From these observations, a centred dipole can be ruled out. Alternative models include a dipole that is offset along its axis (parameters: i, β, $B_{\rm d}$, a), or a collinear dipole plus a quadrupole (parameters: i, β, $B_{\rm d}$, $B_{\rm q}$), with i the inclination angle of the star with respect to the line of sight, β the inclination angle of the magnetic field with respect to i, $B_{\rm d}$ the strength of the dipole, $B_{\rm q}$ the strength of the quadrupole, and a the offset of the dipole with respect to the star's centre. The models have to make a good match with four observables: the maximum and the minimum of both the longitudinal magnetic field and the magnetic field modulus. Both models are equivalent to first order.

Additional constraints on the magnetic field geometry can come from the crossover and the mean quadratic magnetic field. A collinear dipole plus a quadrupole and an octupole give good first approximations in many cases (Landstreet and Mathys 2000). The dipole primarily accounts for the longitudinal magnetic field, the quadrupole gives the field strength contrast between the poles, and the octupole is responsible for the equator-to-pole field strength contrast. Asymmetric variation curves can be determined from some magnetic field moments. They exist, if the magnetic field is not symmetric about an axis passing through the centre of the star (Mathys and IAU Coll 1993) and can be described with a generalised multipolar model (Bagnulo 2000, and references therein). The input observables for these models are all available observables of the magnetic field: $\langle B_z \rangle$, $\langle x B_z \rangle$, $\sqrt{\langle B^2 \rangle + \langle B_z^2 \rangle}$, $\langle B \rangle$, and the BBLP. A χ^2 minimisation between the predicted and the observed values of the observables at phases distributed throughout the rotation period will determine the final model for the geometric structure of the magnetic field.

Ultimately, a direct inversion of the line profiles recorded in all four Stokes parameters will allow one to derive magnetic field maps without a priori assumptions. Since the inversion is an ill-posed problem, a regularisation condition is needed. This is achieved with the magnetic Doppler imaging technique (Piskunov and Kochukhov 2002). It is very demanding in terms of the signal-to-noise ratio in the data, spectral resolution, and phase coverage. So far, these inversions are restricted to a few individual stars (e.g. Lüftinger et al. 2010; Kochukhov 2004).

5 Field Strength Distribution and Rotation

The mean longitudinal magnetic field distribution extends all the way down to the detection limit of 100 G or less (Landstreet 1982). The rms mean longitudinal magnetic field averaged over a stellar rotation period is of the order of 300 G for "classical" Ap stars, and larger ($\sim$1 kG) for hotter He weak and He strong Bp stars (Landstreet 1982).

The mean magnetic field modulus much better characterises the intrinsic stellar magnetic field than the mean longitudinal magnetic field, which is much more dependent on the geometry of the observation. Most Ap stars with magnetically resolved lines have a mean magnetic field modulus (averaged over the stellar rotation period) comprised between 3 and 9 kG. But there is a lower cutoff of the distribution at 2.8 kG. One expects to be able to resolve lines down to 1.7 kG or lower at some rotation phases of some stars, but only for one target it is observed down to 2.2 kG. The lower limit of the magnetic field distribution is roughly temperature independent; hotter stars may have stronger magnetic fields than cooler stars (Mathys et al. 1997).

Ap star variation periods span five orders of magnitude. Until recently, there seemed to be no systematic differences between short and long period stars. A confirmation that very long periods are indeed rotation periods has been brought by BBLP (Leroy et al. 1994). The systematic study of Ap stars with resolved magnetically split lines has doubled the number of known stars with $P > 30$ days. The

distribution of periods longer than 1 year is compatible with an equipartition on a logarithmic scale. No star with $P > 150$ days has a mean magnetic field modulus exceeding 7.5 kG. More than 50 % of the stars with resolved lines and shorter periods have a magnetic field modulus above this value (Mathys et al. 1997). In the collinear dipole plus quadrupole and octupole model, the angle between the magnetic and rotation axis β is generally smaller than 20° for stars with $P > 30$ days, unlike for short period magnetic Ap stars, for which this angle is usually large (Landstreet and Mathys 2000).

6 HgMn Stars

HgMn stars are chemically peculiar stars with spectral type B8 to A0 and $T_{\rm eff} = 10{,}000$–$14{,}000$ K. They show extreme overabundance of Hg (up to 6 dex) and/or Mn (up to 3 dex). They display the most obvious departures from abundances expected within the context of nucleosynthesis (Cowley and Aikman 1975). More than 150 HgMn stars are known, many of which are found in young associations (Sco-Cen, Orion OB1). They are among the most slowly rotating stars on the upper main sequence and have exceptionally stable atmospheres with an average rotational velocity of $\langle v \sin i \rangle = 29\,{\rm km\,s^{-1}}$, which leads to extremely sharp-lined spectra. They are the best suited targets to study isotopic and hyperfine structure. More than two-thirds of the HgMn stars belong to SB systems with a prevalence of $P_{\rm orb} \approx 3$–20 days. Many HgMn stars are in multiple systems. The spectrum variability seen in HgMn stars is due to the presence of chemical spots. They do not have strong large-scale organised magnetic fields, but tangled magnetic fields are possible. They do not have enhanced strengths of rare earth elements, but of the heavy elements W, Re, Os, Ir, Pt, Au, Hg, Tl, Pb, and Bi, which makes them a natural laboratory for the study of heavy elements. They also show anomalous isotopic abundances for the elements He, Hg, Pt, Tl, Pb, and Ca.

Schöller et al. (2010) studied the multiplicity of late-type B stars with HgMn peculiarity. From observations of 57 HgMn stars obtained at the VLT with the NACO instrument in K_s with the S13 camera, they found 34 companion candidates in 25 binaries, three triples, and one quadruple (see Fig. 2). Nine companion candidates were found for the first time; five objects are very likely chance projections. Only five stars in the total sample show no indication of multiplicity, taking into account that 44 systems are confirmed or suspected spectroscopic binaries. On the other hand, in a study of rapidly oscillating Ap (roAp) stars, Schöller et al. (2012) found a total of six high probability companion candidates in a survey of 28 roAp stars. The roAp stars pulsate in high-overtone, low-degree, non-radial p-modes, with periods in the range from 5.6 to 21 min and typical amplitudes of a few millimagnitudes (e.g. Kurtz 1982). They are ideal targets for asteroseismology. The intriguing question is if and how multiplicity can shape the appearance of chemically peculiar stars. An overview about the prevalence of binaries in different classes of CP stars and normal stars can be found in Table 2.

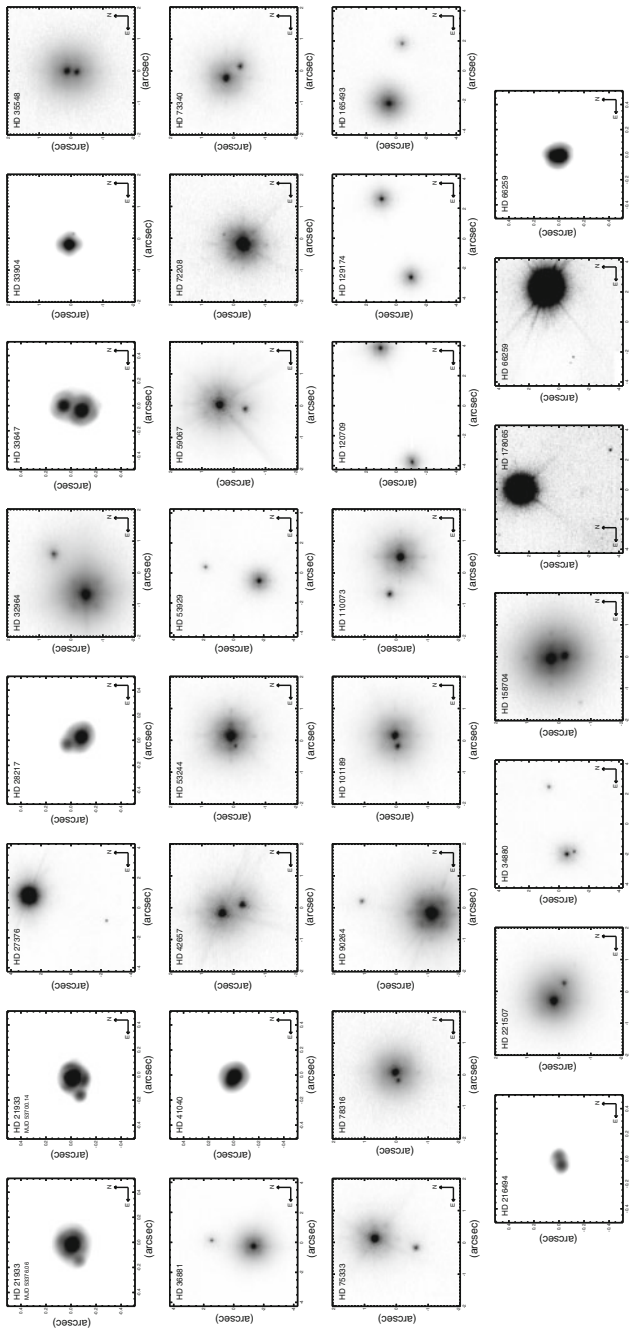

Fig. 2 Companion candidates to HgMn stars, detected with NACO by Schöller et al. (2010). *Credit* Schöller et al. (2010), reproduced with permission ©ESO

Table 2 Multiplicity of different stellar types

Type	Percentage (%)	Reference	SB
Normal A	∼35	Kouwenhoven et al. (2005)	
Normal B	∼30	Kouwenhoven et al. (2005)	
Magnetic Ap	43	Carrier et al. (2002)	Very few SB2
Magnetic Bp	∼20	Renson and Manfroid (2009)	Very few SB2
HgMn	>90	Schöller et al. (2010)	2/3
Am	>90	Renson and Manfroid (2009)	>90 %
roAp	24	Schöller et al. (2012)	2 out of ∼45

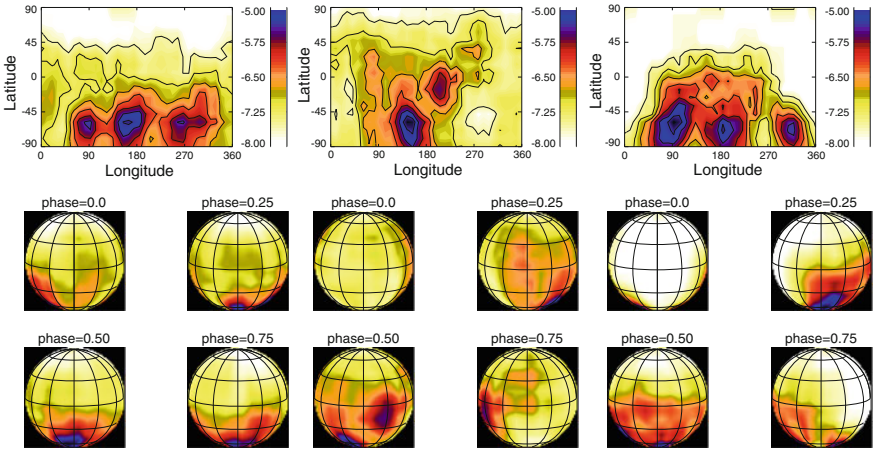

Fig. 3 Maps of the abundance distribution for Fe (*left*), Sr (middle), and Y (*right*) on the surface of the primary in the system AR Aur. *Credit* Hubrig et al. (2012), reproduced with permission ©ESO

One of the most exciting objects containing a HgMn star is the triple system AR Aur. The inner two stars constitute the only known eclipsing binary encompassing a HgMn star. This binary has an orbital period of 4.13 days and an age of 4 Myr. The two stars are of spectral types B9 V and B9.5 V, and while the primary HgMn star is exactly on the ZAMS, the secondary is still contracting (e.g. Nordström and Johansen 1994). Hubrig et al. (2012) used observations with SOFIN at the Nordic Optical Telescope to study the distribution of different elements over the surface of the primary HgMn star, using the Doppler mapping technique (see Fig. 3). From the same data set, they also determined the magnetic field in both primary and secondary components (Fig. 4). AR Aur shows a similar behaviour to other HgMn systems discussed by Hubrig et al. (2012). The results suggest the existence of a correlation between the magnetic field, the abundance anomalies, and the binary properties. For the synchronously rotating components of the SB2 system AR Aur, it looks as if the stellar surfaces facing the companion star usually display low-abundance element spots, or no spots at all, and negative magnetic field polarity (Hubrig et al. 2010).

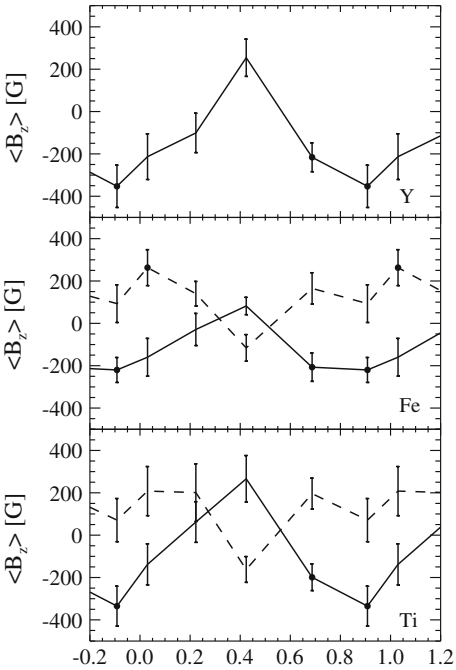

Fig. 4 Measurements of the mean longitudinal magnetic field presented as a function of the rotation phase for AR Aur. They were carried out separately for the elements Ti, Fe, and Y (from *bottom* to *top*). The solid line denotes the primary component, while the dashed line denotes the secondary component. Filled circles indicate 3σ measurements. *Credit* Hubrig et al. (2012), reproduced with permission ©ESO

The surface of the opposite hemisphere, as a rule, is covered by high-abundance element spots and the magnetic field is positive at the rotation phases of the best-spot visibility (Hubrig et al. 2012). However, the discussion about the presence of weak magnetic fields in HgMn stars is still ongoing (see Kochukhov et al. 2013).

7 Summary

Chemically peculiar stars are probably the most challenging main sequence stars to model due to their magnetic fields, and the element segregation and stratification. They are ideal atomic physics laboratories. They are the best objects to learn about magnetic field models, to be applied to other classes of stars. Binarity and multiplicity for the different classes is different, which potentially leads to new insights into star formation mechanisms.

References

Babcock HW (1947) ApJ 105:105
Babcock HW (1960) ApJ 132:521
Bagnulo S, Landolfi M, Mathys G, Landi Degl'Innocenti M (2000) A&A 358:929
Carrier F, North P, Udry S, Babel J (2002) A&A 394:151
Castelli F, Hubrig S (2004) A&A 425:263
Cowley CR, Aikman GCL (1975) ApJ 196:521
Cowley CR, Hubrig S, Ryabchikova TA et al (2001) A&A 367:939
Hubrig S, North P, Mathys G (2001) ApJ 539:352
Hubrig S, Cowley CR, Bagnulo S (2002) In: Tout CA, van Hamme W (eds) Exotic stars as challenges to evolution. ASP conference series, vol 279, p 365
Hubrig S, Savanov I, Ilyin I et al (2010) MNRAS 408:L61
Hubrig S, González JF, Ilyin I et al (2012) A&A 547:A90
Kochukhov O, Bagnulo S, Wade GA et al (2004) A&A 414:613
Kochukhov O, Makaganiuk V, Piskunov N et al (2013) A&A 554:A61
Kouwenhoven MBN, Brown AGA, Zinnecker H et al (2005) A&A 430:137
Kurtz DW (1982) MNRAS 200:807
Kurucz RL (1993) SYNTHE spectrum synthesis programs and line data, CD-ROM, No. 18
Kurucz RL (1997) In: Philip AGD, Liebert J, Saffer RA (eds) The 3rd conference on faint blue stars. L. Davis Press, Schenectady, p 33
Landstreet JD (1982) A&AR 4:35
Landstreet JD, Mathys G (2000) A&A 359:213
Leroy JL, Bagnulo S, Landolfi M, Landi Degl'Innocenti E A&A 284:174
Leroy JL (1995) A&AS 114:79
Lüftinger T, Kochukhov O, Ryabchikova T et al (2010) A&A 509:A71
Mathys G (1993) IAU Coll 138:232
Mathys G (1995a) A&A 293:733
Mathys G (1995b) A&A 293:746
Mathys G, Hubrig S, Landstreet JD et al (1997) A&AS 123:353
Michaud G (1970) ApJ 160:641
Nordström B, Johansen KT (1994) A&A 282:787
Piskunov N, Kochukhov O (2002) A&A 381:736
Renson P, Manfroid J (2009) A&A 498:961
Ryabchikova T, Piskunov N, Kochukhov O et al (2002) A&A 384:545
Schöller M, Correia S, Hubrig S, Ageorges N (2010) A&A 522:A85
Schöller M, Correia S, Hubrig S, Kurtz DW (2012) A&A 545:A38

Magnetic Fields

Markus Schöller and Swetlana Hubrig

Abstract In this chapter, we give a brief introduction into the use of the Zeeman effect in astronomy and the general detection of magnetic fields in stars, concentrating on the use of FORS 2 for longitudinal magnetic field measurements.

Keywords Stars: magnetic field · Methods: data analysis · Techniques: spectroscopic

1 Magnetic Fields in Stars

Magnetic fields are found everywhere in the cosmos, from very weak fields in the interstellar medium to the fields of magnetars, which are many orders of magnitude stronger than any field ever generated by a human. It is probably true that every star has a magnetic field. When reading in the literature that a star is magnetic, this usually means that it is strongly magnetic, or even clearer, its magnetic field is strong enough to be detected. To get an idea of the strength of the magnetic fields in different kind of stars, we give a brief overview here:

- Vega: <1 G
- Sun: 0.5–4 G, in sunspots 2–5 kG
- Babcock's (Ap) star: 34 kG
- White dwarfs: 10^3–10^9 G
- Neutron stars and magnetars: 10^9–10^{15} G

M. Schöller (✉)
European Southern Observatory, Karl-Schwarzschild-Str. 2, 85748 Garching, Germany
e-mail: mschoell@eso.org

S. Hubrig
Leibniz-Institut für Astrophysik Potsdam, An der Sternwarte 16, 14482 Potsdam, Germany
e-mail: shubrig@aip.de

E. Niemczura et al. (eds.), *Determination of Atmospheric Parameters of B-, A-, F- and G-Type Stars*, GeoPlanet: Earth and Planetary Sciences,
DOI: 10.1007/978-3-319-06956-2_23, © Springer International Publishing Switzerland 2014

Magnetic fields in astronomy are typically measured in Gauss, where 1 G corresponds to 0.1 mT. Technically generated magnetic fields on earth are on the order of tens of Tesla for permanent fields, or tens of kT for short-lived fields, which is still six to seven orders of magnitude smaller than the strongest fields in the neutron stars.

Generally, astronomers have a love–hate relationship with magnetic fields. They are hated, since they make everything complicated, e.g. breaking the symmetries in models. On the other hand, magnetic fields are loved, because they are used as potential culprits for differences between theory and observation.

Magnetic fields in stars may come from two different sources. They might be of fossil origin, which implies that the magnetic flux BR^2 from the cloud they were born from, was at least in part conserved during the cloud's collapse. The magnetic flux is the product of the magnetic field strength B and the square of the radius R. While the magnetic flux levels in the parent cloud are very low, the resulting magnetic fields in the star would be enormous due to the huge reduction in R during the contraction before the star's birth; thus, an efficient method is needed to lose the excessive magnetic flux. Another source for the magnetic field could be a dynamo process, which permanently regenerates the magnetic field using a seed field. Dynamo action leads to the sun's magnetic field and the solar cycle.

Magnetic fields are responsible for various processes in stars. They can dominate the accretion process in pre-main sequence stars, they are responsible for stellar activity like spots or flares, they can lead to chemical peculiarities, they heat the corona, which then produces X-rays, they brake stellar rotation and thus slow stars down, and they accelerate cosmic ray particles in neutron stars and are responsible for the pulses in the pulsars, a good example for oblique rotators.

2 The Zeeman Effect

The Zeeman effect describes the splitting of a spectral line into several components in the presence of a static magnetic field. The distance between the Zeeman sub-levels is a function of the magnetic field B, linear for weak fields. It is proportional to the square of the wavelength, λ^2. For strong magnetic fields, the splitting is governed by the Paschen-Back effect. Transitions responsible for the spectral lines follow the selection rule that allows the difference of the magnetic moment Δm_J to assume only values of 0 (the π component) or ± 1 (the σ components). In a magnetic field parallel to the line of sight, the π component vanishes and the σ components are circularly polarized, with opposite directions. This allows us to determine the longitudinal magnetic field through measurements of circularly polarized light. The Zeeman effect can be used to directly measure the magnetic field in stars or in laboratory plasmas. The resulting line splitting is ± 0.012 Å for the Zeeman π–σ component separation for 5,000 Å and a 1 kG magnetic field. The Zeeman effect is named after the Dutch physicist Pieter Zeeman, who won the Nobel Prize in 1902. Figure 1 shows the effect of the magnetic field on the solar spectrum over a sun spot.

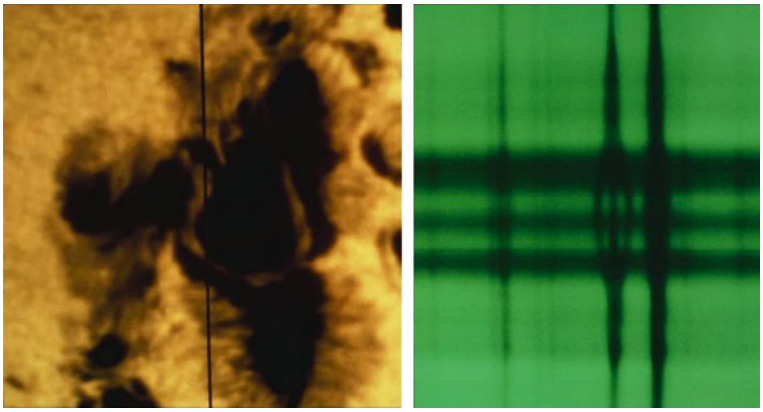

Fig. 1 A complex sunspot picture, taken at 15:30 h UT on 1974 July 4. The *vertical black line* on the *white light image* (*left*) indicates the location of the slit for the spectrograph that took the spectrum, shown on the *right*. The division of one spectral line into three parts is a clear demonstration of the Zeeman effect. In fact, the Zeeman splitting of this line, at 5,250.2 Å and coming from iron, indicates a record field strength of 4,130 G. This picture was taken at the McMath-Pierce Solar Facility on Kitt Peak. *Credit* NOAO/AURA/NSF

3 Detecting Magnetic Fields

While magnetic fields in stars can also be detected from integral light (Stokes I) spectra, if the fields are strong and the stars rotate very slowly, most of the work in this area is done with spectropolarimeters. The work horses for stellar magnetic field research are the low-resolution spectrograph FORS 2 at the VLT on Paranal, and the high-resolution spectrographs ESPaDOnS at the CFHT on Mauna Kea, HARPSpol at the ESO 3.6 m on La Silla, and NARVAL at the TBL on Pic du Midi.

Polarized light comes in two flavors, linearly and circularly polarized light. For the magnetic field detection, we are particularly interested in the left and right circularly polarized light. A polarimetric instrument makes use of three types of optical components. A Wollaston prism splits linearly polarized light into ordinary and extraordinary beams. A half wave plate rotates a polarization axis by 90°. A quarter wave plate changes linearly polarized light into circularly polarized light and back.

Different experiments measure different aspects of the magnetic field. While the magnetic field is in every location a 3d-vector $\mathscr{B} = (B_\mathrm{x}, B_\mathrm{y}, B_\mathrm{z})$, we measure typically, averaged over the stellar disk:

- the longitudinal magnetic field $\langle B_\mathrm{z} \rangle$,
- the magnetic field modulus $\langle |B| \rangle$,
- the crossover effect $v \sin i \langle x B_\mathrm{z} \rangle$, and
- the mean quadratic magnetic field $\sqrt{\langle B^2 \rangle + \langle B_\mathrm{z}^2 \rangle}$.

These different characteristics of the magnetic field are measured from different indicators in the spectra (e.g. Mathys 1993). The longitudinal magnetic field $\langle B_\mathrm{z} \rangle$ is

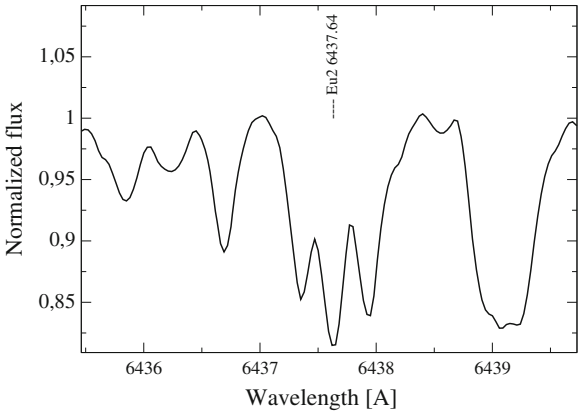

Fig. 2 The spectrum of the Ap star HD 92499 in the spectral region around the Eu II line λ 6437.6 Å. The splitting in this picture results from a magnetic field with a mean magnetic field modulus of 8.5 kG. *Credit* Hubrig and Nesvacil (2007, Fig. 4)

derived from measurements of wavelength shifts of spectral lines between right and left circular polarizations. The crossover $v \sin i \langle x B_z \rangle$ is determined from measurements of the second-order moments of line profiles in Stokes V, i.e. the difference of line width between opposite circular polarizations. The mean quadratic magnetic field $\sqrt{\langle B^2 \rangle + \langle B_z^2 \rangle}$ is calculated from measurements of the second-order moments of line profiles in Stokes I, i.e. the total line widths in integral light.

The mean magnetic field modulus $\langle |B| \rangle$ is derived from measurements of the wavelength separation of resolved magnetically split components of spectral lines in Stokes I. For example, Hubrig and Nesvacil (2007) found a mean magnetic field of 8.5 kG in HD 92499 (see Fig. 2) from Zeeman splitting in unpolarized light. Johns-Krull et al. (1999) found a magnetic field of 2.6 ± 0.3 kG in BP Tau from the broadening of the Ti I line at 2.2233 μm.

From broad-band linear polarization (Q, U) a meaningful constraint on the magnetic field can be derived from considerations of the path followed by the star in the (Q/I, U/I) plane (e.g. Leroy et al. 1996).

4 Detecting Longitudinal Magnetic Fields with FORS 2

With FORS 2 in spectropolarimetric mode, we are observing the mean longitudinal magnetic field. The mean longitudinal magnetic field $\langle B_z \rangle$ is the component of the magnetic field parallel to the line-of-sight averaged over the stellar hemisphere visible at the time of observation and weighted by the local emergent spectral line intensity. It depends strongly on the angles between the line-of-sight, the rotation axis, and the magnetic axis, as well as the rotation phase. Thus, it is very useful to follow stellar

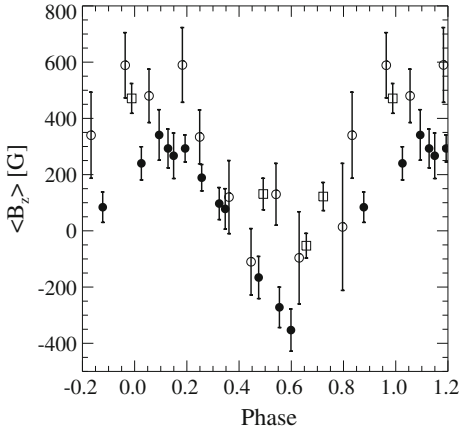

Fig. 3 $\langle B_z \rangle$ versus the rotation phase for θ^1 Ori C. *Open circles* Observations by Wade et al. (2006) with MuSiCoS at the TBL. *Open squares* Observations by Petit et al. (2008) with ESPaDOnS and Narval. *Filled circles* FORS 1 measurements by Hubrig et al. (2008). *Credit* Hubrig et al. (2008), reproduced with permission ©ESO

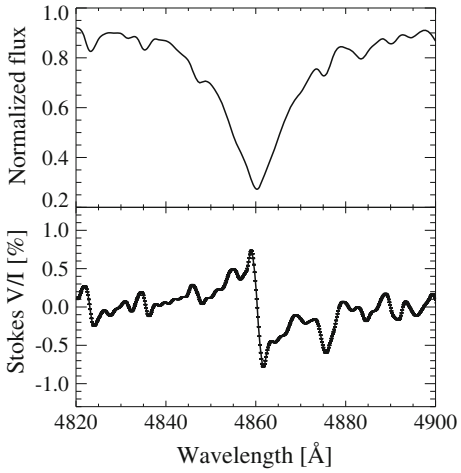

Fig. 4 Stokes I (*top*) and V/I (*bottom*) spectra of the Ap star HD 157751 in the vicinity of the Hβ line. In the V/I spectrum, a typical Zeeman pattern can be seen, evidence for a longitudinal magnetic field of the order of 4 kG. *Credit* Hubrig and Nesvacil (2007, Fig. 2)

rotation, but it is very limited in detecting magnetic fields from single observations. Figure 3 shows measurements of the longitudinal magnetic field of θ^1 Ori C.

In the oblique rotator model, we assume that we observe a magnetic field, tilted with respect to the rotation axis, from different viewing angles, while the star rotates. This magnetic field does not need to be a dipole, which can nicely be seen in the work by Donati et al. (2006) on τ Sco.

For FORS 2 spectropolarimetric observations, we use a quarter wave plate to go from circular polarization to linear polarization and a Wollaston prism to split the light with a 22″ beam divergence. The spectral resolution achieved with FORS 2 depends on the grism used, and is typically between 2,000 and 4,000.

In a typical observing sequence, the retarder waveplate is set to e.g. +45°, an exposure is taken, which leads to two, the ordinary and the extraordinary, spectra, then the retarder waveplate is set to −45°, and another exposure is taken. With this

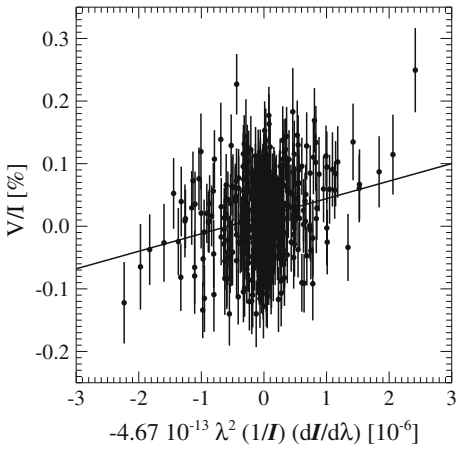

Fig. 5 Linear regression detection of a ∼300 G longitudinal magnetic field in the β Cep star ξ^1 CMa. *Credit* Hubrig et al. (2006)

sequence we have now obtained four spectra. In order to obtain a larger number of these sets of four spectra, we would continue with further pairs of retarder waveplate settings, typical $-45°/+45°$, $+45°/-45°$, $-45°/+45°$, etc., moving the retarder waveplate only every second exposure to ensure symmetry in time. From the four or more spectra, we calculate the V/I spectrum according to

$$\frac{V}{I} = \frac{1}{2}\left\{\left(\frac{f^{\rm o}-f^{\rm e}}{f^{\rm o}+f^{\rm e}}\right)_{\alpha=+45°} - \left(\frac{f^{\rm o}-f^{\rm e}}{f^{\rm o}+f^{\rm e}}\right)_{\alpha=-45°}\right\}, \tag{1}$$

where α indicates the position angle of the retarder waveplate and $f^{\rm o}$ and $f^{\rm e}$ are the ordinary and extraordinary beams, respectively. A typical V/I spectrum for a star with a rather strong magnetic field can be seen in Fig. 4. The V/I spectrum can be described by

$$\frac{V}{I} = -\frac{g_{\rm eff} e \lambda^2}{4\pi m_e c^2}\,\frac{1}{I}\,\frac{{\rm d}I}{{\rm d}\lambda}\langle B_{\rm z}\rangle, \tag{2}$$

where V is the Stokes parameter that measures the circular polarization, I is the intensity in the unpolarized spectrum, $g_{\rm eff}$ is the effective Landé factor, e is the electron charge, λ is the wavelength, m_e the electron mass, c the speed of light, ${\rm d}I/{\rm d}\lambda$ is the derivative of Stokes I, and $\langle B_{\rm z}\rangle$ is the mean longitudinal magnetic field. We have measured the left side of the equation, and can calculate the factor before $\langle B_{\rm z}\rangle$ from the Stokes I spectrum. Next, we fit a linear function to the data pairs we have just generated. The slope of this function gives the longitudinal magnetic field. An example for such a linear regression can be seen in Fig. 5.

While FORS1/2 has a remarkable potential to detect magnetic fields, it is advised to confirm these detections with high-resolution spectropolarimetry, wherever possible. A review of FORS1 uncertainties can be found in Bagnulo et al. (2012). Detec-

tions of a magnetic field in a number of Ap/Bp stars, as well as pulsating B- and massive O-type stars with low-resolution spectropolarimetry have subsequently been confirmed with high-resolution spectropolarimetry. This was not only possible for stars exhibiting stronger mean longitudinal magnetic fields of the order of a few hundred Gauss (e.g. Hubrig et al. 2006, 2011), but also for stars with rather weak magnetic fields of the order of 100 G and less (Hubrig et al. 2009; Sodor et al. 2014).

References

Bagnulo S, Landstreet JD, Fossati L, Kochukhov O (2012) A&A 538:A129
Donati J-F, Howarth ID, Jardine MM et al (2006) MNRAS 370:629
Hubrig S, Briquet M, Schöller M et al (2006) MNRAS 369:L61
Hubrig S, Nesvacil N (2007) MNRAS 378:L16
Hubrig S, Schöller M, Schnerr RS et al (2008) A&A 490:793
Hubrig S, Briquet M, De Cat P et al (2009) AN 330:317
Hubrig S, Ilyin I, Schöller M et al (2011) ApJ 726:L5
Johns-Krull CM, Valenti JA, Koresko C (1999) ApJ 516:900
Leroy JL, Landolfi M, Landi Degl'Innocenti E (1996) A&A, 311:513
Mathys G (1993) In Dworetsky MM, Castelli F, Faraggiana R (eds) ASP conference ser, vol 44, p 232
Petit V, Wade GA, Drissen L et al (2008) MNRAS 387:L23
Sódor Á, De Cat P, Wright DJ et al (2014) MNRAS 438:3535
Wade GA, Fullerton AW, Donati J-F et al (2006) A&A 451:195

Spectral Synthesis Codes and Methods of Analysis

Tatiana Ryabchikova

Abstract This lecture gives a short description of a few of the more important codes for spectrum synthesis applied for calculations of the output flux in one-dimensional (1-D) plane-parallel stellar atmosphere in the approximation of the local thermodynamic equilibrium (LTE). Some of the codes have options for NLTE spectral synthesis. The advantages and disadvantages of each code are briefly discussed. Comparisons of the synthetic spectra calculated with different codes show that they agree within 1 % in the centres of strong lines. For the integrated over line-profile flux (equivalent width) the difference is up to 3 % for weak lines and decreases to 1.5 % for strong lines. Iron abundance derived with different codes does not differ by more than 0.02 dex in wide range of line intensities, providing the use of the same line parameters.

Keywords Astrochemistry · Line: formation · Methods: data analysis · Stars: fundamental parameters · Stars: abundances · Techniques: spectroscopic

1 Introduction

The full set of atomic parameters required for the description of the spectral line formation was considered in my previous lecture ("Atomic Data: Where to Get Them, How to Use Them"). Besides the line data we also need model atmosphere—distribution of temperature, pressure and density with optical/geometrical depth, to calculate the output flux which may be compared to the observed stellar spectrum. This comparison allows us to derive the global parameters of stellar atmosphere, i.e. effective temperature, surface gravity and atmospheric abundances. Main principles

T. Ryabchikova (✉)
Institute of Astronomy, Russian Academy of Sciences,
Pyatnitskaya 48, 119017 Moscow, Russia
e-mail: ryabchik@inasan.ru

E. Niemczura et al. (eds.), *Determination of Atmospheric Parameters of B-, A-, F- and G-Type Stars*, GeoPlanet: Earth and Planetary Sciences,
DOI: 10.1007/978-3-319-06956-2_24,

of the model atmosphere calculations were presented in the lecture by R. L. Kurucz ("Model Atmosphere Codes: ATLAS12 and ATLAS9"). He also considered briefly his code for synthetic spectrum calculations SYNTHE. Below I give a short description of a few other codes for spectral analysis via synthetic calculations.

2 MOOG: An LTE Stellar Line Analysis Program

MOOG is a Fortran code designed by Sneden (1973) for LTE line analysis in plane-parallel 1-D stellar atmosphere. It calculates disk-integrated flux or specific intensity from the star's centre either integrated over the line profile (equivalent width) or in the format of synthetic spectrum. Typical usage is the determination of the chemical composition of a star. In many ways MOOG follows the formalism developed in WIDTH and SYNTHE codes by R. L. Kurucz. MOOG has two main options:

- *abfind*—fits previously measured observed equivalent widths to the calculated ones to derive atmospheric parameters and chemical abundances.
- *synth*—computes a set of synthetic spectra for different model parameters. The user may plot observed and synthetic spectra and derive the abundance either by visual inspection or by minimization of the O–C diagram.

For on-line graphics, MOOG uses the SuperMongo plotting package implemented in Fortran, although it can work without graphical output. MOOG supports different model atmosphere formats [(e.g. ATLAS9 (Kurucz 1993) and MARCS (Gustafsson et al. 2008)] with 'rhox' and 'tau' depth scales.

Three input files are used by MOOG: Parameter file, Model Atmosphere file and Line Data file. The data in the last file are entered in a formatted or unformatted manner. Line Data file is provided by the user and includes wavelength, element code, line excitation potential (eV), oscillator strength, gf or $\log(gf)$, van der Waals damping parameter, dissociation energy for a molecular feature. In Parameter file the user has to specify which molecules are included in calculations, for what elements abundances are changed relative to the 'standard', and indicate all input and output files. Be careful with the oscillator strengths. Better set them in non-logarithmic form because MOOG interprets automatically negative numbers as $\log(gf)$ and all positive ones as simple gf-value.

Two modes of spectrum synthesis are available:

- *synth*—varying atomic abundances.
- *isotop*—varying isotopic abundances.

A description of program and downloading instructions are given on the MOOG web page: http://www.as.utexas.edu/~chris/moog.html.

3 Spectrum Investigation Utility

Spectrum Investigation Utility SIU is a Fortran code built into IDL (Interactive Data Language) environment (Reetz 1991). Unlike MOOG and other codes that will be discussed later, it does not work without IDL. SIU calculates the emergent specific intensity or disk-integrated flux from plane-parallel 1-D stellar atmosphere both in LTE and NLTE approximations. The code includes continuous opacity due to bound-free transitions of H I, $H2^+$, H^-, He I, He II, metals up to Fe, Rayleigh and Thompson scattering.

SIU works with a grid of MAFAGS- OS atmospheric models (Grupp 2004) built into an IDL shell, as well as with individual models from other codes converted into special binary format which includes partial pressures for all elements in first three ionization stages.

All parameters (wavelength region, atmospheric parameters, spectral resolution, microturbulent, macroturbulent and rotational velocities) are specified inside the IDL environment. The total line list consists of 1900 blocks by 200 lines each and is kept separately as an external file in binary format. An adaptive wavelength grid is used.

The hydrogen lines calculations are performed with VCS Stark broadening tables (Vidal et al. 1973) limited to temperatures $T \leq 20{,}000$ K and to electron number densities $>10^{10}$ cm^{-3}. Hydrogen Stark profiles are convolved with radiative and Doppler broadening profiles and the resultant profile is further convolved with the resonance broadening profile (H+H interaction). Because of the temperature and density restrictions, SIU works successfully for spectrum calculations in the atmospheres of F, G and K stars of III–V luminosity classes.

Abundance determinations in SIU are made either by visual inspection of the quality of profile fits or by visual inspection of the O–C diagram produced by code on user's request.

4 Synth3

SYNTH3 (Kochukhov 2007) is designed to calculate spectra emerging from the static, 1-D model atmosphere, under the assumption of LTE. These approximations are adequate for a wide range of main-sequence stars. In practice, the code is successfully used to model stars of spectral classes from early-B to late-M.

In the standard mode, SYNTH3 computes intensity by solving numerically the scalar radiative transfer equation for a set of (typically) 7 limb angles. On the next step, an external IDL routine `s3div` is used to produce a disk-integrated flux spectrum from SYNTH3 intensity spectra for a specified radial-tangential macroturbulent velocity and projected rotational velocity. By default, this procedures assumes a spherically symmetric star.

SYNTH3 itself is independent of the latter assumptions of disk integration and can supply intensity spectra for a more sophisticated disk integration procedure (e.g.

modelling of spectroscopic binaries, rotationally distorted stars, stars covered by temperature/abundance spots, etc.)

SYNTH3 is able to compute spectra emergent from stellar atmospheres with depth-dependent abundances.

The format of the input file for SYNTH3 is that of the output returned by the VALD 'Extract Stellar' request. The input file also contains the name of the model atmosphere file loaded in special 'krz' format. This file is obtained by transformation of the standard ATLAS9 'mod' format with a program KURKOL provided together with SYNTH3 code.

The SYNTH3 program is written in Fortran 77, which ensures portability to all major computer platforms and straightforward interfacing with alternative software modules. The code does the following set of operations:

- Reading input model atmosphere ('krz' format) and atomic/molecular line list (VALD format). Depth-independent abundances and microturbulent velocity are read from the line list (default) or from the model atmosphere header. Depth-dependent chemical abundance can be specified in the input model atmosphere file.
- Computation of the concentration of different ions and molecules based on the advanced equation of state solver (Valenti et al. 1998) which includes the treatment of ≈200 diatomic and polyatomic molecules. Calculation of continuous opacities (as in ATLAS9, see Kurucz' Lecture in Chapter), line centre opacities, Voigt function parameters. Refinement of the depth grid (adaptive grid).
- Intensity at several limb angles is computed with the help of the quadratic DELO radiative transfer algorithm (Piskunov and Kochukhov 2002), using precomputed metallic line opacity and hydrogen line opacity evaluated according to Barklem et al. (2000). The refinement of the line profiles is carried out by adding frequency points, until description of the spectral line shapes is sufficiently precise (adaptive grid).

The codes (executables for Linux and Intel Mac computers) are available on http://www.astro.uu.se/~oleg/download.html.

The graphical comparison between the computed and observed spectra is performed with BINMAG3 code written by O. Kochukhov.

4.1 BinMag3

BINMAG3, available from http://www.astro.uu.se/~oleg/download.html, is an IDL code. It reads observations in `*.asc` and `*.fits` formats and synthetic spectra in `*.out` or `*.prf` (specific intensity/flux) formats. Besides simple comparison, BINMAG3 provides the following operations:

- Parameter Fit—calculates the radial velocity, rotational ($v \sin i$) and macroturbulent (ζ_{RT}) velocities.

- Equivalent Width—calculates the equivalent width of the line by direct integration and write it in the output line list for use in subsequent abundance calculations.
- Profile Fit—approximates the observed line profile by Gaussian or Doppler profiles and writes the calculated equivalent width in the output line list; for blend fits a superposition of synthetic profiles to observed (synthetic) spectrum.
- Show Line—shows atomic parameters of the chosen spectral line.
- Abundance Fit—automatically changes element(s) abundance(s) to provide the best fit to the observed line profiles; does the same via changing oscillator strength and writing the corrected value to the copy of input line list.

For Abundance Fit operation, BINMAG3 requires a Unix-like environment and SYNTH3 or SYNTHV_NLTE executables in the default search path. As a result the user automatically gets the abundance from the individual spectral line/blend of lines for pre-calculated model atmosphere. It is possible to extract the average abundance from several spectral lines. With pre-calculated *b*-factors the user automatically gets NLTE abundance.

Up to 6 observations and 6 synthetic spectra may be loaded simultaneously. BINMAG3 provides graphical (postscript) and text (ASCII) outputs.

5 synthV_NLTE

SYNTHV_NLTE was written by Tsymbal (1996). Similar to SYNTH3, SYNTHV_NLTE calculates spectrum emerging from the static, 1-D model atmosphere under both LTE and NLTE assumptions, and can be used for modelling stars of spectral classes from early B to late M. The format of the input line list is the same as in SYNTH3. SYNTHV_NLTE is also able to compute spectra for chemically stratified stellar atmospheres.

The main differences are:

- SYNTHV_NLTE is running with 'krz', 'mod', and MARCS model atmosphere formats.
- Constant wavelength step (0.01 Å by default) is used in spectrum calculations.
- Calculation of continuous opacities and radiative transfer algorithm is the same as in Kurucz' codes.
- Hydrogen lines and 20 He I lines are calculated with VCS (Vidal et al. 1971, 1973) Stark broadening treatment.
- Two types of output file are possible depending on the filename extension
  - if extension is '.out' then the code produces the output file similar to SYNTH3 (specific intensity for 7 limb angles)
  - if extension is '.prf' then the code produces normalized disk-integrated flux spectrum.

SYNTHV_NLTE requires an external file `SynthV.config`, where you put filenames with the pre-calculated *b*-factors (a result of DETAIL code). SYNTHV_NLTE

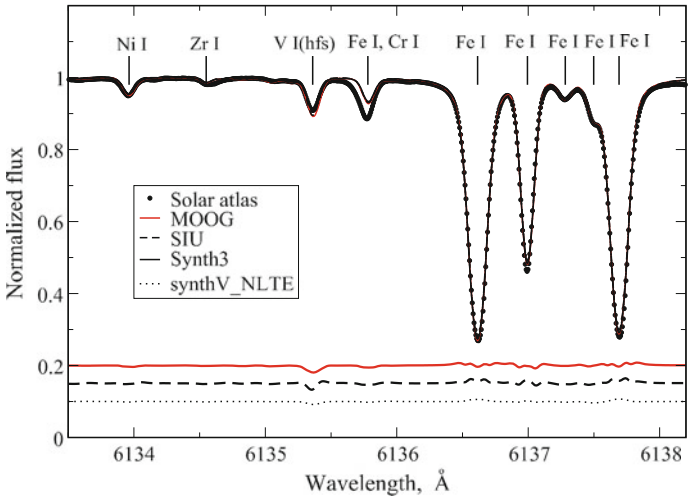

Fig. 1 Comparison of the synthetic spectrum calculations with different codes. The *lower part* of the plot shows deviations relative to calculations with SYNTH3. For comparison purposes they are shifted in *vertical direction*

compares species names and wavelengths in the input line list with the corresponding data in the DETAIL `*.pop` file and calculates NLTE synthetic profiles for the lines found in the `*.pop` file. For all other lines LTE calculations are carried out. If `*.pop` filenames are commented, SYNTHV_NLTE works in the LTE regime. The SYNTHV_NLTE codes and executable are available at http://vald.inasan.ru/~vadim/downloads/.

Both SYNTH3 and SYNTHV_NLTE operate in the following sequence:
ATLAS9/MARCS(model)⟶VALD3(line list)⟶
SYNTH3/SYNTHV_NLTE⟶synthetic spectrum.

The user should not prepare the input line list; it is received by the standard request 'Extract Stellar' from VALD database. The user may adjust this file either manually or automatically.

Figure 1 shows a comparison between synthetic spectrum calculations with four different codes. Calculations are performed for the solar spectrum and are made with the same line lists and model atmosphere. Any difference does not exceed 0.01 in the line centres. For equivalent widths the difference is less than 3 % for weak lines and less than 1.5 % for strong lines with developed wings. For iron lines the corresponding abundance difference does not exceed 0.02 dex in equivalent width range of 8–150 mÅ. These estimates are made with respect to SYNTH3 code. The difference in the output flux may partly be attributed to the slightly different partition functions in different codes.

6 Spectroscopy Made Easy

Spectroscopy Made Easy (SME) (Valenti and Piskunov 1996) is a tool for fitting the theoretical spectra to the observations. Fitting parameters include global stellar parameters ($T_{\rm eff}$, $\log g$, metallicity, $\xi_{\rm t}$, $\zeta_{\rm RT}$) plus line parameters, radial velocity, instrumental broadening and continuum level. It can also be used for simple synthetic spectrum calculations. SME consists of two parts: Graphical User Interface (GUI) `sme` and solver `sme_main`.

The GUI is used to read line data and observations, set model parameters, define fitting masks, create SME input and output files when the job is done. The input consists of line list, initial values of radial velocity, atmospheric parameters ($T_{\rm eff}$, $\log g$, metallicity), broadening parameters ($\xi_{\rm t}$, $\zeta_{\rm RT}$, $v \sin i$, and instrumental resolution) and a list of parameters to be fitted (if any). Observational data may include multiple (possibly overlapping) spectral regions. The user has a possibility to edit a mask for excluding regions from a fit or declaring regions as continuum. The input data is compiled and checked for completeness by the GUI and stored as an input structure for the solver.

The SME solver is an IDL implementation of the Marquardt-Levenberg non-linear optimization algorithm that uses an external library for solving the molecular and ionization equilibrium (`EOS`), computing continuous (`CONTOP`) and line opacities (`LINEOP`) and solving the radiative transfer (`RTINT`). The external library is written in C++ and Fortran.

The solver's IDL routines prepare spectral synthesis and perform optimization, while the external library is used for synthetic spectrum calculations.

Ionization equilibrium solver, `EOS`, has partition functions for up to 6 ionization stages of the first 99 atoms in the periodic table and for 257 molecules (up to four atoms) fitted over the range from 10 to 8,000 K. Molecular partition functions were initially adopted from Irwin (1988) and Sauval and Tatum (1984), but later many of them were re-computed by Barklem and Collet for the range of 1 K to 10,000 K (Piskunov et al. in preparation). Atomic partition functions come from Kurucz with few additions/corrections made by VALD team. The `EOS` is robust enough to handle a wide range of temperatures (300–300,000 K) and pressures (10^{-8}–10^{6}) for a reasonable set of chemical compositions.

Continuous opacities have been adopted from Kurucz' ATLAS12 (Kurucz 2005) modified to take absorbers density directly from the `EOS`. The following absorbers: H, H_2^+, H^-, He, He^+, He^-, Si, Si^+, Mg, Mg^+, Al, C, Fe, Ca^+, N, O, Ne, S, and scatterers: H, H_2, He, e^-, are included in continuous opacity calculations.

The radiative transfer solver is based on the Bézier attenuation algorithm (de la Cruz Rodríguez and Piskunov 2013) that can handle both plane-parallel and spherical environments. The Voigt function is used for the line shapes except for hydrogen. For hydrogen lines the recipe proposed by Barklem is used that combines Stehlé (1994) and Vidal et al. (1973) approximations for different lines, regimes and distances from the line centre. Similar to SYNTH3 the radiative transfer produces specific intensity

Table 1 Atmospheric parameters determination with SME and by non-spectroscopic methods

Star	SME			Literature		
	$T_{\rm eff}(K)$	$\log g$	[Fe/H]	$T_{\rm eff}(K)$	$\log g$	[Fe/H]
Procyon	6,671	3.94	+0.02	6,626	3.98	0.00
Sun	5,774	4.45	−0.01	5,777	4.44	0.00
δ Eri	5,051	3.77	+0.08	5,060	3.83	+0.08

spectra at different limb angles that are integrated over the stellar disk accounting for (rigid) rotation.

The SME output structure is the SME input structure, but with additional fields containing the solver output results. These include the values of free parameters for each iteration, the initial and final spectral synthesis and the characterization of the fit. SME can work with the observations in either ASCII or FITS formats. The format of input line list is the output format of VALD 'Extract Stellar' request. SME has model libraries of Kurucz' models (Kurucz 1993) and the latest version of MARCS models (Gustafsson et al. 2008).

A detailed description of SME is given in `SME_Manual` and `SME_Tutorial` included in SME package which can be downloaded from www.stsci.edu/~valenti/sme.htm.

The results of the comparison between atmospheric parameters derived with SME and by independent non-spectroscopic methods for Procyon, Sun, δ Eri are presented in Table 1. Effective temperatures and metallicities determined by infrared flux method (IRFM) are taken from Casagrande et al. (2010), while surface gravities determined by asteroseismology or binarity are taken from Bruntt et al. (2010). For the Sun we use the standard solar data. SME analysis was based on UVES spectrum for Procyon (Ryabchikova et al. 2008), on HARPS spectrum for δ Eri, on solar flux atlas (Kurucz et al. 1984) for Sun, and MARCS models grid (Gustafsson et al. 2008). We were fitting four spectral regions: 4,485–4,590, 5,100–5,200, 5,600–5,700 and 6,100–6,200 Å, using the same line mask for all stars.

Acknowledgments This work was partially supported by Praesidium RAS Program "Non-stationary Phenomena in Objects of the Universe" and by the Federal Agency for Science and Innovations (grant No.8529).

References

Barklem PS, Piskunov N, O'Mara BJ (2000) A&A 363:1091
Bruntt H, Bedding TR, Quirion P-O et al (2010) MNRAS 405:1907
Casagrande L, Ramirez I, Melendez J, Bessell M, Asplund M (2010) A&A 512:A54
de la Cruz Rodríguez J, Piskunov N (2013) ApJ 764:33
Grupp F (2004) A&A 420:289
Gustafsson B, Edvardsson B, Eriksson K, Jorgensen UG, Nordlund Å, Plez B (2008) A&A 486:951

Irwin AW (1988) A&AS 74:145
Kochukhov O (2007) Spectrum synthesis for magnetic chemically stratified stellar atmospheres. In: Kudryavtsev DO, Romanyuk II (eds) Physics of magnetic stars, p 109
Kurucz RL (1993) ATLAS9 stellar atmosphere programs and 2 km s^{-1} Grid CD-ROM 13
Kurucz RL (2005) Mem Soc Astron Ital Suppl 8:14
Kurucz RL, Furenlid I, Brault J, Testerman L (1984) National solar observatory Atlas no.1: solar flux Atlas from 296 to 1300 nm. National Solar Observatory, Sunspot
Piskunov N, Kochukhov O (2002) A&A 381:736
Piskunov N et al, in preparation.
Reetz JK (1991) Diploma thesis, Universität München
Ryabchikova T, Kochukhov O, Bagnulo S (2008) A&A 480:811
Sneden C (1973) ApJ 184:839
Tsymbal VV (1996) STARSP: a software system for the analysis of the spectra of normal stars. In: Adelman SJ, Kupka F, Weiss WW (eds) Astron Soc of the Pacific Conf Series 108:198
Stehlé C (1994) A&AS 104:509
Sauval AJ, Tatum JB (1984) ApJS 56:193
Valenti JA, Piskunov N (1996) A&AS 118:595
Valenti JA, Piskunov N, Johns-Krull CM (1998) ApJ 498:851
Vidal CR, Cooper J, Smith EW (1971) JQSRT 11:263
Vidal CR, Cooper J, Smith EW (1973) ApJS 25:37

A Gentle Introduction to SME

Nikolai Piskunov

Abstract This short overview of the Spectroscopy Made Easy (SME) package is meant as a summary of the capabilities, input data, steps and best practice in using SME for determination of fundamental parameters of stars. This overview is not an introduction to stellar spectroscopy and not even a reference to the SME. The tutorial by Ulrike Heiter distributed with the package comes much closer to a reference and the upcoming paper by Piskunov & Valenti (2014) will cover all the physics implemented in the library. Thus the main intention of this paper is to provide support to a starting SME user, outline the restrictions of the spectral synthesis approach and help bringing expectations in match with reality.

Keywords Stars: atmospheres · Stars: abundances · Techniques: spectroscopic · Line: profiles

1 Introduction

Determination of stellar parameters is a classical astrophysical problem. Stellar temperature, surface gravity and chemical composition are crucial ingredients in many theoretical models from formation and evolution of individual stars to galaxy evolution and cosmology. An additional interest in accurate stellar parameters was brought by the study of exoplanets. The main paradox of stellar spectroscopy is that with all the improvements of atmosphere models, atomic and molecular data and numerical methods in the last 25 years the accuracy of e.g., abundance determination did not improve much beyond 0.1 in log scale. Crossing this barrier requires perhaps a

N. Piskunov (✉)
Department of Physics and Astronomy, Uppsala University, Box 516, 75120 Uppsala, Sweden
e-mail: piskunov@fysast.uu.se

E. Niemczura et al. (eds.), *Determination of Atmospheric Parameters of B-, A-, F- and G-Type Stars*, GeoPlanet: Earth and Planetary Sciences,
DOI: 10.1007/978-3-319-06956-2_25,

Fig. 1 SME components and data flow. The *top part* represents the GUI and the input data. It produces the input structure for the solver that is using an external library for computationally-intensive steps. The resulting output structure can be read and analysed using the GUI

combination of different techniques but spectroscopy will keep its central role. SME was designed as a tool that allows performing analysis of stellar spectra using spectral fitting techniques in a consistent and reproducible way.

2 SME Structure

SME consists of two rather independent parts: one is a Graphical User Interface (GUI) and the other is the actual solver. The two parts communicate via data structures stored in files. The schematic view of SME is presented in Fig. 1. The GUI is a useful part for learning how to use SME as well as for initial exploration of new spectral regions and new domain of stellar parameters. It helps doing all data preparation steps interactively and inspecting the results of spectral fitting. For systematic processing of large amount of observations one may consider automating the preparation of input structures recycling some components that have been tuned interactively. Such automated procedures were implemented by several groups and in some cases the corresponding tools can be obtained by contacting them directly (see, for example, Shen et al. 2007; Lebzelter et al. 2012; Curtis et al. 2013).

The GUI is written in IDL and requires a valid IDL license. The solver is also written in IDL but it can also be run in IDL virtual machine without a separate license. The library components are written in C++ (continuous and line opacities, radiative transfer solver etc.) and in Fortran (equation of state). Library is available for various platforms (LINUX, Mac OS X, Windows XP/7).

The GUI consists of a main widget with a number of nested menus that often bring up more widgets. Normally when creating a new input structure from scratch one follows the menus from left to right and sub-menus from top to bottom. In the next section we will give a quick review of crucial menus. The creation of the new structure is completed by giving it a name and saving it to a file.

The solver parses the input structure to figure out if it should fit the observations or simply compute a synthetic spectrum. In the end of calculations the results are combined with the input data to form the output structure.

The job (object) name selected in GUI will be used for storing the input and the output structures and the log file if one follows the SME convention. This convention for file naming is:

input structure `<job_name>.inp`
output structure `<job_name>.out`
solver log `<job_name>.log`
solver batch `<job_name>.bat`

The solver itself does not read or write the input/output structures. Therefore, the work flow is given in a batch file. It includes three steps: restoring the input structure from the disk, running the solver and saving[1] the output structure. Users are invited to inspect a batch file and reproduce its steps manually for better understanding of solver operation.

While both the input and the output structures in IDL are associated with the same variable name `sme`, they are different and the solver will not run with the output structure as a parameter. The GUI can read and visualize both the input and the output structure but it can only produce/store the input structure. The solver of course produces an output structure.

3 GUI and the User-Supplied Data

The GUI is started by entering `sme` to the IDL prompt. The GUI menus (Fig. 2) are covered in detail in the SME Manual. The SME Manual and tutorial are distributed with SME. They can also be found on-line at http://www-int.stsci.edu/~valenti/sme.html. Here we simply note a few useful facts simplifying the use of GUI. The main widget contains a number of drop-down menus along the top and a message window below. Error, warning and information messages are sent to the message window. All of them are kept throughout the lifetime of the main widget and you can scroll this

[1] "Restoring" and "saving" refer to the IDL `restore` and `save` procedures.

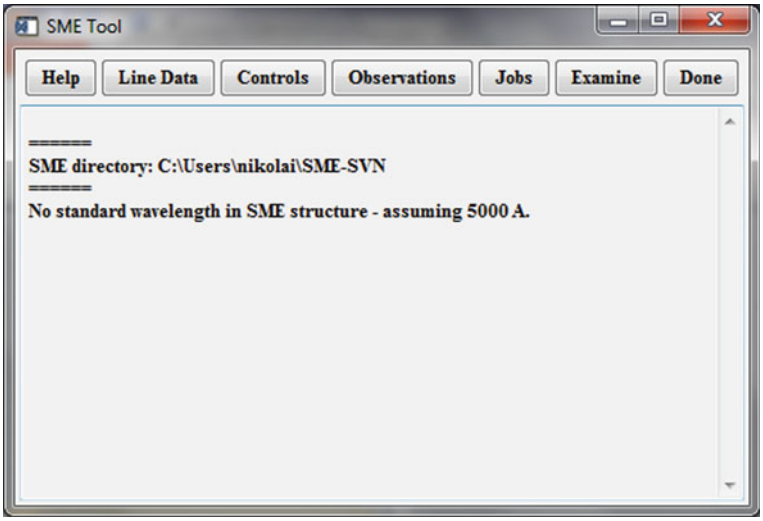

Fig. 2 The four buttons on the *top* of the GUI widget starting with `Line Data` are used for compiling the input structure. The SME results are imported and analysed using the `Examine` menu

window to view older messages. The GUI session keeps its status so exiting the main widget but staying in IDL allows you to restart the GUI and you will find yourself at the point where you left. You need to save your data though if you plan to leave IDL. This is done by entering the `Object` name in `Jobs` menu. By default it will be used to form the file name for storing the input structure. Before you actually save the input structure, its content is verified for completeness and consistency. If the check fails you will receive an error message and no output structure will be written to a file.

The main data component required for creating a new structure is the line list. The observations are mandatory if one would like to perform parameter fitting. Both of these data can be read from external files and existing SME structures. In this way you can, for example, re-use line data tuned on your reference observations, etc. Line data can also be read from one or several ASCII files in VALD (Piskunov and Ryabchikova 2014) format (both short and long) using `Line Data` menu. Multiple formats of observations are supported and distinguished by file extension. Read the SME Manual for further information. Model atmosphere required for spectral synthesis are usually interpolated from model grids included in the distribution. It is also possible to use your own model stored in an ASCII file. In addition, SME has a build-in atlas of the Sun (http://kurucz.harvard.edu/sun.html) that is particularly useful for verifying the line list. All these options are available from the `Observations` menu.

The initial stellar parameters are set in `Controls→Global Parameters` menu. In the same menu one selects the source of model atmosphere. Current

grids include ATLAS9,[2] MARCS (Gustafsson et al. 2008) and some others. The `Control` menu also contains a few other important options: `Free Parameters`, `Wavelength Set`, `Abundances`, `Line Parameters` and `Instrumental Profile`. For new users we recommend not to experiment with the last two entries that deal with disk integration and the precision of the radiative transfer solver. Instrumental broadening is often important, so try to have a measured value from data reduction.

4 Preparation for the Analysis

At this point one should apply the knowledge of spectroscopy and think carefully about the strategy and the tactics. Depending on the temperature range, luminosity class and metallicity, one may select different diagnostics for stellar parameters: ionization balance, hydrogen lines, molecular bands etc. It is a good idea to start by selecting spectral range(s). SME can fit multiple spectral intervals simultaneously. The next step should be the verification of the line list. Such verification can be done using a spectrum of a star or stars with well-known parameters. Spectral synthesis will reveal the best sub-intervals where the original line data produces a good fit. Intervals with poor fit can be de-selected by editing the mask. SME mask is associated with observations. It marks the continuum points and bad points that will not be used in the fitting. If not enough good points was found one my consider changing spectral intervals or/and tuning line parameters using reference spectra.

The next step is to start working with observations of the target objects. The first thing is to compute the spectral synthesis possibly allowing the SME to fit the radial velocity and verifying the normalization of the observations. Only then one can proceed with fitting of stellar parameters.

5 Free Parameters

SME allows fitting an effective temperature $T_{\rm eff}$, surface gravity $\log g$, metallicity [m/H], radial velocity $V_{\rm rad}$, rotational velocity $v \sin i$, macroturbulent and microturbulent velocities $\zeta_{\rm RT}$ and $\xi_{\rm t}$ (hereafter denoted as $V_{\rm macro}$ and $V_{\rm micro}$), abundance of individual elements, continuum level, the width of the instrumental profile and line parameters: oscillator strength $\log gf$ and van der Waals broadening constant Γ_6. Obviously, some of these parameters are degenerate and some need specific features in stellar spectra. For example, one should be careful when fitting metallicity and line parameters simultaneously.

[2] http://kurucz.harvard.edu/grids.html

6 Fitting Strategies

Once the line list is verified and the spectral intervals are defined, one can start the fitting procedure. It is a good practice to start with a subset of global parameters that affect all parts of the spectrum: $T_{\rm eff}$, $\log g$, metallicity and $v \sin i$. After making the first run one should revisit the mask to see if it needs adjustments. Note that SME comes with a tool for replicating the mask from one SME structure to another provided that both have radial velocities defined. This helps analysing spectra of similar objects taken with the same instrument with the same spectral resolution.

SME has multiple ways of treating the continuum. The main options are scalar and linear correction for each spectral intervals. Higher order corrections should be done outside SME.

The `Examine` menu helps reading and analysing the results.

7 Parameter Uncertainties

SME stores the formal fitting uncertainties (covariances) in the output structure. These are of course purely numerical and give only low limits for the real values. The following methods seem to be the best for deriving the true uncertainties.

For the global parameters ($T_{\rm eff}$, $\log g$, metallicity) one can take a simplified Monte Carlo approach stepping away from the solution, re-running the fit and comparing the results. Useful offset values are of the order of 2–5 % and one should step in both directions. You may experiment with perturbing one or several parameters at the time to find an optimal compromise between correct error estimates and speed. For abundance of individual elements, the strategy is different. In case you have many spectral lines of the same element you can fix all parameters and let SME adjust the oscillator strengths of these lines. The corrections to the oscillator strength will give you spread in abundance as if it will be determined from each line separately.

8 Exporting SME Results

All SME fitting results are contained in an output structure and the SME Manual covers all the fields in detail. The `Examine` menu allows exporting the line list in the VALD format (in case the line list was merged and/or tuned) and a separate tool can export the final model atmosphere in a "krz" format ("krz" format description can be found at http://marcs.astro.uu.se/krz_format.html).

The export of the final spectral synthesis is trivially done by restoring the output structure and writing the corresponding fields to external file(s).

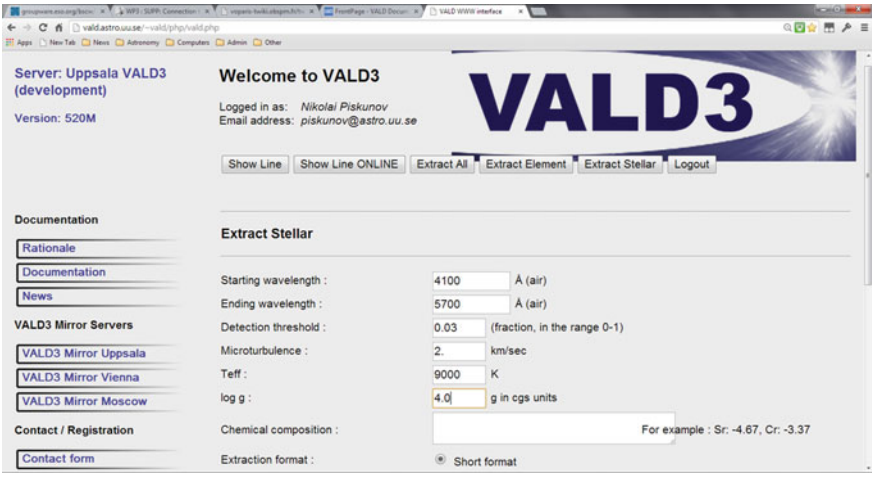

Fig. 3 VALD request to extract relevant lines for our target

9 Example

As an example we used a spectrum of an A-type dwarf KIC 12153021 = HD 179617. The data was available for two spectral regions: 4,200–4,510 and 4,700–5,100 Å. We start by submitting request to VALD3 (Piskunov and Ryabchikova 2014) using its web interface (Fig. 3) and specifying the spectral range, approximate temperature, surface gravity and microturbulence. The selection threshold is set to 3 % of continuum and we use the default (solar) abundances. We do this separately for the two spectral regions and receive two line lists that we import to SME. We select the initial parameters for our target to be $T_{\rm eff} = 9{,}000\,{\rm K}$, $\log g = 4$, $V_{\rm micro} = 1\,{\rm km\,s^{-1}}$, $v \sin i = 0\,{\rm km\,s^{-1}}$, and solar metallicity in the corresponding sub-menu of `Control` menu (see left panel in Fig. 4). In a first run free parameters consist of radial and rotational velocity. We assume the observations to be continuum normalized. We choose the spectra intervals from the line lists and import the observations.

Spectral resolution is known to be 85,000 (HERMES@Mercator spectrograph) and we use this value for the Gaussian instrumental profile. The initial spectral synthesis with radial and rotational velocity adjustment is shown in the top part of Fig. 5. The resulting radial velocity is $0.9\,{\rm km\,s^{-1}}$, and projected rotational velocity of $19.6\,{\rm km\,s^{-1}}$. We use this spectral synthesis to inspect the mask. Mask can be edited to exclude bad pixels and indicate the location of continuum. In this case no obvious bad pixels were found and we just marked a few points as continuum (lighter background colour) even though it makes no difference since the observations are declared to be continuum normalized.

At this point we are ready to perform the tuning of the stellar global parameters. The free parameters consist of $T_{\rm eff}$, $\log g$, and metallicity. We let SME to fit the temperature, the surface gravity and the metallicity of KIC 12153021. The procedure

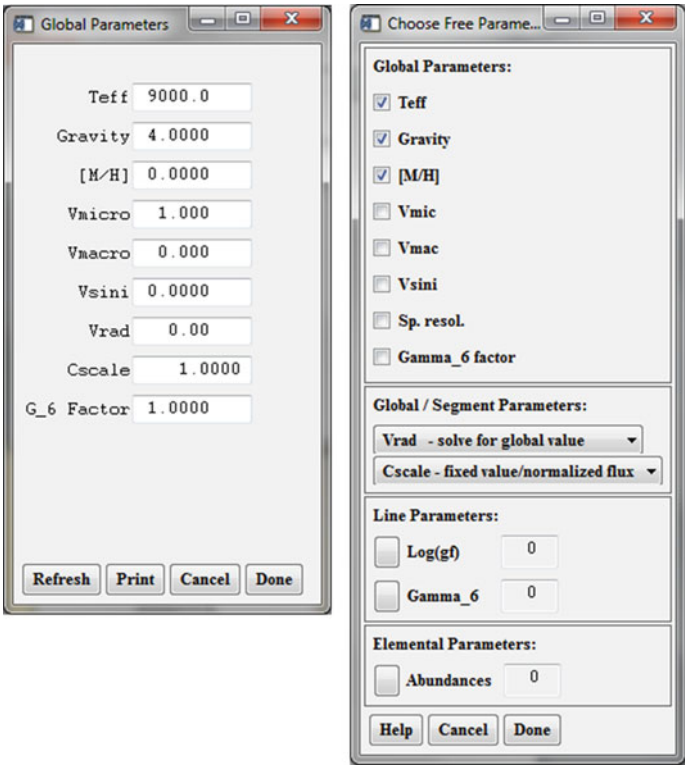

Fig. 4 Initial stellar parameters and free parameters

took a bit longer (3 iterations) but the fit is improved significantly reducing χ^2 from 11.7 to 0.98. The SME fitting produced the following results: $T_{\rm eff} = 9{,}411$ K, $\log g = 3.86$ and [m/H] $= 0.08$. The corresponding synthesis is shown in the bottom part of Fig. 5. Tkachenko et al. (2013) derived $T_{\rm eff} = 9,010 \pm 80$ K, $\log g = 3.50 \pm 0.10$, [m/H] $= -0.05 \pm 0.15$ and $v \sin i = 18.0 \pm 2.7$ km s^{-1} for KIC 12153021, based on automatic spectral fitting of lower resolution spectrum ($R = 32{,}000$). The authors used 4,700–5,700 Å spectral region for fitting. We repeated the SME procedure for spectrum of KIC 12153021 kindly sent to us by A. Tkachenko and for our spectrum using the same spectral region 4,700–5,700 Å. The results are:

- $T_{\rm eff} = 9{,}260$ K, $\log g = 3.78$, [m/H] $= +0.04$ and $v \sin i = 18.2$ km s^{-1}—Tkachenko's spectrum
- $T_{\rm eff} = 9{,}230$ K, $\log g = 3.74$, [m/H] $= +0.13$ and $v \sin i = 19.5$ km s^{-1}—our spectrum.

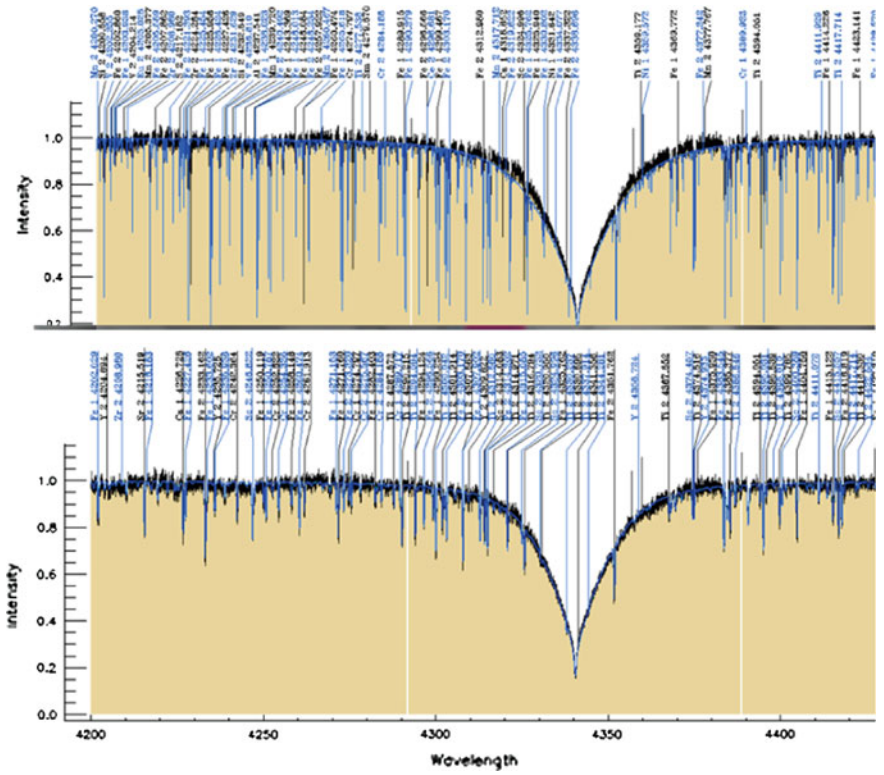

Fig. 5 Initial (*top*) and final (*bottom*) spectral synthesis is shown in *blue*. Observations are in *black*. Only about 4 % of all lines are marked

This comparison shows that the derived parameters depend on the spectral regions used, and the real errors in parameters determination are: ± 150 K in temperature, ± 0.2 in gravity, and ± 0.15 in metallicity.

References

Curtis JL, Wolfgang A, Wright JT, Brewer JM, Johnson JA (2013) AJ 145:26
Gustafsson B, Edvardsson B, Eriksson K, Jørgensen UG, Nordlund Å, Plez B (2008) AA 486:951
Kupka F, Piskunov N, Ryabchikova TA, Stempels HC, Weiss WW (1999) AAS 138:119
Lebzelter T, Heiter U et al (2012) AA 547:108
Piskunov N, Ryabchikova TA et al (2014) AA (in preparation)
Piskunov N, Valenti JA (2014) ApJ (in preparation)
Shen Z-X, Liu X-W, Zhang H-W, Jones B, Lin DNC (2007) ApJ 660:712
Tkachenko A, Lehmann H, Smalley B, Uytterhoeven K (2013) MNRAS 431:3685
Valenti JA, Piskunov N (1996) AAS 118:595

ARES + MOOG: A Practical Overview of an Equivalent Width (EW) Method to Derive Stellar Parameters

Sérgio G. Sousa

Abstract This chapter describes the important practical aspects in the use of an equivalent width (EW) method for the determination of spectroscopic stellar parameters. A general description of the fundamental steps required by any EW method is given, together with possible differences that may be found in different methods used in the literature. Then ARES + MOOG is used as an example where each step of the method is described in detail. A special focus is given for the specific steps of this method, namely the use of a differential analysis to define the atomic data for the adopted line list, the automatic EW determinations, and the way to find the best parameters at the end of the procedure. Finally, a practical tutorial is given, where we focus on simple exercises useful to illustrate and explain the dependence of the abundances with the assumed stellar parameters. The interdependences are described and a clear procedure is given to find the "final" stellar parameters.

Keywords Stars: fundamental parameters · Stars: abundances · Techniques: spectroscopy · Methods: data analysis

1 Introduction

For the determination of spectroscopic stellar parameters people choose between two possible methods. One is normally referred to as the "spectral synthesis method", the other as the "equivalent width (EW) method". The spectral synthesis method typically starts with the synthesis of theoretical spectra which are then compared

S. G. Sousa (✉)
Centro de Astrofísica, Universidade do Porto, Rua das Estrelas, 4150-762 Porto, Portugal
e-mail: sousasag@astro.up.pt

S. G. Sousa
Departamento de Física e Astronomia, Faculdade de Ciências, Universidade do Porto, Rua do Campo Alegre, 4169-007 Porto, Portugal

E. Niemczura et al. (eds.), *Determination of Atmospheric Parameters of B-, A-, F- and G-Type Stars*, GeoPlanet: Earth and Planetary Sciences,
DOI: 10.1007/978-3-319-06956-2_26,

to the observed spectrum. In this case the "final" parameters are found when the corresponding synthetic spectrum fits the observational spectrum. Alternatively, the EW method starts directly with the observed spectrum, measuring the strength of selected and well-defined absorption lines which are translated into individual line abundances, assuming a given atmospheric model. Then, a comparison between the computed abundances and the respective theoretical predictions is performed in order to find the "final" parameters.

It is clear that both approaches have their own advantages and disadvantages. On the one hand, the EW method can be faster than the synthetic method since it is focused on only a specific number of lines, while the synthetic method needs a more complete description of the spectrum. On the other hand, if the individual lines used by the EW method cannot be properly isolated then this may lead to inaccurate results.

In this chapter we give a description of the "ARES + MOOG method" which is based on EWs. ARES is the code for automatic EW measurements of the observed spectrum (see Sousa et al. 2007), and MOOG is used to perform the individual abundance calculations (see Sneden 1973). The method ARES + MOOG, like other EW methods, allows us to derive the stellar atmospheric parameters: effective temperature ($T_{\rm eff}$), surface gravity ($\log g$), microturbulence ($\xi_{\rm t}$), and the iron abundance ([Fe/H]). The method makes use of the excitation and ionization balance from the iron lines where the [Fe/H] is used as a proxy for metallicity. This method has been successfully applied to several large samples of F, G, and K (FGK) solar type stars (see Sousa et al. 2008, 2011).

2 EW Method: A General Overview

Figure 1 gives the workflow describing, as an example of the EW method, the ARES + MOOG procedure to derive the stellar atmospheric parameters. From this diagram we can easily identify the general steps for an EW method based on the excitation and ionization balance of iron lines:

1. A list of iron absorption lines with the corresponding atomic data is selected for the analysis;
2. The observational spectrum is analysed and the EWs are measured independently in a line-by-line analysis;
3. A stellar atmospheric model is adopted given the atmospheric parameters;
4. The measured EWs and the atmospheric model are used to compute the individual line abundances;
5. The "final" spectroscopic parameters are found once the excitation and ionization balance is achieved for all the individual lines analysed, otherwise we go back to step 3 and adopt different parameters.

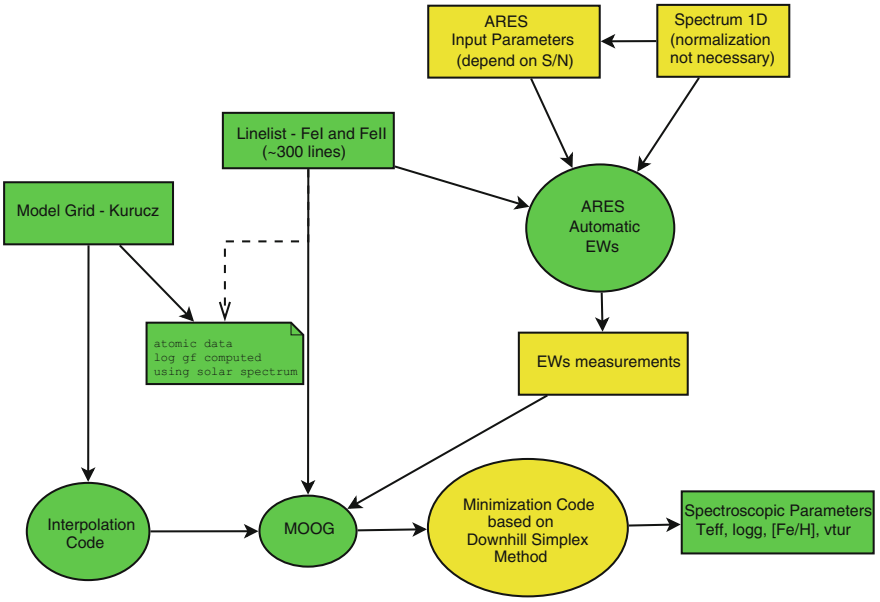

Fig. 1 The workflow diagram of the ARES + MOOG method

These are the basic steps required for the use of an EW method. The differences between the EW methods found in the literature are typically centred on the use of different line lists, models and codes used in each step.

2.1 Line List

The selection of the lines to be used in the analysis (first step) is crucial for the accuracy and precision of this method. Some authors use a large set of lines with the aim to increase the statistical significance of the derived spectroscopic stellar parameters. Others authors use a reduced and very well-defined set of absorption lines which are considered to be well known, or at least very well adapted for a specific type of stars (e.g. giant stars).

Together with the line selection, the adopted atomic parameters for each line are also of paramount importance. Although we can find very accurate wavelengths and excitation potentials for each line, the oscillator strengths ($\log gf$) are not so precisely known. The uncertainties of these values, which can be measured in laboratory, can propagate and affect dramatically the precision and accuracy of the derived spectroscopic parameters.

2.2 Measurement of EWs

Although the definition of an EW is quite simple, its measurement from observed spectra can still be tricky (second step). The determination of the correct position of the continuum level continues to be an important source for the uncertainties in these measurements. Another important aspect is to understand if a given line that needs to be measured is completely isolated (the ideal case) or if there are close-by lines that are blended together. In the latter case the correct identification of all lines is fundamental for a good measurement.

Moreover, for the EW measurements is important to define the profile function used for the line fit and corresponding strength calculation of each lines. The Gaussian profile is widely used and is considered to be an almost perfect approximation for weak absorption lines. However, some caution should be taken when measuring strong lines (typically EW > 150 mÅ). In this case, since the Gaussian profile cannot perfectly fit the wings of the line, several authors prefer to use the Lorentzian profile.

Until recently, these measurements were only feasible using interactive routines such as the "splot" task in IRAF.[1] In this case, people have to go through the spectrum line by line, marking the continuum position by eye and make the EW measurement. This is, of course, a quite boring and very time consuming task. Even worse, the subjectivity involved in such interactive routines may lead to inconsistency between the measurements of different lines. To overcome these issues, automatic codes are now on the market (e.g. ARES, Sousa et al. 2007; DAOSPEC, Stetson and Pancino 2008) that measure the EWs in a more efficient and consistent way.

2.3 Model Atmospheres

The literature offers the possibility to choose from a wide variety of model atmospheres (third step) and often this choice can be affected by subjectivity. Models like ATLAS9 (Kurucz 1993) and MARCS (Gustafsson et al. 2008) standout as the most used set of atmospheric models for the derivation of spectroscopic and elemental abundances.

The way the models are created and used in each method can also differ. Some authors prefer to create the models on the spot making use of available codes. As an alternative, and in order to increase the efficiency of each method, grids are created with pre-computed model atmospheres, which can be directly selected for each step of the iteration, or instead, the grid of models can be used for interpolations allowing this way a better refinement in the search of the "final" stellar parameters.

[1] IRAF is distributed by National Optical Astronomy Observatories, operated by the Association of Universities for Research in Astronomy, Inc., under contract with the National Science Foundation, USA.

As one could expect, for the creation of the models there are a series of important physical parameters and approximations that need to be defined and used for the correspondent computation. For instance, for FGK solar-type stars the plane-parallel approximation has proved to be a safe approach, but specific models may be necessary when dealing with "special" types of stars (e.g., metal-poor stars, giant and evolved stars).

2.4 Computing Abundances

In step number four we have the computation of the iron abundance (or any other chemical element). This step clearly depends on the measured strength of the line as well as the selection of the atmospheric model.

As for such models, local thermodynamical equilibrium (LTE) is commonly assumed as a valid approximation for FGK solar-type stars. However, this approximation may not be completely valid for other types of stars (e.g., for very metal-poor stars) non-LTE corrections may be necessary to apply (Bergemann et al. 2012).

2.5 Finding the Correct Parameters

In step five we need to achieve the excitation and ionization equilibria. The correlation between the excitation potential and the iron abundance of each line constrains the effective temperature, the correlation between the reduced equivalent width and the individual abundance constrains the microturbulence, and the ionization balance between the mean abundance of Fe I and Fe II fixes the surface gravity. The "final" stellar parameters will be obtained when no correlations are present, i.e. when all lines give the same individual abundances we stop the process and keep the parameters from the adopted model atmosphere. The iron abundance comes as an additional result from this analysis and is taken as the mean abundance from all lines.

The main difference between the various EW methods in this step may be related with the way in which the parameters are found and constrained. There are different minimization algorithms that may be used to explore the parameter space and the respective inter-dependences. Finally the constraints used to stop the method and check for the correct convergence of the parameters (i.e. what is the definition of no correlation from the data, e.g. does a slope with a value of 0.01 represent no correlation?) are crucial for the final decision of each method that may change the resulting parameters.

3 ARES + MOOG: The Method

So far we have described a general overview of an EW method. Here we will go through the steps once again and describe the specific choices made in ARES + MOOG (whose workflow is described in Fig. 1).

3.1 Line List

Since this method was designed to be completely automatic, for the compilation of the line list we have selected as many lines as possible. This increases the statistical significance of the derived parameters. However, each line was carefully selected in order to be considered stable for this method (for further details on the stability of the lines see Sousa et al. 2008).

Regarding the atomic data, in order to overcome the uncertainties in $\log gf$ described before, we made use of a differential analysis technique. This technique consists in selecting a benchmark star (typically the Sun) with very well constrained parameters. The goal of this analysis is to recompute the $\log gf$ using an inverse analysis. We first measured EWs for our selected lines in the solar spectrum. Then, assuming the solar parameters (e.g. $T_{\rm eff} = 5{,}777\,{\rm K}$, $\log g = 4.44\,{\rm dex}$, $\xi_{\rm t} = 1.00\,{\rm km\,s^{-1}}$, and $\log \varepsilon({\rm Fe}) = 7.47$), the values for each $\log gf$ were changed until we derive the "correct" individual abundance for each line.

Using this differential analysis it is possible to reduce both the errors on the atomic parameters and the errors on measurements of the equivalent widths. When measuring the lines in a benchmark star we are also including errors given by its spectrum itself. For instance, the existence of small undetected blended lines or the intrinsic bad position of the continuum for each line will introduce errors when computing the $\log gf$. The differential analysis will allow us to partially compensate for such kind of errors by assuming a systematic measurement of the EW for the same lines of the stars analysed. An obvious drawback from this analysis is that the results strongly deteriorate as we use the same $\log gf$ in stars that become more and more different from the benchmark star.

3.2 Measuring EWs

The equivalent widths of the lines were automatically determined using ARES[2] code (Sousa et al. 2007) following the approach of Sousa et al. (2008) and Sousa et al. (2011) to adjust the $rejt$ parameter of ARES according to the S/N of each spectrum. In the next section the input parameters for ARES will be described in detail and some advices will be given in order to select the best input parameters.

[2] The ARES code can be downloaded at http://www.astro.up.pt/~sousasag/ares/.

3.3 Model Atmospheres

We used the 2013 version of the code MOOG[3] (Sneden 1973) to compute the line-by-line abundance for each star assuming LTE conditions. In our standard method we used a grid of Kurucz ATLAS9 plane-parallel model atmospheres (Kurucz 1993) in order to generate the appropriate model atmosphere through interpolation. This model is then fed as an input into MOOG to compute the abundances through the driver *abfind*.

3.4 Finding the Final Parameters and the Iron Abundance

We use the Downhill Simplex Method (Press et al. 1992) as the minimization algorithm to determinate the best stellar parameters. Moreover, in order to identify outliers caused by incorrect EW values, we performed a 3-σ clipping for the Fe I and Fe II lines after a first preliminary determination of the stellar parameters. After this, the procedure was executed once again without the rejected lines. For a wider discussion about the full automatization of this method see Santos (2004), Sousa et al. (2011) and Saffe (2011).

4 ARES + MOOG: Quick Tutorial

The tutorial presented here follows the procedures and codes that were made available at the "Spring School of Spectroscopic Data Analyses". The codes are available either at the respective web-pages or are accessible from the School web-page: http://spectra.astro.uni.wroc.pl/.

As described before, the first step for the ARES + MOOG method is the definition of the line list. We will use the very well defined line list composed of nearly 300 iron lines presented in Sousa et al. (2008). If the reader is interested in a recent update of the line list see Tsantaki et al. (2013).

4.1 Using ARES

A complete description of ARES can be found in Sousa et al. (2007). In this document we will only point out the essential steps required to properly run the code.

[3] http://www.as.utexas.edu/~chris/moog.html.

A sketch of the ARES procedure is presented in Fig. 1 of Sousa et al. (2007). The basic steps of ARES are: (1) the reading of both the spectrum and the line list; (2) the local normalization of the spectrum which is performed for each line in each iteration; (3) the detection of the set of lines that are needed to be fitted (in case of blended lines); (4) the fit and the measurement of the EWs; (5) the storage of the EWs in an output file.

4.1.1 Preparing the Spectrum

The first step to properly use ARES is the preparation of the observed spectra. The available version of ARES only works with one-dimensional FITS spectrum. In the respective FITS header of the spectrum, the CDELT1 and CRVAL1 keywords need to be defined as a requirement.

Another fundamental condition is that the spectrum should be corrected in radial velocity so that the absorption lines are found at the rest frame, otherwise ARES will not be able to find the correct line position for the analysis.

4.1.2 Line List

The only requirement for the line list to be fed in ARES is the correct wavelength. The file with the list of lines should consist of a column with the wavelength. ARES will read this file line-by-line for the respective EW measurement. It may be also useful to keep in this file the atomic data for each line that will be required later on. Table 1 presents a sample of line list from Sousa et al. (2008), where for each line is defined the rest wavelength (λ), the excitation potential (χ_l), the oscillator strength ($\log gf$), the element identification (Ele. and Num.) and the EW measured in a solar spectrum ($EW_{\odot}$).

4.1.3 ARES Input Parameters

The input parameters for ARES are the following:

- *specfits*: The name of the 1D fits file with the spectrum corrected for radial velocity (e.g. HD1234_rv.fits).
- *readlinedat*: The name of the file with the list of lines to be measured (e.g. line list.dat).
- *fileout*: The name of the file that will contain the output of the results (e.g. HD1234.ares).
- *lambdai*: Initial wavelength to search the lines (e.g. 3,000 Å).
- *lambdaf*: Final wavelength to search the lines (e.g. 7,000 Å).
- *smoothder*: Smooth value for the derivatives that are used for the line detection procedure (e.g. 4—recommended value for high resolution spectra and good S/N).

Table 1 Sample of the line-list presented in Sousa et al. (2008)

λ (Å)	χ_l	log gf	Ele.	Num.	$EW_\odot$
6079.01	4.65	−1.008	Fe I	26.0	45.8
6082.72	2.22	−3.566	Fe I	26.0	34.5
6084.11	3.20	−3.774	Fe II	26.1	20.9
6089.57	4.58	−1.273	Fe I	26.0	35.3
...	...	...	...	...	...

- *space*: Size of the local spectrum interval in Angstroms around each line. Only this interval is used for the individual computations of each line (e.g. 3 Å—recommended value).
- *rejt*: Parameter for the calibration of the continuum position. This value strongly depends on the S/N of the spectrum. A good reference for the values to be used here can be found in Sousa et al. (2008, 2011) (e.g. 0.996 for spectra with S/N ∼ 400).
- *lineresol*: This parameter sets the line resolution of the input spectra. This parameter is helpful for distinguishing real lines from noise (e.g. 0.1 Å—recommended value for high resolution spectra).
- *miniline*: Lines with strength weaker than this value are not printed in the output file (e.g. 2 mÅ).
- *plots_flag*: Flag for the plots (0—runs in batch, 1—shows the plots and stops for each line calculation).

There are specific input parameters that are very important to obtain correct EWs. A proper selection of the *rejt* parameter is fundamental in order to track the correct continuum position. Wrong values of this parameter may systematically give larger (or smaller) EWs. Although there is a clear dependence between this parameter and S/N we choose to leave this as a free parameter given the high degree of subjectivity when defining the continuum position. If some authors want to define their own S/N dependence, we advise the reader to select only a few isolated lines for a few spectra with different S/N and to make use of the plots to select the best values for each S/N. For more details on such exercise see Mortier et al. (2013). For the other parameters, the recommended values should be kept fixed. We may only consider to tweak the *smoothder* parameter at higher values in case of very low S/N spectra. This may help for the correct identification of real lines in noisy spectra.

4.2 Generating a Model Atmosphere

The computations of specific model atmospheres in ARES + MOOG is done by an interpolation code which in turn uses a grid of pre-computed ATLAS9 models. The interpolation of models was chosen here for efficiency purposes and consists of

two separate Fortran codes: the first code performs the interpolation itself, while the second one accommodates the model in a file with a specific format readable by MOOG. A script named `make_model.bash`[4] is provided in order to run both codes directly. The script needs as input the astrophysical parameters ($T_{\rm eff}$, $\log g$, $\xi_{\rm t}$, and [Fe/H]) to generate the model which will be stored in a file named `out.atm`.

4.3 *Using* MOOG

MOOG is a code that performs a variety of LTE line analysis and spectrum synthesis tasks. The typical use of MOOG is to assist in the determination of the chemical composition of a star. In our case we want to measure individual iron line abundances to derive the stellar parameters.

There are several drivers available to run MOOG for several different purposes. The MOOG user's manual has a complete description of the several drivers. For ARES + MOOG we make use of the *abfind* driver.

One of the chief assets of MOOG is its ability to do on-line graphics. However in ARES + MOOG the graphics are not used at all. The visualization of different plots is quite useful to see the dependences of the different parameters with the individual abundance determination. Together with a modified MOOG version (where the internal plots were ignored since it requires a proprietary library), there was provided a simple Python code to perform the plots (named `read_moog_plot.py`)[4]. This code is used to illustrate the parameter dependences and respective correlations (see the next sections).

Another important input for MOOG is the list of atomic data for each line in order to perform individual abundance calculations. For this purpose, an additional script was provided (`make_linelist_local.bash`)[4]; this script reads the output of ARES and the initial line list to create the required format file for MOOG.

4.4 *Search for the Correct Model*

For this tutorial we will make use of the solar type star HD 1461 for which an HARPS@La Silla spectrum with high resolution and high S/N was analysed by Sousa et al. (2008). The final parameters derived for this star and obtained by the authors with ARES + MOOG are: $T_{\rm eff} = 5765 \pm 18$ K, $\log g = 4.38 \pm 0.03$ dex, $\xi_{\rm t} = 0.97 \pm 0.02\,{\rm km\,s^{-1}}$ and [Fe/H] = 0.19 ± 0.01 dex.[5]

[4] This script can be found together with other codes used in the school in: http://spectra.astro.uni.wroc.pl/code.php.

[5] For a proper description on the estimation of the errors with the ARES + MOOG method, see Sousa et al. (2011).

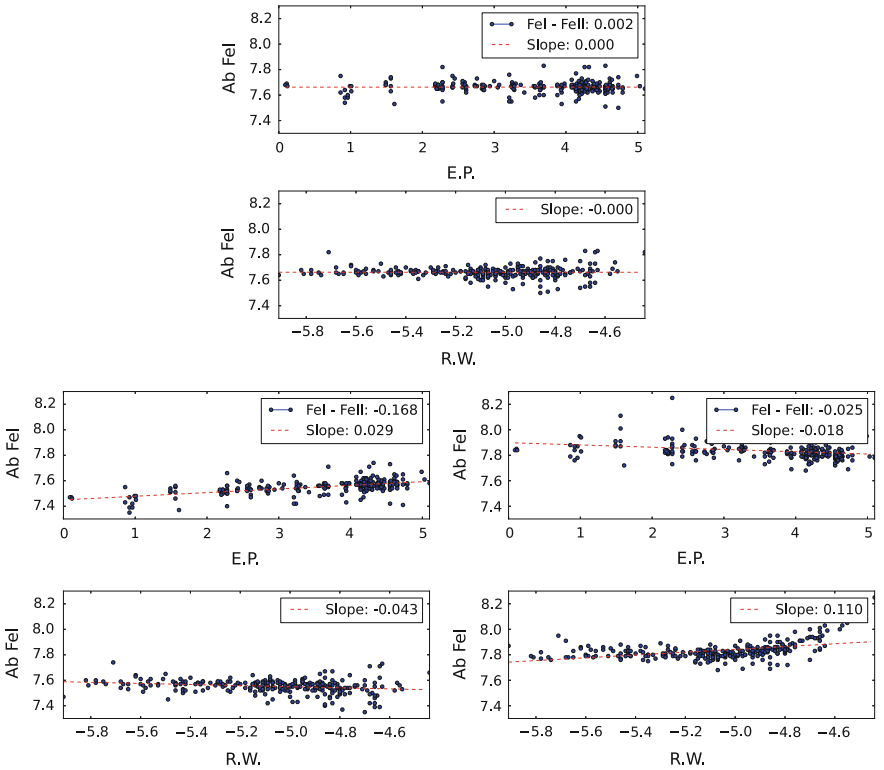

Fig. 2 Abundance of Fe I as a function of excitation potential (E.P.) and reduced wavelength (R.W.). The *top panel* shows the result for the "final" stellar parameters, while in the *bottom panels* temperature was changed to a lower value (5,600 K; *left panel*), and to an upper value (5,900 K; *right panel*)

Figure 2 shows correlations between the iron abundance (Ab(Fe I)) and the excitation potential (E.P.) and the reduced equivalent width (R.W.) for all used iron lines of HD 1461. In the same figure, there is also indicated, together with the respective slopes of the correlations, the difference between the average abundances of Fe I and Fe II ($\langle$Ab(Fe I)$\rangle$ − $\langle$Ab(Fe II)$\rangle$). From the values indicated in the figure we can see that the slopes of the correlations obtained with the "final" stellar parameters are close to zero, as well as the difference between Fe I and Fe II.

From theoretical studies, it is possible to demonstrate that $T_{\rm eff}$ has a strong influence in the correlation Ab(Fe I) versus E.P., microturbulence in the correlation Ab(Fe I) versus R.W., and surface gravity is connected directly with $\langle$Ab(Fe I)$\rangle$ − $\langle$Ab(Fe II)$\rangle$ (see, e.g. Gray 2005). Therefore, here and in what follows, we will make a series of exercises with the aim to show the dependence of each correlation with the spectroscopic parameters, and to illustrate how the "final" stellar parameters were derived for HD 1461. In particular, we will show these dependences in a practical way making use of the codes provided for the ARES + MOOG method.

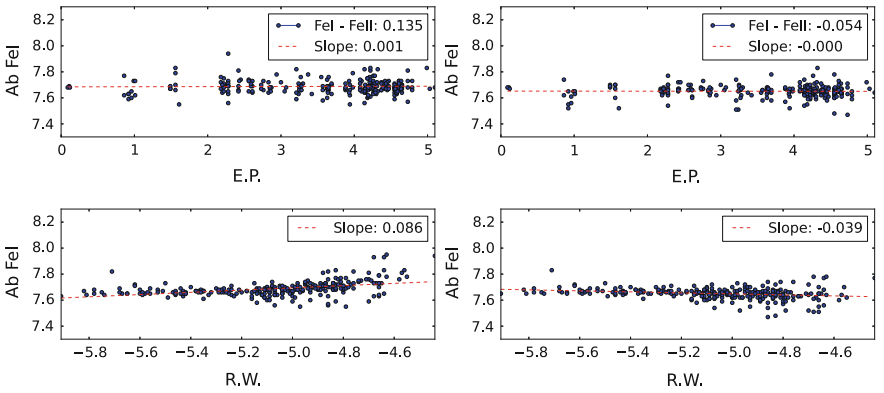

Fig. 3 Same as Fig. 2 but instead of changing temperature, here we changed surface gravity to a lower value (4.10 dex; *left panel*), and an upper value (4.50 dex; *right panel*).

4.4.1 Effective Temperature Dependence

The lower panels of Fig. 2 show the computed abundances for a model with exactly the same parameters as the final ones with exception of the temperature. It is clear that the slopes of the correlations change dramatically. Not only the Ab(Fe I) versus E.P. changes but also the same happens for Ab(Fe I) versus R.W. showing that the stellar parameters are strongly inter-dependent.

Hence, these plots show how Ab(Fe I) versus E.P. varies with the changes in temperature so we can react accordingly to find the correct temperature. In particular, when we underestimate the temperature the slope is positive, while when we overestimate the real temperature, the slope becomes negative. Therefore, the slope gives us information about the direction where the correct temperature is.

4.4.2 Surface Gravity Dependence

A similar exercise can be done for surface gravity. Here temperature was set back to its "final" value and only the gravity was changed to observe how $\langle$Ab(Fe I)$\rangle - \langle$Ab(Fe II)$\rangle$ varies accordingly. Figure 3 shows the results. In particular, when we underestimate surface gravity $\langle$Ab(Fe I)$\rangle - \langle$Ab(Fe II)$\rangle$ is positive, while when we underestimate surface gravity $\langle$Ab(Fe I)$\rangle - \langle$Ab(Fe II)$\rangle$ is negative.

One interesting fact is that the changes in surface gravity have nearly no effect on the Ab(Fe I) versus E.P. relation (see Fig. 3). This means that $\log g$ derived through this method is almost independent of temperature, and vice-versa. This is certainly an advantage of this method, given that temperature and iron abundance are independently well constrained. A clear disadvantage here is that $\log g$ is not very well constrained, due to the reduced number of ionized iron lines compared to Fe I lines. This means that extra caution should be exercised on the derived values of surface gravity. For more details on this issue see Torres et al. (2012).

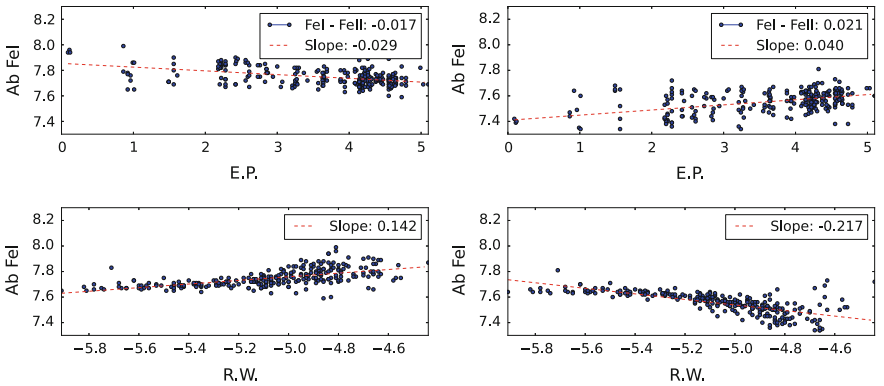

Fig. 4 Same as Fig. 2 but instead of changing temperature, here we change microturbulence to a lower value (0.5 km s^{-1}; *left panel*), and an upper value (1.5 km s^{-1}; *right panel*) than the final ξ_t

4.4.3 Microturbulence Dependence

A final exercise can be made for microturbulence. Again all parameters are set to the "final" values with the exception of the adopted microturbulence. This parameter is connected with the saturation of the stronger iron lines. A good value for microturbulence will allow us to derive the same abundances for weak and strong iron lines.

The left panel of Fig. 4 gives the abundances when the microturbulence is underestimated. The slope of Ab(Fe I) versus R.W. is positive in this case. This means that the "final" value for microturbulence should be higher. The opposite happens when we overestimate microturbulence, as can be seen from the right panel of Fig. 4.

4.4.4 Final Remark

Finally, an additional detail regarding the model atmosphere should be considered. When the final parameters are derived, the resulting iron abundance (derived from the average of the measured line equivalent widths) must be compatible with the metallicity of the model atmosphere.

5 Summary

We have described in practical terms the use of the EW method to derive spectroscopic stellar parameters. We gave a general overview of the several steps required to use this method. We described several options used by different authors, namely the use of different line lists and model atmospheres.

The ARES + MOOG method was described in some detail where we tried to give the best advice for a proper use of it, especially in regard to the use of the ARES code to automatically measure equivalent widths.

The details on how the method finds the "final" set of stellar parameters have been discussed. From the practical point of view, the essential steps of the method were described and can be used as a guideline for future works. Some additional points to fully complete the description of ARES + MOOG were not discussed. These include the minimization algorithm which allows a proper automatization of the full process and the estimation of the uncertainties.

Acknowledgments S.G.S acknowledges the support from the Fundação para a Ciência e Tecnologia (Portugal) and FSE/POPH in the form of the grants SFRH/BPD/47611/2008 and the scientific cooperation project FCT/Poland 2011/2012 (Proc. 441.00 Poland). S.G.S also acknowledges the support by the European Research Council/European Community under the FP7 through a Starting Grant (ERC-2009-StG-239953).

References

Bergemann M, Lind K, Collet R et al (2012) MNRAS 427(1):27
Gray DF (2005) The observation and analysis of stellar photospheres, 3rd edn. Cambridge University Press, Cambridge
Gustafsson B, Edvardsson B, Eriksson K et al (2008) A&A 486:951
Kurucz RL (1993) ATLAS9 stellar atmosphere programs and 2 km/s grid. Kurucz CD-ROM No. 13. Smithsonian Astrophysical, Observatory, Cambridge
Mortier A, Santos NC, Sousa SG et al (2013) A&A 557:A70
Press WH, Teukolsky SA, Vetterling WT, Flannery BP (1992) 2nd edn. Cambridge University Press, Cambridge
Saffe C (2011) Revista Mexicana de Astronomía y Astrofísica 47:3
Santos NC, Israelian G, Mayor M (2004) A&A 415:1153
Sneden CA (1973) PhD thesis
Sousa SG, Santos NC, Israelian G, Mayor M, Monteiro MJPFG (2007) A&A 469:783
Sousa SG, Santos NC, Mayor M et al (2008) A&A 487:373
Sousa SG, Santos NC, Israelian G et al (2011a) A&A 526:A99
Sousa SG, Santos NC, Israelian G et al (2011b) A&A 533:A141
Stetson PB, Pancino E (2008) PASP 120:1332
Torres G, Fischer DA, Sozzetti A et al (2012) ApJ 757:161
Tsantaki M, Sousa SG, Adibekyan VZh (2013) A&A 555:A150